Experimental Investigation of Finite-Sized Inertial Particles Dynamics in Wind Tunnel Grid Generated Turbulence

Muhammad Nauman Qureshi

UNIVERSITÉ JOSEPH FOURIER- GRENOBLE – I

PhD Dissertation

to obtain the grade of

Doctor of Philosophy: UNIVERSITÉ JOSEPH FOURIER

prepared at: **Laboratoire des Écoulements Géophysiques et Industriels**

under l'**Ecole Doctorale de I-MEP2**

Major: **Mécanique des fluides, Energétique, Procédés.**

Entitled as:

Experimental Investigation of Finite-Sized Inertial Particles Dynamics in Wind Tunnel Grid Generated Turbulence

Co-advised by:

Christophe BAUDET & Mickaël BOURGOIN

Presented and Defended Publicly by:

Muhammad Nauman QURESHI

on 4th May, 2009

In Front of Jury Members:

Mr. Yves GAGNE	President
Mr. Zellman WARHAFT	Reviewer
Mr. Alain PUMIR	Reviewer
Mr. Jean-François PINTON	Examiner
Mr. Alex M. TAYLOR	Examiner
Mr. Nicolas MORDANT	Examiner

This dissertation is dedicated to my parents.

Acknowledgements

First of all I thank God, the Almighty, for blessing me with courage, patience, perseverance, and all one needs to accomplish a doctoral dissertation. At this moment in time, when I look back, I see a long list of people who helped me achieve this important milestone in my life and to those I feel obliged to express my gratitude. The first among those is Mr. Gérard Lavergne who initially helped me finding this exciting research work. The lab's ex-director Alain Cartellier, my thesis directors Christophe Baudet and Mickaël Bourgoin are next in the list for accepting me as a doctoral student. I am indebted to the extremely efficient technicians of my lab particularly Mr. Joseph Virone without whose help I could not have conducted my research experiments at such a rapid pace. The always sociable and supportive nature of Mr. Yves Gagne allowed me to discuss anything with him. His time to time guidance meant a lot. I would also like to thank my reviewers, Prof. Zellman Warhaft and Dr. Alain Pumir, whose comments helped me refine my work. I owe special thanks to my friends Asad Hasan for proof reading my thesis and Muhammad Tayyab for helping me compiling it.

Out of all the people I mentioned above, given his contribution and support, I would like to write a few more lines about my co-director of thesis Mr. Mickaël Bourgoin, a person with high moral and ethical values. For me he has been a source of motivation, a morale booster and a great support. At times when I felt down, he talked to me like a friend; mentored me when I was stuck in my work; even buoyed me out of personal problems. I must say that whatever I have been able to do would have been very difficult, if not impossible, had he not been there. I thank him from the core of my heart for all he did for me.

I am thankful to my colleagues, Shyama Prasad Das with whom I discussed and shared a lot of viewpoints and ideas, and Unäi Arrieta for exchanging the richness of his culture and humor.

I owe special thanks to the Pakistani colleagues with whom I shared my moments of grief and happiness, and who have helped me brave the difficult times that I went through during my stay in Grenoble.

I owe unfathomable indebtedness to my parents and wife whose prayers and support remained with me at all times, and my children who are a source of life for me. The country I hail from, very few people are fortunate enough, owing to diverse reasons, to follow through a doctoral degree despite their urge for higher studies. My completing the dream has become possible by courtesy of my parents' and wife's constant support, the Government of Pakistan who sponsored me for my Masters program in France earlier on and the French Ministry of Education for my Doctoral funding.

Resumé en Français

Introduction

Malgré l'accroissement exponentiel des connaissances scientifiques observé au siècle dernier, des problèmes non résolus dans le domaine des sciences et plus particulièrement en physique n'ont toujours pas trouvé de solution; les *Sursauts Gamma* en constituent un premier exemple récent (2003); le plus grand dispositif expérimental (*Large Hadron Collider*) construit pour élucider le "*mystère des tous premiers instants de notre univers*" en est un second encore plus récent. De même, la compréhension de la *Turbulence des Fluides* continue à susciter de nombreux débats, travaux de recherches et expériences. La question de départ ne consiste pas à en donner une description mathématique appropriée mais plutôt de trouver des solutions analytiques aux équations qui la régissent. Grâce aux travaux de Leonhard Euler, Claude L.M.H. Navier and George D. Stokes nous sommes, en effet, capable d'écrire ces équations.

Dans les écoulements Turbulents coexistent une très large gamme d'échelles spatiales, de l'ordre de 10^{23}m dans le cas de la galaxie IC1101 jusqu'à 10^{-1} m dans un film de savon. La complexité des écoulements turbulents, associée à cette multiplicité d'échelles spatiales et temporelles, constitue un enjeu majeur pour les chercheurs comme pour les ingénieurs. Des progrès constants ont été réalisés sur les plans tant théorique, qu'expérimental et numérique depuis le XIX^{ème} siècle et ont permis de mieux comprendre l'origine et la complexité inhérentes à ce phénomène. Plus particulièrement, au cours des dix dernières années, les approches numériques et expérimentales ont connu un essor significatif grâce au développement rapide des moyens de calcul et aux perfectionnements des instruments de mesure.

La plupart des écoulements naturels ou d'origine humaine est de nature turbulente et, parmi ces écoulements, quelques uns sont chargés de particules. Pour ne citer que quelques exemples de tels écoulements, on peut mentionner les gouttes de pluie dans les nuages, la dispersion de polluants en environnement, la dispersion et le mélange de brouillard dans les chambres de combustion, les réacteurs chimiques, la dissémination du plancton océanique, etc ... La question qui est posée dans ce contexte est la suivante : *quel est le rôle joué par la turbulence dans ces écoulements ?* La réponse est simple : comparée à la simple diffusion moléculaire, la turbulence a la propriété remarquable d'augmenter le mélange de quantité de mouvement, de chaleur et de masse. Par conséquent, le transport, le mélange et la dispersion de particules en suspension dans un écoulement porteur dépendent fortement des caractéristiques turbulentes de l'écoulement. Par ailleurs, dans certaines situations ces particules réagissent en retour sur l'écoulement porteur et modifient ses propriétés turbulentes, un phénomène connu sous le nom de *Two-Way Coupling*, c'est à dire une interaction à double sens entre les particules transportées et le fluide porteur. Dans ces situations, de premières réponses à des problèmes simples ont conduit à de nombreuses nouvelles problématiques. Comment définir les phénomènes turbulents ? Comment le transport de particules, leur dispersion et leur mélange sont ils influencés par la turbulence? Quels sont les mécanismes impliqués dans ces effets? En dépit de plus d'un siècle et demi de recherches approfondies, les réponses à ces problèmes ne bénéficient toujours pas d'un cadre de description unifié ce qui limite toujours la précision et la validité des approches empiriques. La raison en est simple : la plupart des études ont reposé sur une description Eulérienne des écoulements, description peu adaptée à l'analyse des phénomènes de transport, de dispersion et de mélange de particules. Pour accéder à des

informations pertinentes sur ces phénomènes, il est intrinsèquement naturel et essentiel de recourir à une description Lagrangienne de l'écoulement fondée sur le suivi dans l'écoulement des trajectoires de points ou de particules fluides [98]. Nous reviendrons en détail, plus loin dans ce chapitre et dans le chapitre suivant, sur l'importance d'une description Lagrangienne des écoulements ainsi que sur le rôle des mesures Lagrangiennes dans l'étude des écoulements turbulents.

L'étude expérimentale que nous présentons repose sur une étude du transport turbulent de particules de taille finie par des mesures Lagrangiennes. Notre objectif principal consistait à explorer l'influence de la taille et de la densité des particules sur leur dynamique de transport par un écoulement turbulent. Toutes les expériences ont été menées à un même nombre de Reynolds et dans la même configuration d'écoulement. La taille et la densité relative des particules ayant été variées de façon systématique, les propriétés statistiques de la vitesse et de l'accélération des particules ont été mesurées et analysées. Après une brève introduction à la phénoménologie de la turbulence dans Chapitre 1 nous discuterons les différents types de particules et les équations qui régissent leurs dynamiques dans le Chapitre 2 Nous évoquerons également dans ce chapitre l'influence du nombre de Reynolds particulaire. Quelques résultats importants concernant l'accélération Lagrangienne des particules seront passés en revue et discutés dans le contexte de notre étude dans le Chapitre 3. Le dispositif expérimental, la configuration de l'écoulement, la, technique de suivi des particules et l'algorithme de traitement des données sont décrits dans le Chapitre 4. Les Chapitres 3 et 4 sont consacrés à la discussion et à l'analyse des résultats expérimentaux de ce travail de recherche. Ces chapitres traitent respectivement des propriétés statistiques de la turbulence en un et deux points (un temps et deux temps).

Chapitre 1

Ce chapitre de revue présente un bref historique de la turbulence. Les différentes échelles de la turbulence sont définies et discutées. Nous décrivons la phénoménologie de Kolmogorov de 1941 (K41) et les lois d'échelles qui en découlent. Ces relations offrent une première caractérisation de la nature multi-échelle du problème et révèlent les difficultés intrinsèques de l'étude de la turbulence. Une étude plus détaillée des échelles turbulentes est présentée en termes d'incréments spatiaux (représentation Eulérienne) et temporels (représentation Lagrangienne) de la vitesse du fluide. Les prédictions de K41 ne sont vérifiées expérimentalement que pour les fonctions de structure (moments statistiques des incréments) d'ordre bas ; à titre d'exemple on peut citer la loi de « 4/5ème » et le spectre en « -5/3 ». Pour les fonctions de structures d'ordre élevé, des déviations par rapport aux prédictions de K41 sont toutefois été observées. Celles-ci caractérisent le phénomène d'intermittence, qui reste l'une des grandes énigmes de la turbulence. L'intermittence se traduit notamment par une signature différente des fluctuations turbulentes selon l'échelle : alors que les fluctuations des incréments de vitesse à grande échelle (spatiale ou temporelle) présentent une statistique gaussienne, les incréments à petite échelle sont fortement non-gaussiens.

Chapitre 2

Nous présentons une revue détaillée de l'état de l'art sur la question de la modélisation de la dynamique de particules dispersées en écoulement turbulent. Les particules sont classées en deux grandes familles selon leur comportement par rapport à l'écoulement porteur : les traceurs (qui se comportent comme des particules de fluide) et les particules inertielles (dont la dynamique dévie par rapport à celle de la phase continue porteuse). Alors que la dynamique des traceurs est décrite par l'équation de Navier-Stokes, écrire une équation du mouvement pour les particules inertielles reste une question ouverte pour laquelle des propositions n'existent que dans certains cas limites. Notamment, dans le cas de particules supposées ponctuelles et avec un nombre de Reynolds particulaire faible, l'équation BBOT (Basset-Boussinesq-Oseen-Tchen), revisitée en 1983 par Maxey-Riley et Gatignol, est la plus couramment utilisée. Des simplifications courantes de cette équation sont ensuite discutées ainsi que diverses corrections empiriques proposées dans la littérature pour le cas où le nombre de Reynolds des particules devient plus grand que 1. Enfin, nous discutons le problème des particules de taille finie et la nécessité dans ce cas d'affiner les modèles existants par la prise en compte de divers facteurs tels que la force d'histoire, les corrections de Faxèn ou encore la force de portance.

Chapitre 3

Nous présentons dans ce chapitre les principaux efforts expérimentaux et numériques, réalisés au cours des deux dernières décennies, concernant la caractérisation des effets de taille et de densité sur l'accélération de particules inertielles en écoulement turbulent. Ces résultats sont rassemblés dans un diagramme représentant l'espace des paramètres (φ, Γ) où φ représente le diamètre des particules considérées adimensionné par l'échelle de kolmogorov de l'écoulement porteur (D/η) et Γ représente la densité des particules adimensionnée par la densité de l'écoulement porteur (ρ_p/ρ_f). Dans le cas de particules traceurs $(\varphi << 1 \; et \; \Gamma = 1)$ les expériences comme les simulations numériques trouvent des statistiques d'accélération fortement non-gaussiennes avec une plus grande probabilité dans les ailes des événements de forte accélération. Dans le cas de particules inertielles, les principales études existantes concernent essentiellement les limites (i) de particules de petite taille et de forte densité $(\varphi << 1 \; et \; \Gamma >> 1)$ ou (ii) de particules éventuellement de grande taille $(\varphi > 1)$ mais faiblement inertielle $(\Gamma \gtrsim 1)$. Dans le cas (i) il est observé que, à mesure que l'inertie des particules augmente, les statistiques d'accélération tendent à devenir gaussiennes et que leur variance diminue de façon monotone. Ce comportement est interprété dans les simulations numériques comme un effet de filtrage temporel de la dynamique des particules dû à l'augmentation de leur temps de réponse. Dans le cas (ii) aucun changement significatif de la signature statistique de l'accélération des particules ne semble être observé lorsque leur inertie augmente.

Chapitre 4

L'étude réalisée dans cette thèse vise à compléter l'espace des paramètres (φ, Γ) présenté dans le chapitre précédent en considérant le cas de particules pouvant être à la fois grandes et beaucoup plus denses que le fluide porteur. Plus précisément nous avons considéré des particules dans les gammes $(10 < \varphi < 26)\ and\ (1 < \Gamma < 65)$. Ce chapitre présente les outils expérimentaux mis en œuvre pour ce travail : écoulement turbulent en soufflerie ; production de particules de taille et densité ajustables ; suivi Lagrangien acoustique des particules. L'écoulement est produit en aval d'une grille dans une soufflerie ; le nombre de Reynolds, maintenu constant tout au long de l'étude, est de l'ordre de 160. Comme particules nous utilisons des bulles de savon gonflées à l'air ou à l'hélium et dont nous pouvons ajuster indépendamment la taille et la densité dans la gamme ci-dessus. Enfin le suivi Lagrangienne est assuré par vélocimétrie Doppler ultrasonore. Nous suivons les particules sur une bonne fraction du temps intégral de l'écoulement porteur tout en résolvant leur dynamique à petite échelle. La fréquence instantanée du signal ultrasonore (image de la vitesse des particules) est extraite par un algorithme paramétrique de type maximum de vraisemblance approchée (MVA). Nous avons analysé 22 séries de données correspondant à autant de points dans l'espace (φ, Γ). Pour chaque série de données plusieurs milliers de trajectoires ont été enregistrées pour une étude fine des statistiques Lagrangiennes de vitesse et d'accélération des particules.

Chapitre 5

Dans ce chapitre nous présentons les résultats concernant les statistiques vitesse et d'accélération en fonction de la taille et de la densité des particules. Dans un premier temps nous analysons les effets de taille finie pour des particules iso-densité avant de présenter les effets conjoints de la taille et de la densité. Nous trouvons que les statistiques de vitesse suivent toujours une distribution gaussienne dont la variance reste identique à celle de l'écoulement porteur (mesurée indépendamment par anémométrie à fil chaud) quelque soit la taille et la densité des particules. Ceci est en contraste avec les prédictions usuelles basées par exemple sur le modèle de Tchen-Hinze. Un effet clair est toutefois observé lorsque les statistiques sont calculées localement à l'échelle de chaque trajectoire : prises individuellement les trajectoires présentent des fluctuations moindres à mesure que la densité des particules augmente. Ce comportement à petite échelle est confirmé par l'analyse fine des statistiques d'accélération. L'accélération normalisée à variance 1 présente une distribution statistique non-gaussienne très robuste, indépendante de la taille et la densité des particules, contrairement aux prédictions usuelles dans l'approximation de particules ponctuelles. Ceci montre que les effets inertiels sur la dynamique particulaire ne sont pas trivialement reliés à l'intermittence (Eulérienne ou Lagrangienne) de l'écoulement porteur. Nous observons une influence notable de la taille et de la densité sur la variance de l'accélération. Dans le cas des particules iso-densité la variance décroît avec la taille des particules selon une loi en $\varphi^{(-2/3)}$. Nous proposons un modèle simple en accord quantitatif avec ces effets de taille finie, basé sur un effet d'intégration spatiale du champ de pression de l'écoulement porteur à l'échelle de la particule. Dans le cas des

particules lourdes à taille fixée, la variance d'accélération décroît avec la densité et atteint, pour les grandes densités une valeur limite dépendant de la taille des particules. De façon contre-intuitive, cette valeur limite augmente avec la taille des particules pour des dimensions proche de l'échelle de Taylor de l'écoulement. Ce comportement ne peut pas être interprété simplement en termes d'un effet de filtrage dû au temps de réponse des particules. Nous proposons une explication qualitative en termes d'un effet d'échantillonnage préférentiel du champ turbulent porteur.

Chapitre 6

Nous nous intéressons dans ce chapitre à l'étude multi-échelle des statistiques Lagrangiennes par une étude détaillée des incréments de vitesse. Nous observons que la dynamique des particules est toujours intermittente (gaussienne à grande échelle et non-gaussienne à petite échelle) quelque soit la taille et la densité. Nous explorons la déformation des PDFs des incréments de vitesse à travers les échelles à partir de l'évolution de leur coefficient d'aplatissement en fonction de l'incrément temporel. Nous trouvons que la signature de l'intermittence Lagrangienne dépend de la nature des particules considérées. Les particules de forte densité présentent notamment une chute abrupte du coefficient d'aplatissement pour des incréments temporels proche de l'échelle de dissipation de l'écoulement porteur. Nous étudions enfin les auto-corrélations de vitesse et d'accélération. Nous trouvons notamment que pour les particules iso-densité le temps de corrélation de la vitesse présente un minimum pour des particules de taille de l'ordre de l'échelle de Taylor de l 'écoulement porteur et que, à taille fixée, le temps de corrélation augmente avec la densité des particules. L'auto-corrélation d'accélération nous permet enfin de définir un temps caractéristique du forçage subit par la particule. Nous montrons que ce temps peut différer par plusieurs ordres de grandeur du temps de Stokes défini habituellement et qu'il reste toujours comparable au temps de dissipation de l'écoulement porteur. Ceci explique pourquoi les modèles basés sur la force de Stokes (tels que ceux couramment employés dans la limite de particules ponctuelles par exemple) ne peuvent décrire correctement la dynamique de particules de taille finie.

Conclusion

L'utilisation conjointe d'une nouvelle technique de vélocimétrie Doppler et d'un dispositif versatile de production de particules nous a permis d'explorer l'influence de la taille et de la densité relative (par rapport à celle du fluide porteur) de particules sur leur dynamique de transport Lagrangien par un écoulement turbulent. Dans le cadre de cette étude nous avons couvert les domaines, jusque là inexplorés, des particules de tailles $10 \leq \varphi \leq 30$ (correspondant au domaine inertiel de la turbulence) et de densités relatives $1 \leq \Gamma \leq 70$. En premier lieu, nous avons étudié en détail les statistiques de la vitesse Lagrangienne et son auto-corrélation. En second lieu, nous nous sommes intéressés aux propriétés statistiques de l'accélération particulaire, cette dernière fournissant une image directe des forces exercées par la turbulence sur les particules. Enfin, nous avons également étudié le phénomène d'intermittence Lagrangienne.

Concernant les statistiques de vitesse Lagrangienne, nous montrons que les distributions statistiques de la composante longitudinale de vitesse suivent une loi de Gauss pour toutes les classes de particules étudiées. Nous constatons que la vitesse quadratique des particules ne dépend ni de la taille ni de la densité relative des particules, contrairement aux prédictions du modèle de Tchen & Hinze et à ses développements ultérieurs [23, 42, 88]. En outre, nous observons que les moments des statistiques à un point de la vitesse Lagrangienne des particules sont identiques aux moments statistiques de la vitesse Eulérienne de l'écoulement porteur. Nos mesures montrent que l'échelle de temps intégrale de la vitesse Lagrangienne pour une même taille de particule dépend de leur densité relative, les particules les plus lourdes ayant le plus long temps de corrélation. Pour des particules iso densités, le temps de

corrélation passe par un minimum lorsque le diamètre des particules est voisin de la micro-échelle de Taylor : $D \sim \lambda$. Ce résultat devra être confirmé par des expériences réalisées à différents nombres de Reynolds.

Les lois de distributions de l'accélération Lagrangienne normalisée sont fortement non Gaussiennes. Après normalisation, nous montrons que ces lois de distributions normalisées sont indépendantes de la taille et de la densité relative des particules dans le domaine que nous avons exploré ce qui confirme la robustesse des statistiques de l'accélération normalisée. Les lois de distribution statistiques obtenues dans nos expériences reproduisent celles obtenues par ailleurs avec des particules de taille inférieure à l'échelle de Kolmogorov ($\varphi \sim 0.01$) dans une expérience analogue en soufflerie [4]. Ce résultat indique que :

(i) si il existe une influence de la taille des particules sur la distribution statistique de l'accélération normalisée comme le prédisent les modèles de particules ponctuelles, celle ci n'est attendue que pour des particules de taille encore plus petite (comme suggéré dans [5]);

(ii) la loi asymptotique de distribution de l'accélération est atteinte très rapidement dès que les particules sont de taille finie.

Une autre constatation intéressante concerne le fait que les distributions statistiques de l'accélération normalisée de particules de taille finie mesurées dans les expériences menées en soufflerie ne coïncident pas avec celles mesurées dans les expériences de type écoulement de von Kármán. Ces résultats soulèvent la question de la (non)universalité de la dynamique de particules de petites tailles : comment les propriétés à grande échelle de l'écoulement (par exemple l'anisotropie, le confinement)

affectent elles la dynamique de particules de petite dimensions (petite échelle) ? Cette question devrait faire l'objet d'études ultérieures.

Contrairement au fait que les distributions statistiques de l'accélération normalisée ne dépendent ni de la taille ni de la densité des particules, nous observons clairement un effet de ces deux paramètres sur la variance de l'accélération. Nous constatons que, pour des particules lourdes, les effets de taille finie ne peuvent être pris en compte ni par une simple extrapolation de la limite de particules ponctuelles lourdes ni par une extrapolation de la limite de particules de taille finie et iso densité. En effet, ces deux limites prédisent une décroissance monotone de la variance de l'accélération avec les effets d'inertie en désaccord avec la tendance que nous avons observée pour des particules lourdes et de taille de finie.

Les effets de taille finie et de densité relative des particules ne peuvent être expliqués par une simple opération de *filtrage* associée uniquement à un effet du nombre de Stokes, comme dans les cas de particules ponctuelles. Un scénario d'*échantillonnage conditionnel*, dans l'esprit des mécanismes de *sweep-stick* paraît plus approprié pour éventuellement décrire l'influence conjointe de la densité et de la taille. Les mesures d'auto-corrélation de l'accélération obtenues pour l'ensemble des classes de tailles et de densités de particules, nous conduisent à penser que le temps de réponse des particules au forçage turbulent est toujours de l'ordre de l'échelle de temps de Kolmogorov. Ce résultat suggère que le temps de réponse effectif des particules est distinct du temps de Stokes habituel qui dans nos expériences varie sur plus de trois ordres de grandeurs.

Les statistiques de l'accélération Lagrangiennes sont intermittentes pour l'ensemble des classes de particules étudiées. Le caractère intermittent de l'accélération dépend de la densité relative des particules. L'influence de la densité relative des particules sur l'intermittence est révélée par l'évolution du facteur d'aplatissement (*flatness*) en fonction de l'incrément temporel sur lequel est calculée la différence de vitesse Lagrangienne. Quel que soit la densité relative des particules, nous trouvons le même facteur d'aplatissement aux plus petites échelles de temps (i.e. l'accélération est la même). En revanche, une dépendance en fonction de la densité relative est mise en évidence lorsque l'incrément temporel augmente : plus les particules sont lourdes, plus la décroissance du facteur d'aplatissement est rapide lorsque l'incrément temporel augmente et passe du domaine dissipatif au domaine inertiel. Ce résultat suggère que :

(i) à petite échelle la dynamique Lagrangienne est contrôlée par le même mécanisme de forçage (très vraisemblablement dominé par le gradient de pression de l'écoulement porteur) indépendamment de la densité relative des particules.

(ii) les effets inertiels associés à la densité relative des particules affectent principalement la dynamique Lagrangienne aux échelles de temps caractéristiques du domaine inertiel de l'écoulement porteur.

Notre étude soulève des questions importantes concernant la dynamique du transport de particules dans les écoulements turbulents. Pour étendre nos résultats il serait intéressant de répéter des mesures similaires à différents nombres de Reynolds de l'écoulement porteur afin, par exemple, de confirmer la diminution du temps de corrélation Lagrangien au voisinage de la condition $D \sim \lambda$ et pour explorer la dépendance en fonction du nombre de Reynolds de l'écoulement de la forme des lois de

distribution statistiques de l'accélération normalisée. En outre, une étude plus détaillée de l'influence des propriétés à grande échelle de l'écoulement porteur (par exemple l'anisotropie et le confinement) sur la statistique de l'accélération des particules s'avère nécessaire. Il serait également intéressant d'étudier la dynamique de particules plus légères que le fluide porteur ($\Gamma < 1$). Les mesures de [90], réalisées sur des bulles d'air dans un écoulement d'eau de type von Kármán suggèrent que cela pourrait aider à valider le scénario d'échantillonnage conditionnel mentionné plus haut puisque l'on peut s'attendre à ce que des particules plus légères que le fluide se concentrent préférentiellement dans les régions de plus forte vorticité et échantillonne ainsi des régions de l'écoulement turbulent complémentaires de celles échantillonnées par les particules lourdes. Pour conclure, nous espérons que cette étude exhaustive pourra contribuer à la prise en compte des effets de taille finie et de densité relative dans les modèles dynamiques existants.

Contents

Introduction

Even with the exponential scientific advancements of the last century, efforts still continue for deciphering the codes of unresolved problems in the field of science and more specifically in physics; the recent being Gamma Ray Bursts (2003); the world's largest experiment undertaken to unravel, yet another so called unresolved mystery of the formation of universe. Similarly, *Turbulence* remains a widely discussed, researched, and experimented problem still to be deciphered. The primary problem doesn't lie in its description, but in finding analytical solution to its governing equations. Thanks to the efforts made by Leonhard Euler, Claude L.M.H. Navier and George D. Stokes we are at least able to write them down.

Turbulent flows are confronted at different length scales from 10^{23}m in case of IC1101 galaxy to 10^{-1} m in soap films. Furthermore, the complex multiple scale nature of turbulent flows both in time and space, makes its investigation a real challenge for both scientists and engineers. However, continuous mathematical, experimental and numerical efforts have been made since nineteenth century to understand its origins and to comprehend the complexities involved herein. Moreover, during the last decade or so, numerical and experimental studies have experienced significant advancements due to the rapid innovation and development of computing and state-of-the-art experimental measuring equipment.

Most of the natural and manmade flows are turbulent and among these flows, several are particle laden. Few examples of such flows include raindrops in the clouds, pollutant dispersion in environment, dispersion and mixing of spray in combustion

chamber, chemical mixers, plankton in oceans etc. The question arises here is, *what role does turbulence play in these flows?* The answer is simple: turbulence has a remarkable tendency to enhance mixing momentum, heat and mass as compared with simple molecular diffusion. Therefore the transport, mixing and dispersion of particles suspended in the carrier flow rely mainly upon the characteristics of turbulent flows. On the other hand, in some particular cases these particles back-react, on carrier turbulent flow and modify the turbulent flow characteristics, a phenomenon which is also known as *Two-Way Coupling*, i.e. a two way interaction between the transported particles and the carrier fluid. But, here simple answers have raised extremely different questions further ahead. How to define these phenomena? How is the particle transport, dispersion and mixing affected by the turbulence? What are the driving factors which imply these changes? Despite a century and half of sincere investigations the answers to these problems still lack basic details and their prediction through empirical approximations still have limited accuracy and validity. The reason again being simple: most of the studies were done using Eulerian description of the flow which is inappropriate to probe the transport, dispersion and mixing phenomena. In order to extract this relevant information it is natural, inherent and essential to use Lagrangian description of flow which involves tracking of fluid, point or material particles along their trajectories [98]. We will revert later to this chapter and the chapter ahead to the importance of Lagrangian description of flow and the role of Lagrangian measurements in turbulent flows in detail.

The present experimental study is on the Lagrangian measurement of the finite-sized particles transported in turbulent flows. Our main objective remained to explore the effects of particles finite size and density on their dynamics in turbulent flows. All

the experiments were performed at same Reynolds number under same flow configuration. The particles size and relative density were varied systematically and their Lagrangian velocity and acceleration statistics were calculated and analyzed. After briefly introducing the phenomenology of turbulence in Chapter 1, the particles classes and their dynamical equations are discussed in Chapter 2. We also discuss the particles finite Reynolds number effects in this chapter. Some important results on the particles Lagrangian acceleration are reviewed and discussed in the context of present study in Chapter 0. The experimental setup, flow configuration, particle tracking technique and data processing algorithm are presented in Chapter 4. Chapter 5 and Chapter 6 are dedicated to the discussion and analysis of results obtained during the present research work. These chapters include the one-time and two-time statistics respectively.

Chapter 1

Turbulence:

Eulerian & Lagrangian Viewpoints

1.1 The Ancient Era Turbulence

The study of turbulence dates back to the fifteenth century, when the picture of turbulence was depicted through an analogy of water surface motion with curly hairs by Leonardo da Vinci. He not only observed this phenomenon but also named it as *"turbolenza"*, his description and sketch on the water surface flow are as under:

"Observe the motion of the surface of the water,
which resembles that of hair,
which has two motions,
of which one is caused by the weight of the hair,
the other by the direction of the curls;
thus the water has eddying motions,
one part of which is due to the principal current,
the other to the random and reverse motion."

FIG. 1.1 - The description of turbulence and a sketch of free water jet emanating from square hole into a pool as drawn by Leonardo da Vinci [32].

Chapter 1

It is very well recognized now that Turbulence is a complex problem; it is even much more complex to define. This is why there exist several definitions of it. Not a single definition is complete and comprehensive, some attribute it as having disorganized chaotic and random behavior others as a problem containing multiple length and time scales, three dimensional and intermittent. Sir Horace Lamb once expressed his views on the complexity and difficulty of studying and explaining turbulence flows by saying:

"I am an old man now, and when I die and go to heaven
there are two matters on which I hope for enlightenment.
One is quantum electrodynamics and the other is the turbulent motion of fluids.
And about the former I am rather optimistic."

Despite all these difficulties of defining and explaining turbulence, we can at least write a mathematical description of the fluid motion which is equally valid for turbulent flows. These flow equations are considered to be the extension of Euler equations and are known as Navier-Stokes equations, named after an eminent French engineer and physicist C.L. Navier and famous British mathematician and physicist G.G. Stokes. These equations for incompressible Newtonian flows in the absence of body forces look like (1.1) which must be used with a condition of mass conservation (1.2) and boundary conditions.

$$\partial_t \vec{u} + (\vec{u}.\vec{\nabla})\vec{u} = -\frac{1}{\rho}\vec{\nabla}p + \nu \Delta \vec{u} \tag{1.1}$$

$$\vec{\nabla}.\vec{u} = 0 \tag{1.2}$$

where, $\partial_t \vec{u}$ is the unsteady acceleration, $(\vec{u}.\nabla)\,\vec{u}$ is the convective acceleration (the nonlinear term). On the r.h.s. we have the gradient of pressure field ($\vec{\nabla} p$) and diffusion due to viscosity ($\nu\,\Delta\,\vec{u}$). Using L, U and ρU^2 as reference length, reference velocity and reference pressure respectively, the normalized variables for fluid velocity, position, time and pressure are defined as $\vec{u}_+ = \frac{\vec{u}}{U}$, $x_+ = \frac{x}{L}$, $t_+ = \frac{tU}{L}$ and $p_+^* = \frac{p}{\rho U^2}$ respectively. The non-dimensional form of (1.1), now can be written as:

$$\partial_{t+} \mathrm{u}_+ + (\mathrm{u}_+ . \nabla_+)\,\mathrm{u}_+ = -\nabla p_+^* + Re^{-1}\,\Delta_+\,\mathrm{u}_+ \tag{1.3}$$

The above equation is completely non-dimensional, where the only parameter taking into account the flow characteristics is the Reynolds number ($Re = UL/\nu$). It can be noticed that a greater Reynolds number leads to the decay of viscous dissipation term as compared with non linear convective term on the l.h.s., hence the flow becomes turbulent due the diminution of viscous damping. The Navier-Stokes equation holds true even for high Reynolds numbers, even when the flow becomes highly unpredictable and chaotic. Or in other words, the symmetries on the basis of which N-S equations were developed are broken in the case of turbulent flows, but these symmetries are somehow regained in a statistical sense [32].

1.2 Scales in Turbulence and Kolmogorovs Theory

1.2.1 The Notion of Scales

The concept of scales in turbulence was first introduced by Lewis Fry Richardson in 1922 [80]. He attributed turbulence as a multiple scale phenomenon which contains

eddies of different sizes and scales. According to him, in turbulent flows the energy is injected through large eddies which are named as energy containing eddies or also known as large scale structures. As these eddies become unstable, they split into many small eddies hence transferring their energy to the smaller ones, this process goes on until the Reynolds number of smallest scale structures becomes unity, resulting in the stability of eddies and hence, their energy is damped through viscous dissipation. The reader naturally ponders here; what are these scales? How these scales are linked to each other? What are the inside mechanisms driving this energy exchange?

" Big whorls have little whorls

That feed on their velocity,

And little whorls have lesser whorls

And so on to viscosity"

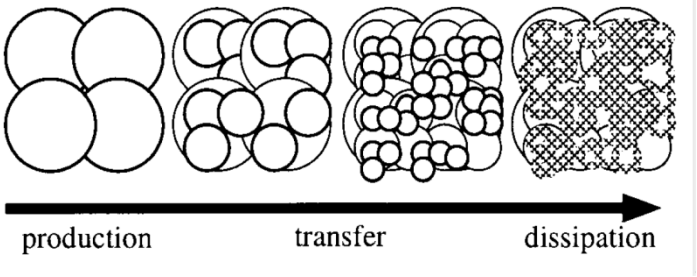

FIG. 1.2 – Richardson's description on the notion of scales in turbulence (left) and Kolmogorov's illustration of Richardson's idea as cascade of scales (right) [54].

The idea of multiple scale nature of turbulence was formulated in the form of theory by A.N. Kolmogorov in 1941. Using a few hypotheses he devised a phenomenological theory which is known as Kolmogorovs Phenomenology of turbulence or in short as K41. Before going into the discussion on the Kolmogorovs phenomenology, which was actually based upon the Richardson's cascade theory, it is essential to define few characteristic length scales that are present in turbulent flows.

i. *Flow length scale or large scale L*: This length scale is the characteristic of turbulence generation mechanism and mostly based upon the flow geometry.

For example, while studying wakes behind a cylinder or sphere, this scale is the diameter of cylinder or sphere; in case of grid generated wind tunnel flow it is the mesh size of the grid etc.

ii. *Integral length scale l_0*: In the developed turbulent flow region the integral length scale corresponds to the size of the largest eddy present therein. The integral length scale can be defined as under:

$$l_0 = \int_0^\infty R_{uu}(x)dx \tag{1.4}$$

where, $R_{uu}(x)$ is the velocity autocorrelation defined as $R_{uu}(x) = \frac{\langle u'(\vec{x})\, u'(\vec{x}+\Delta\vec{x})\rangle}{\langle u'(\vec{x})\, u'(\vec{x})\rangle}$, which could be measured experimentally through hot-wire measurements at a fixed point in space and employing Taylor's frozen turbulence hypothesis for time transformation in space. The Reynolds numbers based on integral length may be defined also as $Re_t = \frac{u' l_0}{\nu}$.

iii. *Dissipative or Kolmogorov length scale η*: This length scale is considered to be the smallest length scale present in turbulent flows at which all the injected energy that was transferred through the intermediate scales dissipates due to viscous dissipation.

iv. *Taylor micro-scale* (λ) *:* This is an intermediate length scale which is much smaller than integral length scale and much greater than dissipative length scale. By definition, the Taylor micro-scale is obtained by fitting the velocity autocorrelation function at $\Delta\vec{x} \approx 0$ by an osculatory parabola. The abscissa where this parabola intersects the x-axis gives the Taylor micro-scale [77]:

$$\lambda = \left(-\frac{1}{2} \frac{\partial^2 R_{uu}(0)}{\partial x^2} \right)^{-1/2} \tag{1.5}$$

From the above definition we can observe that the Taylor micro-scale is related with second order velocity derivative and could also be defined as next:

$$\frac{2u'^2}{\lambda^2} = \left\langle \left(\frac{\partial u}{\partial x} \right)^2 \right\rangle \tag{1.6}$$

One may define another Reynolds number based on Taylor micro-scale as $R_\lambda = \frac{u' \lambda}{\nu}$.

Most of the complexities and the richness of turbulence lie in the range of scales between the integral and dissipative lengths. In this range also known as inertial range; multi-scale structures coexist and interplay in the energy cascade process.

1.2.2 Kolmogorov Theory (K41 Phenomenology)

Kolmogorov's first hypothesis of local isotropy, states that in the case of fully developed turbulence the small scales statistics $(l \ll l_0)$ are independent of their generation mechanisms [46]. This implies the statistical restoration of symmetries which actually were broken by the turbulence generation mechanisms. This is valid for small scale structures away from boundaries. According to this proposition the large

scales may still be anisotropic but the isotropy is recovered at inertial and dissipative scales.

Furthermore, in his first similarity hypothesis Kolmogorov stated that in the limit of high Reynolds number, the statistics of turbulent structures having scales much smaller than integral length scale ($l \ll l_0$) can be universally determined only by viscosity ν and mean dissipation rate ε [47]. In Kolmogorov's phenomenology the characteristic length, time and velocity scales below which the viscous effects dominate are determined through classical dimensional analysis as:

$$\eta = (\nu^3/\epsilon)^{1/4} \tag{1.7}$$

$$\tau_\eta = (\nu/\epsilon)^{1/2} \tag{1.8}$$

$$u_\eta = (\varepsilon\, \nu)^{1/4} \tag{1.9}$$

These dissipative length, time and velocity scales are often named after his name as kolmogorov length scale η, kolmogorov time scale τ_η and kolmogorov velocity scale respectively. The Reynolds number based upon these length and velocity scales verifies the relation:

$$Re_\eta = \frac{\eta\, u_\eta}{\nu} = 1 \tag{1.10}$$

Note, that the above mentioned length, time and velocity are known to be the smallest scales present in any turbulent flow and these represent the smallest eddies which dissipate in the form of heat, all of the energy they have received from larger

structures. The Reynolds number based on these scales is unity which conforms to the energy cascade idea of Richardson.

The second similarity hypothesis of Kolmogorov, states that in every turbulent flow at sufficiently high Reynolds number, the statistics of the motions at inertial range scales $(l_0 \gg l \gg \eta)$ have a universal form independent of viscosity ν and uniquely determined by the energy dissipation rate ε [46].

1.2.3 Inter-Scale Relations

In the light of K41 theory, the integral and dissipation length scales along with the inertial range scales can be related to each other using following fact:

$$\langle \varepsilon_P \rangle = \langle \varepsilon_T \rangle = \langle \varepsilon_D \rangle = \varepsilon$$

where ε_P is the energy production rate, ε_T is the energy transfer rate and ε_D is the energy dissipation rate. The energy dissipation rate corresponding to integral length scale follows $\frac{u'^3}{l_0}$ scaling, whereas the scaling in inertial range with Taylor micro-scale is given by $\frac{u_\lambda^3}{\lambda}$ and finally for dissipative scales it leads to $\frac{u_\eta^3}{\eta}$ scaling. Using the former scaling, the integral and kolmogorov length scales are related in the following manner:

$$Re_t = \frac{u' l_0}{\nu} = \frac{\varepsilon^{\frac{1}{3}} l_0^{\frac{4}{3}}}{\nu}$$

or

$$Re_t^{\frac{3}{4}} \sim l_0 \left(\frac{\varepsilon}{\nu^3}\right)^{\frac{1}{4}}$$

which leads to the following relation:

$$\frac{l_0}{\eta} \sim Re_t^{\frac{3}{4}} \tag{1.11}$$

The link between the Taylor micro-scale and the kolmogorov length scales may be given using the definition of kolmogorov length scale and the following definition of Taylor micro-scale given by [52]:

$$\lambda = \left[\frac{\nu \langle |u'|^2 \rangle}{\varepsilon}\right]^{1/2} \tag{1.12}$$

from where it could be written $\varepsilon = \frac{\nu u'^2}{\lambda^2}$ and using (1.7) yields:

$$\eta \sim \left(\frac{\nu^3}{\frac{\nu u'^2}{\lambda^2}}\right)^{1/4} \sim \left(\frac{\nu \lambda}{u'}\right)^{\frac{1}{2}}$$

then

$$\frac{\eta}{\lambda} \sim R_\lambda^{-1/2}$$

or

$$\frac{\lambda}{\eta} \sim R_\lambda^{1/2} \tag{1.13}$$

Using (1.11) and (1.13), we may relate also integral length and Taylor micro-scale as next:

$$\frac{\lambda}{l_0} \sim \frac{R_\lambda^{1/2}}{R_t^{3/4}}$$

also from the definition of the two Reynolds numbers,

$$\frac{R_\lambda}{Re_t} = \frac{\lambda}{l_0} \tag{1.14}$$

which leads to the following relation between Taylor micro-scale and integral length scale:

$$\frac{R_\lambda}{Re_t} = \frac{\lambda}{l_0} \tag{1.15}$$

Again using (1.13) we may write the scaling between two Reynolds number as under:

$$R_\lambda = Re_t^{1/2} \tag{1.16}$$

Thus we obtain:

$$\frac{\lambda}{\eta} \sim Re_t^{1/4}$$

or

$$\eta \sim \lambda\, Re_t^{-1/4} \tag{1.17}$$

Different length scales discussed reveal the multiple scale nature of turbulence, in addition to which these scales are not independent and linked with each other through certain relations which have been shown in the current section. Furthermore, it was found that Taylor micro-scale follows $\lambda \sim l_0\, Re_t^{-1/2}$ and the kolmogorov length scale is linked with turbulence Reynolds number with $\eta \sim \lambda\, Re_t^{-1/4}$. This implies that for flows with large Reynolds number the inertial range will be much wider than small Reynolds number case and for Taylor micro-scale which corresponds to inertial subrange, we will have $\eta \ll \lambda \ll l_0$. As from the K41 phenomenology the structures in inertial subrange are independent of energy production mechanisms and also

independent of energy dissipation. This is why different experiments and numerical simulations are compared using Reynolds number defined using a scale in the inertial range i.e. the Taylor micro-scale based Reynolds number (R_λ).

For a length scale in the inertial subrange such that $\eta \ll l \ll l_0$, Kolmogorovs second hypothesis of similarity implies that the statistics of second order velocity increments depends only on mean dissipation rate ε. Where the velocity increments (longitudinal component) may be defined as the velocity difference between the two points separated by a distance l and given as:

$$\delta_l u = u(\vec{x} + l.\hat{e}_x) - u(\vec{x}) \tag{1.18}$$

Thus according to K41, the second order longitudinal velocity increments (also known as second order structure function) must be independent of viscosity and follows:

$$S_2(l) \equiv \langle(\delta_l u)^2\rangle = C_2\, \varepsilon^{2/3} l^{2/3} \tag{1.19}$$

where, C_2 is a universal constant of proportionality. Similarly, according to K41 for the higher order moments the velocity structure functions must follow:

$$S_p(l) = \langle(\delta_l u)^p\rangle \sim \varepsilon^{p/3} l^{\zeta_p} \tag{1.20}$$

where, the exponent $\zeta_p = \frac{p}{3}$.

Furthermore, Kolmogorov derived another famous law for the third order structure function. This law is considered to be most exact within the assumptions of homogeneity, isotropy and the finite non-vanishing mean energy dissipation rate ε. This law, known as four-fifth law is given by:

$$S_3(l) \equiv \langle(\delta_l u)^3\rangle = -\frac{4}{5}\,\varepsilon\, l \tag{1.21}$$

Based upon the K41 phenomenology which resulted in the definition of different length scales present in turbulent flows and their relationship, a turbulent energy spectrum can be depicted in the wave number domain. The wave number is defined as $k = {2\pi}/{l}$ and the turbulent energy can be related to wave number as $q = \int_0^\infty E(k)dk$, where q is the turbulent kinetic energy which is given by $q = \frac{1}{2}\langle u_i\, u_i\rangle$. The sketch of turbulence energy spectrum is shown in (a) in which length scales defined above have been shown along with their respective wavenumbers. The width of inertial subrange depends upon the flow Reynolds number, the higher Reynolds number will result in large inertial subrange and the Taylors micro-scale lays herein. In the inertial subrange the energy spectrum $E(k)$ follows a scaling of $k^{-\frac{5}{3}}$ which theoretically can also be shown through simple dimensional analysis. This scaling has been proven correct through numerous experimental and numerical studies of turbulent flows.

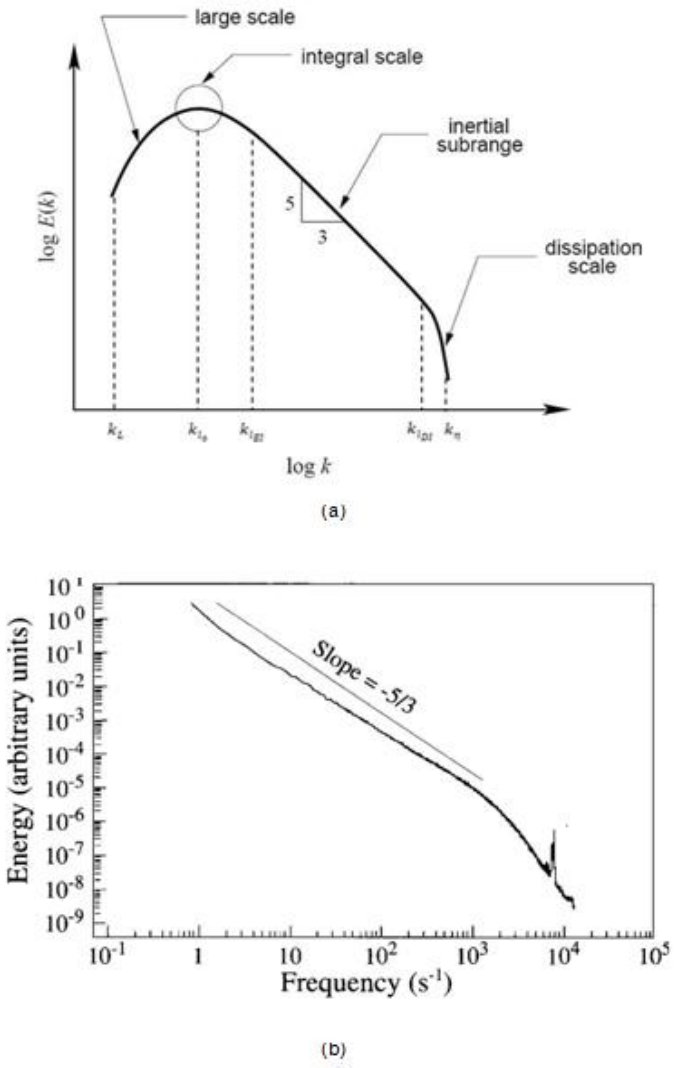

FIG. 1.3 – Turbulence energy spectrum. (a) A sketch showing different length scales (wavenumber domain). (b) Experimentally measured showing a slope of $-5/3$ for at least three decades of frequency [33].

However, in the case of higher order velocity structure functions, if K41 phenomenology is to be considered exact, the exponent ζ_p must vary linearly with the order p. The experimental measurements of the velocity increments have shown deviations from K41 scaling for orders higher than 3 (refer to FIG. 1.4).

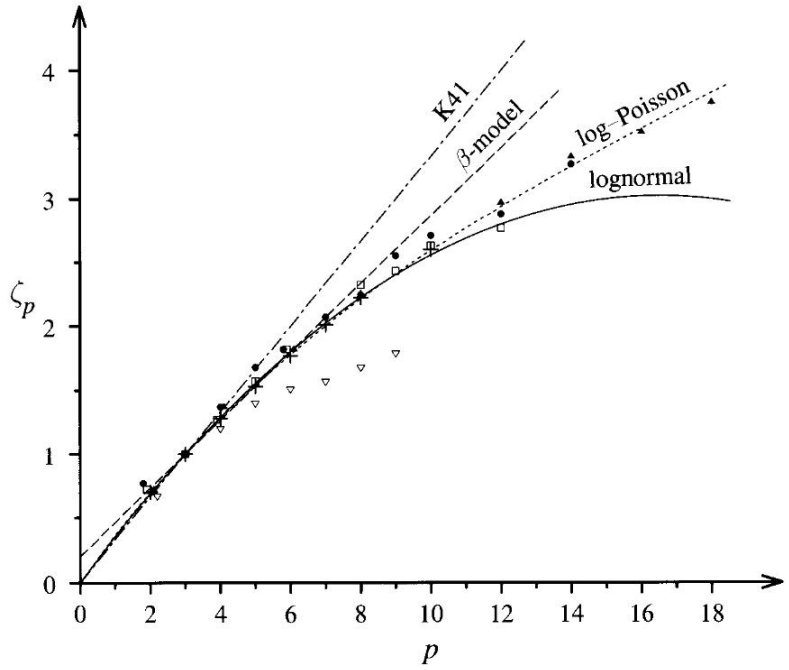

FIG. 1.4 – Variation of exponent ζ_p as a function of order p of the Eulerian velocity structure function. K41 scaling is given in dash-dot line. In shapes are given experimental data which indicates a shift from K41 scaling [32].

This departure from K41 behavior is named as intermittency. Intermittency may also be defined as, or attributed to the difference in statistical signature of velocity increments with respect to their increments or in other words the statistics of velocity increment change with the spatial increment itself. This statistical difference is often examined through the probability density function (PDF hereafter) of the velocity increments. It has been observed that for large spatial increments the distribution is Gaussian while it deviates from Gaussian (PDF tails tend to spread wider hence decaying to zero slower than Gaussian) as spatial increment is decreased. This deformation of Eulerian velocity increments PDFs from gaussian at large scale to non-gaussian at small scales is clearly inconsistent with K41 predictions. For instance, this

can be easily checked by means of the flatness of the velocity increments $\left(\mathcal{F}(l) = \frac{\langle(\delta_l u)^4\rangle}{\langle(\delta_l u)^2\rangle^2}\right)$. K41 predicts $\mathcal{F}(l)$ to be independent of scale l :

$$\mathcal{F}(l) \equiv \frac{C_4 (\varepsilon\, l)^{4/3}}{C_2^2 [(\varepsilon\, l)^{2/3}]^2} = \frac{C_4}{C_2^2} \tag{1.22}$$

while the change of shape of increments PDF across scales shows that $\mathcal{F}(l)$ is a decreasing function of l.

The K41 phenomenology was further questioned by Landau in 1944 with objections being mainly raised upon the validity of constant mean dissipation rate assumption. He stated that the second order longitudinal velocity structure function at a particular instant may be expressed as a universal function of dissipation rate, at that particular instant only. He further supported his argument by highlighting the fact that the energy dissipation rate variations have a characteristic time which is of the order of integral length scale, which could be different for different flows and hence it could not be universal. Kolmogorov and Obukhov in 1962 [73] refined the K41 theory to include intermittency effects, by defining a dissipation rate which was not averaged globally but locally over the volume of sphere having a radius equal to spatial increment l.

1.2.4 Eulerian & Lagrangian Descriptions

Whatever we have discussed so far on the scales of turbulence and the Kolmogorovs phenomenology is based upon the spatial analysis or spatial description of turbulent velocity field. This perspective of spatial study of turbulent flows is known to

be an Eulerian description of flow. The turbulence has been studied through Eulerian viewpoint for long times and it has proven quite useful while predicting the overall flow field properties. Numerous theoretical, experimental and numerical works have been done and are available with this particular description of turbulent flows. In the Eulerian description of flow, the time evolution of flow properties is studied at a fixed point. These spatial measurements at different fixed points form an Eulerian field, or in other words Eulerian flow field is a set of streamlines, and it is described by $\vec{u} = (\vec{X}, t)$. The Eulerian measurements can be done experimentally using hot-wire anemometry, Particle Image Velocimetry (PIV) and Laser Doppler Anemometry (LDA) etc.

Another perspective of studying turbulent flow is Lagrangian which involves the temporal tracking of an individual fluid particle along its trajectory or a group of fluid particles forming an elemental volume along their trajectories. These *"fluid particles"* are indexed by their initial positions at any initial time t_0 by $\vec{x}_i = \vec{X}(\vec{x}_i, t_0)$. Hence the Lagrangian field is a set of pathlines and it can be described by function $\vec{X}(\vec{x}, t)$, which gives, for any time t, the coordinates $\vec{X}$ of all possible *"fluid particles"* identified by the values of some parameter $\vec{x}$. For any time $t > t_0$ the velocity of the fluid particles is therefore given by:

$$\vec{v}(\vec{x}, t) = \left[\frac{\partial \vec{X}\,(\vec{x}, t)}{\partial t}\right]_t \tag{1.23}$$

The Lagrangian and Eulerian velocities can be related with each other using following expression:

$$\vec{v}(\vec{x}, t) = \vec{u}(\vec{X}(\vec{x}, t), t) \tag{1.24}$$

Both Eulerian and Lagrangian flow descriptions are important, necessary and complementary, in order to determine completely the turbulence flow characteristics. Moreover, it depends mainly upon the nature of problem under consideration that favors one approach over the other. Eulerian point of view in turbulence is mainly concerned about the spatial evolution of turbulence, which is dominated by the sweeping effects, whereas the Lagrangian approach enables to access the temporal behavior of turbulence. Furthermore, the Lagrangian description of flow is essential in order to understand basic phenomena which are encountered in turbulent flows. Flows involving transport of material particles, turbulent mixing, dispersion of pollutants in the environment, combustion chamber reacting flows, passive scalar etc. As the mixing of passive scalars and the dispersion of contaminants are dominated by the advection of disorderly velocity fluctuations in time and space, in order to study the turbulent transport it is conceptually natural and practically necessary to use the Lagrangian description of flow, i.e. following the motion of infinitesimal fluid elements or material particles along their trajectories.

In the case of homogeneous flows it can be shown that the velocity statistics remain identical both in Eulerian and Lagrangian descriptions. For example if one measures velocity statistics using an Eulerian technique (as hot-wire anemometry or PIV for instance) to investigate the flow velocity field or a Lagrangian technique (as PTV) to investigate velocity along particle trajectories, the values of mean, root mean square velocities, and more generally the whole velocity PDFs, are the same in both descriptions. This often serves as an important validating point for Lagrangian velocity measurements in comparison with more classical Eulerian measurements.

1.2.5 Lagrangian Predictions of K41

The Kolmogorov phenomenology could also be molded for Lagrangian framework. The temporal increments of velocity are therefore given as under:

$$\delta_\tau \vec{v} = \vec{v}(t+\tau) - \vec{v}(t) \tag{1.25}$$

In a similar fashion than K41 Eulerian predictions we can write the pth order Lagrangian structure function as following:

$$S_p^L \equiv (\delta_\tau \vec{v})^p = C_p^L (\varepsilon \tau)^{\zeta_p^L} \tag{1.26}$$

where, $\zeta_p^L = \frac{p}{2}$ according to K41 Lagrangian predictions.

A case with particular interest is when $p = 2$, as the second order Lagrangian structure function S_2^L is directly related to important statistical quantities like the Lagrangian velocity autocorrelation $\left(R_{vv}^L(\tau) \equiv \frac{\langle \vec{v}(t)\vec{v}(t+\tau)\rangle}{\langle \vec{v}(t)\vec{v}(t)\rangle} = 1 - \frac{S_2^L}{2\langle \vec{v}(t)\vec{v}(t)\rangle}\right)$ and the Lagrangian energy spectrum $E_\omega^L \equiv T.F.(R_{vv}^L)$. From the Lagrangian velocity autocorrelation we can define the Lagrangian integral time scale:

$$T_L = \int_0^\infty R_{vv}^L(\tau)(\tau) d\tau \tag{1.27}$$

Moreover, it is essential to highlight the time scaling in Lagrangian turbulence between the integral and kolmogorovs time scales, which in short is given as:

$$\frac{T_L}{\tau_\eta} \sim Re_t^{1/2} \sim R_\lambda \tag{1.28}$$

In the context of K41 phenomenology for inertial range time scales ($T_L \ll t \ll \tau_\eta$) the second order structure function follows the scaling:

$$S_2^L \equiv (\delta_\tau \vec{v})^2 = C_2^L \, \varepsilon \, \tau \tag{1.29}$$

which corresponds to Lagrangian energy spectrum:

$$E(\omega) = \frac{C_2^L}{\pi} \, \varepsilon \, \omega^{-2} \tag{1.30}$$

This has been observed experimentally and reported by Mordant et al. in [68, 70] and also shown here in FIG. 1.5.

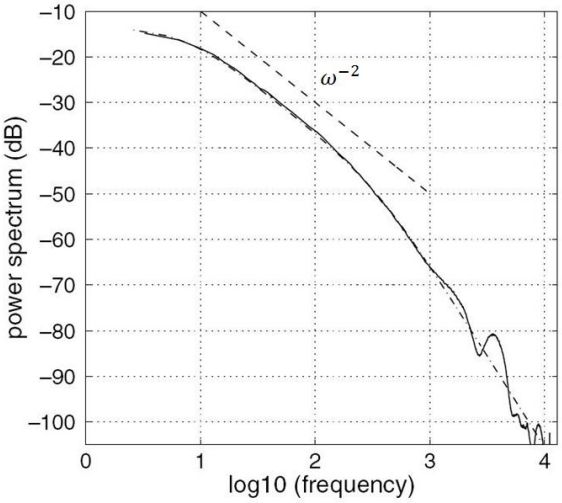

FIG. 1.5 – Lagrangian Turbulence spectrum as obtained by Mordant et al. [68, 70]. Dashed line represents the Kolmogorovs Lagrangian scaling for energy spectrum of ω^{-2}.

Concerning the higher order structure functions experimental and numerical studies [41, 67, 68, 70, 95] have revealed that for moments $p > 2$, the K41 scaling for ζ_p^L deviates very quickly from K41 prediction $\zeta_p^L = \frac{p}{2}$ (refer to FIG. 1.6). This

observation gives a notion of Lagrangian intermittency. It has been observed that the deviation from linearity of exponent ζ_p^L are much more pronounced than ζ_p^E, though a relation between ζ_p^L and ζ_p^E has been proposed in the context of multi-fractal models [12, 11, 18].

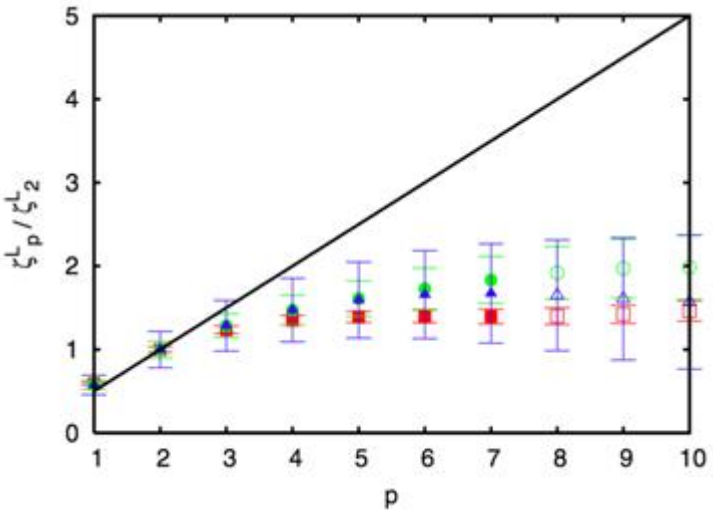

FIG. 1.6 – Evolution of scaling exponent ζ_p normalized with scaling exponent of 2nd order ζ_2 as a function of order p. Solid line indicates the K41 scaling for Lagrangian velocity increments. In circle, triangle and square are shown the normalized exponents determined from experimentally measured Lagrangian velocity statistics [95].

Relation (1.28) together with relations ((1.11) and (1.16)) quantify the complex spatio-temporal multiple scale nature of turbulent flows, and indicate why investigation of turbulence (in particular Lagrangian measurements) in high Reynolds number flows, is so difficult. For instance for $R_\lambda = 1000$ to perform an accurate investigation of the whole range of inertial scales both in space and time these relations show that a dynamical resolution over 3 decades of time and more than 4 decades in space is required. Such spatio-temporal higher resolution measurements have only become

possible in the last decade thanks to the development of state-of-the-art optical and acoustical techniques. It is worth noting that the same constraints apply to the numerical simulations. This also explains the difficulties to perform high Reynolds number Direct Numerical Simulations due to extremely high computational cost and very long computational time.

We have discussed in the current chapter the Eulerian and Lagrangian predictions of K41 phenomenology for fluid particles. In most of the particle laden flows, we encounter the inclusions of '*material*' particles which possess physical mass, boundaries and hence volume. In this case the dynamics of material particles is described by specific governing equations. In the next chapter we review these governing equations for dispersed particles dynamics in turbulent flows.

Chapter 2

Equations Governing Dispersed Particle Dynamics in Turbulent Flows

Research on 'dispersed particle dynamics in continuous phase', leads to several diverse situations; known so far, these situations can be mainly characterized by three parameters. The first, is the nature of carrier flow or continuous phase, the second is attributed to the kind of particles (dispersed phase) being transported in the flow and the third is the volume fraction of the dispersed phase. All of these contribute significantly in defining the particle transport in the flow and hence the physical phenomena involved herein. In the case of particle motion in a steady and uniform flow it is easier to write a simple equation of particle motion with certain hypotheses, which could be fairly justified in most of the cases. On the other hand the spatio-temporal complexity of the turbulent flows restrains the domain of validity of these equations and assumptions, as non-linear terms appear in these equations which cannot be neglected. From the dispersed phase point of view, the problem is even worse. In the limit of fluid particles or tracers (particles behaving as fluid particles), use of the well known Navier-Stokes equations provides a good understanding of turbulent forcing. Numerous questions arise when the particle's relative velocity and/or its diameter becomes finite. In addition to that, some more challenges are awaiting attention in cases where dispersed phase volume fraction is higher than a certain limit; a limit that allows not only the interaction from turbulent flow to the particle, but also the modulation of the

continuous phase by the particles itself (i.e. two-way coupling). Particle volume fractions higher than this limit further complicate these interactions.

In short, the author would like to say that modeling particle dynamics in a turbulent flow seems to be a very complicated problem. Even if a number of significant efforts make possible the writing of model particles equation of motion, their range of applicability is not wide and their validity is not well established. Furthermore, the hypotheses involved are strongly questioned sometimes always confronting a researcher's mind, whether to use these models or not.

In spite of the fact that turbulence is a complex problem, we still know that turbulent flows are governed by Navier-Stokes equations; but unfortunately we do not know how to resolve these equations in general. In the case of particle transport in turbulent flows, the situation becomes even worse, as we do not even know how to write the equation which describes their dynamics (except for some particular cases).

The main objective of this chapter is to review in detail the models or equations which govern particle motion in continuous phase. The main question addressed here will allow us to highlight some important issues while evaluating turbulent forcing $\vec{F}_{turb}$ on the transported particle, which is simply written as $m_p \vec{a} = \vec{F}_{turb}$, where m_p and $\vec{a}$ are the particle's mass and acceleration respectively. It should be noted that particles acceleration gives a direct measure of turbulent forcing experienced by them; therefore the main emphasis of the experimental and numerical studies has always been its determination.

In the next section a brief characterization of particles will be done based upon their dynamical behavior in the carrier fluid or upon which the models of particle motion equations are based. We will briefly summarize the literature relevant to our objectives, along with experimental and numerical efforts done so far, in order to capture the physical phenomena involved in particle dynamics.

2.1 Particle Types in Turbulence

In the framework of studying particle transport in turbulent flows, the particles can be coarsely classified into two main types; first which tag the fluid motion perfectly; and second which resist obeying the fluid particle motion. The first class of particles is known as fluid tracers as they behave like fluid particles which can be used in determining the fluid particles velocity field using particle imaging techniques (PIV, LDV, PTV etc.). The second kind is the one that doesn't follow fluid motion and has a tendency of not tracking the fluid particle motion; such type of particles is known as inertial particles. Of course there are reasons for showing such behavior. In case of fluid tracers the particles have a density, same as that of the carrier fluid (i.e. neutrally buoyant) and their size is much smaller than the smallest scale of the corresponding turbulent flow, the kolmogorov length scale η; this is why the dynamics of these particles reflects the fluid particles motion. Few examples of tracer particles used in water flows are small colloids (generally made of polystyrene), which can be fluorescently tagged (using rhodamine or flourescein for example) or made phosphorescent. On the other hand there could be several reasons for which the inertial particles do not tag the fluid particles. First, the inertial particles may have a

density which is not the same, as compared with the carrier fluid (heavier or lighter particles); second, their size may be greater than the kolmogorov length scale (finite size); other reasons may be related to the shape and deformability of the particles in case the particles are not perfectly rigid such as vesicles. The problem is much more complex when the particle seeding density is high enough that two-way coupling effects arise. Several groups studying particle dynamics have used different types of particles, the choice of which depends upon the nature of experimental setup and the particle dynamics to be investigated. For example, in case of air being the carrier fluid, in a vertical wind tunnel flow Snyder & Lumley have used spherical beads of different kinds like hollow glass, corn pollen, glass and copper [86], Fessler & Eaton have also used glass and copper spheres [28], another group at Cornell has used water droplets in an active grid turbulence [4], in our case we have used soap bubbles [78, 79]. In case of water: gas, fluid and solid particles have been used by different research groups. The examples include the use of; gas bubbles in the case of [58, 91]; oil emulsion by [31]; glass particles by [70, 90, 94]; glass, steel and tungsten carbide spherical balls in the experimental setups of [71, 97].

Our main concern in this chapter is to probe and discuss the forces exerted by the carrier flow on the particles and how this forcing changes as we change particle types. Furthermore, we want to discuss the models that already exist for predicting particle motion and briefly discuss their limitations.

2.2 Particle Dynamics Equations

2.2.1 Fluid Particles or Tracers

The dynamics of fluid particles or tracers (i.e. the particles having density the same as that of carrier fluid and size smaller or equal to the kolmogorov length scale of turbulence) is governed by simplified Navier-Stokes equation. Particle acceleration and hence the forcing experienced by these particles is given as:

$$\vec{a} = -\frac{\nabla p}{\rho} + \nu \Delta \vec{v} \tag{2.1}$$

In the above particular situation, the particles act as fluid tracers and experience large magnitudes of accelerations. The DNS of [89] have also shown that fluid particle acceleration can be described through (2.1). They have also observed that the contribution of this acceleration due to viscous forces term is very small compared with the pressure gradient contribution in (2.1), being only 7.6% for small Reynolds case they have studied ($R_\lambda = 21$) and this reduces gradually with the increase in Reynolds number and drops to only 1.6% in case of $R_\lambda = 235$. These results attribute the intermittent behavior of fluid particle acceleration to pressure gradients. Same behavior for tracer particles acceleration has also been observed in the experimental studies of [49, 66, 91, 92]. Large magnitudes of accelerations observed by the particles are due to the fact that being neutrally buoyant and having size smaller or equal to kolmogorov length scale, these particles experience velocity fluctuations of all scales, up to dissipative ones. Several numerical and experimental results on fluid particles and tracers acceleration along with their interpretations will be discussed and compared

with other particle types in the next chapter; here we will restrict ourselves up to dynamical equations only.

2.2.2 Inertial Particles

For particles with diameter in sub-kolmogorov scale range, the inertial effects are observed if the particle density is not the same as that of carrier fluid. In case of heavier particles, these particles resist or tend to resist the velocity fluctuations exerted by the fluid on them. Particles with size greater than kolmogorov scale do not behave as fluid particles too, even if their density is same as that of carrier fluid i.e. the neutrally buoyant finite-sized particles are not tracers [92]. They exhibit inertial effects which are mainly due to their finite size. Further complications to such size and density effects are related to the collective effects; a special case in which either the inertial particles are seeded into the flow with high frequency or the seeded particles sample themselves in the carrier flow in a specific way hence forming high particle concentration zones, in which they start interacting with each other in addition to the carrier flow [2]. These collective effects result in increase of particles settling velocity and modulation of turbulent flow due to their presence. We will cover these effects in a bit more detail in the next chapter; here our emphasis will only be on reviewing their dynamical equations and models. As mentioned earlier, the particles can show inertia due to two main reasons or effects:

i. *Density Effects:* Particle density being different than the carrier phase, $\rho_p \neq \rho_f$.

ii. *Size Effects:* Particle size larger than the smallest scale of turbulence, $d_p > \eta$.

In case of inertial particles there exist certain models that can approximate particle dynamics in an unsteady non uniform flow. One of the main parameters in this

study is the particles Reynolds number Re_p , which is the Reynolds number based upon the relative velocity of the spherical particle and the fluid velocity at the position of particle's center as if the particle is not present in the flow and its diameter:

$$Re_p = \frac{d_p \left\| \vec{u} - \vec{v}_p \right\|}{\nu_f} \tag{2.2}$$

where, d_p is the particle diameter, $\left(\vec{u} - \vec{v}_p\right)$ is the particles velocity relative with the carrier flow or slip velocity and ν_f is the kinematic viscosity of the fluid. In the limit of creeping flows i.e. $Re_p \ll 1$, we fall to the simplified case of Stokes flow (steady solution), where the force exerted on the particle is only the viscous drag in the absence of non linear advection term in the Navier-Stokes equations. This condition of $Re_p \ll 1$ could hold true only if the particle diameter is sufficiently small and/or its relative velocity is adequately small. Most efforts concerning the modeling of particles dynamics have been carried in the limit of small particles (point like particles) with $Re_p < 1$. We will first describe this limit before discussing the finite size corrections.

2.2.2.1 Point or Numerical Particles

The first transient equation for the particle motion in a uniform flow was derived by Basset (1888) [8], Boussinesq (1885) [13] and Oseen (1927) [74] also known as BBO equation (BBO hereafter). The BBO equation is however valid only for an isolated, non-rotating, small (point), rigid, and spherical particle under the hypothesis of creeping flow. Several corrections were made to BBO equation by Odar & Hamilton [39] in case of finite particles Reynolds number $0 \leq Re_p \leq 62$, which we will address later in this

section. The most rigorous equation for the dynamics of point particles in a non uniform creeping flow with zero initial relative velocity is considered to be the one given by Gatignol [34] and Maxey-Riley [55]:

$$m_p \frac{d\vec{v}_p}{dt} = 3\pi\mu_f d_p \left(\vec{u} - \vec{v}_p + \frac{1}{24} d_p^2 \nabla^2\vec{u}\right) + \frac{1}{2} m_f \frac{d\left(\vec{u} - \vec{v}_p + \frac{1}{24} d_p^2 \nabla^2\vec{u}\right)}{dt} + m_f \frac{D\vec{u}}{Dt} + \frac{3}{2} d_p^2 \sqrt{\pi \rho_f \mu_f} \int_{-\infty}^{t} \frac{d\left(\vec{u} - \vec{v}_p + \frac{1}{24} d_p^2 \nabla^2\vec{u}\right)}{dt} \frac{d\tau}{\sqrt{t-\tau}} + \left(m_p - m_f\right)\vec{g} \quad (2.3)$$

where, $m_f = \rho_f \pi \frac{d_p^3}{6}$ is the mass of the fluid displaced by the particle and μ_f is the carrier fluids dynamic viscosity. The terms on the r.h.s. in the order of appearance are:

- The Stokes drag force, which is due to the relative velocities of particle and fluid.
- The added mass force (also known as virtual mass force), purely an inertial force which is the force exerted by the fluid displaced by the particle resisting particles acceleration and deceleration.
- The pressure gradient term, this is equivalent to the fluid particle acceleration at the position of the particle center.
- The history term, which takes into account the entire history of the particle motion in the carrier fluid up to time instant t and it mainly takes into account the interaction of the particle with its own wake.
- The Archimedes force, which is the net force due to gravity and buoyancy.

The derivatives $\frac{d\vec{v}_p}{dt}$ and $\frac{d\vec{u}}{dt}$ are taken along the *material* particle trajectories, whereas $\frac{D\vec{u}}{Dt}$ is the material or Lagrangian derivative representing the fluid element acceleration along fluid particles. One can notice an additional term $\frac{1}{24}\, d_p^2\, \nabla^2\vec{u}$ appearing with the relative velocity terms which is firstly due to the non-uniformity of the fluid velocity field and secondly, due to the disturbances created in the flow field by the particle. These second order corrections for the curvature of the flow field are known as Faxén terms or Faxén corrections proposed by Faxén in 1922 [25], indeed taken into account in 1983. On the other hand the Faxén terms has a scaling of $\frac{d_p^2}{L^2}$ (where L is the characteristic length scale of the unperturbed flow) which in case of $\frac{d_p}{L} \ll 1$ can be easily neglected. The spatial derivatives in the preceding equation are calculated at the particle center, which in case of uniform velocity fields becomes zero, hence reducing above equation to BBO equation.

The Gatignol and Maxey-Riley equations for point particles looks very complex to model, therefore, different groups doing DNS [9, 10, 17, 49, 83, 90] have proposed simplified models taking into account only the Stokes drag force or in some cases the added mass force too [90].

$$\frac{d\vec{v}_p}{dt} = \beta\, \frac{D\vec{u}}{Dt} + \frac{1}{\tau_p}\left(\vec{u} - \vec{v}_p\right) \tag{2.4}$$

where, $\beta = 3\rho_f/(\rho_f + 2\,\rho_p)$ is the coefficient taking into account added mass and pressure gradient forces and $\tau_p = d_p^2 \,/\, (12\,\beta\,\nu_f)$ is the particle viscous response time. When the above equation is made dimensionless with kolmogorov length, time and velocity scales i.e. η, τ_η and u_η respectively; it resembles the following form:

$$\vec{a} \equiv \frac{d\vec{v}_p}{dt} = \beta \frac{D\vec{u}}{Dt} + \frac{1}{St}\left(\vec{u} - \vec{v}_p\right) \tag{2.5}$$

In above dimensionless equation, $St = \tau_p / \tau_\eta$ is the particle Stokes number, and acceleration is in non-dimensional units, given also by Heisenberg-Yaglom [65] famous relation based upon kolmogorov phenomenology,

$$a_0 = \frac{\langle a^2 \rangle}{\varepsilon^{3/2}\, \nu^{-1/2}} \tag{2.6}$$

where, a_0 is also known as normalized acceleration variance. We can observe from

(2.5) that point particles acceleration is mainly described by two dimensionless parameters β and St. The degree of the particles inertness is described with the help of Stokes number, which is the ratio of particles response time and the appropriate flow characteristics time scale (τ_η in present case). The greater the particle response time or Stokes number, the greater will be the inertness exhibited by the particle. The role of parameter β is to take into account the particle density effect in the added mass term, for the particle density equal to, or close to carrier fluid's $(\rho_p \approx \rho_f)$, this term reduces to fluid particle acceleration. On the other hand for $\rho_p \gg \rho_f$ it becomes very small but could be still compared with Stokes drag force. In case of bubble flows with particles lighter than carrier fluid this term becomes dominant. Whereas, the particle's response to fluid velocity fluctuations is taken into account using Stokes number.

2.2.2.2 Finite Reynolds Number Effects

The Gatignol and Maxey-Riley equation is considered to be the most accurate for describing particle motion in a non-uniform creeping flow, assuming reasonable hypotheses that will be satisfied under most of the two-phase flows experienced in physical and engineering world. However, there are some particular situations where the particles Reynolds number is finite or moderate. This could either be due to the large particles relative velocity and/or large particles size (i.e. particle diameter larger than kolmogorovs length scale). The case of finite particles Reynolds number was first addressed in 1964 by Odar & Hamilton and up until the present this has been area of prime interest. We will discuss these effects term by term:

I. Drag Force $(\vec{F}_D)$

The drag force can generally be written as:

$$\vec{F}_D = \frac{1}{8} C_D(\vec{u} - \vec{v}_p)\, \pi\, d_p^2\, \rho_f \left\|\vec{u} - \vec{v}_p\right\| \left(\vec{u} - \vec{v}_p\right) \tag{2.7}$$

We have omitted the Faxén corrections for the time being, the steady drag coefficient in above expression can be obtained from standard drag curve. In case of finite Reynolds number, this drag coefficient is invalid and becomes particles Reynolds number dependent. The modified form of drag force is hence given by:

$$\vec{F}_D = \frac{1}{8} C_D(Re_p)\, \pi\, d_p^2\, \rho_f \left\|\vec{u} - \vec{v}_p\right\| \left(\vec{u} - \vec{v}_p\right) \tag{2.8}$$

Several empirical relations for particle Reynolds number based drag coefficient exist. Among them the best fit to the experimental observations for a range of particle Reynolds number is the one given by Clift et al [19]. Clift et al have given seven different

expressions for drag coefficients for different ranges of particles Reynolds number. The only disadvantage of their correlations is the unavailability of a single expression which could be valid for the whole range of particles Reynolds number. These coefficients for first three Reynolds number ranges are given as:

$$C_D = \begin{cases} \dfrac{24}{Re_p} + \dfrac{3}{16} & \text{for} \quad Re_p \leq 0.01 \\ \dfrac{24}{Re_p}\left[1 + 0.1315\, Re_p{}^{(0.82 - 0.05\, log_{10}\, Re_p)}\right] & \text{for} \quad 0.01 < Re_p \leq 20 \\ \dfrac{24}{Re_p}\left[1 + 0.1935\, Re_p{}^{0.6305}\right] & \text{for} \quad 20 < Re_p \leq 260 \end{cases} \tag{2.9}$$

Mei & Klausner [61] have also proposed an empirical correlation based upon their numerical study, however, the most effective is considered to be the one given by Brown & Lawler [14]. In their review of drag and settling velocity of spherical particles, they have fitted all the data available and they have also found that best fit of drag coefficient is obtained through empirical relations proposed by Clift et al. Moreover, they have proposed another expression for drag coefficient which satisfactorily fits the data for particles Reynolds up to 2×10^5 :

$$C_D = \frac{24}{Re_p}\left[1 + 0.150\, Re_p{}^{0.681}\right] + \frac{0.407}{1 + \dfrac{8.710}{Re_p}} \qquad \text{for} \qquad Re_p < 2 \times 10^5 \tag{2.10}$$

Using above empirical correlation for drag coefficient, we can have a better estimate of drag force exerted on the particle for large range of particles Reynolds number.

II. Added Mass Force $(\vec{F}_{AM})$

Omitting again the Faxén corrections of the Gatignol and Maxey-Riley equations; the added mass force is given by:

$$\vec{F}_{AM} = \frac{1}{2}\ m_f\ \left(\frac{d\vec{u}}{dt} - \frac{d\vec{v}_p}{dt}\right) \tag{2.11}$$

The above term was same in the case of BBO equation, the first correction to above term was made by Odar & Hamilton [39] for finite Reynolds number $0 \leq Re_p \leq 62$, by determining experimentally the added mass coefficient for sudden and gradual particle accelerations in a viscous fluid.

$$\vec{F}_{AM} = m_f\ C_A \left(\frac{d\vec{u}}{dt} - \frac{d\vec{v}_p}{dt}\right) \tag{2.12}$$

where, C_A is the added mass coefficient determined to be $C_A = 1.05 - \frac{0.066}{0.12+A_c^2}$, with $A_c = \frac{\|\vec{u}-\vec{v}_p\|^2}{d_p} \Big/ \frac{d\|\vec{u}-\vec{v}_p\|}{dt}$ being the acceleration number taking into account the particles acceleration effects on the added mass coefficient. Auton et al in 1988 [3] have proposed the following form of added mass term:

$$\vec{F}_{AM} = m_f\ C_A \left(\frac{D\vec{u}}{dt} - \frac{d\vec{v}_p}{dt}\right) \tag{2.13}$$

Auton et al have also proposed a value of $C_A = \frac{1}{2}$ for spherical particles. Another important difference is the use of fluid acceleration calculated following a fluid element, rather than following the particles trajectory. This difference i.e. $\left(\frac{D\vec{u}}{dt} - \frac{d\vec{u}}{dt}\right)$ is considered to be negligible in creeping flows, but could become significant in the case of

finite particles Reynolds number case, because particles contain inertia which could not be neglected. This difference vanishes also in uniform flow case too. Further discussions on the added mass force for finite Reynolds number case could be found in [60]. The results of Numerical simulations of Rivero et al 1991 [81], Mei et al 1991 [64], and Chang & Maxey 1994 [15] have shown that added mass force for finite Reynolds number flows is same as that of creeping and potential flows which is also given by Auton et al. with $C_A = \frac{1}{2}$.

In a recent numerical simulation Wakaba & Balachandar [7] have also studied the dependence of added mass coefficient on particles Reynolds and acceleration number. For a range of acceleration numbers studied, they have shown that irrespective of Re_p and A_c the added mass coefficient for a sphere is 0.5, within an accuracy of 0.1%. They have also claimed that the added mass coefficient is shape-dependent rather than on Re_p and A_c. These results were supported in detail, with discussions for three different cases, drastic particle acceleration, gradual small acceleration and abrupt particle deceleration. The acceleration or deceleration was applied in a very short time interval of $\Delta t = 2.5 \times 10^3$. The reason for obtaining same added mass coefficient value for the above three cases was due to the prevailing effects of potential flow over the sphere. In their studied case of quick particle acceleration (Fig. 2 a-f in [7]), they have found that the wake which was present behind the sphere before applying particle acceleration first moves to the rear after shrinking of separation line and then as the time passes the wake is completely detached from the sphere without being reversing towards the sphere. Later on this circulation zone becomes very small and escapes from the flow domain. A new wake is supposed to form corresponding to new particles

Reynolds number (after being accelerated), this development however takes place on slow viscous time scale. In the second case, where the particle was gradually accelerated to a small value by increasing particle Reynolds number from 50 to 50.625 in a very short time, they observed the wake which was present on the back of the sphere (Fig. 3 a-c in [7]) before accelerating is tends to detach and then finally detaches from sphere later at a time which correspond the end time of acceleration application. After the particle underwent the applied acceleration the wake again reattached to the sphere and remained attached to it. Even when the recirculation zone detaches from the sphere it never moves rear and remains close to the sphere and after the end of acceleration application it reattaches which means no significant change in flow topology is observed which will lead to a changed magnitude of added mass coefficient. In their last case i.e. of quick deceleration by decreasing particles Reynolds number from 50 to 37.5, they have observed an interesting phenomenon. The wake which was present behind the sphere, on the application of sudden deceleration moves upstream and surrounds the whole sphere and the flow topology behave as a potential flow, while the sphere is being enveloped by the recirculation zone (Fig. 3 a-c in [7]). After reaching the final Reynolds number and attaining the steady conditions this recirculation zone retracts and again over the viscous time scale reaches its settled state corresponding to final Re_p. These observations have proven quite useful verifying the concepts and findings of Rivero et al. [81], Mei et al. [64] and Chang & Maxey [15, 16] and known so far to be the recent development on the Reynolds and acceleration number effect on added mass force.

III. History Force $(\vec{F}_H)$

From BBO, Gatignol and Maxey-Riley equations it can be observed that the memory of particle acceleration decays as $(t-\tau)^{-1/2}$.

$$\vec{F}_H = \frac{3}{2} d_p^2 \sqrt{\pi \rho_f \mu_f} \int_{-\infty}^{t} \frac{d\left(\vec{u} - \vec{v}_p\right)}{d\tau} \frac{d\tau}{\sqrt{t-\tau}} \tag{2.14}$$

Odar and Hamilton have proposed a coefficient for this diffusive history force too which is also a function of particle acceleration number. Mei et al. [64], Mei & Adrian [63] and Mei 1994 [62] have been studying the motion of rigid spherical particles and bubbles having finite Reynolds numbers. Mie et al. in 1991 have observed that for particles having finite Reynolds number the history force decays as $(t-\tau)^{-1/2}$ at short time, but for large times, the decay is much faster than $(t-\tau)^{-1/2}$. From the equation of spherical particles proposed by Mei & Adrian 1994; the history force terms is given below:

$$\vec{F}_H = 3\,\pi\,\mu_f\,d_p \int_{-\infty}^{t} K(t-\tau,\tau)\,\frac{d\left(\vec{u} - \vec{v}_p\right)}{d\tau}\,d\tau \tag{2.15}$$

where, the history kernel is given by,

$$K(t-\tau,\tau) = \left\{ \left[\frac{4\,\pi\,(t-\tau)\,\nu_f}{d_p^2}\right]^{1/4} + \left[\frac{\pi\left|u(\tau) - v_p(\tau)\right|^3}{d_p\,\nu_f\,f_H^3\,(Re_t)}\,(t-\tau)^2\right]^{1/2} \right\} \tag{2.16}$$

where $f_H(Re_t) = 0.75 + 0.105\,Re_t(\tau)$; $Re_t(\tau) = d_p \left\| u(\tau) - v_p(\tau) \right\| / \nu_f$. The history kernel given above, decays slowly as $(t-\tau)^{-1/2}$ for short times and then for long time this decays is much drastic which follow the law $(t-\tau)^{-2}$. These

observations were further confirmed during experimental measurements of Mordant et al. [71] and Abbad & Souhar [1] while studying settling of spherical finite sized particles in water.

The Maxey-Riley equation was derived under the assumption of zero initial relative velocity of the particle. However, in the case when particle's initial relative velocity is non-zero Maxey in 1993 [56] added another term in Gatignol and Maxey-Riley equations for creeping flows. This additional term is given by $3/2\, d_p^2 \sqrt{\pi\, \mu_f\, \rho_f}\ (u(0) - v_p(0))/t^{1/2}$. This term is however valid only for creeping flows. In the case of finite particle Reynolds and acceleration numbers Kim et al. 1998 have proposed another history force term kernel. Their expression for history kernel is very robust and reduces to the one given by Mei & Adrian for high acceleration numbers. On the other hand, for low values of acceleration number their history term reduces to Basset history force term. Based upon their DNS results, Kim et al. [45] have also catered for particles finite Reynolds and acceleration numbers into the term added by Maxey in 1993. The reader is referred to their paper for further details and discussion.

IV. Shear Lift Force $(\vec{F}_L)$

Another force which was actually present neither in BBO nor in Gatignol and Maxey-Riley equations is the shear lift force. As turbulent flows contain eddies and velocity gradients at different scales, the lift force becomes important if particles size is of the order or greater than the kolmogorov length scale. Due to the presence of this velocity gradient the particle is subjected to a shear lift force which is also known as

Saffman's lift force named after his work [82]. The expression for Saffman lift force is hence given by:

$$\vec{F}_{L-Saff} = 1.615\,\rho_f\,\nu_f^{1/2}\,d_p^2\,\|\,(\vec{u}-\vec{v}_p)_x\|\,\sqrt{du/dy}\;\;\sin(du/dy) \tag{2.17}$$

The expression (2.17) was assumed to hold valid for $Re_p \ll 1, Re_G = \frac{G\,d_p^2}{\nu_f} \ll 1$, where $G = \left|\frac{du}{dy}\right|$, $Re_\Omega = \frac{\Omega\,d_p^2}{\nu_f} \ll 1$ and $Re_p \ll \sqrt{Re_G}$ or $\varepsilon = \frac{\sqrt{Re_G}}{Re_p} \gg 1$, where Ω is the particles spin velocity. Dandy & Dwyer 1990 [21] studied the shear lift force for finite Reynolds number ($0.1 \le Re_p \le 100$) and finite shear rate ($0.005 \le Re_p \le 0.4$) defined as,

$$\alpha = \frac{d_p\,\left|du/dy\right|}{2\,\|\,(\vec{u}-\vec{v}_p)_x\|} = \frac{1}{2}\,Re_p\,\varepsilon^2 \tag{2.18}$$

They have shown that the Saffmans shear lift force expression is equally valid for $Re_p > 1$, $Re_G > 1$ and $Re_p > \sqrt{Re_G}$. However Mei (1992) [59] found some differences in Dandy & Dwyers and Safmans results and proposed following expression for finite Reynolds number of the particles:

$$\frac{F_L}{F_{L\,Saff}} = \left(1 - 0.3314\,\alpha^{1/2}\right)\exp\left(-Re_p/10\right) + 0.3314\,\alpha^{1/2} \quad \text{for} \quad Re_p \le 40$$

$$= 0.0524\,(\alpha\,Re_p)^{1/2} \quad \text{for} \quad Re_p > 40 \tag{2.19}$$

The above expressions are considered to be most accurate for finite Reynolds numbers of spherical particles. However, care should be exercised in using these

expressions only for non-rotating particles i.e. $Re_{\Omega} = 0$. In case of particles rotation on its own axis or if particles relative rotating velocity is non-zero then another contribution of lift force should be taken into account which is also known as Magnus lift Force.

In this chapter we have briefly overviewed the equations which govern dispersed spherical particles motion in continuous phase. The equations given by Gatignol and Maxey-Riley are considered to be the most complete and most well known in the limit of creeping flows along with certain assumptions. We have also tried to present the key modifications made in these equations for the case of finite particles Reynolds and acceleration numbers. In the following chapter we will discuss the numerical and experimental results obtained while studying the particle dynamics in turbulent flows. Our emphasis will mainly rely upon the Lagrangian measurements of particles acceleration, as it directly provides the answer to the question of finding turbulent forcing on the particle.

Chapter 3

Lagrangian Acceleration Statistics:

Experimental & Numerical Investigation

In the previous chapter we have reviewed the equations governing dispersed particles dynamics in turbulent flows. Models which already exist for describing dynamics of several particle classes being transported in continuous phase were discussed, along with corrections made into Gatignol and Maxey-Riley equations. Also, discussed in the first chapter in order to obtain particle instantaneous acceleration it is essential to track these particles along their trajectories or in other words, Lagrangian measurements are unavoidable in these circumstances.

In the current chapter, we will outline key experimental and numerical Lagrangian measurements done so far for the determination of particle acceleration. After, presenting a brief review of histories of these types of measurements, we will discuss in moderate detail the results obtained in the past two decades. It has been observed that the inertial particle acceleration results in their accumulation into specific zones of the flow known as preferential concentration. This will be briefly reviewed, before diverting our discussion towards the main interest and motivation of the present research work.

In order to have an overview of key results obtained through experimental efforts done in the area of Lagrangian measurements of particle dynamics in turbulent flows, we start with presenting FIG. 3.1. In this figure, we show, in (φ, Γ) space different cases studied experimentally both in von Kármán and grid generated turbulent flows. Here φ, is the particle diameter to kolmogorov length scale ratio, D/η and Γ is the particle density to carrier fluid density ratio ρ_p/ρ_f. The color intensity indicates the particles Stokes number, which is also the ratio of the particles response time and an appropriate flow characteristic time as defined in equation (3.8) of section 3.2.2.

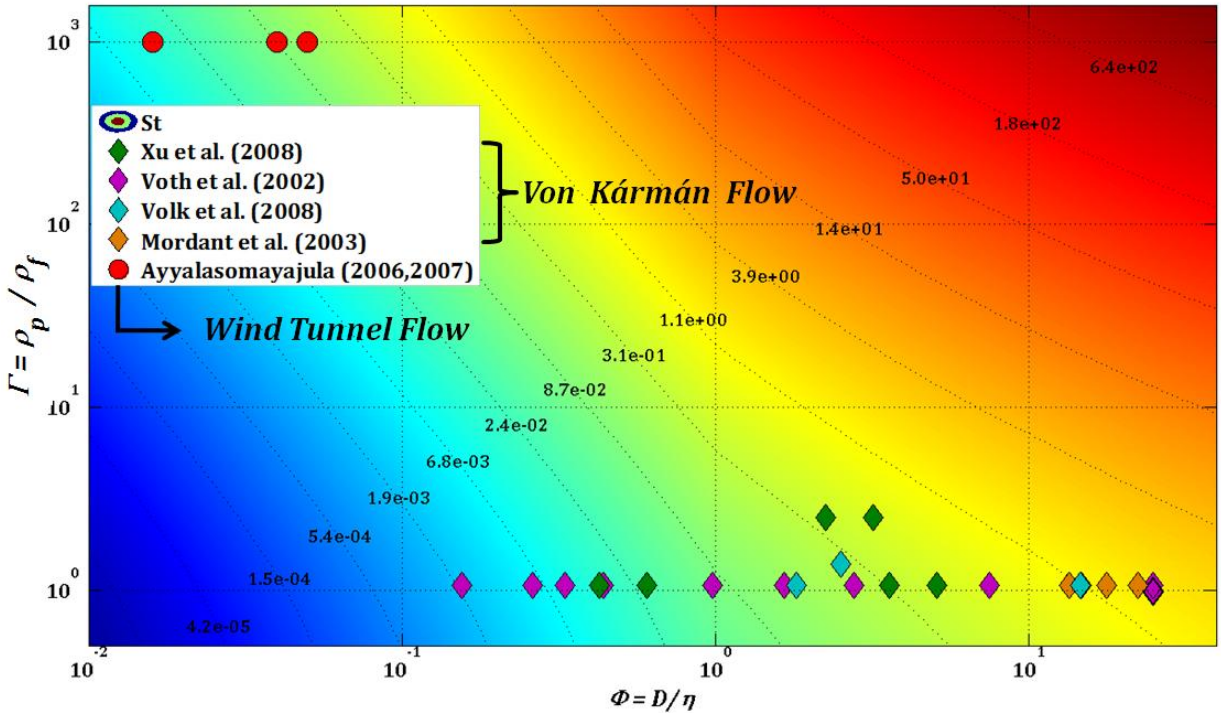

FIG. 3.1 – Some examples of experiments in Lagrangian measurements of particle dynamics in (φ, Γ) space where φ and Γ are the particle diameter to kolmogorov length scale and particle density to carrier fluid density ratios respectively. The color intensity shows the magnitude of particles Stokes number, blue being low and red being high particle Stokes number. Iso-Stokes lines are shown in curve dotted lines with their corresponding Stokes number.

I review experiments in (φ, Γ) space in chronological order. Voth et al. in 2002 [92] have studied in von Kármán water flow the particles Lagrangian acceleration using optical tracking technique. The types of particles studied were; tracers ($\varphi \sim 0.15 \rightarrow 1$) for $140 \leq R_\lambda \leq 970$; and finite-sized particles ($\varphi \sim 1.44 \rightarrow 26$) in fully developed turbulence with $R_\lambda = 970$. Later on Mordant et al. in 2003 [67]; have also investigated the Lagrangian statistics of neutrally buoyant finite-sized particles again in von Kármán water flow at three Reynolds numbers of 312, 740 and 1100, but here they employed Acoustic Doppler Velocimetry as measuring technique. Ayyalasomayajula et al. [4, 5] have studied in a different flow configuration (active grid turbulence) the dynamics of inertial particles (tiny water droplets in air) having very small φ and very high values of Γ at $R_\lambda = 250$, again the optical particle tracking method was used. Recently in 2008, Volk et al. [90] have studied the dynamical behavior of tracers, neutrally buoyant and heavy particles. They also studied the acceleration statistics of lighter bubbles. All of their experiments were performed at $R_\lambda = 850$ in von Kármán water flow as well, using novel measuring technique of Extended Laser Doppler Velocimetry. The (φ, Γ) space was further filled by Xu et al. [94] tracking small tracers, finite-sized neutrally buoyant and slightly heavier particles optically at two different Taylor based Reynolds numbers of 370 and 460. Xu et al. also proposed a modified definition of particles Stokes number which we will discuss in the upcoming section.

On the basis of results obtained during the Lagrangian determination of particles acceleration we can classify particles dynamics into different categories. In the subsequent sections we will discuss in detail these results, class by class, including some

DNS and a few other experimental results, which were omitted in FIG. 3.1 for the reason of clarity.

3.1 Fluid Particle Acceleration

Dynamics of fluid particles and tracers is described by (2.1). The DNS of Vedula & Yeung, Gotoh & Fukayama and Biferale et al. [10, 37, 89], have observed wide spread tails and intermittent dynamics of fluid particles. Specifically, Vedula & Yeung have shown that the normalized acceleration variance a_0 follow a scaling of $a_0 \propto R_\lambda^{1/2}$ for $R_\lambda > 40$. They have also observed that the contribution of this normalized acceleration variation; due to viscous forces term is very small as compared with pressure gradient contribution in (2.1). They have shown the contribution of pressure gradient term in a_0 is one order of magnitude greater than the viscous force term in (2.1). Moreover this pressure gradient term contribution becomes greater and greater as they increased the R_λ and becomes two orders of magnitude greater than the viscous force term contribution for $R_\lambda = 235$, the highest Reynolds number they have studied. They have further supported their results by studying PDFs of pressure gradients, which is also shown in FIG. 3.2(a) where pressure gradient is normalized with its standard deviation, symbols A to D represent R_λ of 38, 90, 140 and 235 respectively. The Reynolds number dependence of pressure gradient PDFs can be clearly observed in FIG. 3.2(a), with wider stretched tails for higher Reynolds number. It is to be noted that for the highest R_λ the PDF decays more slowly than the exponential. These results attribute the intermittent behavior of fluid particle acceleration to pressure gradients.

Biferale et al. [10] in their DNS study for fully developed turbulent 3D flow at $R_\lambda = 284$ have obtained intermittent dynamics of fluid particles Lagrangian velocity

increments. The PDF of their Lagrangian velocity increments for difference time lag is shown in FIG. 3.2(b). For the smallest time lag the velocity increment reflects fluid particles acceleration. It has also been observed that the fluid particle acceleration has wide spread tails. They have assigned this behavior due to the trapping of fluid particle in vortex filaments (FIG. 3.3(a)). Because of the trapping of fluid particles in vortex filaments, the particle observes intense acceleration and velocity fluctuations, and undergoes acceleration up to 30 the rms value. On the other hand, in an experimental study of fluid particles acceleration, La Porta et al [49] have seeded neutrally buoyant particles with size of the order of kolmogorov length scale $\varphi \sim 2.5$ for $R_\lambda = 970$ (the highest Reynolds number case they have studied in a stirred tank von Kármán flow). The three dimensional particle trajectories, resolved in time, were tracked using high temporal resolution technique, an example of which is shown in FIG. 3.3(b). It can be seen that the particle experience intense acceleration magnitudes of the level of 12000 $m.s^{-2}$. For all studied Reynolds numbers $140 \leq R_\lambda \leq 970$, the normalized acceleration PDFs have wide stretched tails with maximum value up to 40 rms (FIG. 3.4(a)) and particles undergo accelerations up to 16000 $m.s^{-2}$.

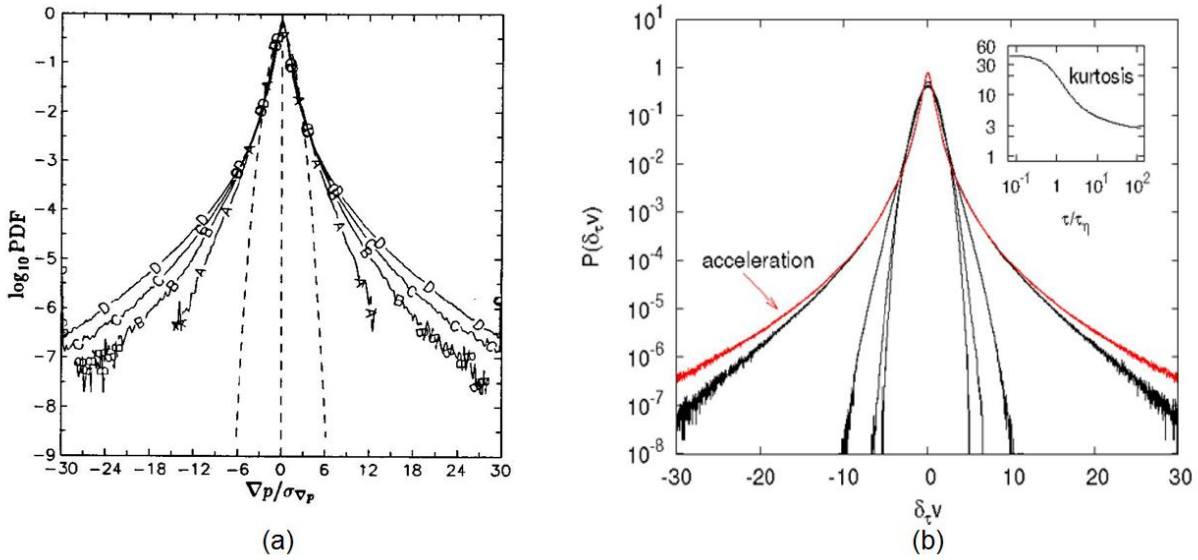

FIG. 3.2 – (a) PDF of pressure gradients, symbols from A-D show R_λ of 38, 90, 140 and 235 respectively. Gaussian distribution PDF is shown in dashed lines [89]. (b) Velocity increments and acceleration PDFs computed at different time lags (97, 24, 6, 0.7) τ_η from inner to outer PDF, acceleration is in the outermost curve [10].

LaPorta et al. have also observed that flatness of particle acceleration PDF increases as R_λ increases and probably saturates to a constant value for $R_\lambda \sim 500$ (see inset of FIG. 3.4(a)). The evolution of normalized acceleration constant a_0 (given by equation (2.6) as a function of R_λ is shown in FIG. 3.4(b), the open circles and squares indicate transverse and axial components of normalized acceleration, whereas filled triangles and circles show the normalized acceleration values computed by Vedula & Yeung and Gotoh & Fukayama respectively. It has been detected that in comparison with DNS studies of Vedula & Yeung and Gotoh & Fukayama; LaPorta et al. have observed higher values for a_0.

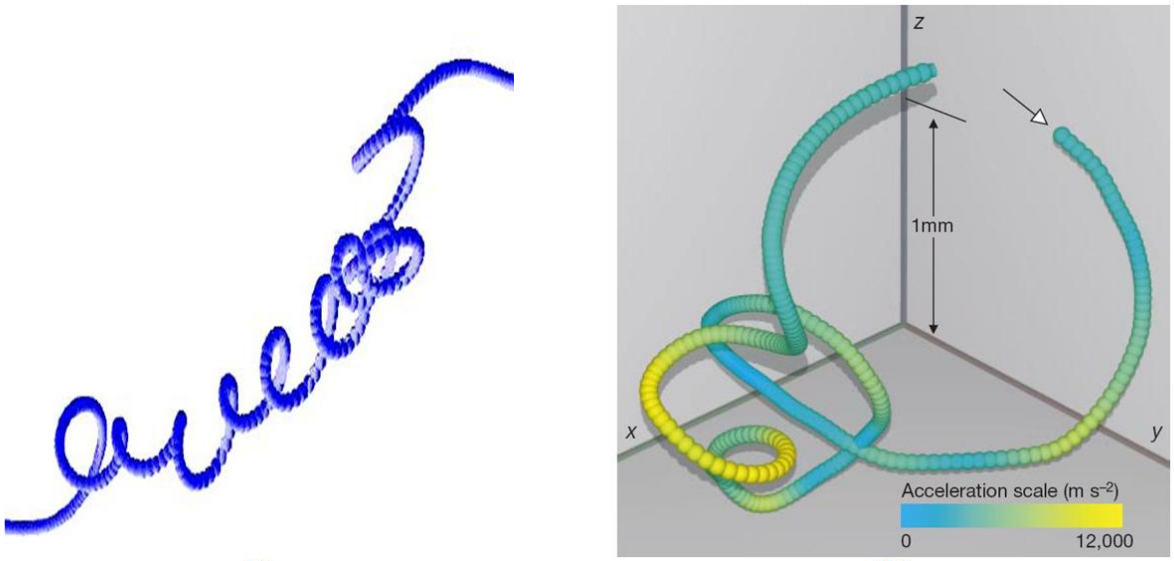

FIG. 3.3 – (a) Three dimensional trajectory of a fluid particle trapped in a vortex filament [10]. (b) Three dimensional trajectory of a neutrally buoyant seeded particle resolved in time [49], colors show the acceleration magnitude.

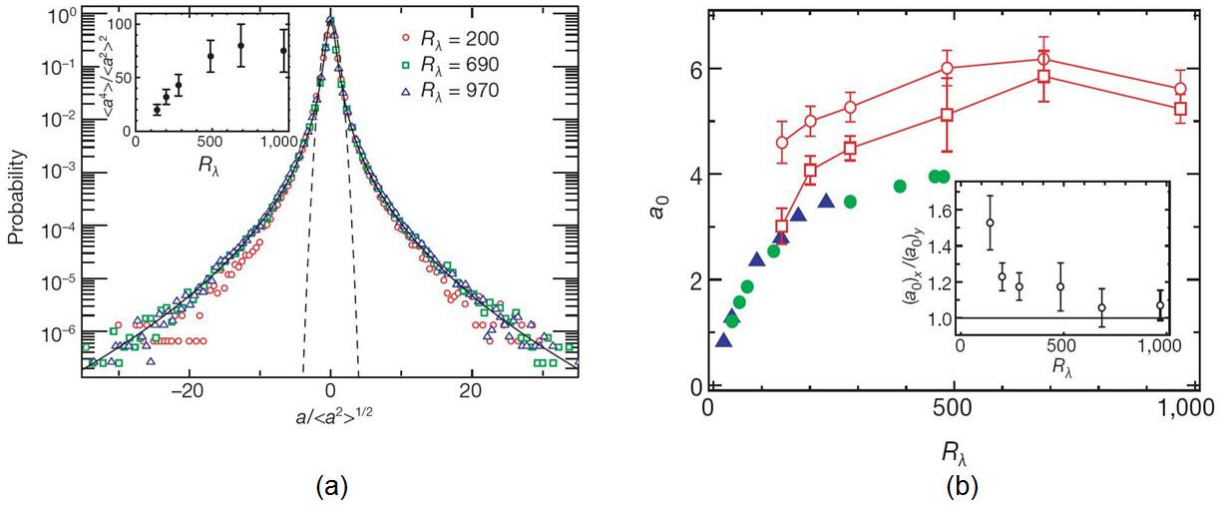

FIG. 3.4 – (a) Acceleration PDFs normalized to variance 1, for R_λ 290, 690 and 970, Gaussian distribution is shown in dashed curve. The inset shows the acceleration flatness as a function of R_λ [49]. Normalized acceleration variance for transverse (open red circles) and axial (open red squares) components as a function of R_λ, in the inset the ratio of normalized transverse and axial acceleration variances as a function of R_λ[49].

The ratios of transverse and axial components of normalized acceleration are shown in the inset of FIG. 3.4(b). Higher values for normalized transverse acceleration components were obtained, as compared to the normalized axial ones, which signify the small scale anisotropy of the von Kármán flows. However, this small scale anisotropy decreases with increasing Reynolds number with ratio that reaches near to 1 asymptotically for highest Reynolds number studied.

Moreover, Mordant et al. [68] have also measured the Lagrangian velocity statistics in fully developed turbulence with $R_\lambda = 740$, in a counter-rotating water flow experiment. They have used neutrally buoyant particles of diameter $250\mu m$ and observed high levels of particle acceleration. Their PDFs of Lagrangian velocity increments, scaled with its standard rms value (FIG. 3.5(a)), also have stretched tails, which for the largest time increment has Gaussian distribution and becomes wider and wider while decreasing the time increment. However, they observed that the tails for smallest time increment are not exponential, like the one obtained for fluid particle acceleration by LaPorta et al., a fact which at that epoch was considered to be possibly due to the filtering effects of the finite-sized particles.

In another experimental study yet again in von Kármán flow at Cornell, Mordant et al. [66] have obtained very high magnitudes of normalized acceleration, where the acceleration flatness reaches up to 55 or even higher, up to 100 [69] (FIG. 3.5(b)). The Reynolds number being $R_\lambda = 690$, near to their previous experiments the high levels of acceleration magnitudes could be due to the smaller particle diameter as compared with kolmogorov length scale.

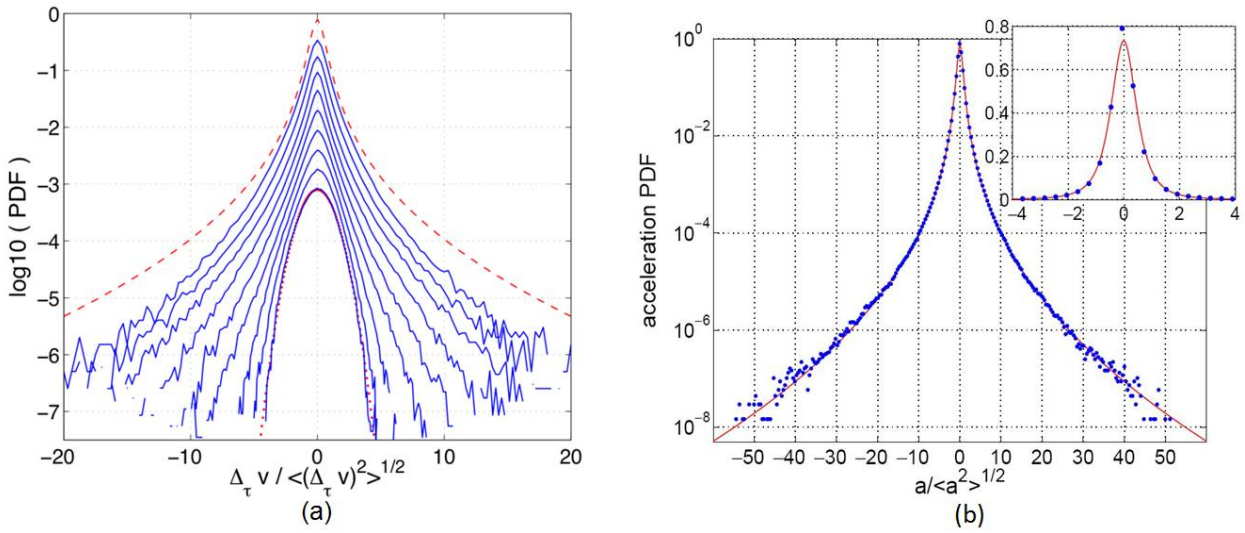

FIG. 3.5 – (a) Lagrangian velocity increments PDFs normalized with rms values for time increments of 0.15, 0.3, 0.6, 1.2, 2.5, 5, 10, 20 and 40 ms (from top to bottom) [68]. Curves are shifted vertically downwards for clarity. The red dashed line represents acceleration obtained by LaPorta et al. (b) PDFs of normalized acceleration for tracers at $R_\lambda = 690$ [66], the red solid line represents the exponential fit given by LaPorta et al., the inset shows the plot in linear coordinates.

In this section we have very briefly reviewed some numerical and experimental results obtained for fluid and tracer particles acceleration. It has been observed that the acceleration PDFs have wide spread exponential tails as particles undergo intense acceleration magnitudes up to 55 times the root mean square value. It has also been learned that Lagrangian velocity statistics are intermittent and the velocity increments PDFs change their shape from Gaussian, for the largest time lag, to have wide spread exponential tails for smallest time increment. Biferale et al. have credited these intense acceleration values as being due to the trapping of fluid or tracer particles in a vortex filament. Not all of the results are discussed here; a few remaining results on fluid particles and tracers acceleration will be discussed in subsequent sections, while comparing these particles with inertial material or point particles.

3.2 Inertial Particles Acceleration

Inertial particles are named after their inert behavior which they exhibit by not following the fluid solicitations perfectly. This could be due to the carrier fluids and particles density mismatch or due to the larger particles diameter than kolmogorov length scale. It is well known now, that the dynamics of finite size neutrally buoyant particles is not the same as that of tracers, again some exceptions exist which have been demonstrated in several experiments.

The dynamics of these inertial particles has been a subject of interest since 1971 and several efforts have been made in order to explore heavy particles behavior in turbulent flows [20, 27, 50, 51, 55, 85, 86]. It has been observed numerically [87, 93, 96] that the inertial particles have a tendency to accumulate in low vorticity and high strain regions of turbulent flow. This has resulted in the formation of zones with high particle concentration, the phenomenon also named as preferential concentration. The question has been raised, whether this preferential concentration of particles due to turbulence, reduces or restricts heavy particles mixing or not?

Wang & Maxey [93] have observed that in the presence of gravity turbulence has a mean effect of sweeping particles in the downward direction thus increasing the settling velocity of these particles. Furthermore, Aliseda et al. [2] have also observed the increase in settling velocity of the inertial particles as a function of stokes number (FIG. 3.6(a)). They have obtained high values of settling velocity near particles Stokes number of unity. Their further investigation on the concentration fields of the particles has revealed that the particles do not sample the turbulent flow homogeneously. They tend to concentrate preferentially into the low vorticity zones in the flow. This

preferential concentration of particles into the flow results in the formation of clusters of particular size (FIG. 3.6(b)). They have also given a notion of the size of these clusters which is of the order of $10 \rightarrow 15\eta$ based upon the study of particles concentration using digital imaging.

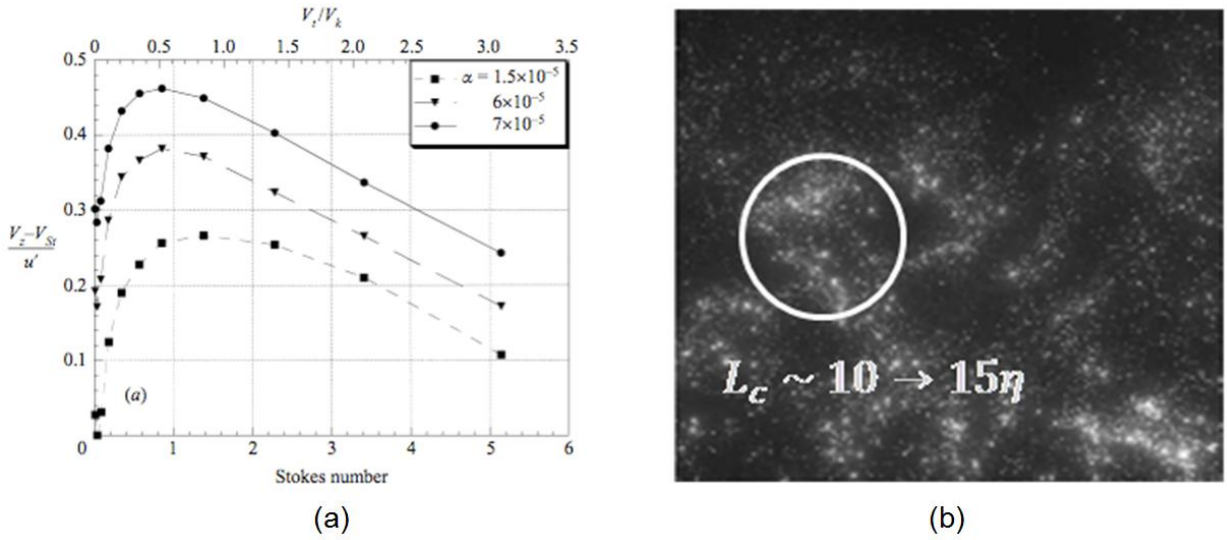

(a) (b)

FIG. 3.6 – (a) Variation in particles settling velocity normalized by fluctuating velocity of the flow as a function of Stokes number for three different volume fractions of seeded particles. One can observe the high values of near Stokes number of unity [2]. (b) The image showing particles concentration field, high particle concentration results in the formation of cluster with characteristic size of $10 \rightarrow 15\eta$ [2].

3.2.1 Point Particles Acceleration

In the case of numerical simulations the inertial particle dynamics is taken into account through (2.4), which includes Stokes drag term, which in turn, includes particles response time and the added mass term that takes into account the inertial effects due to particles added mass. When the particles are considered to be very small in diameter and much heavier than the continuous phase, the added mass term has been mostly neglected [9, 17] and the equation used in this case has the following form:

$$\frac{d\vec{v}_p}{dt} = \frac{1}{\tau_p}\left[\vec{u}(x_p\,, t) - \vec{v}_p(t)\right] \tag{3.1}$$

where, $\vec{v}_p(t)$ is the particles velocity at its position x_p at time t and $\vec{u}(x_p\,, t)$ is the fluid velocity field. In this limiting case, which can also be named as point or numerical particles case, the particles dynamical behavior is mainly described by their response time or in case of normalized equation; by Stokes number. This non-dimensional number is defined as:

$$St_1 \equiv \frac{\tau_p}{\tau_f} = \frac{1}{18}\frac{\rho_p}{\rho_f}\frac{d_p^2\,\varepsilon^{1/2}}{\nu^{3/2}} = \frac{1}{18}\frac{\rho_p}{\rho_f}\left(\frac{d_p}{\eta}\right)^2 \tag{3.2}$$

where particles response time, taken here as $\tau_p = \frac{1}{18}\frac{\rho_p}{\rho_f}\frac{d_p^2}{\nu}$ and the characteristic time scale of flow is the kolmogorov time scale, $\tau_\eta = (\nu/\varepsilon)^{1/2}$. The validity of (3.1) is limited to particles diameter smaller than dissipative length scale and high particles densities, as compared with carrier flow. Several questions arise upon the effectiveness of (3.1) when particle size becomes large and/or particle density is comparable with carrier fluids density.

Bec et al. [9] have done DNS of point particles in homogeneous isotropic turbulence flow with different resolutions giving $R_\lambda = 65, 105$ and 185. The particle inertia was taken into account by attributing them a particular particle response time and covered a range of particles stokes number as defined in of (3.2) 0 to 3.5, i.e. from fluid particles to heavy inertial particles. They have shown for $R_\lambda = 185$ that the PDF tails of normalized Lagrangian acceleration diminish from fluid tracers to inertial heavy particles, as the Stokes number was increased. The PDF tails suppress very quickly with

increasing particles inertia even for Stokes number of 0.16 (FIG. 3.7(a)). They have also observed a drop in normalized acceleration variance with increasing Stokes number for all of the three Reynolds numbers they studied. However, this drop in normalized acceleration variance is very sharp even for very small Stokes numbers of 0 to 0.5 (FIG. 3.7(b)). Furthermore, they have explored that for $St_1 \approx 0.5$ the particles tend to form clusters by accumulating in particular zone of large strain or low vorticity regions, even if the particles were seeded homogeneously in the numerical domain. This was obvious for all the three Reynolds number studied, the maximum clustering (shown by minimum of correlation dimension D_2 in (FIG. 3.8(a)) was observed around Stokes of 0.5. They have also observed that the particle's normalized acceleration variance matches very well with fluid particles acceleration calculated at particles position for $St_1 < 0.4$, this indicates that this inertial particles dynamics is due to their preferential concentration in the low vorticity regions which would be the same even for fluid particles if evaluated not homogeneously in space but at the position of these particles. However, this conditioned fluid particle acceleration attains a minimum around $St_1 \approx 0.5$, a value where particles were found to mostly concentrate in the low vorticiy regions of the flow and as the Stokes number increases it starts increasing again to take higher values and attain fluid particles acceleration again. Bec et al. have claimed that for higher Stokes number the particles acceleration is somewhat defined by the acceleration of fluid tracers calculated along the particle trajectories and low pass filtered by particles response time.

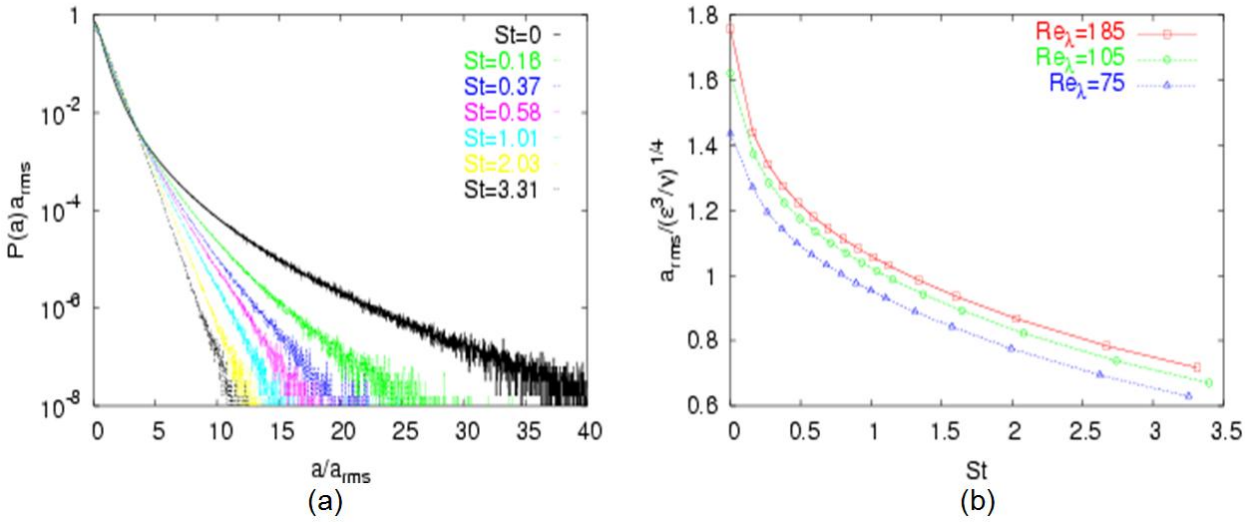

FIG. 3.7 – (a) DNS results on the acceleration PDFs of passive point particles normalized with its rms value for different stokes numbers studied. The PDF tails contract from fluid particles acceleration ($St = 0$) to heavy inertial particles as the Stokes number increases ($R_\lambda = 185$) [9]. (b) Evolution of normalized acceleration variance as a function of Stokes number for three different R_λ studied numerically.

By doing so, they have observed that for $St_1 > 1$ the two accelerations tend to become the same as the Stokes number increases, this has led Bec et al. to a partial conclusion that preferential concentration effects are less important for Stokes greater than unity and that the inertial particle acceleration statistics could be defined by low pass filtering of fluid particles acceleration by inertial particles response time. They were however unable to conclude the physical phenomena which define the acceleration statistics around $St_1 = 1$.

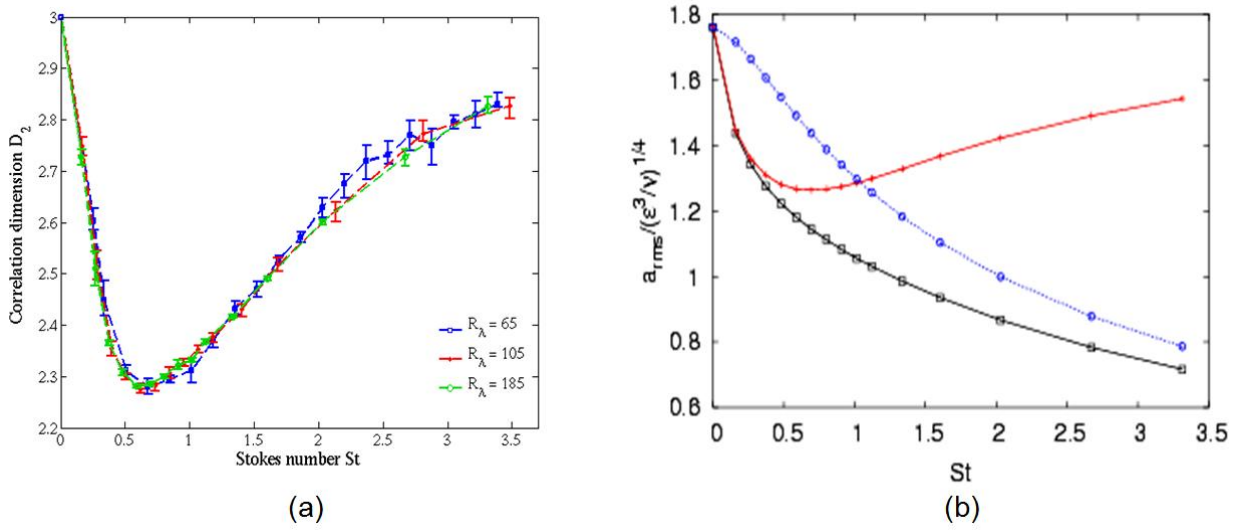

FIG. 3.8 – (a) The correlation dimension D_2 as a function of Stokes number for three Reynolds number cases. This correlation dimension describes the distance between two particles; a minimum indicates that two particles at the particular Stokes number are much nearer to each other [9]. (b) Normalized acceleration variance of particles (squares), fluid particle acceleration conditioned at the particles position (+) and fluid particle acceleration filtered with particles response time.

On the experimental exploration of tiny and very heavy inertial particles acceleration, Ayyalasomayajula et al. [4] have conducted experiments in active grid turbulence at moderately high Reynolds number of 250. Water droplets with sizes in microns, were injected in the flow and tracked using high speed cameras moving along the wind tunnel test section at mean flow velocity. The mean diameters of injected particles distribution were found to be of the order of 17.1 and 21.4μm giving φ of 0.04 and 0.05, and approximate Stokes number of 0.09 and 0.15 respectively. Ayyalasomayajula et al. compared their wind tunnel inertial particle acceleration statistics with tracers in von Kármán swirling flow. The normalized acceleration PDFs for these inertial particles were found to have narrower tails as compared with fluid particles acceleration PDFs (FIG. 3.9(a) and (b)), this difference in normalized acceleration PDF is much pronounced for magnitudes greater than 4. Furthermore, the

acceleration variance of these inertial particles was also found to be reduced in comparison with fluid particles; being 0.8 times the fluid particles acceleration variance in the case of particles with stokes number of 0.15. They attributed the drop in acceleration variance of inertial particles due to the linear damping of the fluid acceleration and the change in shape of the normalized PDFs by virtue of non-uniform sampling of carrier fluid by these particles which has already been shown by Chen et al. and Bec et al.

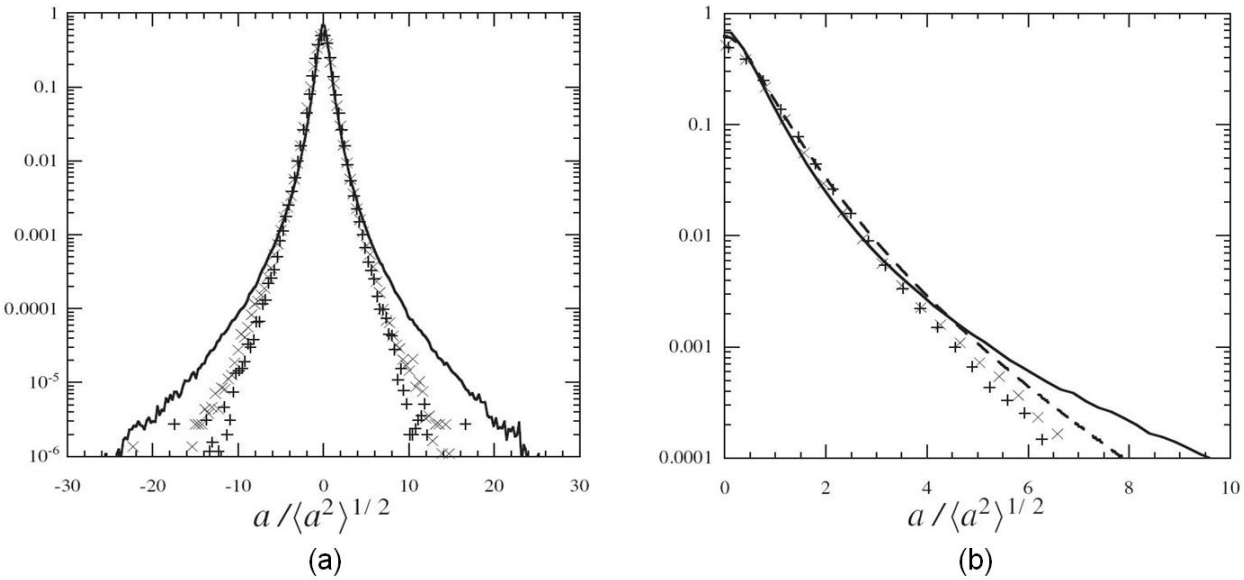

FIG. 3.9 – (a) PDFs of normalized acceleration (normalized with corresponding rms values) for particles having mean Stokes of 0.09 and 0.15 shown by (x) and (+) respectively $R_\lambda = 250$. The solid line represents the fluid particle acceleration PDF obtained by Mordant et al. [66]. (b) Normalized acceleration PDFs compared with inertial particle PDFs computed by Bec et al. [9] for Stokes number of 0.16 (dashed line), the solid black line stands for fluid particle acceleration. Both figures are taken from [4].

Further investigation on the behavior of much smaller size water droplets in the same experimental setup, at same Reynolds number i.e. $R_\lambda = 250$ was done by Ayyalasomayajula et al. [5]. The mean diameter of particle size distribution was of the

order of $7\mu m$, which corresponds to $\varphi = 0.016$ and $St = 0.01$. With these specifications the particles were assumed to behave as tracers, which was further endorsed by the comparison of normalized acceleration PDFs of these minute particles with the fluid particles acceleration of (However the PDFs were not seem to be fully converged). They are compared with DNS results by Bec et al. computed at $R_\lambda = 185$; and the experimental results of Mordant et al. at $R_\lambda = 690$ (FIG. 3.10). The longitudinal and transverse components of normalized acceleration were found to fit well with that of Bec et al., however the fluid particles acceleration PDF tails given by Mordant et al. were found to be more stretched (for acceleration values greater than 10 times the rms) than the rest, which could be due to the higher flow Reynolds number ($R_\lambda = 690$). Ayyalasomayajula et al. have observed that acceleration statistics of small water droplets resembles that of point particles models in DNS [9], both for tiny droplets ($\varphi = 0.016, St = 0.01$) which reflect the statistics of fluid particles ($St = 0$) in case of DNS; and for relatively higher droplet sizes giving $\varphi = 0.04$, 0.05 and $St = 0.09, 0.15$ respectively, the acceleration statistics were well described by point inertial particles having $St = 0.16$.

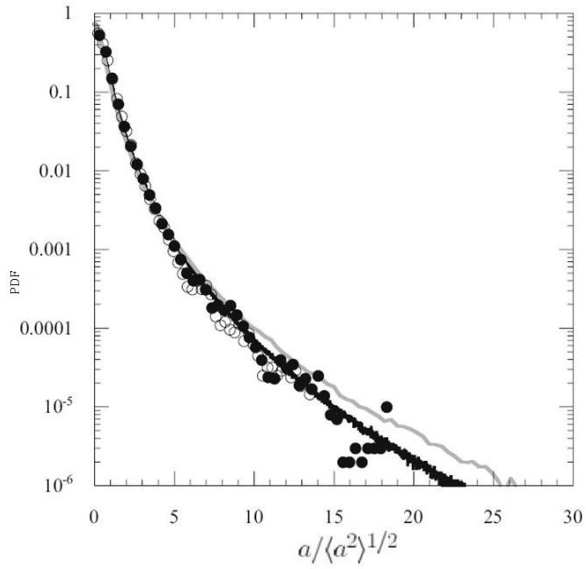

FIG. 3.10 – The normalized acceleration variance components (filled circles: x-component, open circles: y-component) of small $7\mu m$ water droplets having Stokes number of 0.01 [5]. Solid black line is fluid particle acceleration PDF (St = 0) from Bec et al. $R_\lambda = 185$ case [9]. In grey continuous line is the fluid particle acceleration observed by Mordant et al. [66] for experiments at $R_\lambda = 690$.

3.2.2 Finite-Sized Particles

It was Voth et al. [92] who first studied experimentally, the size and density effects of particles on their acceleration. The experiments were done in fully developed turbulence at $R_\lambda = 970$ under the same flow configuration as in the case of small tracer particles. Though the large particles were also named as tracers in their paper, but here the author wants to rename it as neutrally buoyant finite-sized particles. The two main mechanisms which could be held responsible for the difference between tracers and large particles acceleration were identified to be the density-dependent and density-independent effects. First, being due to particle and carrier fluid density mismatch as a result of which the particles will not be affected by fluid accelerations due to their inert behavior. Second highlights the spatial and temporal filtering of the carrier flow which

is by virtue of carrier fluid modifications due to the finite volume of these large size particles. The particle size effects on their acceleration were taken into account by studying four different sized particles with relative density or Γ of 1.06. The particle diameters studied were $26, 46, 135$ and $450\mu m$ which corresponds to $1.44, 2.55, 7.5$ and 26 values of φ respectively. The Stokes number as defined in (3.2) comes out to be 0.12, 0.38, 3.3 and 37.5 respectively from smallest to largest particle diameter studied. The relative density (Γ varying from 0.96 to 1.06) influences were explored by doing experiments in NaCl solution for $450\mu m$ diameter particles. The size range studied by Voth et al. seems to be large as compared with density range they were capable of investigating.

In FIG. 3.11(a) the normalized acceleration PDFs are shown for particles relative sizes and densities (φ, Γ) data sets of (2.55, 1.06), (26, 1.06) and (26, 0.96) represented by open, filled circles and triangles respectively. These normalized acceleration PDFs illustrate no major difference for three data sets presented, especially up to acceleration magnitudes of 10 times the root mean square value. However, the accelerations standard deviation itself shows big differences in all the three data sets presented here, being three times smaller for large size particles in comparison with the smallest one. This particular effect was further explored by Voth et al. and is shown here in FIG. 3.11(b), where normalized acceleration variance is plotted as a function of particle size. Not much difference has been observed in acceleration variance for two smaller size particles $(\varphi \leq 5)$, it remains same within the experimental error, however, the normalized acceleration variance drops drastically for $\varphi = 7.5$ to $\varphi = 26$ and up to 70% between the smallest and largest particle size studied. For particles with $\varphi \geq 5$,

Voth et al. have proposed a $d^{-2/3}$ scaling for acceleration variance, which results from K41 phenomenology by arguing that for a finite-sized particle, the particle acceleration is only due to the flow structures larger than the particles diameter. They further argued that this scaling holds quite well for large particles, but for smaller particles the acceleration becomes independent of particle size. The normalized acceleration variation decreases, as the relative density increases for the same finite size of the particle. However, this drop was found to be small and Voth et al. have concluded that the main discrepancy between the tracers and finite size particles is due to their size and not because of their relative density. Here I point out the small variation of relative densities studied by Voth et al. for the same particle size.

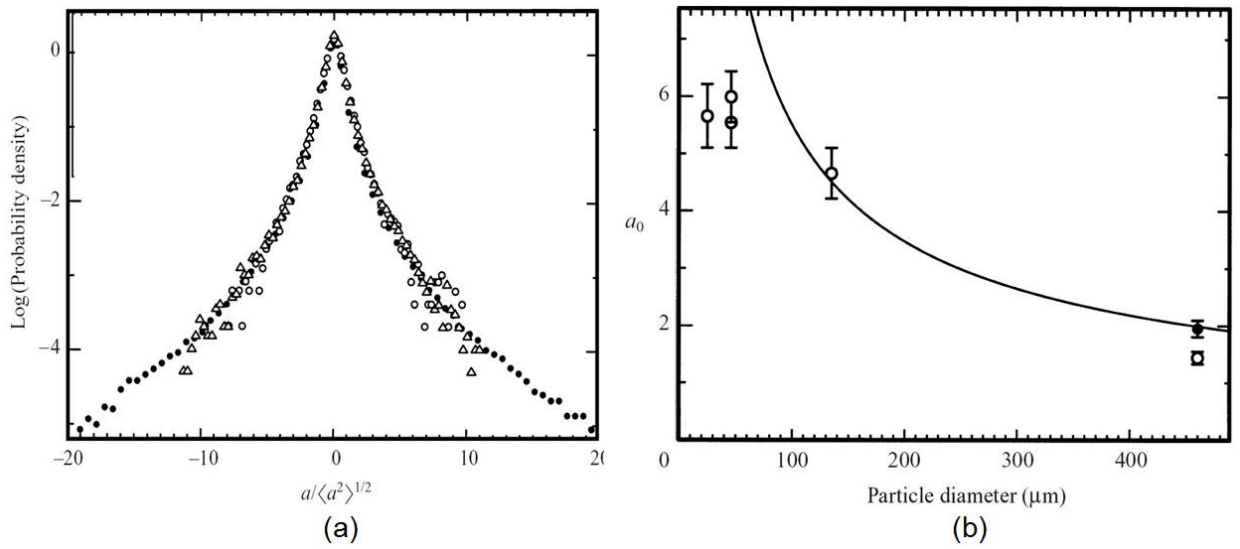

FIG. 3.11 – (a) Particles density and size effects on acceleration PDFs normalized with its standard deviation. Filled, open circles and triangles stand for $(\varphi = 2.55, \Gamma = 1.06)$, $(\varphi = 26, \Gamma = 1.06)$ and $(\varphi = 26, \Gamma = 0.96)$ respectively [92]. (b) Particle size effects on normalized acceleration variance (a_0); open circles signify $\Gamma = 1.06$, filled circles show $\Gamma = 0.96$ [92]. The solid line indicates $d^{-2/3}$ scaling. All results in (a) and (b) are for $R_\lambda = 970$.

In a recent extensive study done by Volk et al. [90], a comparison of numerical and experimental results on the Lagrangian acceleration of tracers, large neutrally buoyant, small heavy particles and large but very light air bubbles has been done. All the experiments were conducted at $R_\lambda = 850$ in a counter-rotating disk flow, where particle tracking was done using Extended Laser Doppler Velocimetry. Neutrally buoyant polystyrene particles ($\Gamma = 1.06$) of diameter 31 and $250\mu m$ were used, which were considered to behave as tracers and large size neutrally buoyant particles. The corresponding particle size normalized with Kolmogorov scale i.e. φ was of the order of 1.82 and 14.7 respectively. For heavy particles, small PMMA (Arcylic Glass) spheres with diameter of $43\mu m$ were used which are slightly heavier than water having $\Gamma = 1.4$ and $\varphi = 2.53$. The last type of particle studied by them was air bubbles in water, with diameter of $150\mu m$ corresponding to $\varphi = 8.82$, which is relatively larger than tracers and heavy particles, but smaller than neutrally buoyant polystyrene particles. The relative density of these bubbles was of the order of 10^{-3}. The Stokes number (as defined in previous chapter) for tracers, heavy, large neutrally buoyant and bubbles were found to be 0.24, 0.58, 16 and 1.85 respectively.

In the numerical simulations, Volk et al. have used the model equation (2.4) that we have already discussed in last chapter. This equation is an extension of simple point particles model equation (3.1) and includes the added mass and pressure gradient effects. In experiments, the normalized acceleration PDFs of all particles studied by Volk et al. were found to be same; up to 10 times the rms acceleration value (FIG. 3.12(a)). For high acceleration magnitudes the tracers were found to have more stretched PDF tails than rest of the particle types; however the difference remains within the

measurement errors and hence considered to be negligible. In comparison with DNS, the normalized acceleration PDFs were underestimated by the numerical results for tracers, heavy and finite size neutrally buoyant particles whereas the PDF was overestimated in the case of bubbles. For three former cases, this could be due to the small Reynolds number of the DNS ($R_\lambda = 180$) as compared with the experiments where the Reynolds number was quite high ($R_\lambda = 850$). In the case of bubbles acceleration the difference was due to the fact that lighter bubbles undergo lift and gravitational forces which were not taken into account in the used particle dynamics model. On the other hand the DNS were not able to differentiate the normalized acceleration PDFs of tracers and large neutrally buoyant particles (FIG. 3.12(b)) as the two curves match each other almost perfectly. This highlights the inability of the model equation to take into account the finite size and hence physical volume effects of particles. A much appropriate model is still required to take into account these effects so as to reproduce the experimental results. However PDF tails of heavy particles were seemed to be suppressed as compared with the other particle types.

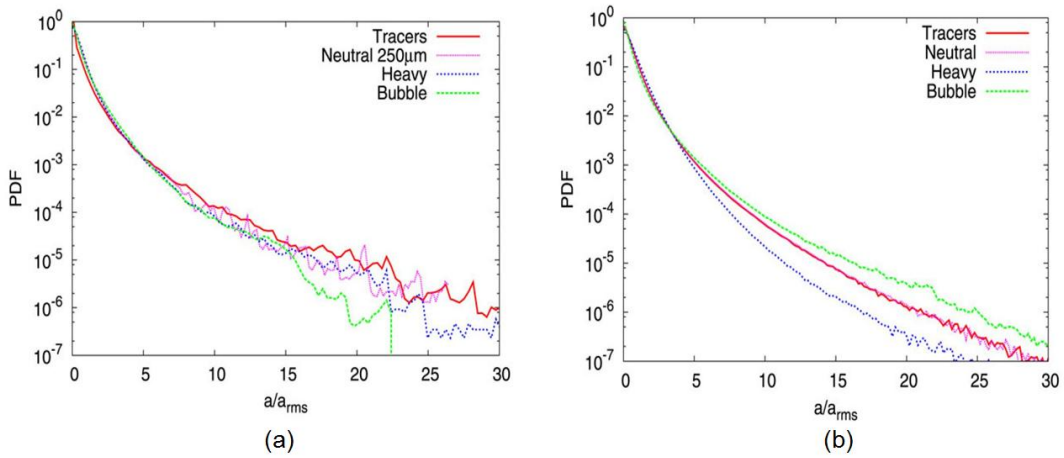

FIG. 3.12 Normalized acceleration PDFs [90] (a) Experiments ($R_\lambda = 850$) (b) DNS ($R_\lambda = 180$).

Some differences were observed in the normalized acceleration variance a_0 of the particles. For tracers, this was found to be 6.4 which were also observed by Voth et al. for fluid particles. The a_0 drops very much from tracers value in case of large neutrally buoyant particles, being 2.2. For heavy small particles it doesn't drop that much ($a_0 = 4.3$). The short time statistics, for all the types of particles were studied through acceleration autocorrelation. Volk et al. have observed that lighter particles acceleration de-correlate quickly as compared with other particle types, whereas, large neutrally buoyant particles have longest correlation time for acceleration. The tracers were found to de-correlate around $2.2\tau_\eta$. The heavier particles were reported to have correlation times a bit longer than the tracers, which is normal due to their large response time. The DNS on the other hand reproduce well the bubbles acceleration correlation, the heavier particles acceleration was found to remain correlated for time longer than what Volk et al. have observed in experiments. Another interesting finding was the inability of model equations to differentiate between tracers and large neutrally buoyant particles short time statistics, as both have same correlation times. This further prompts the scientific community to improve the existing point particle models by taking into account Faxén corrections and material particle finite volume and physical boundaries effects for large size particles.

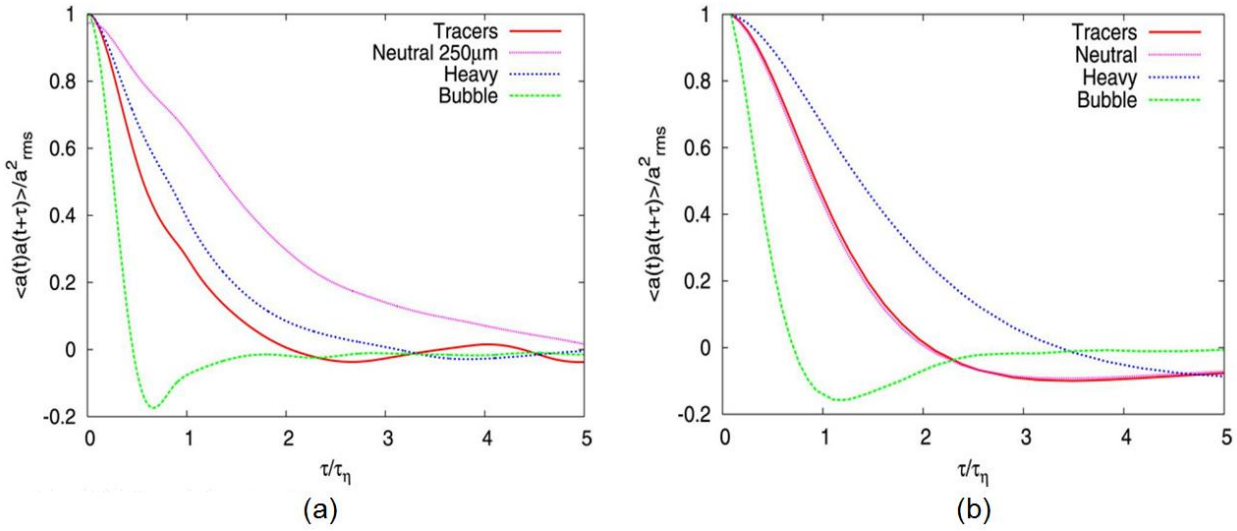

FIG. 3.13 – Acceleration autocorrelation normalized with its variance [90] (a) Experiments ($R_\lambda = 850$) (b) DNS ($R_\lambda = 180$).

Recently, Xu and Bodenschatz [94] have studied and compared the dynamics of small size tracers and large size neutrally buoyant and heavy particles in von Kármán flow for Taylors Reynolds numbers of 370 and 460. Polystyrene particles of sizes 26 and $220\mu m$, were used as tracers and large neutrally buoyant particles with $\Gamma = 1.06$, whereas spherical glass particles of diameter $138\mu m$ were used as large sized heavy particles with a relative density Γ of 2.5. The kolmogorov length scale was of the order of 61 and $43\mu m$ for $R_\lambda = 370$ and 460 respectively. For tracers, large size neutrally buoyant and heavy particles, this gives φ of around 0.43, 3.6, 2.26 respectively in the case for $R_\lambda = 370$ case; and φ of 0.6, 5.12, 3.2 respectively, for $R_\lambda = 460$ flow configuration. Furthermore, in order to take into account the particles finite size and finite Reynolds number they have defined two more Stokes numbers which could represent appropriately the dynamics of particles fulfilling these conditions. For finite size particles, the kolmogorov length scale was not considered to be the appropriate

time scale, instead the time scale of turbulent eddies was chosen; this corresponds to the particles diameter, which according to the phenomenology of K41 was given as:

$$\tau_d = \left(\frac{d_p^2}{\varepsilon}\right)^{1/3} \tag{3.3}$$

This defined another Stokes number, using τ_d as flow time scale:

$$St_2 \equiv \frac{\tau_p}{\tau_d} = \frac{1}{18}\left(\frac{\rho_p}{\rho_f}\right)\left(\frac{d_p}{\eta}\right)^{4/3} \tag{3.4}$$

This definition of particles Stokes number seems to be more appropriate for finite particles size, as the flow time scale derived from particles size scale gives better notion of time, when compared with particles response time. Or in other words, the finite size particles experience fluid velocity fluctuations, which has a characteristic time scale given by (3.3), that should be compared with particles response time. Moreover, the particle response time used in (3.2) and (3.4) is the viscous relaxation time (τ_v) of the particles in creeping flow i.e. for $Re_p \ll 1$. Therefore, in case of large size particles, finite Reynolds number corrections should be made. The particles response time under these conditions is related with viscous relaxation time as:

$$\tau_p = \tau_v / C_f \tag{3.5}$$

where $C_f = \frac{C_D\, Re_p}{24}$,

The drag coefficient corrections for different particles Reynolds number have already been defined in previous chapter. Which are also given by (2.9) for different ranges of particles Reynolds number and by

(2.10) for $Re_p < 2 \times 10^5$. Xu and Bodenschatz have defined the particles Reynolds number as under using turbulent flows fluctuating velocity:

$$Re_p \equiv \frac{u' \, d_p}{\nu} = \frac{\left(\varepsilon \, d_p\right)^{1/3} d_p}{\left(\varepsilon \, \eta^4\right)^{1/3}} = \left(\frac{d_p}{\eta}\right)^{4/3} \tag{3.6}$$

Hence, another Stokes number for large size particles having finite Reynolds number was defined as following:

$$St_3 \equiv \frac{\tau_p}{\tau_d} = \frac{1}{18}\left(\frac{\rho_p}{\rho_f}\right)\left(\frac{d_p}{\eta}\right)^{4/3} \frac{24}{Re_p C_D} \tag{3.7}$$

where, an appropriate expression for drag coefficient (C_D) should be chosen from (2.9) corresponding to particles Reynolds number or simply (2.10) should be used in case of $Re_p < 2 \times 10^5$. Taking the particles response time as defined and used by Volk et al. [90] and accommodating these finite particles size and Reynolds number corrections we can also define another Stokes number,

$$St_4 \equiv \frac{\tau_p}{\tau_d} = \frac{1}{12\,\beta}\left(\frac{d_p}{\eta}\right)^{4/3} \frac{24}{Re_p C_D} \tag{3.8}$$

The above definition of particles Stokes number holds true for all types of particles considered so far including the description of the correct behavior of spherical bubbles taking along the added mass effects in particles response time. Xu and Bodenschatz have already observed that for large particles St_3 is smaller than St_2 which itself is further smaller than St_1. We have found that St_4 is smaller than St_1 and St_2 but greater than St_3.

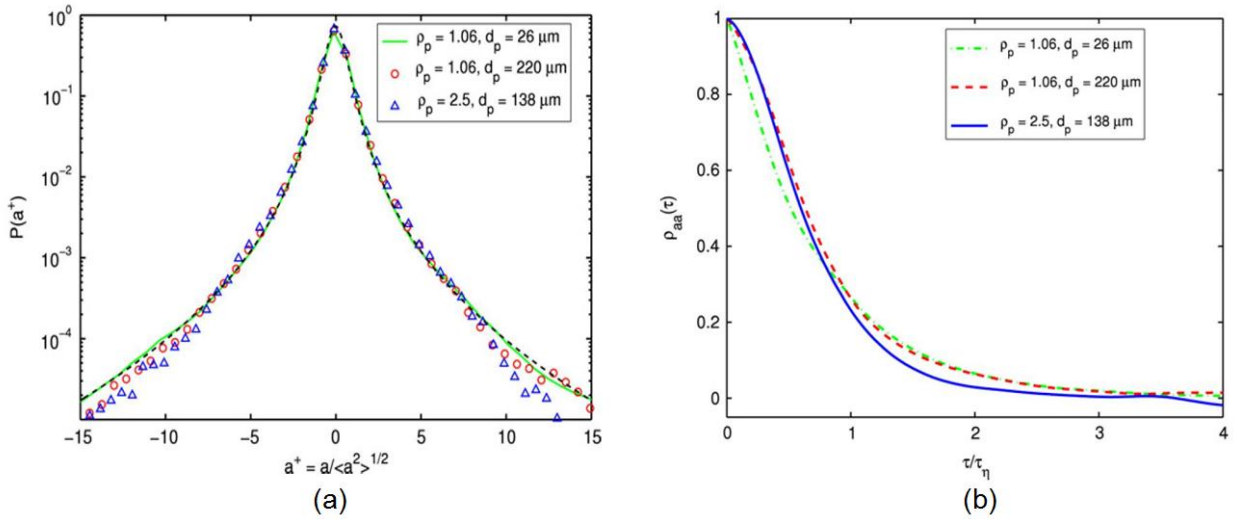

FIG. 3.14 – (a) Normalized acceleration PDFs for experiments at $R_\lambda = 460$ [94], the dashed line indicates the results obtained by Mordant et al. [66] at $R_\lambda = 690$. (b) Acceleration autocorrelation coefficients for experiments at $R_\lambda = 460$ [94].

The experiments of Xu and Bodenschatz have shown that the normalized acceleration PDFs (FIG. 3.14(a)) have same form in case of large neutrally buoyant and heavy particles as compared with tracers for both Reynolds numbers they studied. They have found however slight reduction of PDF tails in case of large particles even at high Reynolds number, the case in which particles Stokes number St_3 increases too. Furthermore they have indicated that the use of new definition of particles Stokes number is much appropriate as compared with its classic definition. As in the case of spherical glass particles the classic Stokes number St_1 for glass particles is a bit smaller than polystyrene particles, but the modified Stokes number St_3 for spherical glass particles is greater than polystyrene particles, which is well translated also by the suppression of normalized acceleration PDF tails of spherical glass particles. The difference in stretching of tails is not enormous and the thesis author presumes here that the normalized acceleration PDFs remain same within the statistical errors.

Moreover the effects of particles larger size is less pronounced as compared with heavy and small or point particles. As in the case of Ayyalasomayajula et al. [4] and Bec et al. [9] where they have observed significant drop in particles normalized acceleration even at small particles Stokes number of the order of 0.1. On the other hand, acceleration variance in the present experiments was observed to be same for all of the three particles at same Reynolds number. This could be due to the fact that for the range of φ explored by Xu and Bodenschatz lies where ($\varphi \lesssim 5$) no effect on particles acceleration variance can be observed due to their size variation, this has already been discovered by Voth et al. [92]. The findings of Voth et al. can be further cemented by the experimental results of Volk et al. [90] in which they have observed reduction in normalized acceleration variance of large neutrally buoyant particles ($\varphi = 14.7$) as compared with small size tracers ($\varphi = 1.82$), where tracers normalized acceleration variance is nearly the same as observed by Voth et al. Moreover, in our present study [78] we have observed the variation in neutrally buoyant particle acceleration variance due to their finite size, where the particles sizes were varied in the range of $10 < \varphi < 26$. These results will be presented and discussed in Chapter 5 in detail. The acceleration autocorrelations were found to be the same for all the three particle types, the correlation time was found to be of the order of $2.2\tau_\eta$. Contrary to the observation of Bec et al. that particles acceleration variance decreases for heavy point particles with increasing Stokes number, Xu and Bodenschatz have observed same acceleration variance for tracers ($\mathrm{St}_1 = 0.02$), finite size neutrally buoyant ($St_3 = 0.15$) and slightly heavier particles ($St_3 = 0.23$). Bec et al. have attributed this drop in acceleration variance to the preferential concentration of inertial particles in the low vorticity high strain regions for particles with $\mathrm{St}_1 < 0.4$. Xu and Bodenschatz have observed that even

the large neutrally buoyant particles do not observe this acceleration variance drop therefore; they have proposed that unlike the heavy point particles as reported by Bec et al., large particles may not escape from high vorticity zones and undergo same accelerations as that of tracers. Or in other words large size particles sample the flow in the same fashion as that of tracers, and the effect on particle acceleration difference is due to the filtering of flow fluctuations due to their finite size. A substantial remark should be made here that a comparison of Lagrangian acceleration statistics in von Kármán flow (Xu and Bodenschatz) is done with DNS and active grid turbulence, which are different flow types. It would have been even better if a comparison is made with similar flow types especially in the case of acceleration variance and acceleration autocorrelations.

In this chapter, we have briefly reviewed the Lagrangian acceleration statistics for three types of particle. First, very small and neutrally buoyant particles which are also called as fluid particles or tracers. It has been observed that PDF of these particles have very wide spread exponential tails and have intermittent dynamics. Second class of particles reviewed have minute size and very high density, we observed suppressed PDF tails for these particles as compared with tracers. Their acceleration variance was also found to have diminished, which was due to the flow sampling of the particles and filtering of particles acceleration by their response time. The third type of particles reviewed were large neutrally buoyant and slightly heavy particles for which we have seen no change in normalized acceleration PDFs but reduction in their acceleration variance was noticed.

In our experimental work, we have carefully explored the Lagrangian acceleration statistics of finite sized $(10 < \varphi < 26)$ neutrally buoyant $(\Gamma \cong 1)$ and large heavy particles $(10 < \varphi < 26)$ and $(1 < \Gamma < 65)$. Our study will help in investigating the physical phenomena involved in the transport of these finite sized neutrally buoyant and heavy particles in turbulent flows.

Chapter 4

Experimental Setup

Lagrangian tracking of particles in turbulent flow has always been a challenge both for physicists and engineers alike. In spite of rapid technological growth and ensuing experimental and numerical advancements made in the area of microelectronics and microprocessors, the scientific community is still unable to completely resolve the multiple scale nature of turbulence, both in time & space and the study of particles dynamics in a turbulent flow still remains in infancy. Numerical and experimental research work had been carried out in Lagrangian tracking of particles, but we still lack a comprehensive understanding of this domain. The dispersion of pollutants in the environment, movement of rain drops in clouds, combustion chamber mixing and mixing in chemical mixers is not yet understood in detail. It is the chaotic nature of turbulent flows that has made it difficult to understand completely their dynamics and physics.

Amongst several experimental efforts made by different groups in the research of Lagrangian particle tracking, we have also studied the dynamics of material particle in wind tunnel turbulence. As particles we have used soap bubbles inflated either with helium or air or carbon dioxide, in order to obtain a combination of size and densities. We have named the particles as *'material'*, because unlike fluid or point particles conventionally used in numerical simulations these material particles possess physical boundaries and hence a physical mass and volume. A state-of-the-art, Ultrasonic

Doppler Velocimetry has been employed using a pair of identical electro-acoustic transducers that permits us to track these material particles in the wind tunnel with high mean flow velocity, while simultaneously resolving the smallest and the largest time scale of turbulence. Employing a versatile particle generator enabled us to perform experiments with a wide range of particle sizes and densities. This in turn enabled us to study particle dynamics and its behavior for particles ranging from neutrally buoyant to inertial ones.

4.1 Flow

4.1.1 Wind Tunnel

All experiments were conducted in a closed circuit wind tunnel where a turbulent flow is generated downstream a grid. Two counter-rotating fans, powered by two continuous current motors of 25 kilowatts (max) each, generate the flow. The motor speed achieve high rpms enabling us achieve a mean flow velocity of the order of $20\, m.s^{-1}$. The test section has a length of 4 meters with $75 \times 75\, cm^2$ cross section and contains four windows of length one meter each. The wind tunnel schematic is presented in the FIG. 4.1.

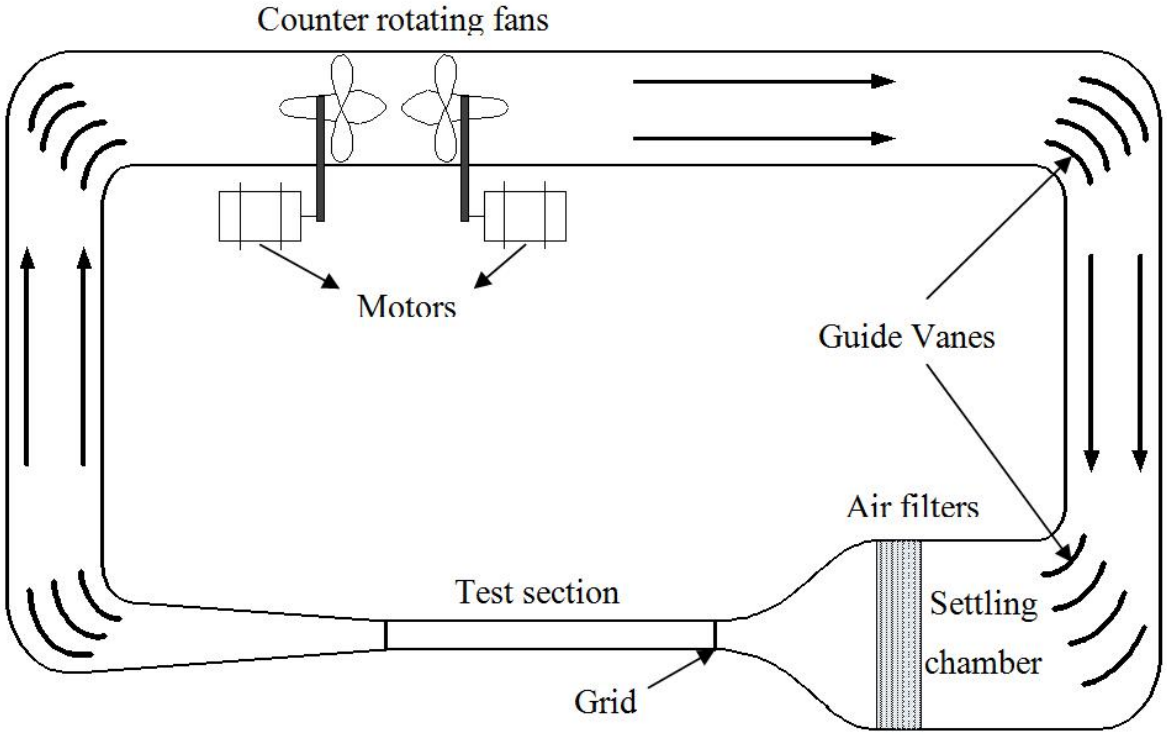

FIG. 4.1 - Wind tunnel schematics.

Ultrasonic Doppler Velocimetry made it necessary to isolate test section walls acoustically in order to avoid reverberations. The sides and bottom walls of last three meters of the test section were isolated with the help of carton sheets. Reverberation effects on the first meter length were expected not to interfere with particle tracking, therefore these walls were left acoustically un-isolated.

The grid comprises of a set of 10 horizontal and 10 vertical square composite bars of 15mm side, which were glued using epoxy resin adhesive. It resulted in a mesh size (M) of 60mm. The solidity ratio; which is the ratio of the area occupied by the grid and the total cross section area, was found to be 0.36. The actual picture of grid is given in FIG. 4.2.

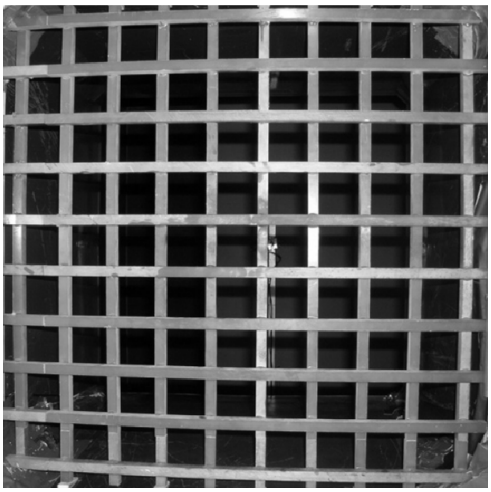

FIG. 4.2 - Grid placed at start of the test section.

The test section is equipped with rails on which is mounted a small trolley powered by three step motors that can transport the trolley both longitudinally and transversally. Two motors responsible for longitudinal and span-wise movements could cover the whole length and span of test section respectively, but the range of vertical movement is somewhat limited. A provision of attaching supports for hot-wire and pitot tube on the trolley made it possible to perform hot-wire anemometry and also allowed us to obtain the mean velocity flow fields and velocity fluctuations not only throughout the test section length but also on cross sections at different mesh distances from the grid.

4.1.2 Flow Characterization

The turbulence generated downstream a passive grid may be visualized in FIG. 4.3. Before performing measurements in the wind tunnel it was absolutely essential to characterize the turbulence generated by the grid. This involved determination of turbulence decay power law, measurement of turbulence intensity, determination of

spatial and temporal scales of turbulence at different mesh distances from grid and also at different points at a particular cross section.

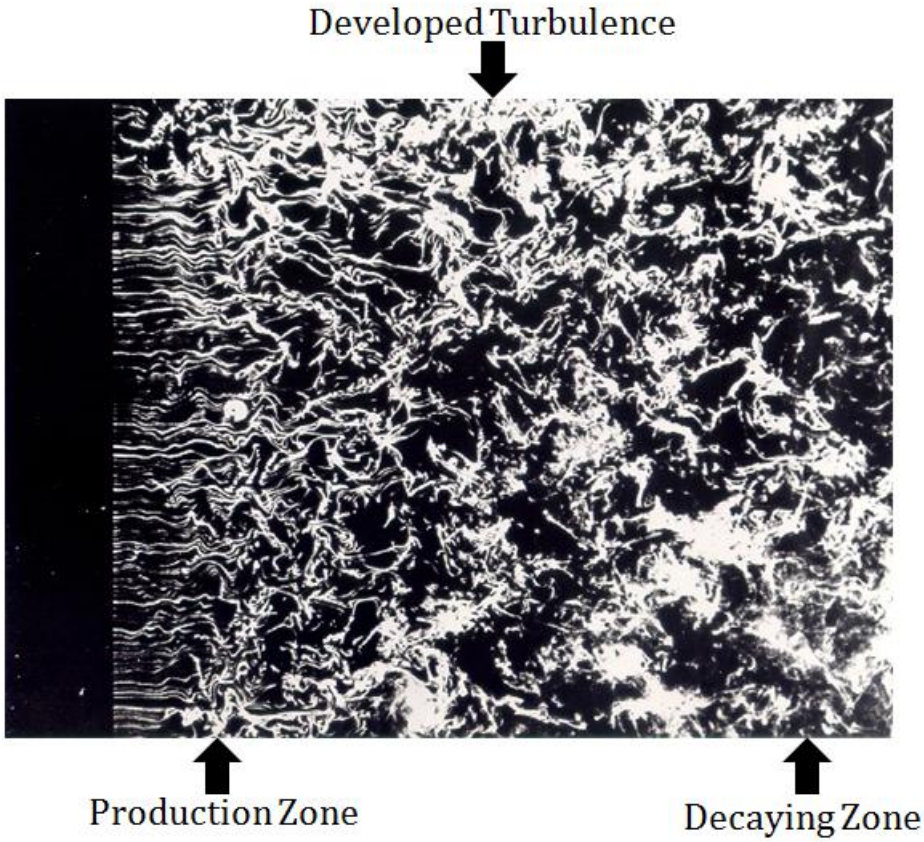

FIG. 4.3 – Turbulence generated downstream a passive grid, different zones are turbulence are indicated. Figure taken from [24].

To achieve the objective of flow characterization the hot-wire anemometry results of [57] were used. In his work, the evolution of axial mean flow velocity field was studied, at the center of cross section, for two Reynolds number based on mesh size Re_M of 4.7×10^4 and 8.2×10^4. The general form of decaying power law is given by, $\left(\frac{\langle u^2 \rangle}{U^2} = A(\frac{x}{M} - \frac{x_0}{M})^{-n}\right)$, where $\langle u^2 \rangle$ is the variance of velocity fluctuations, U is the mean

Table 4.1: Flow characteristics at start center and end of measurement volume, for two mean flow velocities.

Flow velocity	**14 m.s^{-1}**				**15 m.s^{-1}**			
Distance from grid & average values	**42M**	**48M**	**54M**	**Average**	**42M**	**48M**	**54M**	**Average**
Turbulence intensity *(%)*	3.12	2.88	2.68	2.9	3.12	2.88	2.68	2.9
Integral Length Scale, L *(mm)*	58.2	61.5	64.6	61.4	58.2	61.5	64.6	61.4
Taylor miscroscale, λ *(mm)*	5.5	5.9	6.2	5.9	5.3	5.7	6	5.7
Kolmogorov dissipative scale, $\eta(\mu m)$	226	246	266	246.0	215	234	252	233.7
Taylors , R_λ	159.5	157.5	155.6	157.5	165	163	161	163.0
Energy dissipation rate, ε $(m^2.s^{-3})$	1.2878	0.9157	0.6789	0.96	1.584	1.1263	0.8351	1.18
Integral time scale, τ_L *(sec)*	0.1331	0.1528	0.1724	0.15	0.1243	0.1426	0.1609	0.14
Kolmogorov time scale , τ_η *(ms)*	3.4	4	4.7	4.03	3.1	3.6	4.2	3.63

flow velocity, A and n are the decay law's empirical constants, x is the distance from the grid and x_0 is the virtual origin of turbulence. These decay laws were determined by linearly fitting the experimentally measured data for Re_M of 4.7×10^4 and 8.2×10^4 which are given by $0.081\left(\frac{x}{M} - 2\right)^{-1.21}$ and $0.065\left(\frac{x}{M} - 2\right)^{-1.12}$ respectively. As all of our experiments were run for $Re_M \approx 6 \times 10^4$, the decay power law corresponding to this Reynolds number was obtained by interpolation which is $0.073\left(\frac{x}{M} - 2\right)^{-1.17}$. The turbulence intensity at distance $42M$, is of the order of 3.3% which decays up to 2.8% at $54M$; in between lies our measurement zone. In the same manner the interpolated integral length scale dependency on longitudinal distance from the grid was found to follow a particular law of $L = 0.041(x - x_0)^{0.40}$. The Reynolds number based on

Taylor's micro-scale was determined from third order structure function using $\left(S_{3\,max} = 0.82 + 8.48\, R_{\lambda}^{-2/3}\right)$ [57], from where the Taylor micro-scale was determined from the definition $R_{\lambda} = u'\lambda/v$. The flow properties at start, center and the end of measurement zone and their averages are given in Table 4.1, for mean flow velocities of 14 and 15 $m.s^{-1}$.

4.2 Particles

4.2.1 Bubble Generation Machine

As stated earlier, the particles we used are soap bubbles inflated with gas which could either be helium, air or carbon dioxide. The filling gas selection depended upon the required relative densities. With the help of the versatile bubble generator, we were able to study a range of relative densities and bubble sizes. The bubble generator was developed in laboratory and served during the Lagrangian tracking of particles in axi-symmetric jet [35]. In FIG. 4.4, the picture of bubble generation machine is shown. The machine comprises a container in which liquid soap is stored. This reservoir is kept under constant air pressure that can be regulated with pressure regulating knob and the corresponding pressure could be read on pressure gauge. We have three regulating parameters; liquid soap, external air and inner gas flow rates. These three flow rates directly affect the bubble formation through injector nozzle the details of which are shown in following paragraphs.

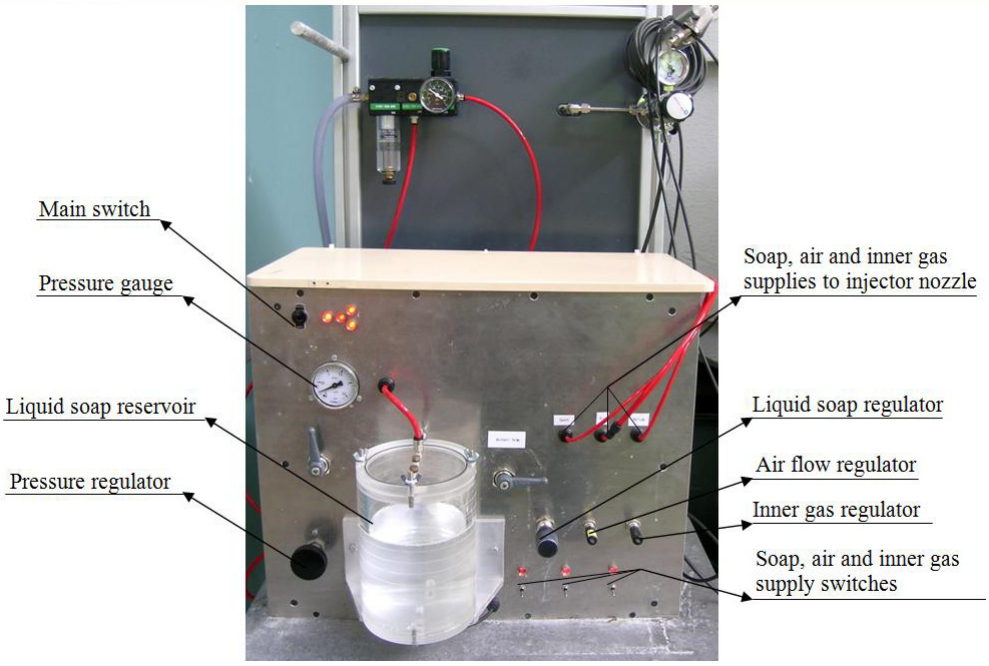

FIG. 4.4 - Bubble generation machine.

4.2.2 Injector Nozzle

The regulated supplies of liquid soap, air and inner gas to the injector nozzle ensure the bubble formation. The injector nozzle comprises of a set of coaxial tubes that can be observed in FIG. 4.5.

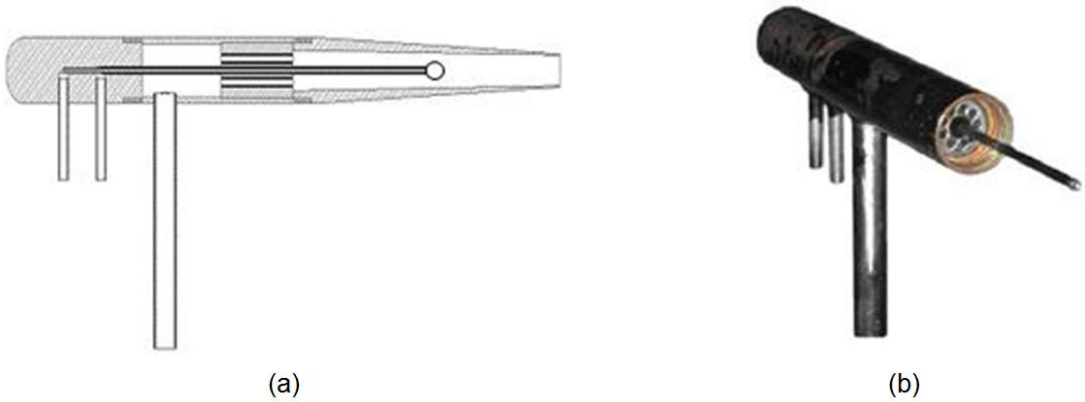

FIG. 4.5 - Injector nozzle (a) Cross section view (b) without conical nozzle

From the above presented views we can observe a few concentric tubes. Around the periphery of outer most concentric tube is an array of small tubes which laminarize the external airflow. The two inner tubes are prolonged for several millimeters, amongst the inner most tube flows the gas which is responsible to inflate the bubble, and around this tube we have a continuous supply of liquid soap, which forms a thin soap film around the inner most tube. This thin soap film is inflated in the form of bubble by the inner gas flow, thus the frequency of bubble generation depends mainly on inner gas flow rate; the higher the flow rate the greater will be the bubble generation frequency and vice versa. Whereas the flow in the remaining staggered tubes and the spaces in between them are responsible for detaching the bubble from injector.

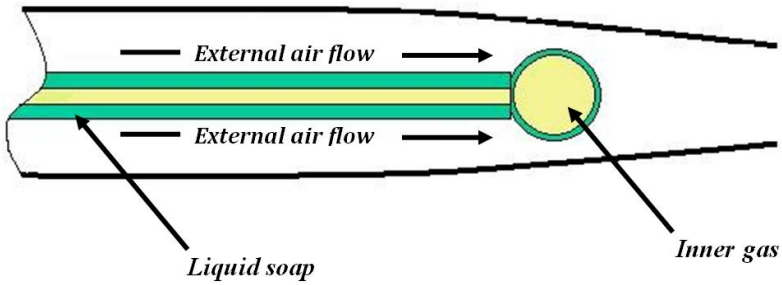

FIG. 4.6 - Injector nozzle flow scheme

For a given inner gas type, a contrast of diameter and relative densities can be obtained by changing the relative flow rates of inner gas, liquid soap and external air. The bubble sizes range from $1.7mm$ to $6mm$, whereas the densities were varied from neutrally buoyant up to 65 times heavier than the environmental air. For neutrally buoyant bubbles helium gas was used so as to compensate the weight of the soap film. For heavier bubbles either air or carbon dioxide was used, the choice depends upon the stable bubble generation state required[1]. For small bubble sizes, high external air flow is necessary so as to detach the bubble quickly from forming tubes, without allowing sufficient bubble growth. In this case, in order to keep the bubble generation continuous and uniform (which is our prime objective) higher flow rates of soap and inner gas are required, which result in formation of bubbles with high frequencies and numbers. As the signal processing algorithm that we have used in our case limits us to track an individual particle at a time, i.e. the velocity signal of passage of only a single bubble at a

[1] Experiments with CO_2 were not taken into account because the life of bubbles inflated with CO_2 was too short; this could be because of solubility of CO_2 in water due to which the gas diffuse very quickly through the soap film thickness resulting in the bubble breakup.

time in the measurement zone can be useful for statistical calculations. Therefore these bubbles were destroyed using a chopper, placed in front of injector that reduces the bubbles quantity and ensured tracking of more individual particles in the measurement volume downstream. The injector itself in case of neutrally buoyant bubbles was placed far upstream at the start of convergent section of wind tunnel. The bubble's life was long enough to track them in the measurement volume few meters downstream, while it was being transported with the mean flow.

To repeatedly find a particular bubble diameter and density production state, is a bit of a tricky task, especially in the case of heavy bubbles; to achieve stable bubble generation with a particular size and density combination is tiresome and need a lot of practice in regulating the three flow rates. As our study is based on the effects of size and density on dynamics of particles employing Lagrangian tracking, therefore it is essential to know particle's accurate size, dispersion and relative densities. The methods devised for size and density measurements are explained in the following sections.

4.2.3 Size Measurements

The exact measurement of bubble sizes and their dispersion was ensured with the help of a home-designed bubble size measurer. Two small lasers are fixed on a strip beaming at a particular angle, which in the absence of bubbles are not detected by their respective photodiodes that are fixed on the other face of strip. The strip itself is mounted on injector at the time of measurements. Whenever a bubble crosses the laser beam it is reflected by the soap film twice, first when bubble enters in the path of laser beam second when the same bubble leaves it. The same happens while this bubble

crosses the second laser beam. As a result we obtain for each bubble a double peak signal for each set of laser-photodiode. The schematics of bubble size measurer is shown in FIG. 4.7(a) where different positions of the same bubble are shown with signal peaks as shown in FIG. 4.7(b). The time between the double peaks of first signal T_1, is the ratio of the bubble diameter D and its speed V. Whereas, the time between the corresponding peaks of two signals T_2 is the ratio between the distance the bubble has traveled during this time and its speed. Here we make a justified assumption that the bubble speed does not vary in between, as the two photodiodes are very near to each other.

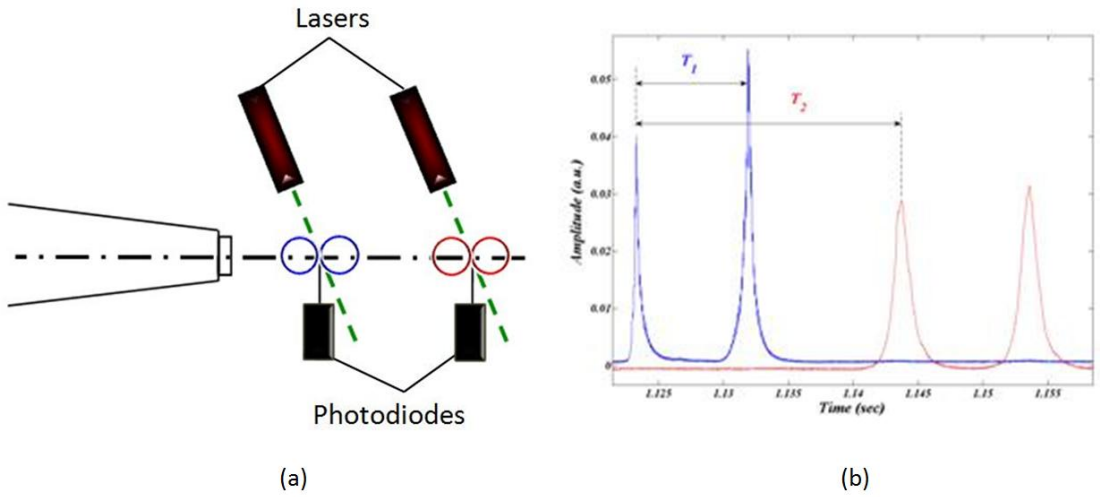

FIG. 4.7 - (a) Bubble size measurer scheme (b) corresponding recorded signal

Thus the bubble diameter is expected to be given by:

$$D \propto T_1 / T_2 \tag{4.1}$$

Possible small deviations to this linear scaling might exist due to a small systematic variation of bubbles velocity between the two photodiodes or because of the effects of the bubble curvature on the deviation of the laser beam. We will therefore consider a more general calibration relation of the form:

$$D = P(T_1 / T_2) \tag{4.2}$$

with P a polynomial function. As shown next, the calibration law is best fitted by a quadratic law, though a linear relation still remains a very good approximation.

For a range of bubble sizes ($1.7mm\ to\ 6mm$) photodiode signals were recorded in parallel with high speed imaging (FIG. 4.8(a)). Raw images were processed in order to extract bubble diameter. From the raw images containing a bubble a reference image was subtracted and then the bubble edges were determined using canny algorithm. By correlating the processed image with prescribed circles of known diameter, the outer edge diameter of the processed image (FIG. 4.8(b)) was determined within one pixel accuracy (2.4% to 1.3% for bubble sizes of $3mm$ to $6mm$ respectively). This procedure was repeated for all the recorded images (around 100 images with bubbles were used for diameter calculation for each setting of bubble generation machine), hence the bubble diameter and dispersion was determined.

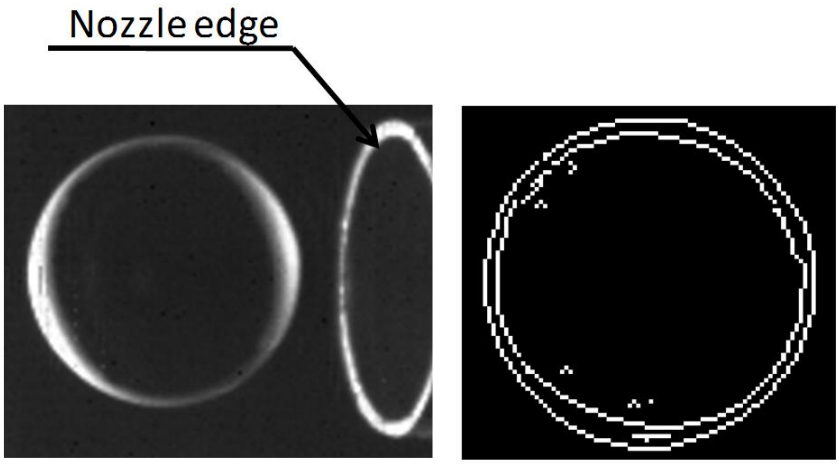

FIG. 4.8 - (a) raw image of a bubble leaving nozzle (b) processed image of a bubble showing bubble edges after using canny algorithm.

A calibration curve was traced by linear and quadratic fitting and relative errors were estimated (FIG. 4.9(a) and (b)) respectively. Both linear and quadratic fits well with the experimental measurements however we have used quadratic fit in our calculations. The percent dispersion in bubble sizes was found to be of the order of 3% for all the bubble generation machine settings except in the case of 1.7mm diameter bubble this percent dispersion was as high as 35% which was mainly due to unstable bubble generation state. This is why we have discarded the 1.7mm diameter data set for concluding results; however for rest of the diameters the bubbles are mono-dispersed, a fact that has permitted us to precisely study the effect of particle size on their dynamics in a turbulent flow.

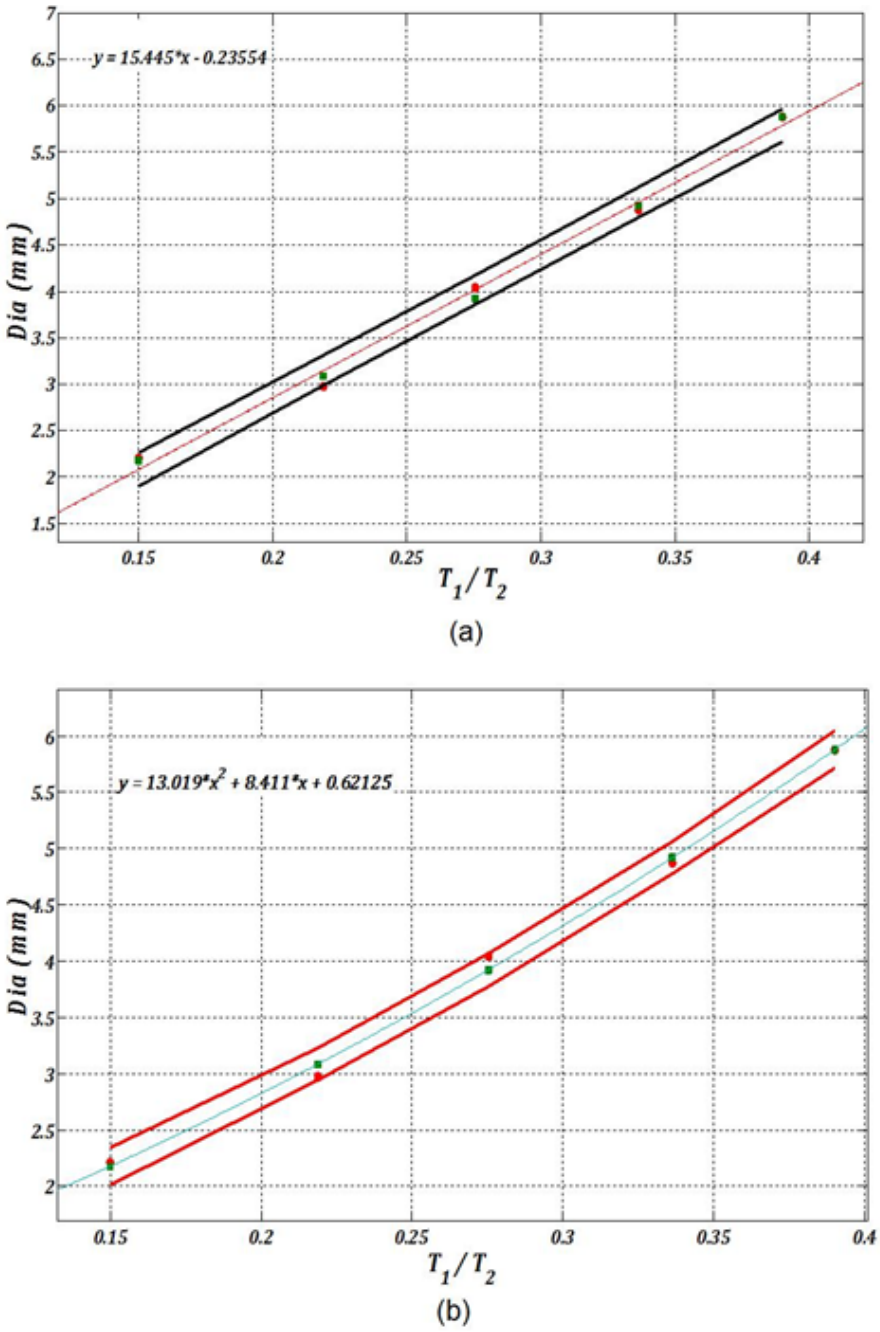

FIG. 4.9- Calibration curve with error estimation (a) linear fit (b) quadratic fit.

4.2.4 Density Measurements

As discussed earlier, the bubbles are formed by inflating a soap film with the help of inner gas of different kinds depending on the desired bubble density. Therefore, the overall density of a bubble ρ_b is given by:

$$\rho_b = \frac{M_b}{V_b} = \frac{M_s + M_g}{V_b} = \frac{M_s}{V_b} + \frac{M_g}{V_b} \tag{4.3}$$

where, M_b and V_b are the bubble total mass and volume respectively; M_s and M_g are the total soap and inner gas masses respectively. As the soap film thickness is very small, compared to bubble's radius ($e/R \sim 10^{-4}$) [35], we assume the volume of gas equal to the bubble volume of same diameter D. Hence the bubble density can be estimated as:

$$\rho_b = \frac{M_s}{V_g} + \rho_g = \frac{M_s}{\frac{4}{3}\pi\left(\frac{D}{2}\right)^3} + \rho_g = 6\,\frac{M_s}{\pi D^3} + \rho_g \tag{4.4}$$

Knowing the inner gas density ρ_g, we only need to measure the mass of soap M_s in each bubble and its diameter D in order to determine bubble's overall density ρ_b.

We have already shown in the previous section how to determine the particle diameter D. We only needed then to determine the mass of soap carried in each bubble. This task was achieved by measuring simultaneously with the bubble generation the soap volume flow rate Q_s and the bubble generation frequency F_b. F_b is easily obtained from the photodiode signal used to measure the bubble diameter. Measuring the soap flow rate turned to be a much complex issue, as it was very small indeed ($1 \times 10^{-6}\ l.s^{-1}$). The final solution consisted using a graduated pipette in which soap flows

from reservoir to the injector and we recorded the change of the volume in the pipette with time. The circuit diagram of heavy bubble generation is given in FIG. 4.10). Measurements over 90 seconds at least were required in order to obtain a change of volume significant enough to be measured accurately. This procedure only allows measuring the average flow rate of soap in time. In order to relate this to the actual quantity of soap in the bubbles a special attention was therefore made to ensure that the bubble generator was operated in a stable state and that no soap was ejected from the injector nozzle without creating a bubble.

Knowing the soap flow rate Q_s , the bubble generation frequency F_b and the soap solution density ρ_s ($\rho_s = 1\ g.cm^{-3}$ in the entire study), the average mass of soap in each bubble, and their corresponding density are given by:

$$M_s = \frac{Q_s \rho_s}{F_b} \tag{4.5}$$

$$\rho_b = 6\ \frac{Q_s\ \rho_s}{\pi\ D^3 F_b} +\ \rho_g \tag{4.6}$$

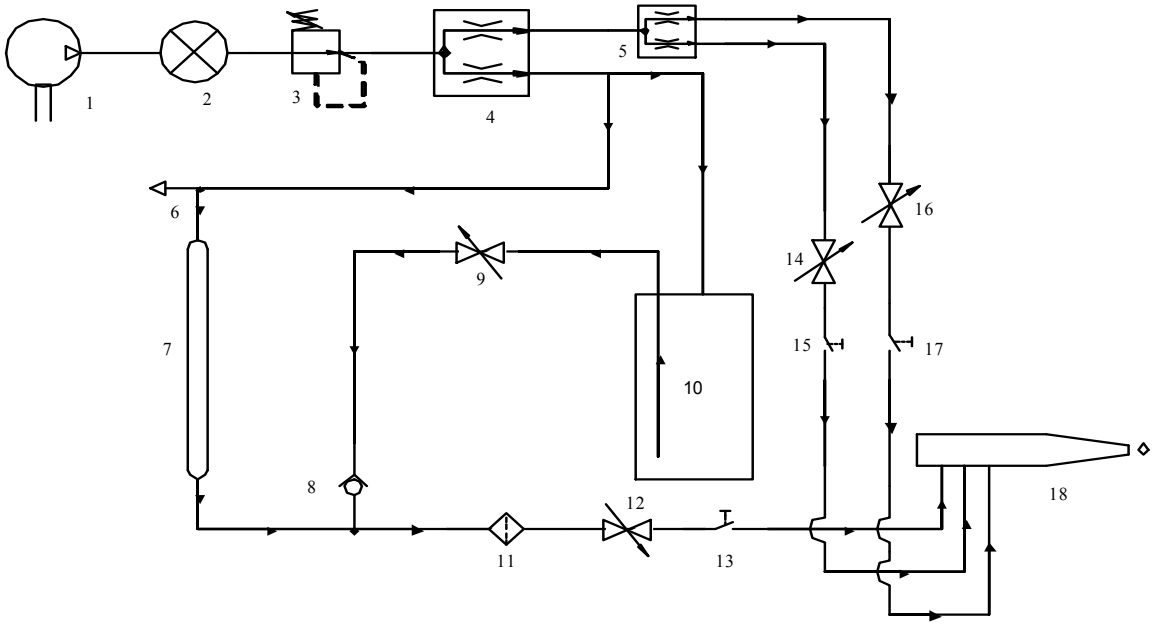

FIG. 4.10- Flow circuit diagram for heavy bubble generation when inflated with air. Air from the compressor (1) is maintained at a specific pressure with the help of pressure relief valve (3), the corresponding pressure can be read on pressure gauge (2). Later on the flow is divided with the help of flow dividers (4 and 5). The soap reservoir (10) is kept under constant air pressure; the soap from reservoir is filled into the pipette with the help of gate (9) and non-return (8) valves. At the moment of pipette filling the plug (6) is removed and the soap supply to the injector nozzle (18) is cut using switch (13). After filling the pipette the plug (6) is switched on and the valve (9) is closed so as to avoid any flow from pipette to reservoir. The switch (13) is opened which permits the soap flow from pipette to injector nozzle after filtering (11) and regulating (12) it. Two air supplies (one for inner gas other for external air) from flow divider (5) are regulated by regulators (14 and 16) and supplied also to injector nozzle; in this manner the heavy bubbles are formed.

From the above equations, it is obvious that the bubble density depends upon the mass of liquid soap in each bubble and the inner gas density; however the first term is dominant in increasing the bubble density. In experiments with heavier bubbles the main challenge is to find a continuous and uniform bubble formation state with close to desired diameter and relative densities. Air and Carbon dioxide were used as inner gases in order to achieve the above objective. This process sometimes took hours to attain or sometimes all efforts were in vain and the next day one has to start from scratch. However, we do not gain much in term of bubble relative densities either using

CO_2 or even SF_6 (that we have not used) as inner gas. Knowing the relative densities of CO_2 and SF_6 are of the order of ~1.4 and ~5.1 respectively, the maximum bubble relative densities that could be obtained would be around 66 and 68 using CO_2 and SF_6 respectively as compared with 65, which we have obtained with air as inner gas, for same mass of liquid soap. Moreover, the bubbles inflated with CO_2, a gas having a good solubility in water, were not stable and a continuous, uniform state of bubble generation was difficult to attain. In the end, for most of our heavy bubble experiments air was used as inner gas, and density was made higher by increasing the soap mass per bubble.

For neutrally buoyant particle tracking experiments with particular bubble diameter, their density was not measured but adjusted visually. We can clearly observe that by changing Helium flow rate the bubbles become heavier or lighter than surrounding air. For particular helium flow rate we can observe that the bubbles neither have a tendency to rise nor to fall, this bubble generation setting was employed for neutrally buoyant experiments.

4.3 Particle Tracking

The instantaneous particle tracking was done employing Ultrasonic Doppler Velocimetry. This technique permitted us to track particles in wind tunnel turbulent flow with high mean velocity, resolving simultaneously the smallest and a good fraction of the largest time scale of turbulence. Before going into the details of our tracking technique and its characteristics it is necessary to highlight some basic physical principles involved.

4.3.1 Acoustic Scattering

Whenever a sound wave encounters an obstacle or inhomogeneity along its propagation path, it is deflected from its original course. This deflected sound wave is called as scattered wave and hence the phenomenon is named as acoustic scattering. The obstacle or inhomogeneity could be, fish or plankton in the ocean, red blood corpuscles in the bloodstream, vortex in a turbulent flow, water droplets or soap bubbles in air flow, or any object with any form and shape offering a contrast of acoustic impedance with respect to ambient propagating medium. The wave scattered due to these obstructions spread out in all directions, could distort and interfere with the incident wave. In general the nature of acoustic scattering depends upon the frequency of incident wave, shape and size of the obstacles and their velocities. If the obstacle is very large compared with the incident wavelength, half of this scattered wave spreads out in all directions whereas, the other half is concentrated behind the obstacle, creating a sharp-edged shadow there. On the other hand for obstacles very small, compared with the wavelength, the entire scattered wave propagates out in all directions with no sharp-edged shadow. In the cases of obstacle sizes comparable with wavelength a variety of curious interference phenomenon can occur. Expressions of scattering from various obstructions like cylinder, inhomogeneities, turbulence, rigid sphere, non rigid sphere, porous sphere etc exist in the literature but here only scattering from rigid sphere will be discussed.

4.3.1.1 Scattering by a Sphere

Consider a plane harmonic pressure wave propagating in a direction parallel to the Z-axis (as shown in FIG. 4.11).

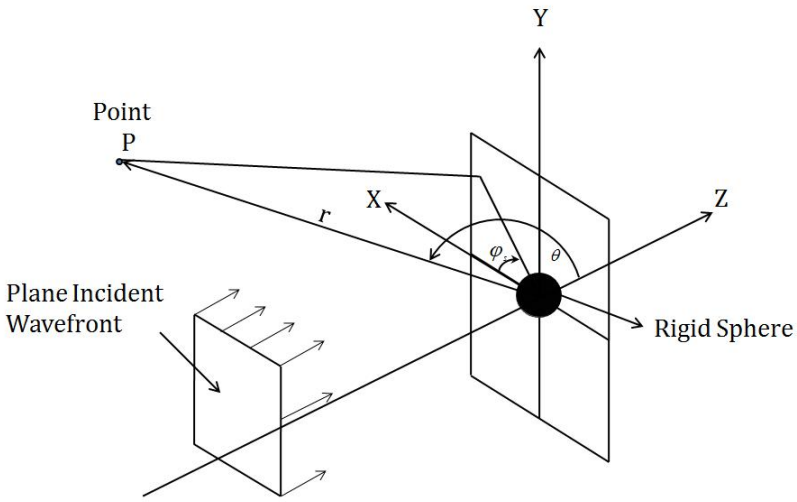

FIG. 4.11 – Geometrical scheme showing acoustic scattering of plane wave by a rigid sphere.

The expression for plane pressure wave is given as:

$$p_i(t) = p_0 e^{iq(ct-z)} \tag{4.7}$$

where, p_0 is the pressure amplitude, q is the wave number, z is the Z coordinate and t represents time. This incident pressure wave is scattered by sphere, and the scattered pressure field at any point P in space is given by the difference of total and incident pressure as following:

$$p_s(t) = \left({}^{p_0 a_s}/_{2r}\right) e^{iq(ct-r)} f(qa) \tag{4.8}$$

where, a_s denotes the sphere's radius, r is the position vector of point P and $f(qa)$ is the reflection form function of the sphere. This form function however depends upon the coordinates of r and θ of the point P but not on φ_s due to symmetry. For rigid sphere the form function is following:

$$f(qa) = -2\left(\frac{qr}{qa_s}\right) e^{iqr} \sum_{n=0}^{\infty} (-i)^{n+1} h_n^{(2)}(qr)\, P_n(cos\theta)(2n+1) \sin\eta_n e^{i\eta_n} \tag{4.9}$$

where, $P_n(cos\theta)$ is the n[th] degree Legendre polynomial, and η_n is parametrical defined as

$$\tan\eta_n = -\left[\frac{(n+1)j_n(qa) - (qa)j_{n-1}(qa)}{(n+1)y_n(qa) - (qa)y_{n-1}(qa)}\right]$$

$h_n^{(2)}$, j_n and y_n are the spherical Bessel functions.

4.3.2 Ultrasonic Transducers

4.3.2.1 Construction and Mounting

The ultrasonic emission and reception was accomplished with the help of two identical plane circular piston type radiators (Sell Type transducers), one serving as emitter while the other performing the reverse operation i.e. reception.

FIG. 4.12 shows a transverse view of a transducer: basically it is a capacitor with a fixed conductor (a circular zinc plate) and a mobile membrane (a Mylar sheet metalized on the outer face).

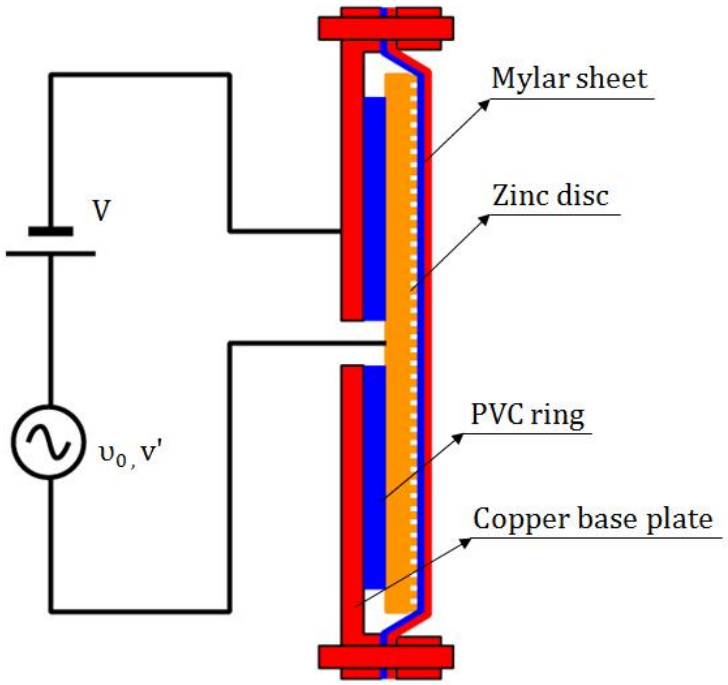

FIG. 4.12 - Electro-acoustic transducer schematics.

These transducers are homemade, developed under the premises of L.E.G.I., except the zinc disc. The surface of the zinc disc facing the insulated side of the Mylar sheet was photo etched for having micro-structure square dot patterns of sizes $100\mu m$ and a depth of $120\mu m$ each. Each of these cavities behaves as a small plane piston radiator. This zinc disc is mounted on a pvc ring, which is screwed with a copper plate, with no connection between zinc and copper plate. On PVC ring a Mylar sheet of 12 microns thickness is glued, one side of which is conductor, whereas the other is an insulator. This PVC ring and glued Mylar is attached with transducer's main body with an aluminum ring. The connection between Mylar conducting surface and copper base plate is made with the help of aluminum ring and screws. The polarization of zinc disc and Mylar sheet creates capacitance between the elemental cavities on the zinc disc and

insulated side of Mylar sheet. As a result the Mylar sheet is stretched. In the case of the emitter, whenever a sinusoidal excitation is made while the Mylar is stretched, it vibrates with the excited frequency hence propagating sound wave in the direction perpendicular to the transducer surface. The transducer is reversible and can be used as a receptor as well: whenever a sound wave vibrates the stretched Mylar sheet, the resulting change of the capacitance between Mylar and elemental cavities generates a modulation of the polarization point; which is at the frequency of the incident wave. Contrary to piezo-electric transducers an interesting property of Sell type transducer is that they can be operated over a wide range of frequencies.

4.3.2.2 Field Characteristics

In order to know and optimize measurement zone's dimensions and to ensure correct particle tracking, it is necessary to know the acoustic field generated by these transducers.

The field established by circular piston type radiator is rather complicated and difficult to determine at all distances and angles. However, the pressure amplitude on the axis of the piston can be given by the following expression [48]:

$$P\,(r, \theta = 0) = \; 2\rho_0 c\, U_0 \left| sin \left\{ \frac{1}{2}\, q\, r \left[\sqrt{1 + \left(\frac{a}{r}\right)^2} - 1 \right] \right\} \right| \tag{4.10}$$

where, ρ_0 is the density of the fluid, c is the celerity of sound, U_0 is the speed amplitude at piston surface, q is the wave number, r the axial distance from piston

center and a is the radius of the piston. For a case with $r/a \gg 1$ and also $r/a \gg qa$ the pressure amplitude on the piston axis has an asymptotic form which is given as:

$$P\,(r, \theta = 0) = \frac{1}{2}\,\rho_0 c U_0 \frac{a}{r} ka \tag{4.11}$$

In our experiments, the excitation frequency is 80 kHz that gives a wave number q ~1465 m^{-1} and the radius of transducers is 3.5cm. In FIG. 4.13, the normalized pressure amplitude (normalized with 2 $\rho_0\, c\, U_0$) as a function of axial distance from transducer is plotted (solid blue line plot). For small values of r we can observe amplitude fluctuations from zero to unity, at some distance $r_c \approx 0.3m$, these oscillations stop and a final peak is reached, which is regarded as the end of *"near-field"* pressure amplitude region or the boundary between near-field and *"far-field"*. For values greater than r_c the pressure amplitude falls steadily. The normalized asymptotic pressure amplitude is also shown in FIG. 4.13 as red dashed lines. It can be noticed that the two plots match well for large axial distances from piston. The same normalized pressure amplitude is plotted in FIG. 4.14 as a function of axial distance normalized by transducer radius. The axial pressure amplitude is given in following figures.

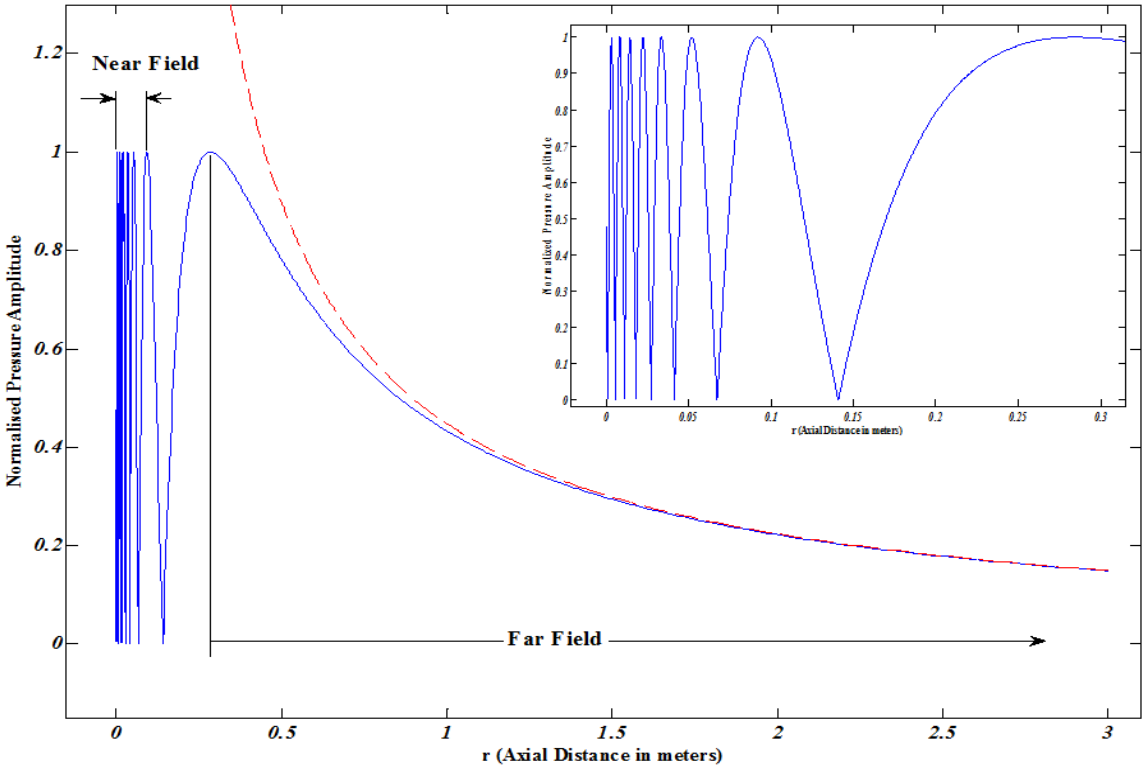

FIG. 4.13 – Normalized pressure amplitude as a function of axial distance from circular piston type transducer of radius 3.5mm while excited with a frequency of 80 kHz. In red dashed line the normalized asymptotic pressure amplitude is plotted. Inset shows the near field region.

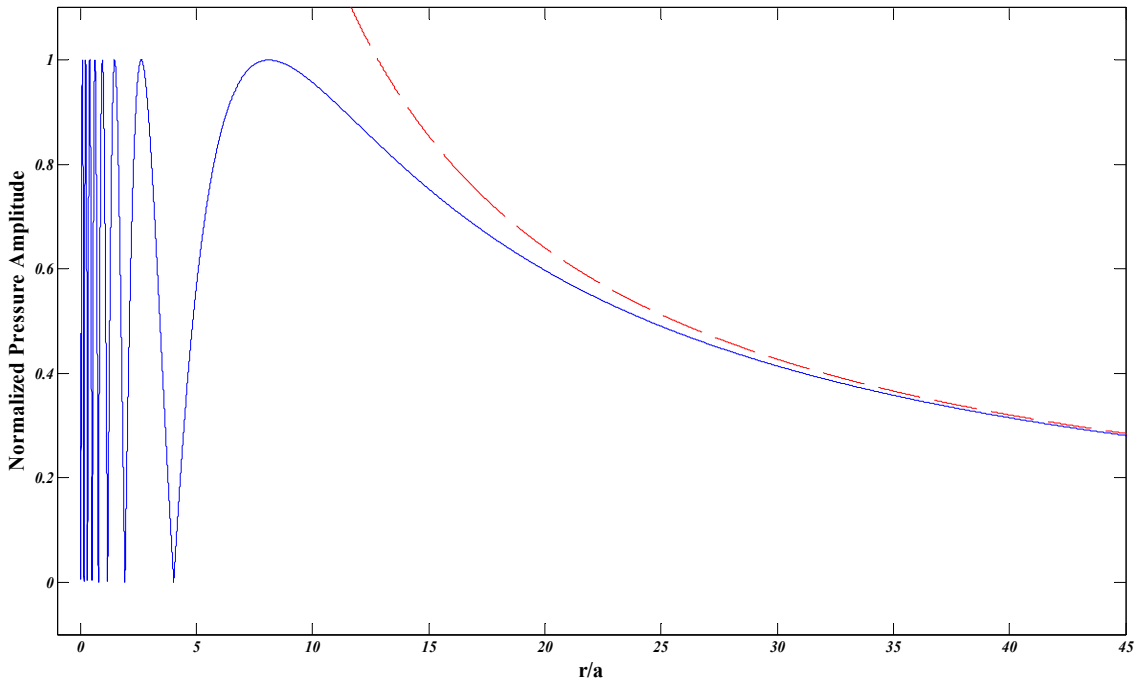

FIG. 4.14 – Normalized pressure amplitude as a function of axial distance normalized with radius of circular piston transducer. In red dashed line is shown the normalized asymptotic pressure amplitude.

The directional effects are taken into account by a directional factor, which multiplied by axial pressure amplitude gives the total pressure field as a function of distance and angle *(θ)* from piston axis.

$$P(r,\theta) = P(r,\theta = 0)H(\theta) \tag{4.12}$$

where, the directional factor is given by, $H(\theta) = \left|\frac{2J_1(qasin\theta)}{qasin\theta}\right|$, J_1 is the Bessel function of first kind with order one. In FIG. 4.15, the functional behavior of directional factor is plotted, we can observe at $\theta = 0$; the factor is unity which corresponds to pressure amplitude at the piston axis. The factor then starts decreasing indicating the decrease in pressure amplitude with increasing angle until it reaches zero which indicates the pressure node with vortex at the piston surface. In between these angles lies the principle lobe. The next relative maximums correspond to maximum pressure amplitudes of secondary lobes; whereas the successive zeros correspond to the pressure nodes of secondary lobes. It can be noticed that there is a factor of 10 between the pressure amplitudes of principal and first secondary lobe.

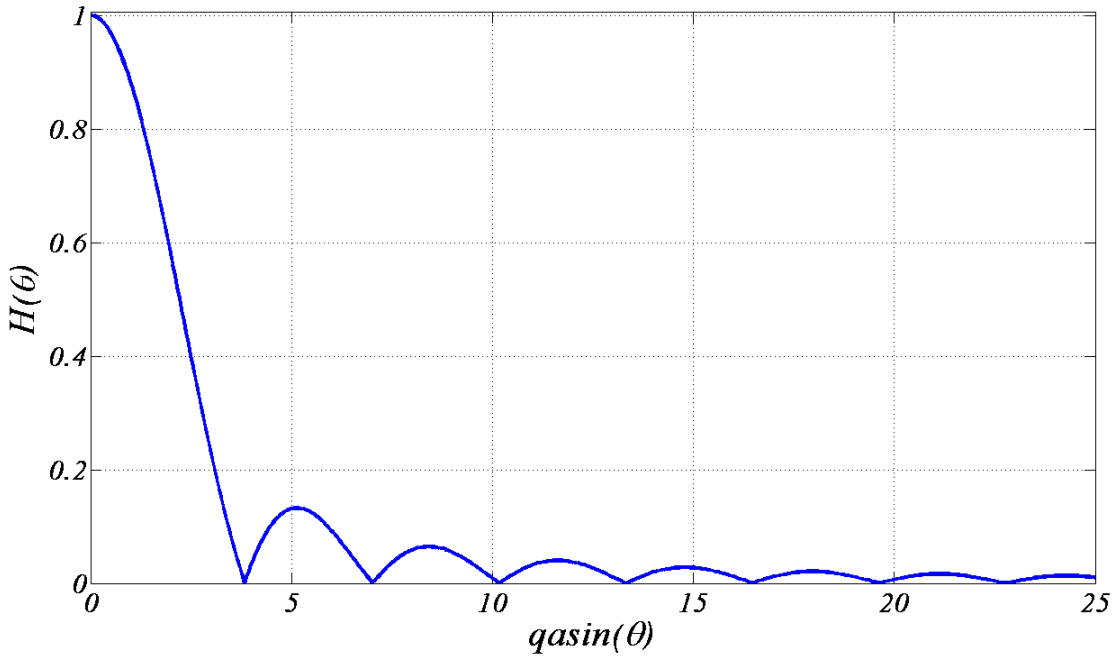

FIG. 4.15 – Functional behavior of $H(\theta)$.

The variation of intensity level with angle; also called as directivity pattern is defined as $b(\theta) = 20 \log H(\theta)$. The beam pattern for circular piston with $qa = 51.3$ is plotted in FIG. 4.16, we can observe the principal lobe is one order of magnitude greater than the first secondary lobe. It can also be noticed that the transducers have high directivity with principal lobe forming between angles $\pm 4.3°$.

It was the high directivity of transducers that allowed us to track the particles only while passing through the measurement volume formed by intersecting the emitter and receiver principal lobes.

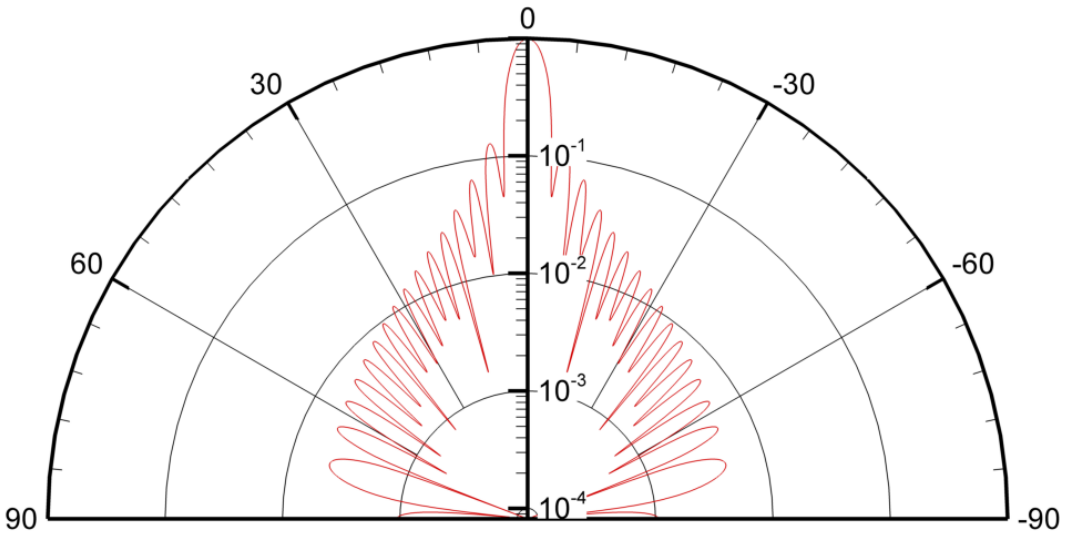

FIG. 4.16 – Beam pattern for a circular piston for $qa = 51.3$.

4.3.3 Ultrasonic Doppler Velocimetry

After having discussed acoustic scattering, electro-acoustic transducers, their characteristics and geometrical arrangements for particle tracking; we will now consider the tracking principle in detail. An ultrasonic sinusoidal wave emanating from ultrasonic emitter propagates with frequency ϑ_0, in a particular direction $\vec{n}_0$. This wave is scattered by a particle which is entered in its propagation zone. As long as the particle remains in measurement volume this scattered wave is being recorded by receiver in a particular direction $\vec{n}$ with scattering angle θ_{scat} as shown in

FIG. 4.17. The scattered signal is received with an instantaneous frequency shift $\delta\vartheta(t) = \vartheta(t) - \vartheta_0$, due to Doppler effect. By definition, the scattered wave vector is given as following:

$$\vec{q}_{scat} = \vec{q}_n - \vec{q}_{n_0} = \frac{2\pi\vartheta}{c}\vec{n} - \frac{2\pi\vartheta_0}{c}\vec{n}_0 \tag{4.13}$$

$$\vec{q}_{scat} = \frac{2\pi\vartheta_0}{c}(\vec{n} - \vec{n}_0) \tag{4.14}$$

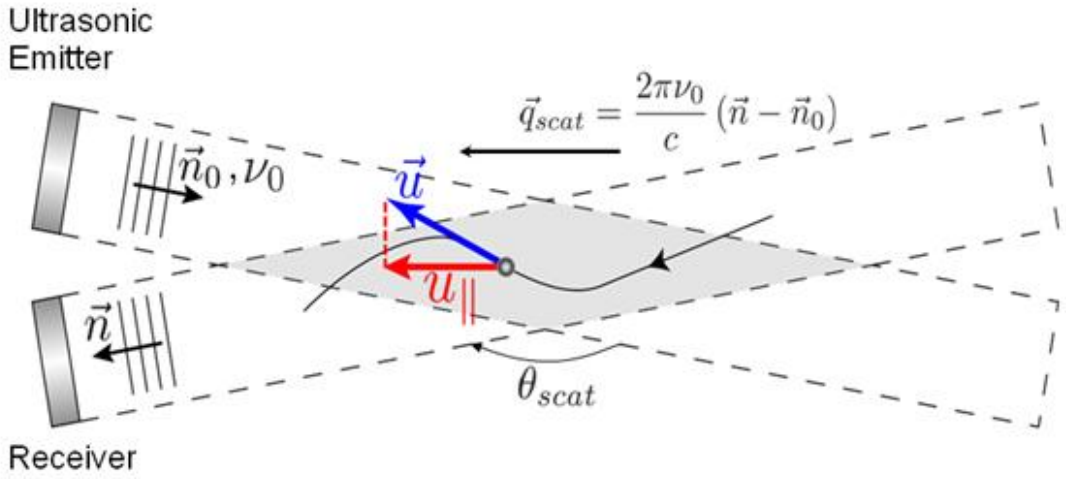

FIG. 4.17 - Ultrasonic Doppler Velocimetry scheme.

where an assumption was made that the emitted and received frequencies are close to each other i.e. $\delta\vartheta = \vartheta - \vartheta_0 \ll \vartheta_0$, which is almost true in our case as the frequency of emission is 80kHz and the received frequency fluctuates around 87kHz. The instantaneous frequency shift expression derived from Doppler effect principle is given by,

$$\delta\vartheta(t) = \vartheta(t) - \vartheta_0 = \frac{1}{2\pi}\,\vec{q}_{scat}\,.\vec{u}(t) \tag{4.15}$$

After some geometrical calculations following expression can be derived from equation (4.15),

$$u//(t) = \frac{c}{2\pi\vartheta_0 Sin\left(\frac{\theta_{scat}}{2}\right)}\,\delta\vartheta(t) \tag{4.16}$$

From equation (4.16), we can easily observe that particle's instantaneous longitudinal velocity is directly proportional to the instantaneous frequency shift. If we are capable of determining the instantaneous frequency shift then we can also obtain particle's instantaneous velocity along its trajectory throughout its passage in the measurement volume. In order to determine this frequency shift several methods exist, these methods are discussed in the upcoming sections.

4.3.3.1 Measurement Zone

As described earlier, the measurement zone is formed by the intersection of emitter and receiver principal lobes. Its dimensions depend upon several factors like; the diameter of transducers, excitation frequency, and angle between emitter and receiver. The larger the transducer diameter the greater will be the measurement volume converse is the case with excitation frequency. While increasing the angle between emitter and receiver the longitudinal dimension of measurement zone increases too. Similarly the location of measurement zone depends upon the center distance and angle between transducers, and the position where emitter and receiver

are placed in the wind tunnel. Knowing the placement window constraints, and to locate the measurement volume in a region where the turbulence is nearly homogeneous and isotropic, required these parameters adjusting accordingly. The transducers were placed in the divergent section after the 4 meters test section so as to have minimum hindrance with the flow. A special attention was made for the alignment of the transducers so as to have the center of measurement volume at the center line of wind tunnel's longitudinal axis. Thanks to the rail and trolley setup the location and dimension of measurement volume was determined. A metallic rod was held vertically in the trolley which was then moved downstream with a constant speed along the axis of test section. At First, the measurement was done placing the rod at the cross section center and the resulting scattered signal was recorded. The rod was then shifted transversally and moved with the same speed. From the recorded signals the intensity of scattered signal was determined and plotted as an image which is given in FIG. 4.18.

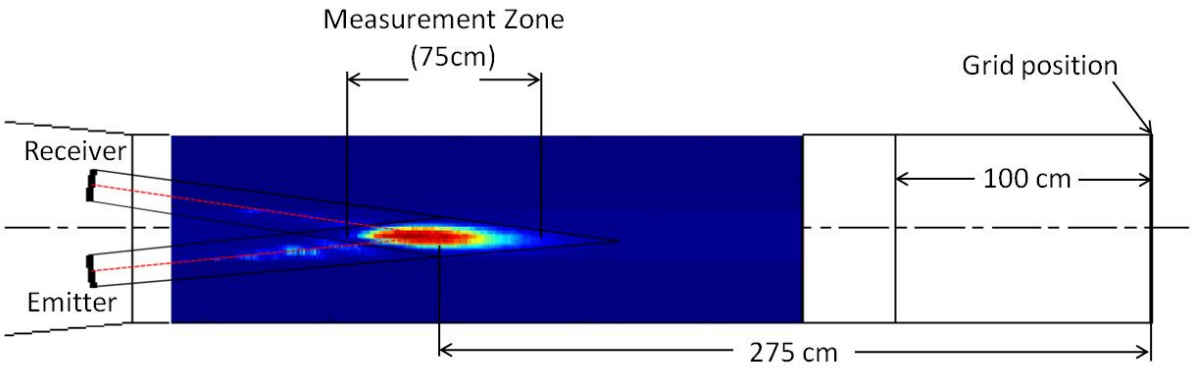

FIG. 4.18 – Experimental determination of the measurement zone in the wind tunnel (figure not to scale).

From FIG. 4.18, we observe the position of the measurement zones from the grid and its size. On the zone of acoustic wave propagation, just before the measurement

zone, we can see the field which results from the emitter's/receiver's principle lobe interference with receiver's/emitter's secondary lobes. This however is much clear in the case of interference with emitter's principle lobe with receiver's secondary lobes. For a comparison we have also calculated the theoretical acoustic field generated by the interference of emitters and receivers acoustic fields while keeping the geometrical and emission parameters approximately the same. This interference pattern is shown in FIG. 4.19. The calculations were done by the discrete integration of Huyghens-Fresnel principle. Qualitatively same patterns have been observed when compared with experimental measurements, with measurement volume having a size of around 60 cm and here the interference of one transducer's principle lobe with the secondary lobes of the other one is identical, which should be the same due to the identical nature of the two transducers.

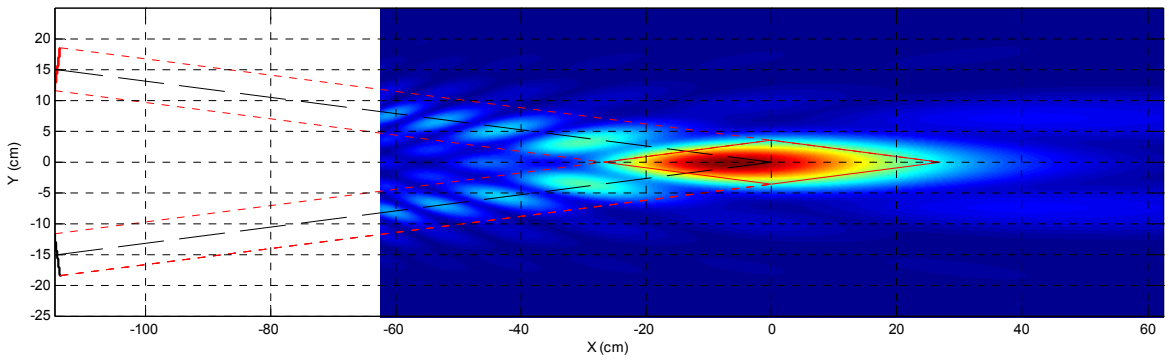

FIG. 4.19 – Acoustic field resulting from emitter and receiver field's interference. The acoustic field is calculated using Huyghens-Fresnel discrete integration.

4.4 Data acquisition and processing

4.4.1 Data acquisition

The acoustic wave emission, reception and acquisition are done with the help of a number of pieces of equipment. The general scheme is given in FIG. 4.20.

A wave form generator of HP 33120A type was used for the emission of a plane sinusoidal wave at a frequency of 80 kHz and amplitude of 5 volts in the test section of wind tunnel. In order to compensate the vibrating membrane inertia and electrical to mechanical energy conversion losses, the signal power is increased by amplifying it using a NF Electronics 4005 high speed power amplifier with a gain of the order of 20. After passing through the emitter polarization box the signal excites the emitter and hence a plane sinusoidal wave is produced and propagates in a particular direction.

On the other hand the receiver which is also polarized with the help of receiver polarization box detects the signal scattered by the particle passing by the measurement zone with a frequency shift. The signal received with a frequency shift is band pass filtered using NI 3628 dual channel programmable filter. The filtered signal is visualized on SRS 2 channel dynamic spectral analyzer screen. Heterodyning of emitted and received signal is done by multiplying the two signals and low-pass filtering. This process enables to shift emission frequency i.e. 80 kHz to zero so as to digitize shifted signal at relatively low sampling frequencies. An Agilent HP E1401B series High Power VXI Mainframe with E1430A VXI 23-bit digitizer and 743 VME High-Performance Precision Architecture Board and an external hard disk is used for data acquisition and

storage. Acquisitions were done at a sampling rate Fs = 32768 Hz. For a each particular size and density of particle, several thousands of trajectories were recorded.

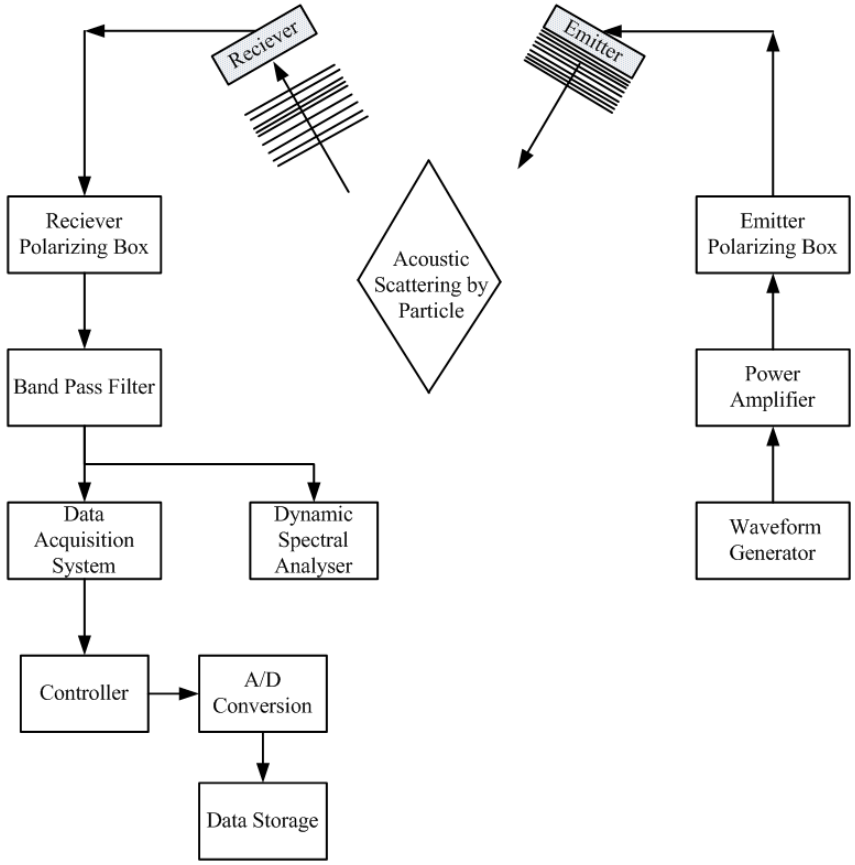

FIG. 4.20 - Flow diagram from acoustic signal generation to data receiving and storage

4.4.2 Data Processing

After the heterodyne down-mixing, the complex signal scattered by an individual particle has an amplitude and instantaneous frequency shift information. The expression for the recorded complex signal can be written as under:

$$z\,(t) = A(t)e^{i2\pi \int_0^t \delta\vartheta(t')dt'} \tag{4.17}$$

In FIG. 4.21(a), a typical example of the amplitude of the signal is plotted versus time; the amplitude peaks represent the passage of either a single or many bubbles in the measurement zone. In FIG. 4.21(b), zoom of an individual bubble passing the measurement volume is presented; the high amplitude peak indicates the bubble passage in far field region, whereas the two subsequent lower peaks signify its passage in the near field region. In FIG. 4.22, the power spectrum of the portion of signal corresponding to the selected bubble (whose amplitude is shown in figure FIG. 4.21(b)) shows that Doppler shift information is centered around the frequency of 6.7 kHz, which correspond to the mean velocities of bubbles. From the width of the Doppler peak we can see that the required information of particle's instantaneous velocity resides in the frequency range of 6.4-7 kHz (note that the total width of the shift is due not only to the turbulent fluctuations of particle velocity but also to the finite time length of the signal). Our prime objective is to determine the instantaneous frequency shift and hence instantaneous velocity, in order to actually resolve in time the turbulent fluctuations of the velocity.

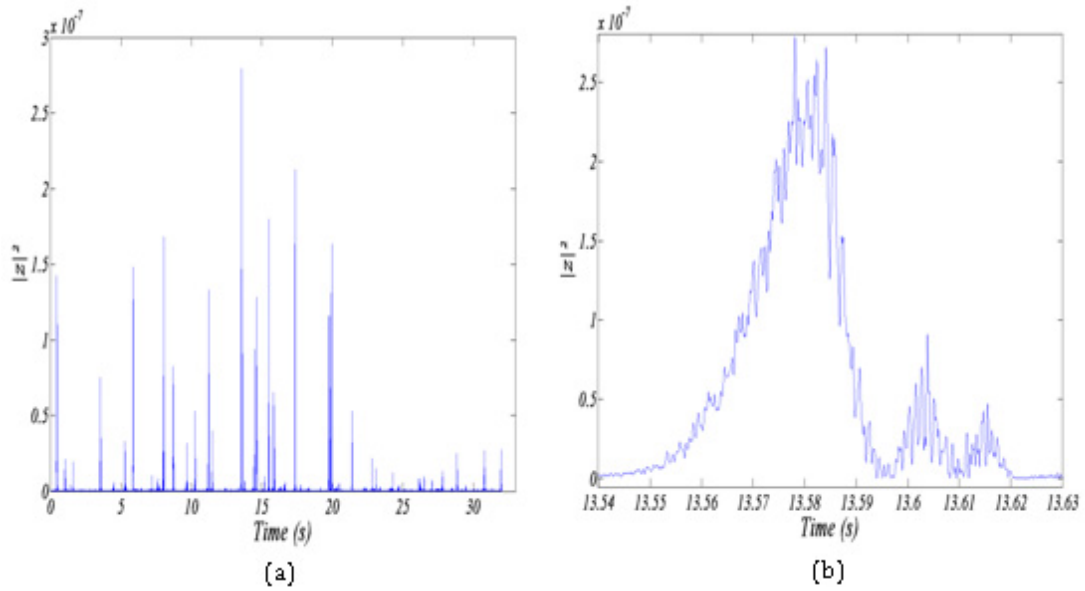

FIG. 4.21 – (a) Complex signal plot amplitude v/s number of points (time), the amplitude peaks indicates the passage of an individual or many bubbles in the measurement zone. (b) Zoom of a single bubble passage, the main peak represents the bubble passage in far field, whereas the two secondary peaks signify its passage in near field region.

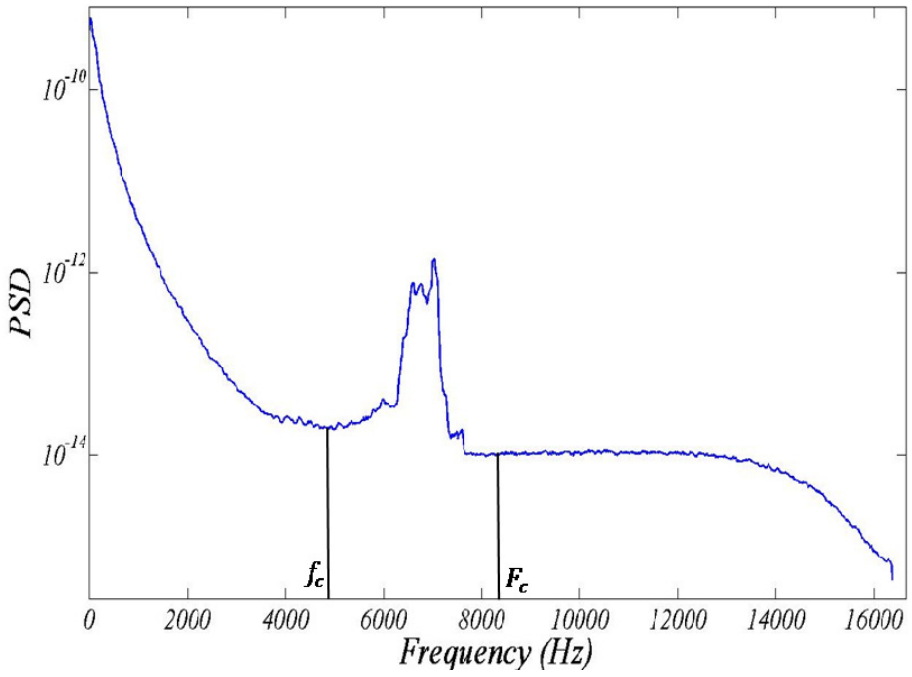

FIG. 4.22 – Power spectrum of the recorded signal, the emission frequency peak has already been shifted to zero by heterodyning signal, the bubbles passage signals are represented by peaks around frequency of ~ 6.7 kHz, which corresponds to mean flow velocities of the bubbles.

There exist several methods that can be used for determining the instantaneous frequency shift, among which are phase differential, time frequency and parametric algorithms. The choice depends upon the signal to noise ratio of the data, resolution required, processing time and adaptability to our recorded signals. For example the phase differential method is very sensitive to signal to noise ratio and only an individual particle's frequency information can be extracted. On the other hand time frequency analysis based on, short-time Fourier transform method has resolution limitations and there is a tradeoff between the resolution in time and instantaneous frequency (Heisenberg uncertainty principle). Enhanced methods, based on reallocation algorithms has been developed [30] to overcome this limitation, however, these approaches remain extensively time consuming in terms of numerical calculation and also it takes long calculation times.

An interesting alternative is offered by parametric approaches, such as Maximum Likelihood Algorithm (MLA), which has already been used by Nicolas Mordant during his PhD work [57] to achieve Lagrangian tracking of particles in a von Kármán swirling flow of water. In our study we have used the same algorithms. Here we will not enter into the depth and details of this approach (which can be found in [57]) however its basic methodology, regulating parameters and the modifications we made to the method according to our application will be discussed.

The idea of this algorithm is to overcome the Heisenberg uncertainty principle, by introducing in the time-frequency analysis some known information of the signal. For instance, when the emitted sinusoidal wave with known frequency and amplitude is scattered by a particle, the corresponding signal received is also expected to be

sinusoidal although its amplitude and instantaneous phase are time dependant; moreover the signal may be affected by acoustic and electronic noise as well as noise due to turbulence. The algorithm generates a synthetic signal with a sinusoidal wave and random noise. The resulting synthetic signal is then matched (amplitude and frequency serve as matching parameters) with the original signal recorded, the residuals are determined named here as a Hessian. A threshold for Hessian which is defined by the user determines whether or not to accept the whole or part of the synthetic signal's instantaneous frequency.

In practice, we apply the MLA to the recorded acoustic signal filtered around the Doppler peak, in order to keep only the frequency information pertinent for our study. In particular, we suppress the large central peak (at f = 0 Hz) corresponding to residual signal (echoes and other reflections, from the direct acoustic wave from the emitter) as well as the large frequency noise.

In order to determine the limits of the filter width to be used around the Doppler peak to conserve the relevant frequency information, we have implemented an iterative version of MLA:

We first proceed to a coarse band-pass filtering of the Doppler peak where the low cut-off frequency, f_c, is chosen at the minimum of the spectra between the central peak and the Doppler peak (for instance $f_c \sim 5$ kHz in FIG. 4.22) and the high cut-off frequency, F_c, is chosen as the symmetric of f_c with respect to the maximum of the Doppler peak ($F_c \sim 8.4$ kHz in FIG. 4.22).

We then apply the MVA algorithm to the resulting filtered signal with a high level of modeled noise (in order to keep the noise in the extracted signal). This leads to a first estimation of the instantaneous frequency of the Doppler signal, which present rapid fluctuations attributed to noise. We have represented in FIG. 4.23 a comparison of the instantaneous Doppler shift $\delta\vartheta_0(t)$ between classical time-frequency based on Fourier analysis and maximum likelihood algorithm (in both cases we have used an analysis window short enough to resolve the rapid noisy fluctuations).

1. From this first estimation, we can see that the actual relevant frequency ranges for $\delta\vartheta_0(t)$ is much narrower than the coarse estimation $[f_c, F_c]$ from step 1. We therefore use the result from the first MLA estimation to narrow the width of the pass-band filter around the Doppler shift based on the maximum ϑ_M and minimun ϑ_m frequency from $\delta\vartheta_0(t)$. We then band-pass filter the original acoustic signal with cut-off frequencies ϑ_m and ϑ_M and proceed to a new MLA estimation $\delta\vartheta_1(t)$. This procedure ensures an adaptive filtering for each individual particle detected. Note that because we have kept the noise level high in the first estimation, we are sure that the new filter width still keeps all the relevant Doppler information. The procedure can be iterated *i* times again to estimate $\delta\vartheta_1(t)$. The question which arises here, how many times should the iterations run? FIG. 4.24 represents the successive spectra of the Doppler signal at different iterations. We see that the most important effect is at the first iteration. FIG. 4.25 and FIG. 4.26 respectively show the MLA estimations $\delta\vartheta_1(t)$ and the corresponding Hessian, after *i* iterations, for $i = 0 \geq 5$. We observe that the first iteration significantly reduces the rapid noisy fluctuations and that

the Hessian level drops drastically, indicating a much better MLA estimation (we have moreover checked from the first iteration, the MLA estimation becomes essentially insensitive to the noise level given as input parameter of the algorithm). The forthcoming iterations ($i > 1$) tend then to smooth further the Doppler shift time evolution, but we notice that for first iteration the hessian reduces remarkably whereas if we iterate further it starts increasing again suggesting that the estimation is poorer. This is probably due to the fact that iterations for $i > 1$ tend to filter too much the signal and to eliminate part of the actual signal. In the following we will therefore use only one iteration step.

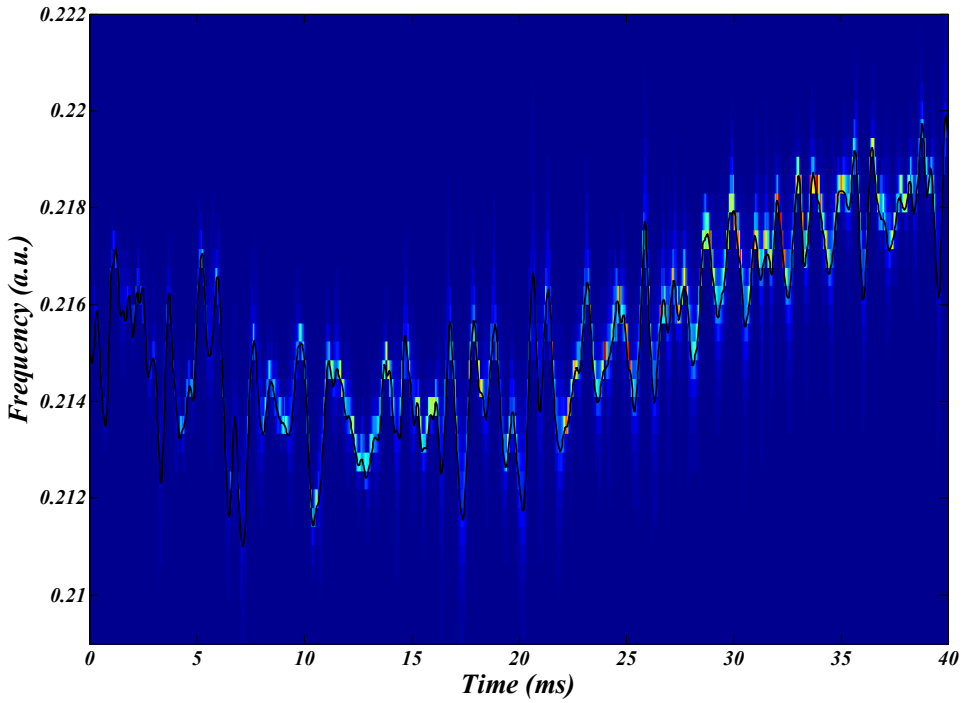

FIG. 4.23 – Comparison of Time-Frequency and MLA.

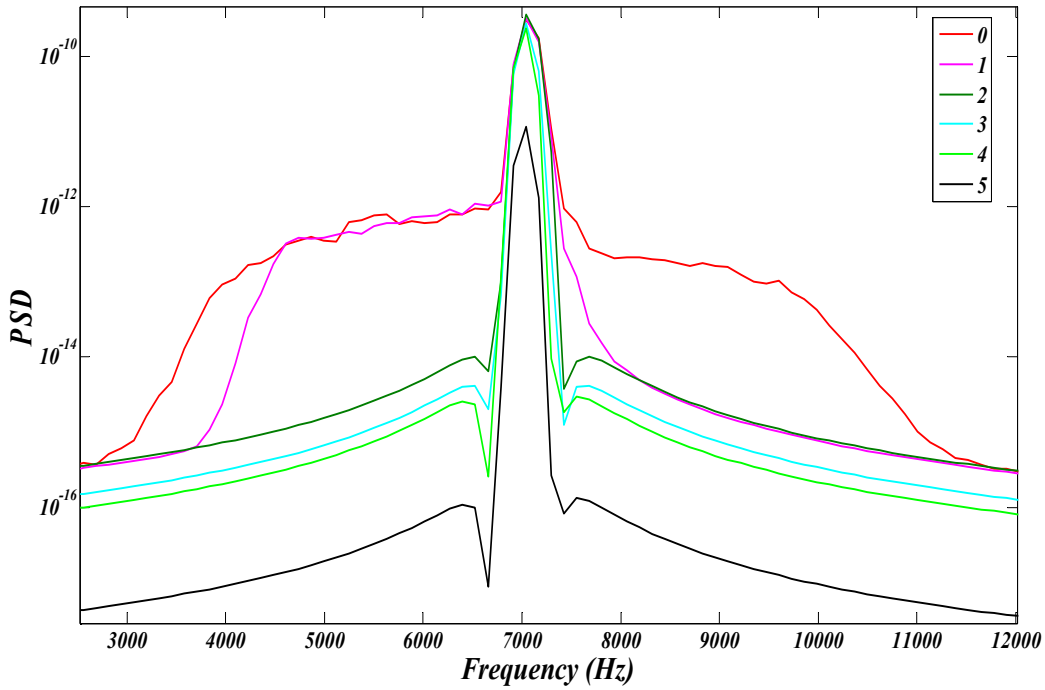

FIG. 4.24 – Power spectrum of particle's signal after first run and successive iterations of MLA.

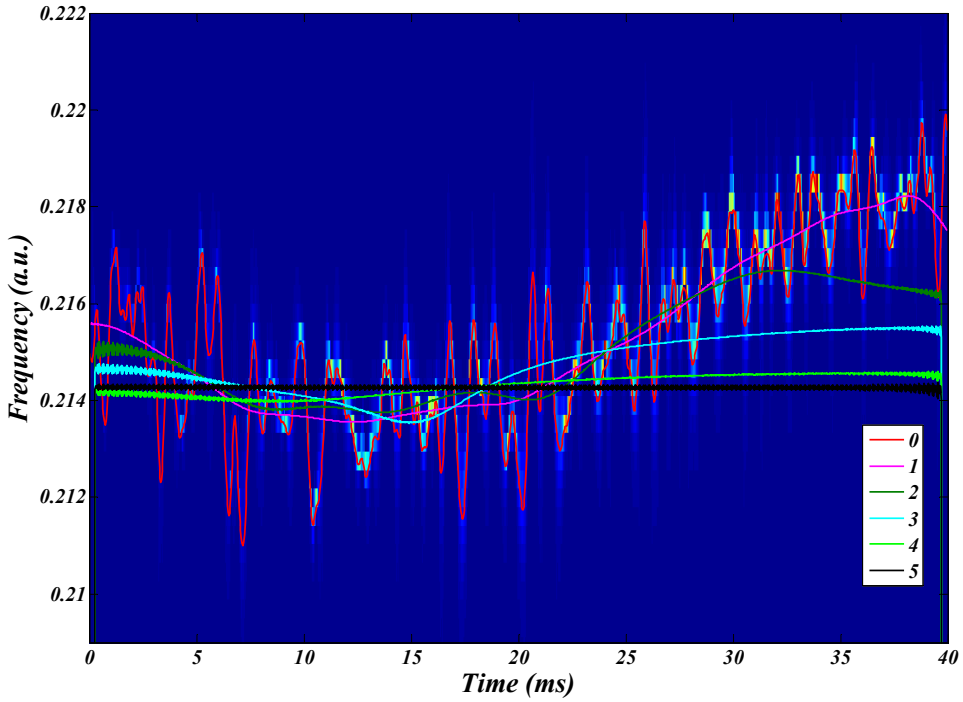

FIG. 4.25 – Comparison of time-frequency, first and successive iterations of MLA.

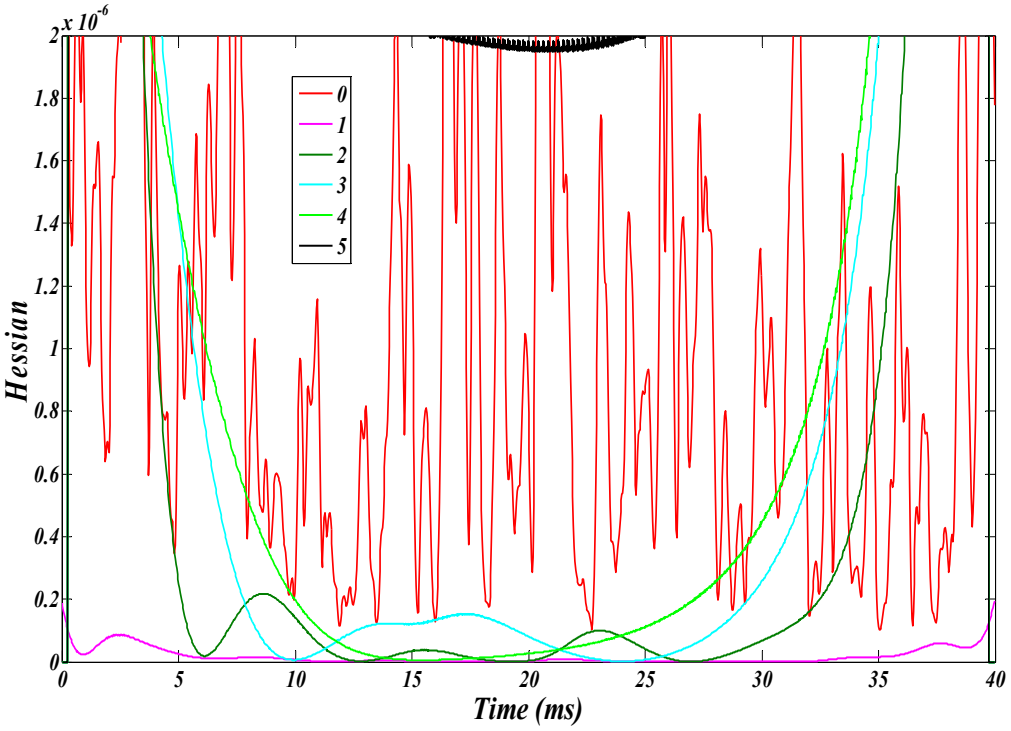

FIG. 4.26 – Hessian of the corresponding signal, for first run and successive iterations of MLA.

In order to test further the iterative MLA, we show an example from a synthetically generated Doppler signal with similar dynamical properties to the signal scattered by our particles in the wind tunnel. The synthetic acoustic signal is defined as:

$$z(t) = A(t)e^{i\int_0^t \delta\vartheta(t')dt'} + 0.2n(t) \tag{4.18}$$

where the signal amplitude has been taken as a hamming window, in order to model the profile of the amplitude of the scattered signal as a particle travels across the measurement volume (as in FIG. 4.27(b)) and $n(t)$ is a random Gaussian noise (we have also considered the case where some noise is also added in the amplitude $A(t)$ which doesn't change the discussion below).

The "physical" Doppler shift $\delta\vartheta(t)$ has been modeled as an offset $\delta\vartheta_{offset}$ plus sinusoidal fluctuation at frequency f_0:

$$\delta\vartheta(t) = \delta\vartheta_{offset}\,(1 + a\,sin(2\pi f_0 t)) \tag{4.19}$$

The offset represents the average Doppler shift due to the mean velocity of the particle (here we have taken $\delta\vartheta_{offset} = 7kHz$ while the sinusoidal fluctuation models the turbulent component of the velocity. The amplitude of the fluctuation has therefore been taken equal to $a = 0.01$ of $\delta\vartheta_{offset}$ (the typical fluctuation level of individual trajectories is of 1% as it will be shown in section 5.4) and f_0 has been chosen to represent a time scale in the inertial range of our turbulent flow here we have taken $f_0 = 50\,Hz$.

The goal of the exercise is now to extract the most accurately the "physical" Doppler information $\delta\vartheta(t)$ from the acoustic signal $z(t)$ synthetized as in (1). FIG. 4.27(a) represents the evolution with time of the original "physical" signal (2) in black, the results from the first MLA estimation ($i = 0$) from $z(t)$ in blue, and the first iteration ($i = 1$) in magenta (we have also represented in red color the estimated Doppler signal using a single MLA path but with an optimized value of the modeled noise level as input parameter); FIG. 4.27(c) shows the corresponding Hessian. We see that the first iteration is almost indistinguishable from the "physical" signal. FIG. 4.27(b) represents relative error between the "physical" signal and the different estimations (first estimation in blue, first iteration in magenta, single path with optimized modeled noise level in red). The iterated estimator clearly gives the best result with less than 0.1%

error. Though it approaches well the desired “physical” signal, the single MLA path with the optimized modeled noise level is not as good as the iterated estimator.

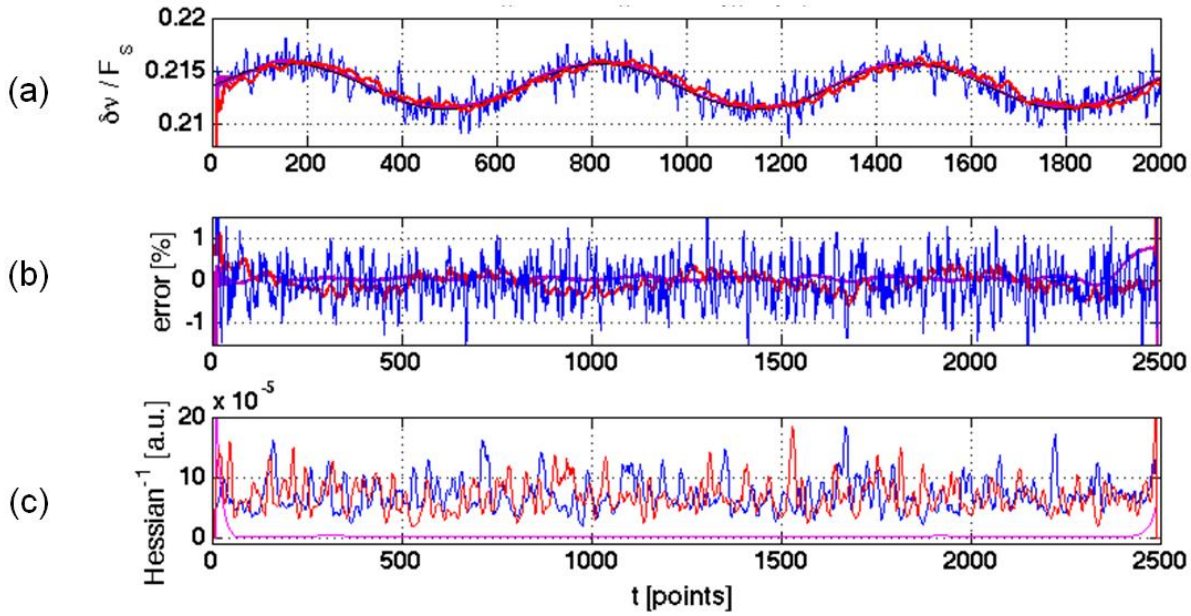

FIG. 4.27 – An example of the application of iterative MLA on a synthetic signal.

A special attention was made to ensure the selection of individual particle signal by selecting only high peak amplitude events and amongst them only those events were chosen for statistical calculations which met very strict Hessian criteria. Thousands of velocity signals for each set of particle size and density were recorded and their Lagrangian statistics were determined.

Chapter 5

Single Time Statistics

This chapter describes the parameter space (in terms of particles sizes and densities) that we have explored. Also, presented is a detailed analysis on Lagrangian velocities and acceleration statistics for whole data set explored while investigating the finite size and density effects. The actual experimentation began following the configuration, testing and verification of the Ultrasonic Doppler Velocimetry; and after having adjusted the data acquisition and processing parameters. First the finite size effects of the neutrally buoyant particles were explored. Later on our emphasis was to determine the inertial effects of these finite size particles, resulting from increase in their density relative to the carrier fluid.

5.1 Studied Data Set

As particles we use soap bubbles of adjustable size and density. These particles have an extremely small Weber number[2] as a result; they do not deform and behave as rigid spheres. The seeding density is extremely low, therefore the particles (injected

[2] The Weber number compares the kinetic energy of the surrounding fluid to the cohesive energy of the soap film. It can be estimated as $We = \frac{\rho u^2 D}{\sigma}$, where ρ is the fluid density, u is the characteristic relative velocity, D is the diameter of the particle and σ is the soap film surface tension. The upper bound Weber number found for our bubbles using measured rms velocity of the particle (see section 5.2.1) as the characteristic velocity is of the order of 5×10^{-2}.

individually) can be considered as isolated and does not back-react on the carrier flow. The particles are therefore characterized by two parameters: φ and Γ, where the former is the ratio of particles diameter D to dissipative length scale of flow η ($\varphi = D/\eta$), and the latter is defined by the ratio of particle and carrier flow density $\left(\Gamma = \rho_p/\rho_f\right)$. These parameters for the data set studied and analyzed are listed in Table 5.1, and can also be visualized in FIG. 5.1. In addition to these parameters, we have also listed parameters such as; the modified particle stokes number and particle response time as defined in (3.8) and total number of samples for each data.

Firstly, the size effects of neutrally buoyant particles were investigated. The particle size was varied while keeping the relative density of particles approximately same as that of environmental air (measurements along $\Gamma = 1$ constant-line in FIG. 5.1). We then considered particles with densities higher than that of the carrier flow, enabling us to explore and characterize inertial effects. Our exploration of parameter space (FIG. 5.1) shows a particularly well resolved data set of density effects at constant size around $\varphi = 16.5$ and three relatively resolved data sets of size effects at constant density for $\Gamma = 1$, $\Gamma = 5$ and $\Gamma = 60$. Put altogether these measurements give a coarse mapping of the parameter space in the range $\Gamma = [1; 70]$ and $\varphi = [10; 30]$. For each set of particle size and density, several millions of samples were recorded and analyzed. The velocity and acceleration statistics were also determined and will be presented and discussed in the following sections.

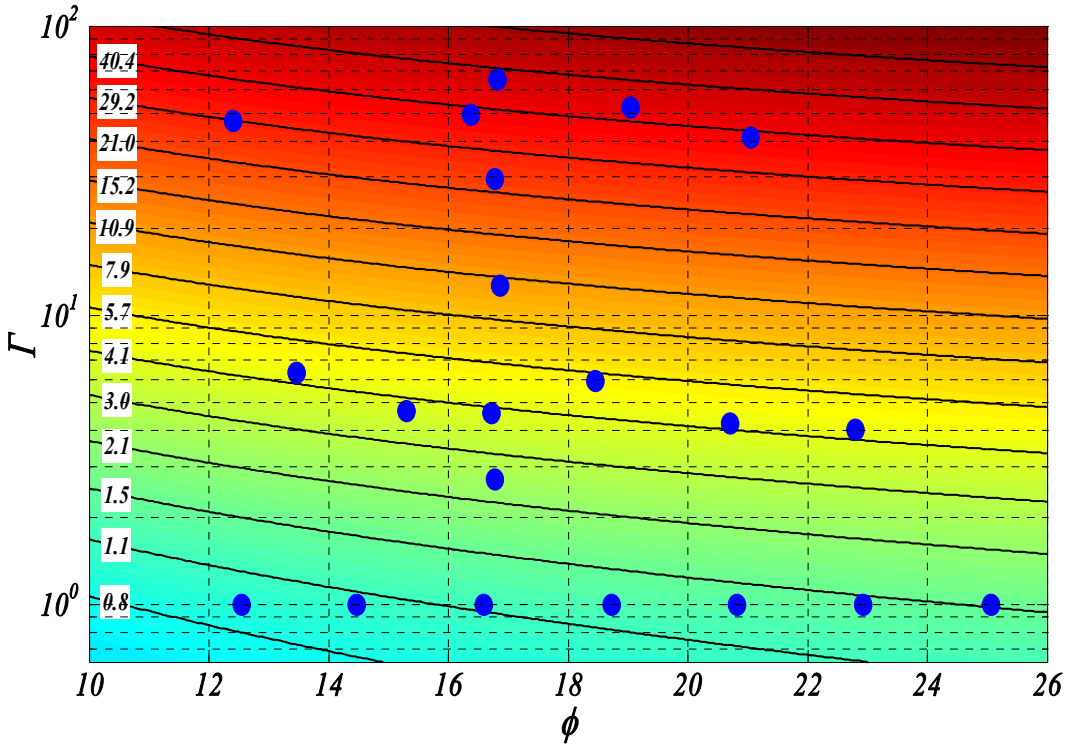

FIG. 5.1 - Pictorial representation of the data set studied in phi and gamma space along with modified Stokes number of particles. The color intensities from green to red show the increase in particles modified Stokes number.

Before presenting our results, it is interesting to place again our exploration of (φ, Γ) parameter space in the context of prior research or experimentation. For this purpose, we have represented in FIG. 5.2 an extended parameter space summarizing most of the existing studies of Lagrangian dynamics of inertial particles. It can be seen that previous studies have considered either very small (sub-kolmogorov) and very heavy particles (it is the case of the studies carried in Z. Warhaft group, referred in FIG. 5.2 as Ayyalasomayajula et al. [4, 5], who studied acceleration statistics of small water droplets in a grid generated turbulence in wind tunnel experiments) or large (up to $\varphi = 30$) but weak inertial particles ($\Gamma < 2.5$) in von Kármán flows of water (Volk et al. [90]). Our study complements these by considering particles which can be both large

and significantly denser than the carrier fluid. The results presented and discussed in the present work will enhance our understanding of these finite-sized inertial particles dynamics in turbulent flows.

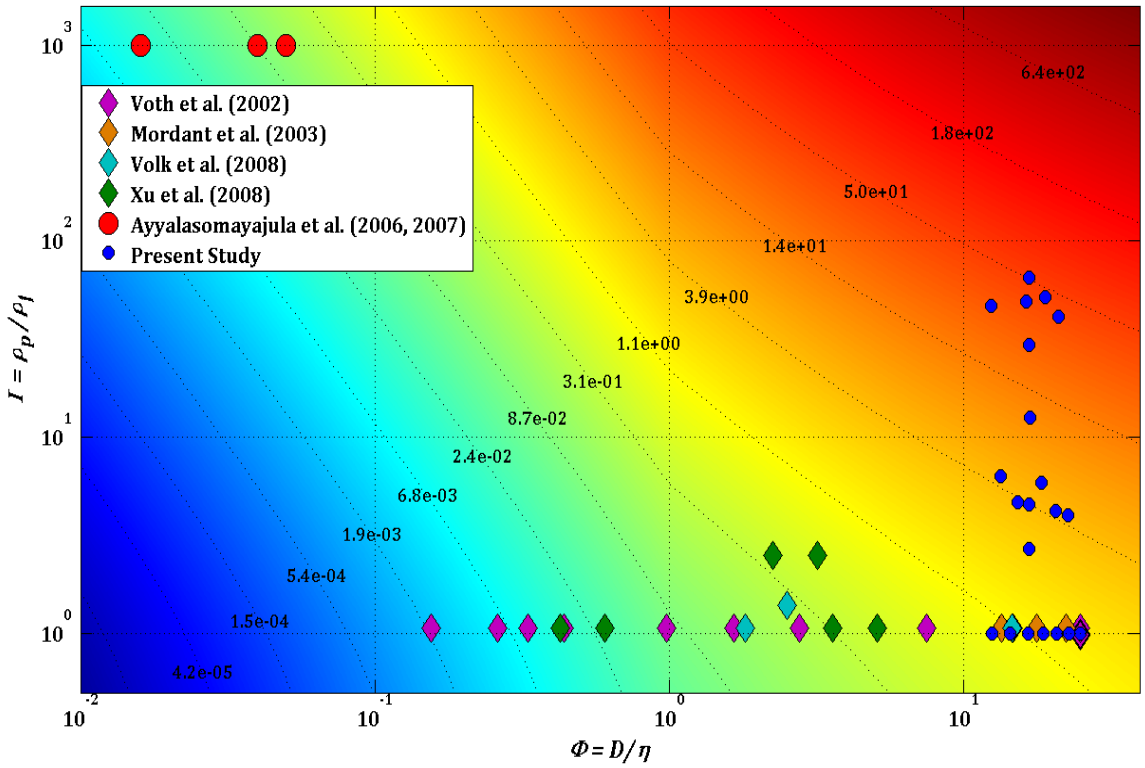

FIG. 5.2- Experimental and numerical studies on Lagrangian dynamics of inertial particles in (φ, Γ) space.

Table 5.1 - Details of particles studied, where φ is the particle diameter to kolmogorov scale ratio, Γ is particles relative density St_p is the modified Stokes number of particle and N_s represents the number of samples in millions.

S.No.	φ	Γ	St_p	N_s(millions)	τ_p (ms)
1.	8.3	1	0.6610	4.92	10.4
2.	12.54	1	0.9269	4.93	12.596
3.	14.46	1	1.0390	5.23	15.917
4.	16.58	1	1.1558	5.26	19.245
5.	18.72	1	1.2674	5.02	22.705
6.	20.82	1	1.3714	4.4	26.393
7.	22.93	1	1.4710	4.56	30.071
8.	25.06	1	1.5674	7.39	33.919
9.	13.46	6.34	4.4734	3.64	93.214
10.	15.30	4.67	3.7427	2.7	80.405
11.	16.71	4.58	3.9380	3.3	90.093
12.	18.45	5.91	5.3560	5.42	131.714
13.	20.70	4.23	4.3059	2.23	110.781
14.	22.80	4.01	4.4027	1.74	120.815
15.	12.40	46.98	29.0752	5.76	595.036
16.	16.77	2.71	2.4937	7.16	51.313
17.	16.86	12.63	10.2500	1.0	246.257
18.	16.77	29.73	23.4950	2.31	588.642
19	16.38	49.45	38.1266	1.63	965.347
20	16.81	65.48	51.3775	2.0	1293.844
21.	19.04	52.19	45.0850	4.7	1200.032
22.	21.05	41.10	38.3331	3.81	1078.183

However, it should be notice that due to experimental specificities, not all these measurements can be quantitatively compared. For instance, von Kármán flows have very different isotropy and confinement properties compared to grid generated turbulence (von Kármán flows are closed and highly anisotropic while wind tunnel experiments are open flows with higher isotropy level). Since these properties are known to affect Lagrangian statistics [44] comparison between von Kármán and wind tunnel experiment will only be considered qualitatively. Moreover, one should keep in mind that the parameter space shown in FIG. 5.2 is only a projection of a higher dimension parameter space where several other axes should in principle be considered; for instance points which appear nearby in the (φ, Γ) projection might correspond to experiments at very different Reynolds number, making an unambiguous quantitative comparison quite difficult. We will however consider the measurements by Ayyalasomayajula et al. [4, 5] for quantitative comparison with ours, as they were carried in similar experimental configurations (grid generated turbulence in wind tunnel experiments at similar Reynolds number). This will allow us to compare Lagrangian statistics for sub-kolmogorov and finite size inertial particles.

Neutrally Buoyant Particles

5.2 Velocity Statistics

5.2.1 Turbulence Intensity

As mentioned earlier, due to the difficulties in precise regulation of the wind tunnel's mean flow velocity, a minor difference in velocity for each data set was observed. This difference is shown in FIG. 5.3 for all neutrally buoyant particle data sets. In the color bar on right, particles modified Stokes number St_p is shown. The mean velocity varies between 14.43 and 14.67 m.s^{-1}, this variation (of the order of 1% with mean at 14.56) is however very small. We can see a small increase in mean velocity setting for experiments with particle sizes φ*=14.46* to *25.1*, this small variation simply reflects the small experimental uncertainty on the regulation of the wind tunnel velocity.

FIG. 5.4 represents the evolution of the root mean square velocity (v_{rms}) for different sizes of neutrally buoyant particles. The root mean square velocities were determined calculating ensemble average of all velocity signals from all particles after having placed them from end to end. For each dataset we consider the ensemble of velocity values $v_{\alpha i}$ were the subscript α identifies a given particle trajectory and the subscript *i* denotes the time along the trajectory; we denote the total length of a given trajectory by L_α, N represents the total number of trajectories per dataset. The ensemble average operator is defined as:

$$\langle . \rangle \equiv \frac{\sum_{\alpha=1}^{N} \sum_{i=1}^{L_\alpha} (.)}{\sum_{\alpha=1}^{N} L_\alpha} \tag{5.1}$$

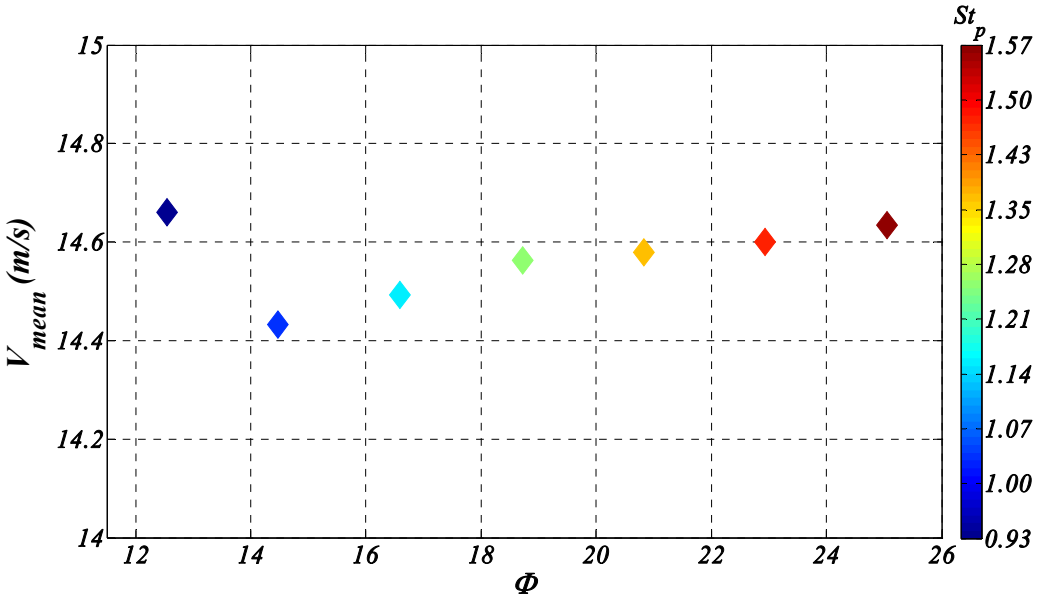

FIG. 5.3 - Mean flow velocity of each data set as a function of φ with corresponding St_p .

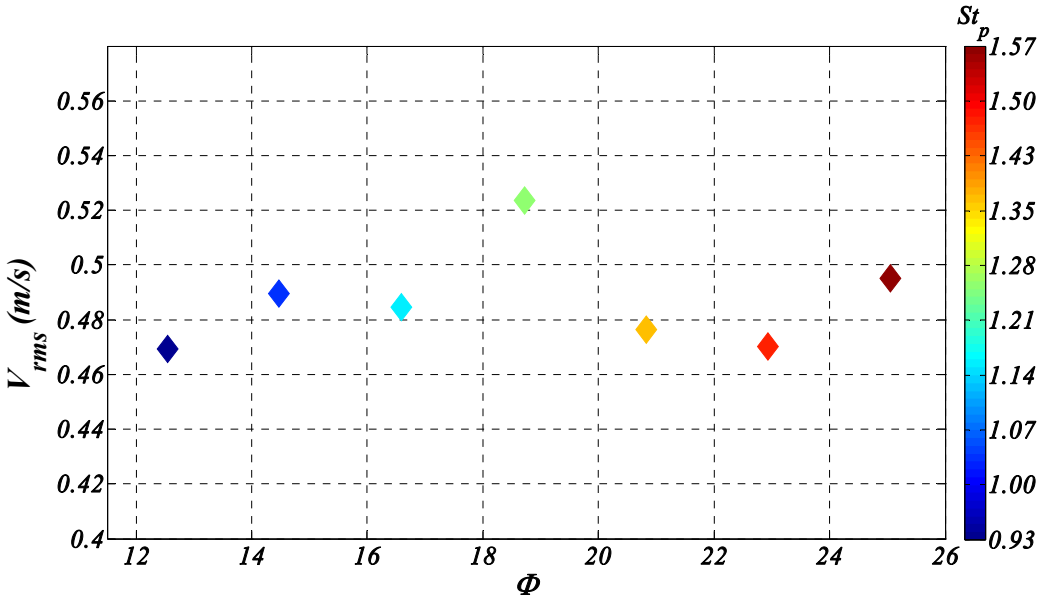

FIG. 5.4 - Root mean square velocity for neutrally buoyant data sets as function of φ with corresponding St_p.

As shown in FIG. 5.4 the root mean square velocity follows no systematic trend with increasing particle normalized size φ. We have also represented the turbulence intensity for these data sets, which is determined by the ratio of root mean square velocity and the mean velocity $\left({}^{v_{rms}}/_{v_{mean}}\right)$; this is shown in FIG. 5.5. It is found to slightly fluctuate around 3.3% with no specific trend with particle size. This value is in agreement with Eulerian hot-wire anemometry measurements [57], and indicates that particles fluctuation level is identical to that of the carrier flow itself (this point will be further discussed in the next paragraph).

We therefore conclude that velocity fluctuation level is not affected by the size or loading of the particles. Even particles as large as $26\,\eta$ (which here represents a significant fraction of the injection scale L) present the same fluctuation level as the fluid itself.

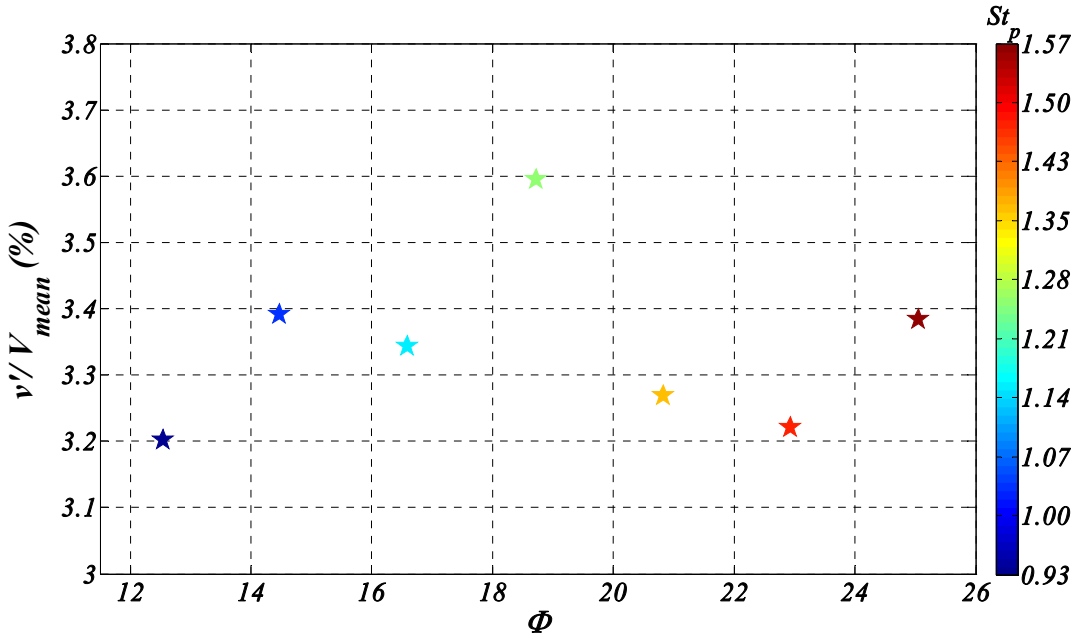

FIG. 5.5 - Turbulence rate for neutrally buoyant particles data sets in percentage.

5.2.2 Velocity Probability Density Functions

The velocity PDFs were determined from the histogram of velocity signals for each data set. For our measurements this served us as a first check for data processing parameters. The velocity PDF in true units for data set $\varphi = 12.54$ is given in FIG. 5.6 with a Gaussian fit of same mean value and standard deviation. The normalized velocity PDFs for all neutrally buoyant particle data sets are shown in FIG. 5.7. A Gaussian with same mean and width is plotted in dashed lines.

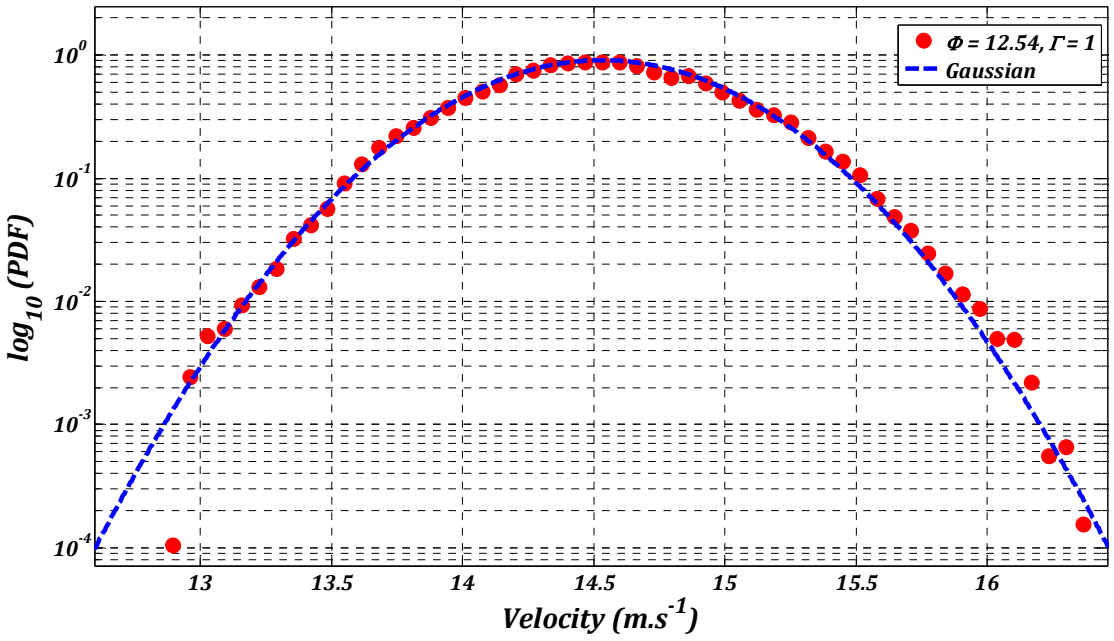

FIG. 5.6 – Probability density function of velocity for φ =12.54 and Γ = 1. In the dashed lines is a Gaussian distribution with same mean value and standard deviation.

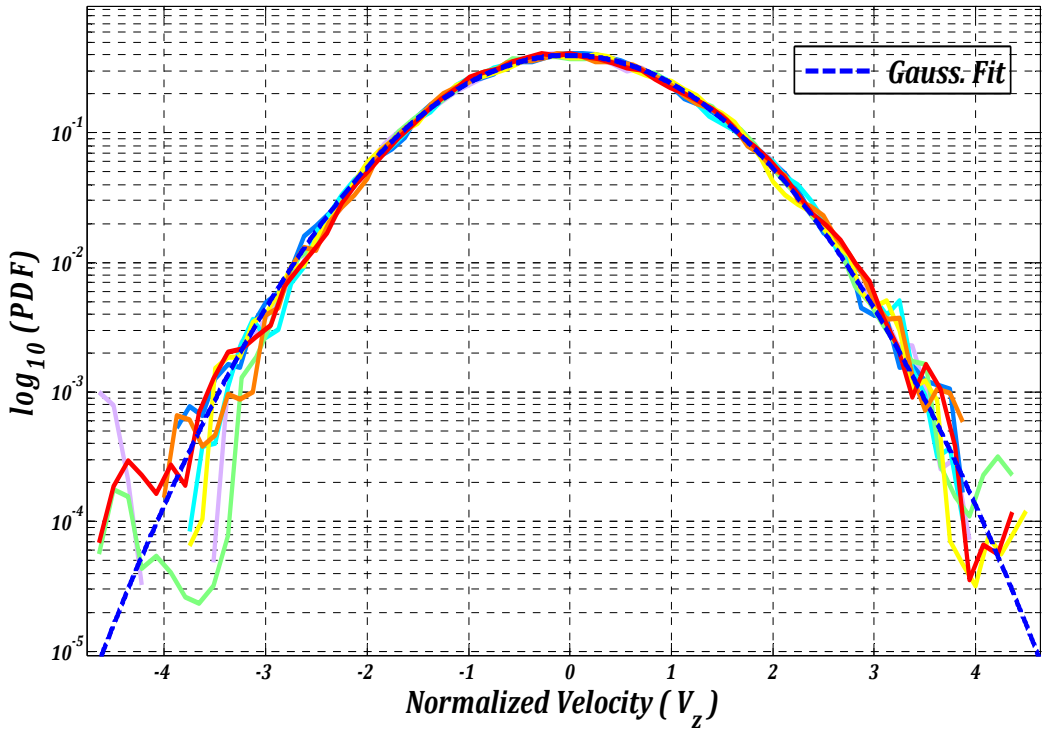

FIG. 5.7 – Velocity probability density functions for all neutrally buoyant data sets. In the dashed lines a normalized Gaussian distribution having variance 1 is shown.

For all data sets we found that velocity PDFs are Gaussian and identical to that of previous hot-wire Eulerian measurements. Such gaussianity is the characteristic of homogeneous turbulence, a case in which Eulerian and Lagrangian velocity statistics are indeed expected to be identical for fluid particles. In case of our smallest particles (which can be expected to behave as tracer) the agreement between classical Eulerian anemometry and our acoustical Lagrangian measurements validates our technique.

Moreover, we do not observe any specific trend for velocity PDF with particle size. This shows that even non tracers particles (we will indeed show later that large neutrally buoyant particles do not behave as tracers) may have velocity statistics identical to that of the carrier flow itself.

5.3 Acceleration Statistics

Determination of acceleration statistics have been the main focus and prime objective of our studies; the reason being that acceleration is the quantity that directly gives the measure of forcing that particles have experienced, while being transported by the turbulent carrier flow. In the first step we were keen to explore how particle's acceleration statistics vary with its size.

The acceleration was determined by convoluting the Lagrangian velocity signals with a differentiated Gaussian kernel. This process simultaneously differentiates and filters the signal from possibly remaining experimental noise [66, 75]. This Gaussian kernel is given as under:

$$\kappa_n(\tau) = \frac{d^n}{d\tau^n}\left[\frac{1}{\sqrt{\pi}\omega} exp\left(\frac{-\tau^2}{\omega^2}\right)\right] \tag{5.2}$$

where, n is the order of the derivative to be calculated. To obtain acceleration from velocity signals $v(t)$ first order Gaussian kernel κ_1 should be used:

$$a(t) = \int_{-\infty}^{\infty} v(t-\tau)\kappa_1(\tau)d\tau \tag{5.3}$$

In practice, as the velocity signals are of finite duration we obviously cannot integrate from $-\infty \rightarrow \infty$ and have to truncate the Gaussian kernel to a finite width T. The truncation process requires the Gaussian kernel κ_1 to be renormalized as:

$$\kappa_a(\tau) = A_a\, \tau \exp\left(\frac{-\tau^2}{\omega^2}\right) + B_a \tag{5.4}$$

in order to obtain a good approximation of acceleration as:

$$a(t) = \int_{-T}^{T} v(t-\tau)\kappa_a(\tau)d\tau \tag{5.5}$$

The coefficients A_a and B_a are obtained by imposing the conditions that,

$$\int_{-T}^{T} \kappa_a(\tau)d\tau = 0$$

and

$$\int_{-T}^{T} (t-\tau)\kappa_a(\tau)d\tau = 1$$

which are the requirements for the derivative of a constant to be zero and the derivative of t to be 1. Hence from these conditions the two coefficients are found to be:

$$A_a = \left[\frac{1}{2}\,\omega^2\left(\omega\sqrt{\pi}\,\mathrm{erf}\left(\frac{T}{2}\right) - 2Te^{-T^2/\omega^2}\right)\right]^{-1} \tag{5.6}$$

and

$$B_a = 0 \tag{5.7}$$

To minimize errors due to truncation we use a minimum kernel width $T = 5\omega$ [75].

The noise level of our data is extremely low, thanks to the iterative MLA procedure, for the time-frequency analysis used to extract the Doppler shift from the acoustic signal. Therefore, a very short Gaussian width (of the order of 5 points only)

was used for the convolution kernel (the convolution window was then truncated to 25 points).

In FIG. 5.8(a), PDF of non-normalized acceleration (in true units) has been plotted for all neutrally buoyant data sets. We observe that the acceleration PDF narrows and peaks around zero for increasing particle size. This narrowing of non-normalized acceleration PDFs, suggests its slight dependence on particle size and it also points out the fact that particles experience the turbulent forcing with different intensity; larger the particles less sensitive they are to extreme turbulent events.

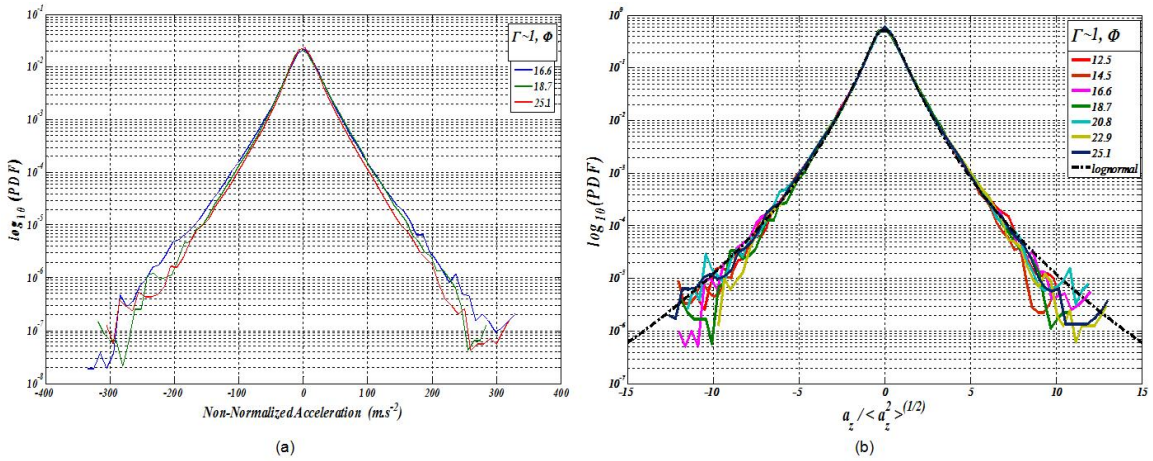

FIG. 5.8 - Acceleration PDF (a) Non-normalized in actual units. (b) Normalized by $a_{z,rms}$ with log normal fit in dashed lines.

When we plot the acceleration PDF normalized to variance 1, we notice that all the PDFs collapse to the same curve (within statistical error bars). This can be noticed from FIG. 5.8(b) in which the PDF of longitudinal acceleration a_z normalized with its standard deviation $a_{z,rms}$ is plotted for all neutrally buoyant experiments. Therefore the global shape of normalized acceleration PDFs (normalized to have variance 1) remains

essentially unaffected with particle size. Furthermore we find that the shape of normalized acceleration PDF is well described by the expression,

$$\mathcal{P}(x) = \frac{e^{3s^2/2}}{4\sqrt{3}} \left[1 - erf\left(\frac{ln\left(\left|x/\sqrt{3}\right|\right) + 2\,s^2}{\sqrt{2}s}\right)\right] \tag{5.8}$$

This PDF form for an acceleration component was previously suggested by Mordant et al. [69] in the case of fluid tracer particles having sizes comparable to dissipative length scale η. Under the condition of isotropic turbulence this PDF shape was also shown to be related with a lognormal distribution (of variance s^2) of the whole vector acceleration magnitude [65]. In our case this function form is also found to correctly describe the acceleration component statistics of finite size particles. Considering good isotropic conditions, as is the case here, this suggests that acceleration magnitude can be expected to be reasonably lognormal. Best fitting parameters were found to be $s \sim 0.62$ which gives distribution flatness $\mathcal{F} = \frac{9}{5}\, e^{4s^2} \sim 8.4$. This flatness value is however significantly smaller than the values previously reported for fluid tracers (of the order of 20) at a similar Reynolds number in von Kármán flows [49, 68, 92]. However a quantitative comparison with these experiments is difficult due to intrinsic differences in the flow configurations (in particular isotropy and confinement conditions are significantly different as von Kármán flows are closed and highly anisotropic while our flow is open and isotropic). The influence of such experimental specificities remains an open question to be addressed in forthcoming studies.

It is an interesting and somehow puzzling finding to observe that the same, identical and non-Gaussian acceleration PDF is conserved even for large particle sizes.

From the classical image of Eulerian intermittency of the carrier turbulent field in which the velocity increments are non-Gaussian at small scales and tend to become Gaussian continuously, as we move to large scales. One might have expected a monotonic trend of particle acceleration statistics towards a Gaussian as the particle size approaches large scales. Similarly, one might have expected the acceleration statistics of particles of size D to be somehow related with the Lagrangian velocity increment statistics calculated along fluid tracer trajectories at a time lag τ_D, which is eddy turnover time at scale D, which because of Lagrangian velocity intermittency would also tend continuously toward a Gaussian at large scales, as predicted for instance by point particle models. Since this is not the case, therefore we can conclude that the turbulent forcing on finite size particles with inertial range sizes is not trivially related to turbulent velocity field intermittency around the particle (neither Eulerian nor Lagrangian). As a consequence the acceleration PDF for particles with a given size cannot be simply deduced from statistics of Eulerian velocity increments at scales corresponding to the particle size. It can neither be deduced, from statistics of Lagrangian velocity increments at time scale corresponding to particle response time or eddy turnover time at particle scale.

Actually, a possible explanation for the absence of trivial relation between velocity increments and size effects on acceleration statistics is that from dynamical point of view, acceleration reflects the forcing undergone by the particle, which for inertial range scales is mainly due to turbulent fluctuations of the pressure gradients in the vicinity of the particle. Under an ergodic assumption, particle acceleration statistics can therefore be related to Eulerian pressure increments statistics, which are indeed not trivially related to velocity increment statistics [40].

To further explore the possible relation between acceleration statistics of finite size particles and pressure increments statistics, we note that since the normalized acceleration PDF is found to be independent of particle size, such a dependence can only affect the variance of acceleration itself. We have developed a simple phenomenological model based on the equation of motion of a finite size particle forced by the turbulent pressure fluctuations around it and have related the variance of acceleration to known properties of pressure increments statistics in turbulent flows[3]. In this context, by integrating pressure forces exerted by the carrier flow on the surface of the particles, the acceleration variance of a particle with diameter D can be related to the second moment of pressure increments at the scale of the particle i.e. $\langle a_z^2 \rangle_{particle}(D) \propto \frac{S_2^P}{D^2}$, where $S_2^P(r) = \langle [p(\vec{x} + \vec{r}) - p(\vec{x})]^2 \rangle$ is the Eulerian second order structure function (which only depends upon $r = |\vec{r}|$ in homogeneous and isotropic conditions). At first order this can be further explained with the help of the simple phenomenology proposed in FIG. 5.9[4]. Considering that a particle's acceleration in the z direction a_z is due to the force exerted by the carrier flow on the particle in that direction i.e. F_z. This force can be modeled (refer to FIG. 5.9) as the force due to pressure increments in the z

[3] In this simple approach we neglect the viscous forces, which have been shown for tracers in DNS to have a contribution to the global acceleration variance almost two orders of magnitude smaller than that of pressure gradients [VedulaPoF1999].

[4] A complete calculation based on the integration of the pressure forces at the surface of spherical particles gives the more complete relation : $\langle a_z^2 \rangle = \left(\frac{3}{8\pi\rho_p}\right)^2 \frac{\langle \delta_D P^2 \rangle}{D^2} \times f$,

where $f = \int_\theta \int_{\theta'} \int_\varphi \int_{\varphi'} \frac{\langle \delta_D P(\theta,\varphi) \delta_D P(\theta',\varphi') \rangle}{\langle \delta_D P(0,0)^2 \rangle} \sin(2\theta) \sin(2\theta') \, d\theta \, d\theta' d\varphi \, d\varphi'$ is a correction factor related to the angular correlation of pressure increments around the particle. In this calculation, the average on the left hand side should be understood as an average over an ensemble of particles. Under an ergodicity assumption, it can be interpreted as a spatial average for the pressure increments term on the right hand side so that acceleration variance calculated over an ensemble of particles can be related to the Eulerian second order structure function of the pressure.

direction at a scale correspond to diameter of the particle i.e. $F_z = \frac{\pi}{6}\,\rho\, D^3\, a_z \propto D^2[P(z+D) - P(z)]$. From these arguments we can find that the acceleration variance in z direction is directly proportional to Eulerian second order pressure structure function and inversely proportional to square of the particle's diameter.

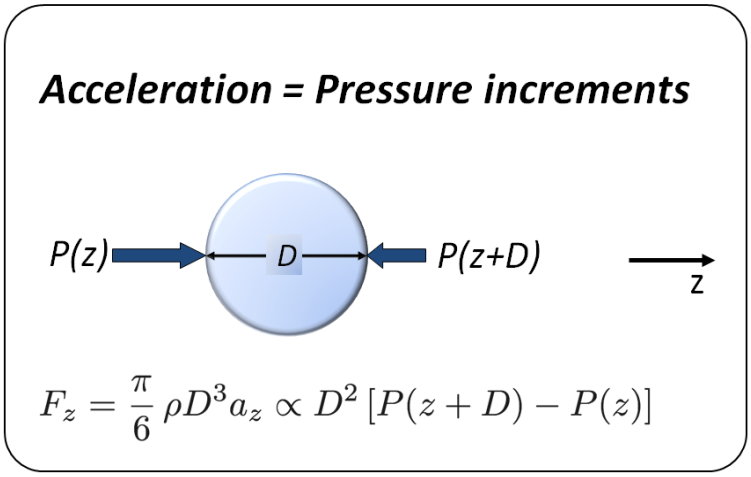

FIG. 5.9 – Proposed model linking particle acceleration with pressure increments at a scale of particle diameter.

In the frame of K41 phenomenology, the classical inertial scaling for $S_2^P(r)$ is $(\varepsilon r)^{4/3}$ [65, 72] (or equivalently for pressure spectrum in wave number space k, $P(k) \propto \bar{\varepsilon}^{4/3}\, k^{-7/3}$). Although this scaling is still controversial as reported in [37, 89], there is experimental and numerical evidence that suggest it is most likely correct in ranges of Reynolds numbers and scales consistent with our flow and particle sizes [38]. As a result, the acceleration variance of particles with diameter D in inertial range scales should follow scaling,

$$\langle a_z^2 \rangle_{particle}(D) = a_0' \, \varepsilon^{4/3} D^{-2/3} \tag{5.9}$$

where a_0' is a dimensionless proportionality constant. Though we have not consider in our study the role of Reynolds number (which is certainly important), in a more general context a_0' has to be very likely considered as Reynolds number dependent i.e. $a_0'(Re)$.

The above scaling is just phenomenological and it can be obtained by simple dimensional analysis too. It is therefore naturally consistent with previous predictions, based on other arguments, for instance by Monin-Yaglom [65] and Voth et al. [92]. In the limit of very small particles (of the order or smaller than the kolmogorov scale) acceleration variance should saturate to an asymptotic value corresponding to the intrinsic acceleration variance of the turbulent flow itself. In this limit, scaling (5.9 which has been derived from inertial range considerations should be replaced by its equivalent small scale (dissipative) form, given by the usual Heiseinberg-Yaglom relation for fluid particles [65]:

$$\langle a_z^2 \rangle_{fluid} = a_0 \, \varepsilon^{4/3} \eta^{-2/3} \tag{5.10}$$

Several groups studying Lagrangian turbulence have determined different values for constant a_0 , which is known to be Reynolds number dependent.

For the studied neutrally buoyant particles the scaling given in (5.10) is observed for sizes $15 < \varphi < 25$ within the measurement errors. The constant a_0' for acceleration is found to be of the order of 18 at the working Reynolds number. This is shown in FIG. 5.10(a) and (b) where acceleration variance normalized with $\varepsilon^{4/3}\eta^{-2/3}$ and the proportionality constant a_0' is determined for different particle sizes respectively. For

sizes $\varphi < 15$ we can notice the deviation from inertial scaling; the normalized acceleration variance tend to saturate to approach a constant value close to that of fluid particle acceleration, of the order of $a_0 = 3$, which was determined by Voth et al. at similar Reynolds number, though in a different experimental flow (von Kármán flow). The crossover from the $D^{-2/3}$scaling to the dissipative limit occurs around $\varphi \sim 10 - 15$; for the smallest particles.

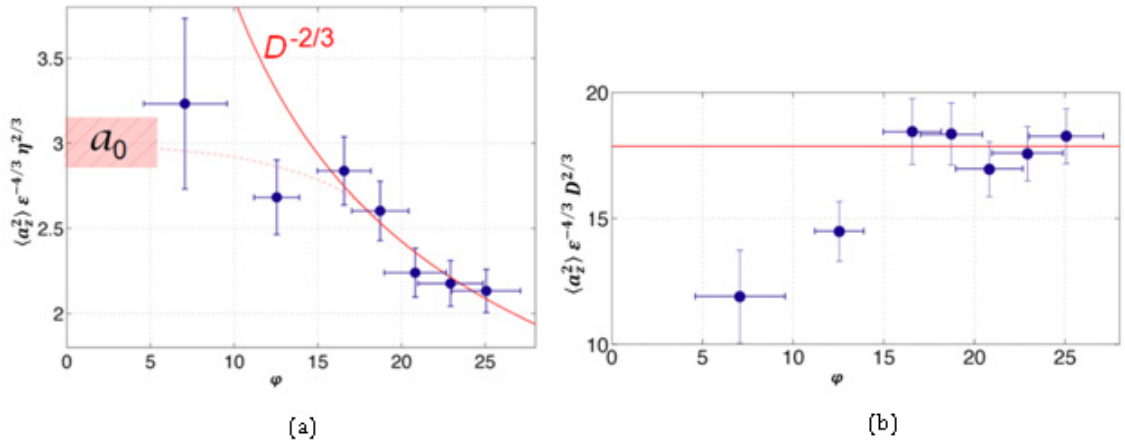

FIG. 5.10 - (a) Normalized acceleration variance as a function of particle size. (b) Acceleration variation normalized with scaling proposed in equation 4.2.

Heavy Particles

After having characterized size effects for neutrally buoyant particles, we consider now the influence of density on the dynamics of inertial particles. Experiments with heavy particles are listed in Table 5.1 (S.No. 9-22), where firstly the particle dynamics is explored for relative densities around $\Gamma \sim 5$ (S.No. 9-14, Table 5.1) and secondly for a fixed particle size $\varphi \approx 16.8$, for several relative densities (S.No. 16-20,Table 5.1). In the end different sizes were studied for high relative density range (S.No. 13, 21 & 22, Table 5.1).

5.4 Velocity Statistics

5.4.1 Turbulence Intensity

The mean flow velocities are shown as a function of size and relative densities in FIG. 5.11. There is a relative variation of only 1% with mean around 14.5 $m.s^{-1}$, which is due to the small uncertainty in the regulation of the wind speed.

In FIG. 5.12 the turbulence intensity for all data sets is shown. The turbulence intensity was found to be of the order of 3.2% with scattering[5] up to 10%, though very few data sets are found with very high or very low scattering. As compared with

[5] It should be noticed that such a scatter for velocity statistics is not surprising: as discussed in chapter 5, velocities correlation time are of the order of several tens of milliseconds which is in general longer than the duration of the recorded tracks. This means that for velocity statistics, each represents of the order of a single statistical sample. As for each set of (φ, Γ) parameters we have a few thousands track, the estimation of velocity statistics is done only over a few thousands samples.

neutrally buoyant experiments the turbulent intensity is slightly lower with no significant trend.

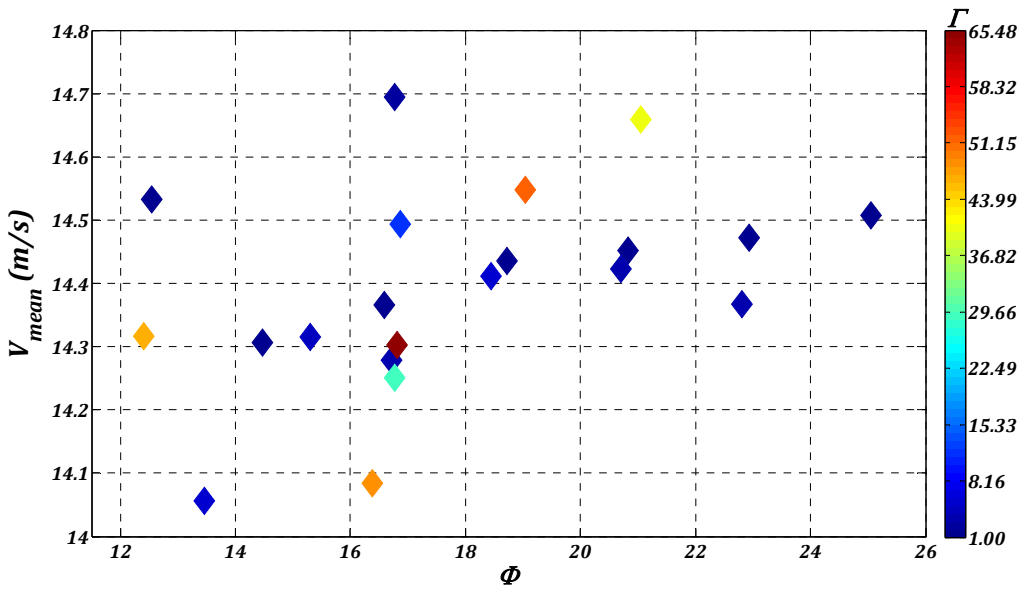

FIG. 5.11– Mean flow velocity as a function of normalized particle size φ for all data sets studied. The color shows particle's relative density as shown in the color side bar.

The turbulence intensity level for each data set was here determined as the ensemble average from all trajectories put one after the other. One may however wonder whether the fluctuation level of each particle taken individually (rather than as an ensemble) is affected by particle size. For this purpose, we define the individual average operator:

$$\langle . \rangle_\alpha \equiv \frac{\sum_{i=1}^{L_\alpha}(.)}{L_\alpha} \tag{5.11}$$

as well as the average individual fluctuation intensity :

$$\tau_{ind} = \frac{1}{N}\sum_{i=0}^{n}\frac{\langle(v - \langle v\rangle_\alpha)^2\rangle_\alpha^{1/2}}{\langle v\rangle_a} \tag{5.12}$$

FIG. 5.13 represents the evolution of τ_{ind} with particle size and density. Not surprisingly, the individual turbulence level is much smaller than the ensemble turbulence level (this could be already visualized in FIG. 5.14 from the velocity tracks). Contrary to the ensemble turbulence level, the individual turbulence level presents systematic trends with particle density. A clear decrease of the individual fluctuation rate of individual tracks can be observed for heavier particles as compared to neutrally buoyant. In particular, the set at fixed size ($\varphi = 16.8$) shows a monotonic decrease of τ_{ind} with increasing particles density. While the ensemble turbulence level only changed about 10% over the entire parameter space of particles, the individual turbulence level is found to change almost about 100%.

The decrease of the individual fluctuation level can be seen as a first clear influence of inertia on the particles dynamics. It reflects the intuitive fact that, as particles have more inertia, their trajectories tend to be smoother and the velocity along its trajectory tends to be less fluctuating (low-pass time filtering effect).

It should be noticed however that the notion of individual fluctuation level is not well defined, as it clearly depends on the length of the recorded tracks for instance. If tracks were much longer than the velocity correlation time, we could expect the individual fluctuations to reflect the ensemble fluctuation, as a particle would explore ergodically the ensemble. In the present case, as the tracks are much shorter than the velocity correlation time, the individual calculation of the turbulence level is somehow related to particle's small scale dynamics while the ensemble average over uncorrelated

tracks is related to the large scale dynamics. The difference observed between the ensemble and the individual calculation tells us that the large scale statistics (such as the root mean square velocity of the average kinetic energy) of the particles remain essentially unchanged and identical to that of the carrier flow itself, regardless of the particle size and density. On the contrary, small scale statistics (such as acceleration ones) might be expected to be affected by size and density effect[6].

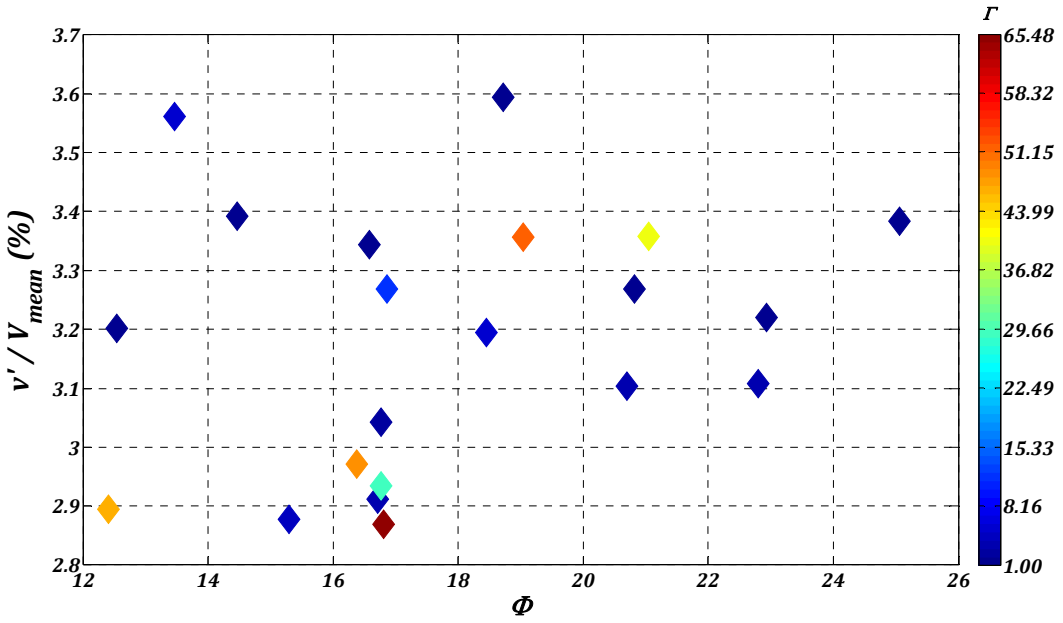

FIG. 5.12 - Turbulent intensity for all data sets studied as a function of φ and Γ.

[6] This was already the case for the study of neutrally buoyant particles, where we have shown that velocity statistics weren't affected by particles size, while acceleration statistics were.

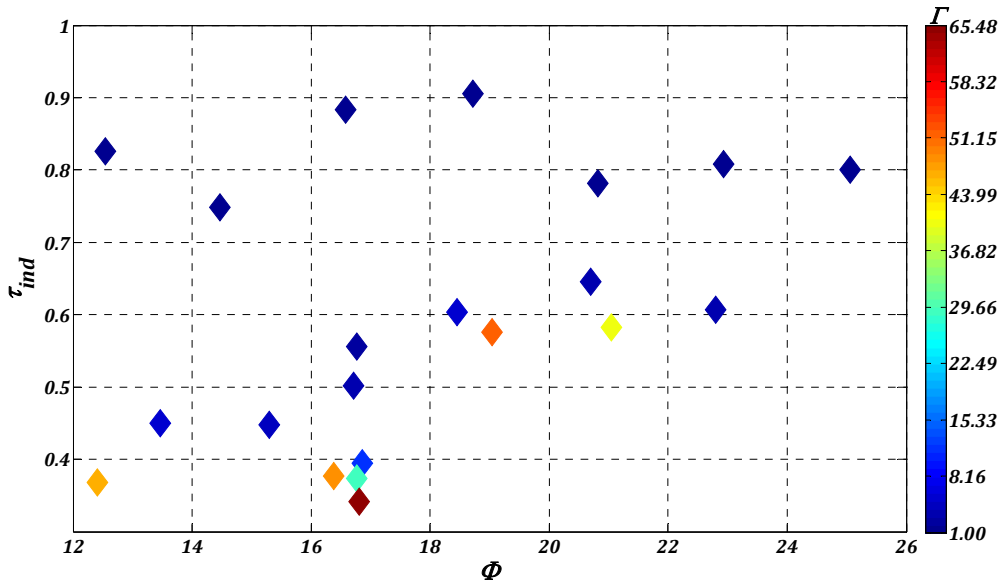

FIG. 5.13 - Turbulence Intensity calculated from the average of individual particles for heavy particle data sets as function of φ and Γ.

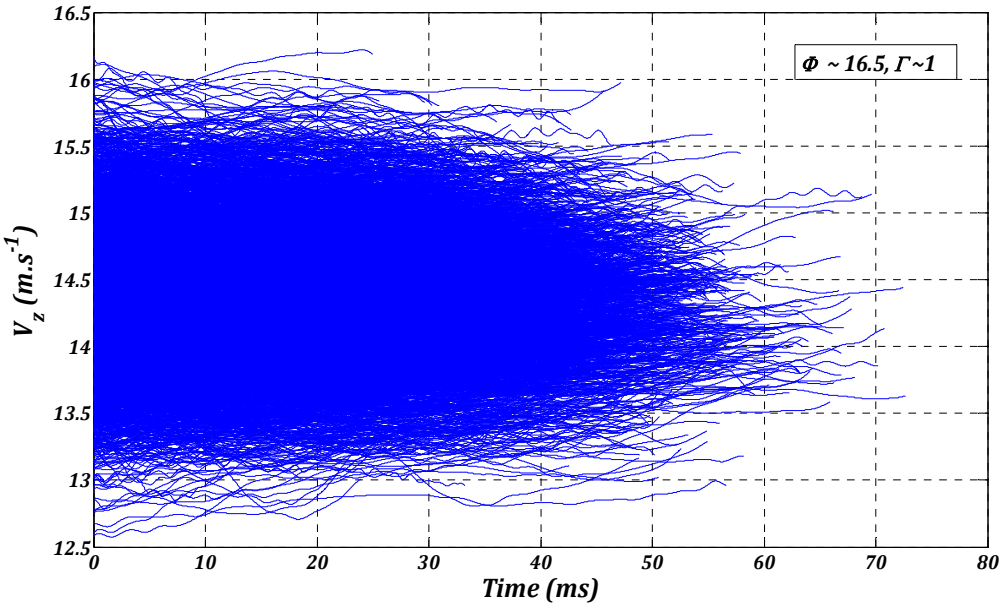

FIG. 5.14 - Individual particle velocity signals for data set $\varphi = 16.5, \Gamma = 1$.

5.4.2 Particle-Turbulence Interaction

Particle dispersion in isotropic homogeneous turbulence has been studied by various groups since 1940s. The Tchen & Hinze theory named after their work on the said domain in 1940 [88] and 1959 [42] respectively was compared with the DNS data and Sawford's stochastic model [84] by Pierre FEVRIER [29] and Pascal FEDE [26]. Tchen modeled particle dynamics in turbulent flow with certain assumptions and Hinze in 1975 found the results based on Tchen's theory and obtained following relation between particle movement and the fluid velocity fluctuations through spectral analysis:

$$E_p(\omega) = \frac{1}{1 + \omega^2 \tau_p^2} E_f(\omega) \tag{5.13}$$

where, E_p and E_f are the Fourier transforms of the particle's and the fluid's Lagrangian velocity autocorrelations. The above relation led us to propose the following relationship between turbulent kinetic energy of particle and fluid:

$$q_p^2 = q_f^2 \frac{T_L}{T_L + \tau_p} \tag{5.14}$$

where, q_p^2 is the turbulent kinetic energy of the particle, q_f^2 is the turbulent kinetic energy of the fluid and T_L is the Lagrangian integral time scale of fluid. The time T_L is estimated from the Lagrangian velocity autocorrelation of our smallest size neutrally buoyant experiment, which was found to be the order of 85ms and particle response time τ_p was determined from equation (3.8), which is also listed in Table 5.1. The results are plotted in FIG. 5.15, where the smallest size neutrally buoyant experiment

turbulent kinetic energy was used as the fluid's turbulent kinetic energy. We can observe that our experimental data doesn't fit well with Tchen & Hinze theory. In particular the data doesn't fall in the range where the turbulent kinetic energy ratio saturates and doesn't change. This deviation could be due to the relatively less appropriate estimation of particles response time which itself changes two orders of magnitudes within our data sets.

If we look further into the details, the Tchen & Hinze theory was based on the assumption that the particles Reynolds number is very small such that the only force acting on the particle is the Stoke's drag. In addition to that, their theory was limited to particles with sizes smaller than kolmogorov length scale such that the particles do not filter turbulent energy fluctuations. In comparison with the theory, in our case the particles possess finite size and volume. For these particles, even if the finite Reynolds number effects were taken into account in the particles response time, they somehow filter the turbulent kinetic energy corresponding to their size and density. As a preliminary conclusion, there exist drawbacks and limitations both in Tchen and Hinze theory (however the particle Reynolds effects were addressed by Deutsch in 1992 [22], which slightly modifies the theoretical curve) and the calculation of particle response time (this point is further discussed in Chapter 6). Clearly what we measure includes the particles finite size and effects, which means it includes all forces that the particle has been undergoing during its Lagrangian tracking, and the turbulent kinetic energy filtering due to its finite size.

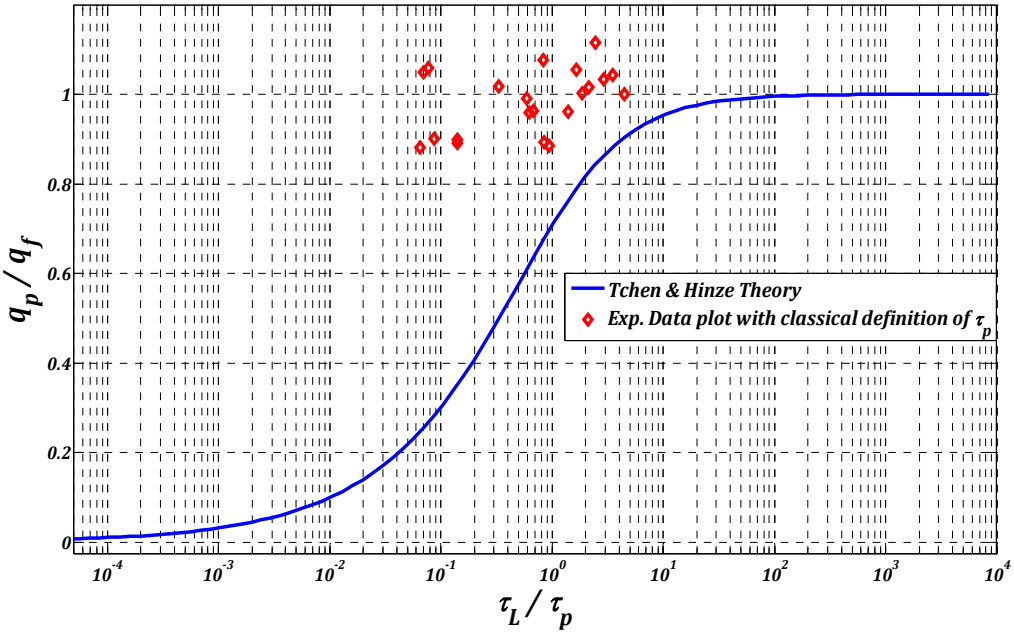

FIG. 5.15 - Comparison of Tchen & Hinze theory with our experimental data, when plotted using conventional definition of particle response time.

5.4.3 Velocity Probability Density Functions

In FIG. 5.16 (a), (b) and (c), some individual velocity PDFs are shown with a Gaussian fit of same mean value and standard deviation. We notice that the velocity distribution remains Gaussian for all particle sizes and densities explored.

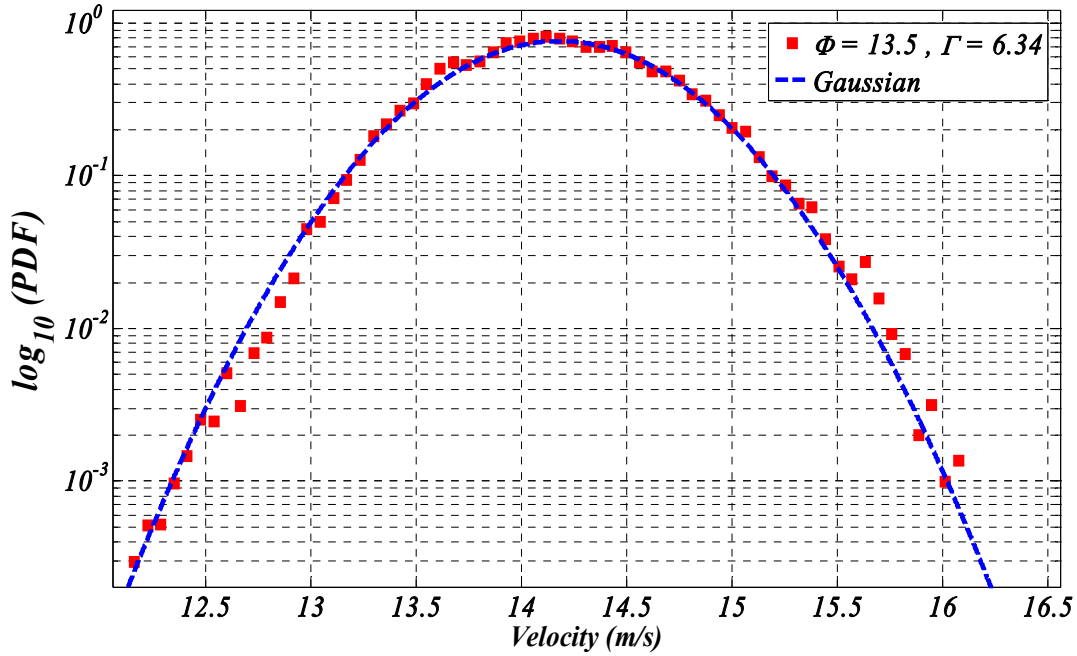
Φ = 13.5 , Γ = 6.34
Gaussian
log10 (PDF)
Velocity (m/s)

(a)

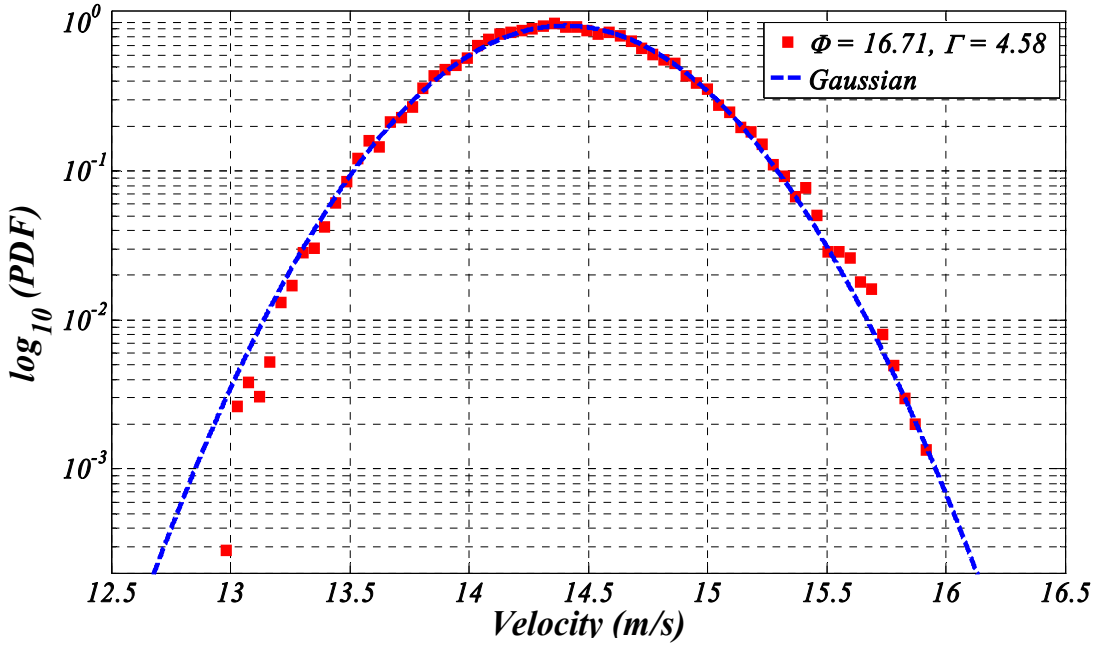
Φ = 16.71, Γ = 4.58
Gaussian
log10 (PDF)
Velocity (m/s)

(b)

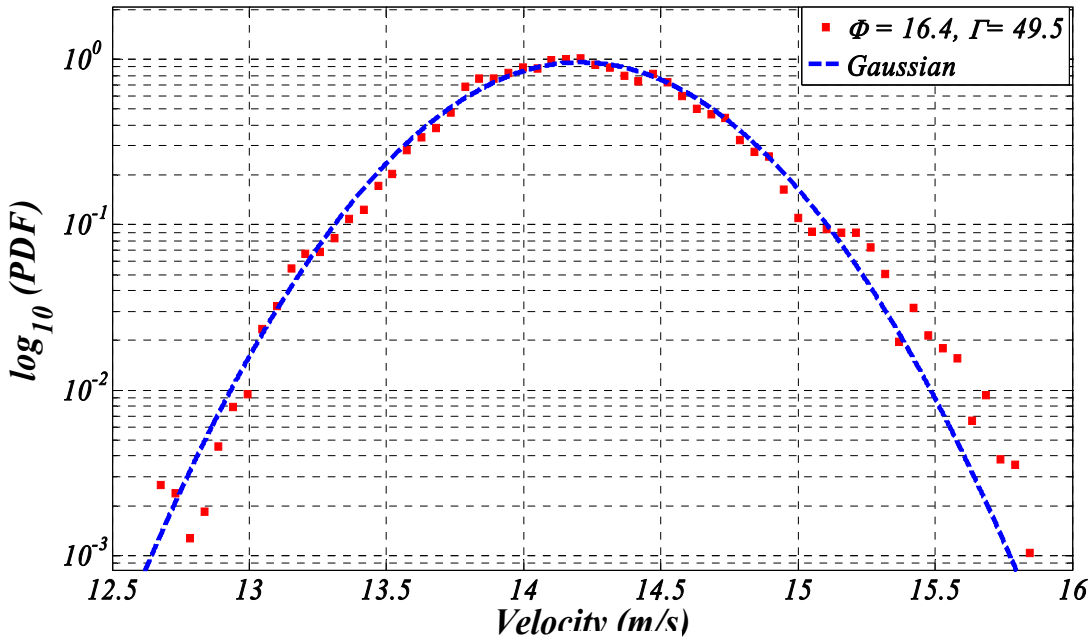

(c)

FIG. 5.16 - Velocity PDFs in true units for three data sets (a) $\varphi = 13.5$, $\Gamma = 16.4$ (b) $\varphi = 6.71$, $\Gamma = 4.58$ and (c) $\varphi = 16.4$, $\Gamma = 49.5$ along with respective Gaussian fits having same mean value and standard deviation.

All velocity PDFs are plotted in FIG. 5.17. We can see that these PDFs do not have same mean value which is due to the difference in flow mean velocities (though the difference is only of the order of 1%). Finally, we have superimposed in FIG. 5.18 velocity PDFs centered and normalized to variance 1 for all particles we have studied as well as a normalized Gaussian which correctly fits all the data sets statistics.

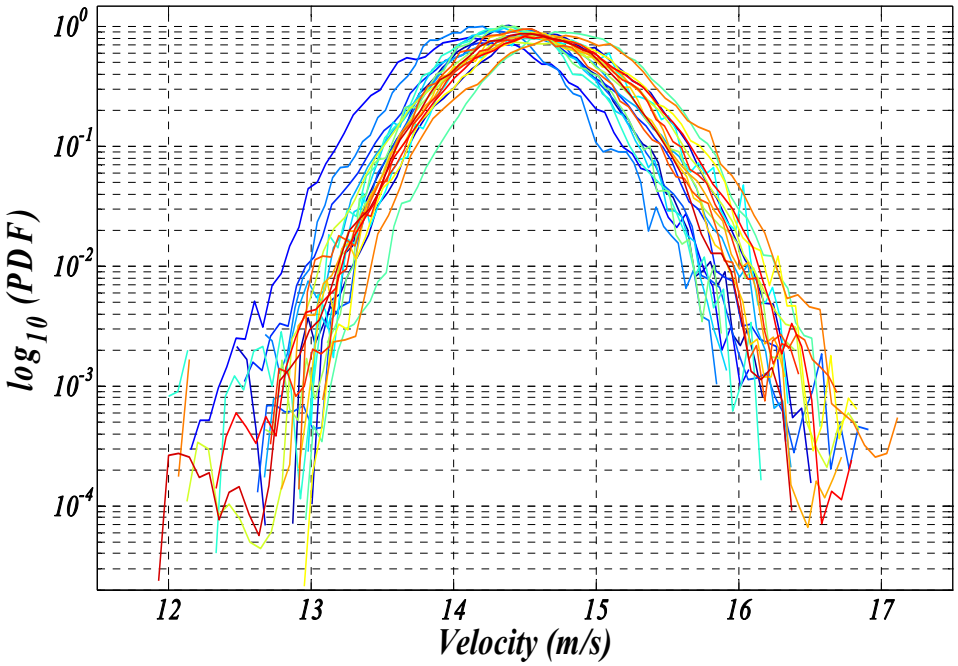

FIG. 5.17 – Velocity PDFs for all data sets in true units.

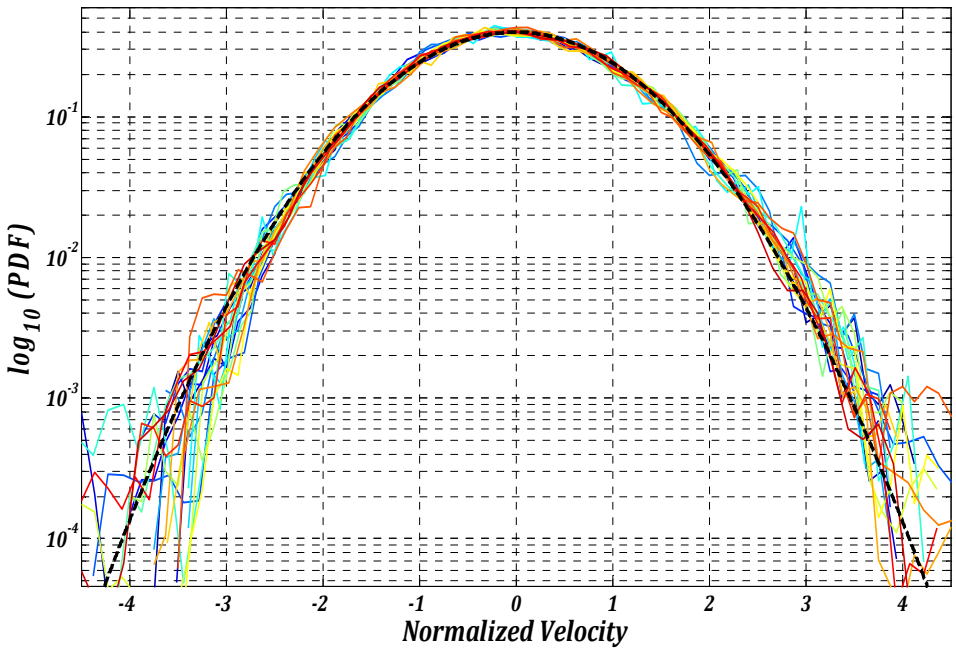

FIG. 5.18 – Normalized velocity PDFs for all data sets. In black dashed line is a Gaussian fit.

5.4.4 Acceleration Statistics

5.4.4.1 Normalized PDFs

In FIG. 5.19, the normalized acceleration PDFs (normalized to variance 1) $\mathcal{P}(a_z)$ of streamwise acceleration component a_z are shown. For all studied data sets acceleration statistics are well converged at least up to fourth order, this can be seen in FIG. 5.20, where $a_z^4\mathcal{P}(a_z)$ are shown.

Remarkably we find that, within the statistical error bars in the rare event tails, all the PDFs almost collapse onto a single curve. This indicates that normalized acceleration statistics depends neither on particle size nor on particle density. In particular the flatness of the PDFs, keep a constant value $\mathcal{F} = 8.4 \pm 10\%$. This result extends in the case of heavy particles. The robustness of the acceleration PDF reported for neutrally buoyant particles in previous section is maintained. Our result is qualitatively consistent with recent measurements in a water von Kármán flow for particles with densities varying in the range $0.5 < \Gamma \leq 2$ [90, 91] although a rigorous quantitative comparison cannot be made due to experimental specificities as grid turbulence and von Kármán flows are have very different large scale anisotropy and confinement characteristics which are known to affect particles Lagrangian dynamics [44, 76].

A quantitative comparison is however possible with recent measurements obtained by Z. Warhaft's group at Cornell University in grid generated turbulence with comparable characteristics (both are wind tunnel experiments with similar isotropic levels), although at a slightly higher Reynolds number ($R_\lambda \sim 250$). Using high speed

optical tracking, they have measured acceleration statistics of sub-kolmogorov water droplets ($\varphi \sim 5 \times 10^{-2}$; $\Gamma \sim 1000$; $St \sim 0.1$), a state we cannot reach at present due to technical limitations of our bubble generator. In black dashed lines (FIG. 5.19) these measurements have been superimposed on normalized acceleration PDFs obtained from our results. We notice that it is almost indistinguishable from our measurements with larger particles. This suggests that acceleration of inertial particles as small as $\varphi \sim 5 \times 10^{-2}$ already exhibit the same robust statistical signature as finite size particles. Point particle models may therefore only apply to even smaller particles [5]. Using smaller water droplets than in their first experiment, Z. Warhaft group has indeed measured that $\varphi \sim 1.6 \times 10^{-2}$ ($St \sim 0.01$) acceleration PDF might become wider in agreement with point particle models predictions (better statistical convergence would however be probably required to be absolutely conclusive). Our measurements show however, the claimed trend for acceleration PDF to become Gaussian as their Stokes number increases, predicted by these models, cannot be extrapolated to finite size inertial particles. Very rapidly, acceleration PDF seems to reach a limit of non Gaussian shape, and even particles with a Stokes number as high as 40 (for our largest and heaviest particle) the acceleration PDF is clearly non Gaussian. More generally, this is a first indication that real particles cannot be simply characterized in terms of just a Stokes number (this will be further discussed later).

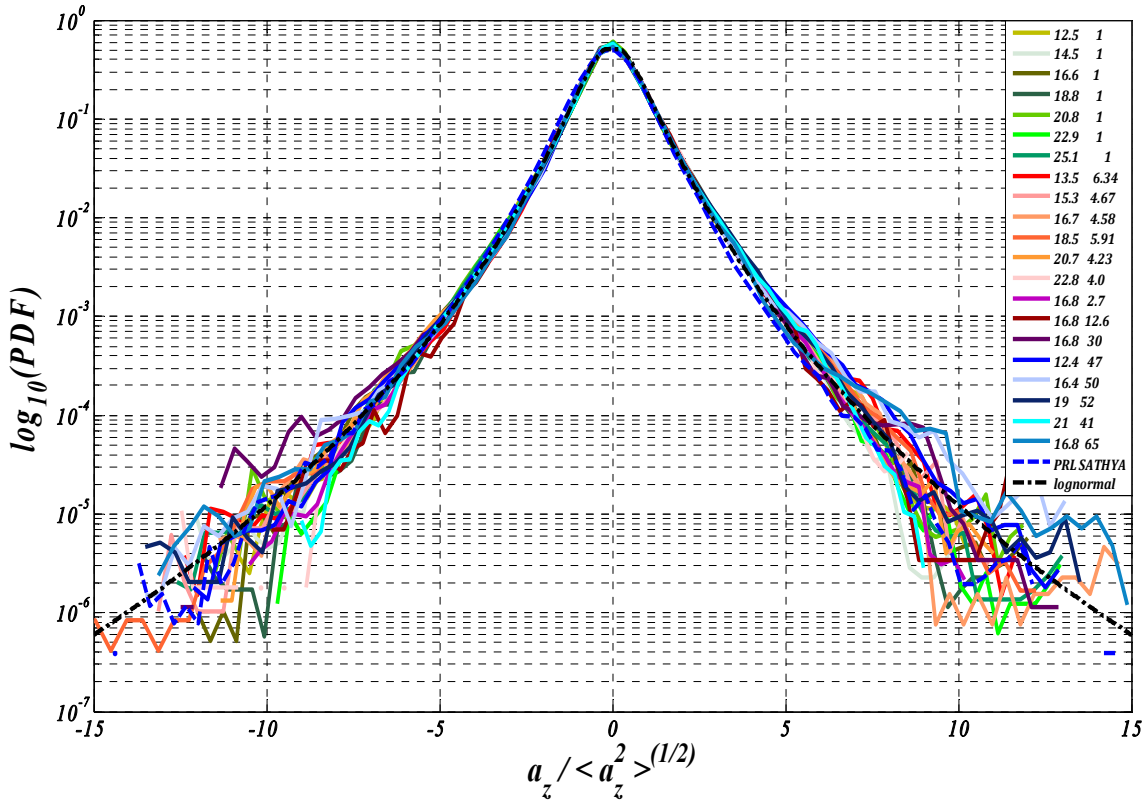

FIG. 5.19 – Normalized acceleration PDFs (normalized to variance 1) of stream wise acceleration component a_z for all data sets studied. The dashed lines represent the experimental measurements of Ayyasomayalula et al. [4] for water droplets (with size $\varphi \sim 5 \times 10^{-2}$ and $\Gamma \sim 1000$). The dot-dashed line shows a fit by relation given in (5.8) associated with lognormal distribution of the acceleration amplitude.

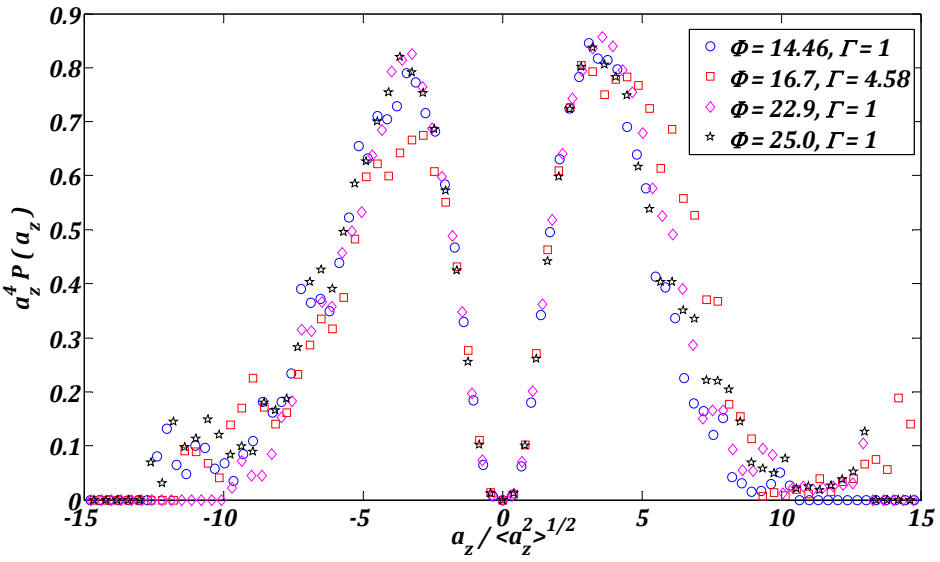

FIG. 5.20 - Acceleration fourth moments for few data sets, showing the acceleration convergence.

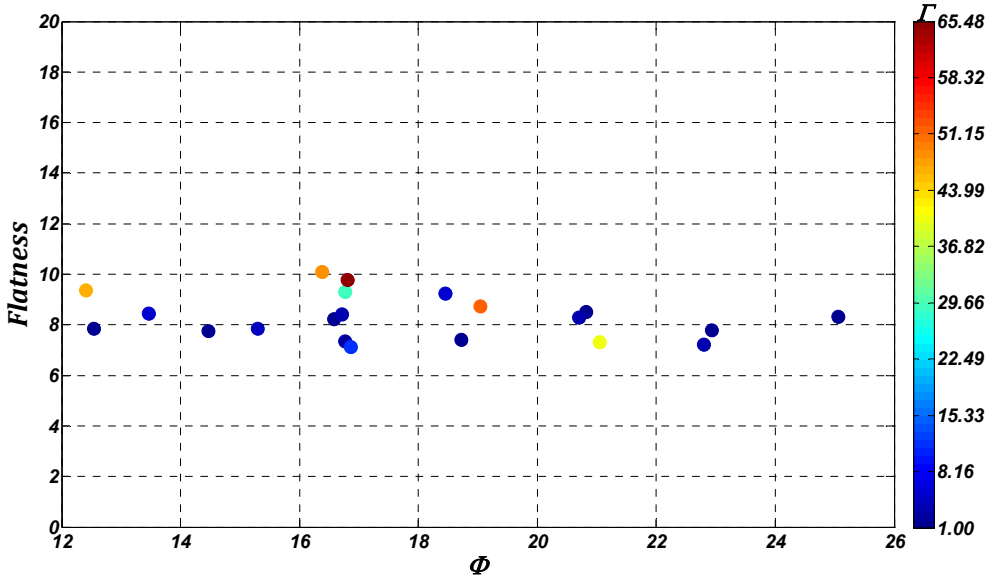

FIG. 5.21 – Acceleration flatness for all data sets in normalized size and density parameters.

5.4.4.2 Acceleration Variance

For a deeper insight into specific effects associated with particles size and density, one has to investigate acceleration variance. Since the statistics of acceleration normalized to variance is essentially found independent of particles size and density, an effect of those parameters can indeed only be expected to affect acceleration variance $< a_z^2 >$ itself. This effect can indeed be observed from FIG. 5.22, where PDFs of non-normalized acceleration in true units are shown. Green tones indicate neutrally buoyant particles and red tones represent heavy particles. It can be noticed, for heavy particles that acceleration variance decreases and the PDF peaks rises.

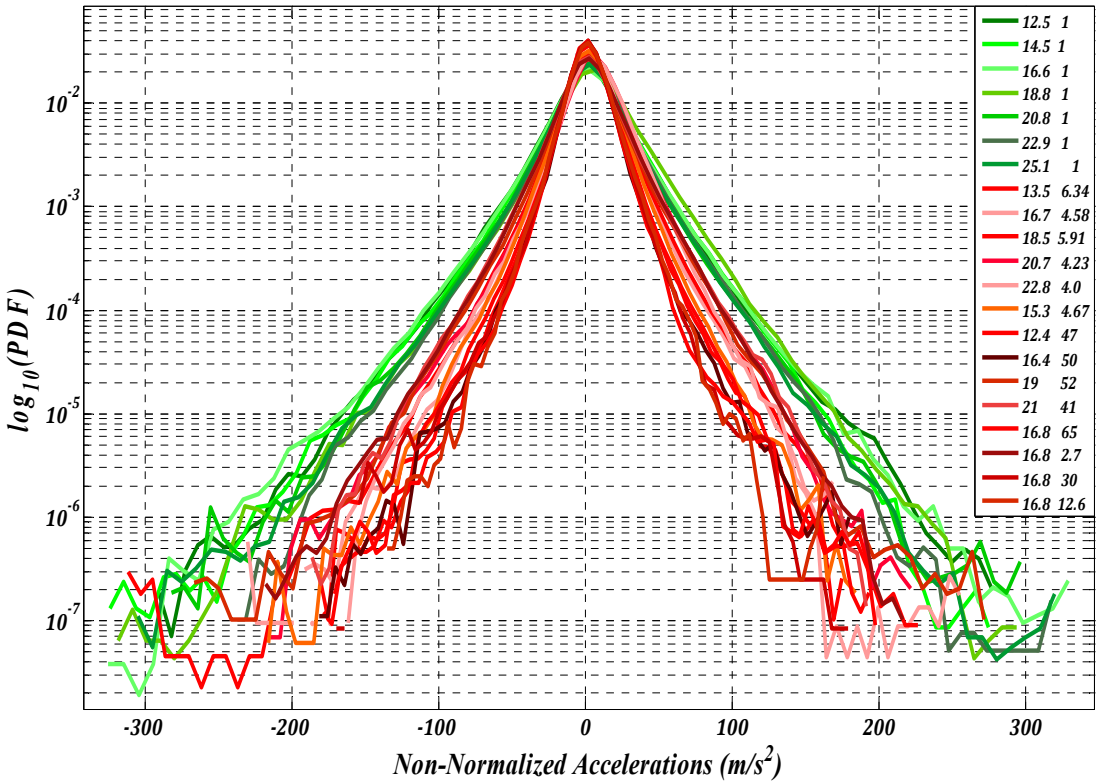

FIG. 5.22 – Non-normalized acceleration PDFs in true units for all studied data sets. Neutrally buoyant particles are shown in green tone, whereas in red tone heavier particles are presented.

A closer analysis of acceleration variance shows a non-trivial dependence with size and density. We report in FIG. 5.23, the acceleration variance for all the measurements we have performed. In the following, we consider the dimensionless acceleration variance normalized according to Heisenberg-Yaglom's scaling:

$$A_0(\varphi,\Gamma) = < a_z^2 > \ \varepsilon^{-2/3}\, \upsilon^{1/2} \tag{5.15}$$

The mapping of the (φ,Γ) parameter space that we have been able to achieve, allows us to infer a rough interpolation of the evolution of $A_0(\varphi,\Gamma)$, represented by the surface in FIG. 5.23. Though only course tendency of this interpolation is relevant, several important qualitative features can still be observed. For small and close to neutral particles $A_0 \sim 2.8$, a value which is consistent with previous measurements [92] and DNS [37, 89] for particles in the fluid tracer limits. If we consider the effect of an increasing density at a fixed particle size (along φ = constant lines), A_0 is always found to decrease and to apparently saturate to a finite limit (noted $a_0^{\infty}(\varphi)$) for the largest densities. This is better quantified in a 2D projection (FIG. 5.24). The $\varphi \sim 16.5$ set of measurements which is our most complete set of density effects at fixed size, shows that the evolution of acceleration variance with density exhibits two different regimes which can be seen in the inset of FIG. 5.24: (i) for low densities $A_0(\varphi,\Gamma) = \ a_0(\varphi)\ \Gamma^{\alpha}$, $(a_0(\varphi))$ corresponds to size effects for the neutrally buoyant case which we have discussed earlier with $\alpha \sim 0.6$ (ii) for larger densities A_0 saturates to the finite limit $a_0^{\infty} \sim 0.7$; the transition between these two states occurs for a characteristic density ratio $\Gamma^* \sim 10$. Although we don't have as many systematic measurements for varying densities for other values of φ, the few available points are compatible with the existence of such two

regimes (FIG. 5.24), with a size dependent saturation value $a_0^{\infty}(\varphi)$ and very likely a size dependent transition density ratio $\Gamma^*(\varphi)$.

If we look more closely size effects at fixed particle density (along Γ = constant lines), as seen in FIG. 5.23, the scenario is rather complex, since depending on the density ratio Γ, A_0 can either decrease or increase with particle size. For neutrally buoyant particles ($\Gamma = 1$), A_0 starts to deviate from the fluid tracer value for particles larger than about $\varphi \sim 15$ and then decreases monotonically as $\varphi^{-2/3}$.

As we have already shown in the neutrally buoyant particle section that this is the expected scaling for inertial range size particles when the main forcing simply comes from the spatial pressure differences of the unperturbed flow around the particle. As we move to larger density ratios, we then observe a continuous transition toward a drastically changed size dependence for the largest densities ($\Gamma > \Gamma^*$) where $a_0^{\infty}(\varphi)$ experience a sudden increase for sizes around $17 < \varphi < 19$. Outside this transition region (i.e. for $\varphi \lesssim 17$ and $\varphi \gtrsim 19$), a_0^{∞} does not exhibit significant dependence on φ (at least in the accessible range of sizes) as also seen on FIG. 5.24, where we have $a_0^{\infty}(13) \simeq a_0^{\infty}(16.5)$ and $a_0^{\infty}(19) \simeq a_0^{\infty}(21)$.

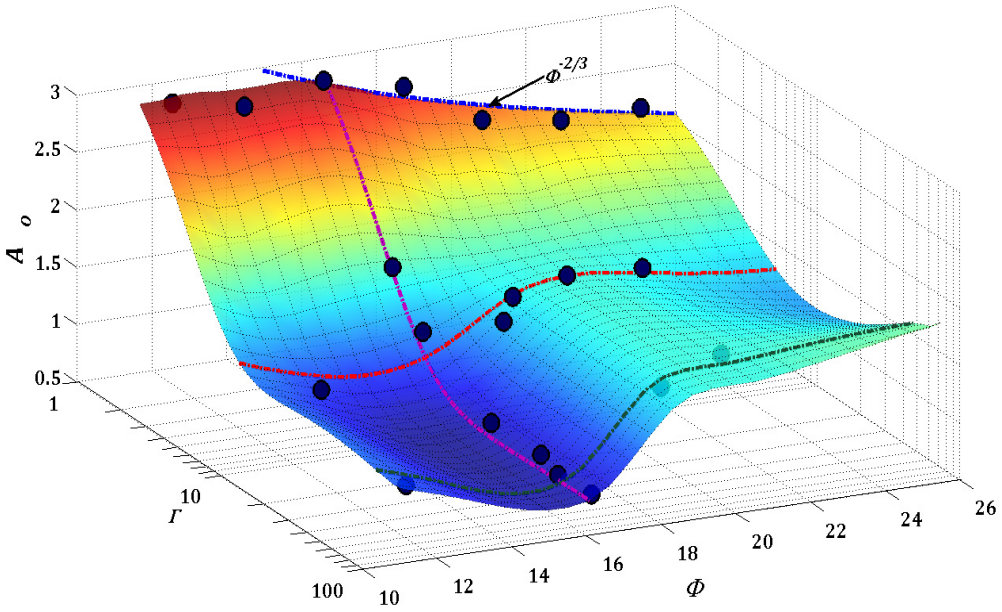

FIG. 5.23 – Acceleration variance in the (φ, Γ) parameter space (dots) for all studied data sets. The surface represents a rough interpolation based on the available measurements. The dot dashed lines materialize the interpolation along the best resolved constant φ-lines and Γ-lines. For the $\Gamma = 1$ set, the dot-dashed line coincides with a $\varphi^{-2/3}$ decay for $\varphi \gtrsim 15$.

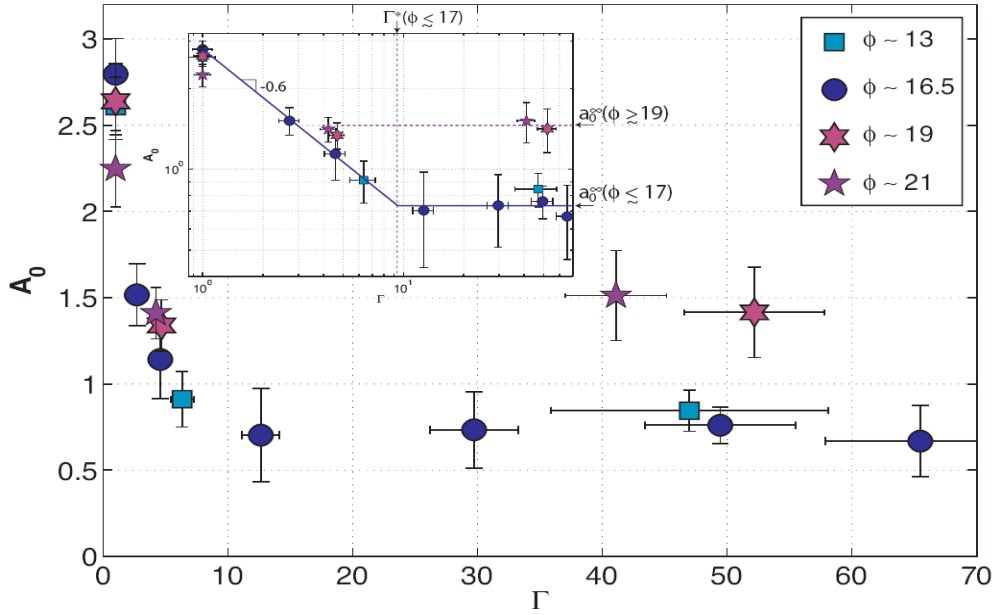

FIG. 5.24 – 2D-Projection on the $(\Gamma - A_0)$ plane of measurements data points on FIG. 5.23, showing the evolution of acceleration variance with density ratio Γ for different particle sizes ($\varphi \sim 16.5$ set (circles) is the best resolved). The inset shows the same data in log-log plot. Errorbars are mostly due to experimental uncertainties in the determination of particle size and density.

5.5 Discussion

In terms of the development of accurate models for the turbulent transport of inertial finite sized particles, important conclusions can be drawn from our measurements. The robustness of normalized acceleration PDF, regardless of particles size and density, and the non trivial size and density dependence of acceleration variance impose strong constraints on the statistical properties of the forcing terms to be included in the equation of motion of particles. For instance models based on Maxey & Riley equation [34, 55] for inertial point particles are contradictory with our observations as they predict a continuous trend of acceleration PDF to gaussianity as well as a monotonic decrease of acceleration variance [6, 9, 90]. In the context of these point particle models, for moderate and large Stokes numbers both of these trends are mostly consequence of a filtering effect due to increasing particles response time. Our findings therefore show that turbulent transport of inertial finite sized particles cannot be simply described in terms of Stokes number and *filtering* effects only. The concrete statistical constraints that we have identified give a first clear experimental diagnose of point-particle models limitations (already analyzed theoretically by Lumley in 1978 [53], and of the requirement for density and finite size effects to be modeled simultaneously and specifically.

A simple qualitative phenomenology for the observed trends of acceleration variance can be suggested based on the idea that *particles tend to reside longer in the quietest regions of the flow*. This intuitive statement can be related to the tendency of inertial particles to preferentially concentrate in low vorticity and low acceleration

regions of the carrier turbulent field along which they are then advected following a *sweep-stick* scenario [17, 36].

In this context, the decrease of particles acceleration variance naturally results from the under *sampling* of intense regions of the carrier flow. Then, a possible interpretation for the increase of acceleration variance with particle size observed for high density ratios can be that while small enough particles can indeed be expected to efficiently *hide* in the quietest regions of the flow, when particles become larger than the typical size L^* of these regions, the *sampling* effect is damped, as particles start experiencing again the influence of more active regions of the turbulent field. Though the existence of such a typical scale is still controversial, recent measurements of preferential concentration suggest that the quiet sticking regions might have a characteristic size L^* in the range of $10\eta - 20\eta$ [2] consistent with the $17 \lesssim \varphi \lesssim 19$ range for which we observe the sudden increase of $a_0^{\infty}(\varphi)$.

Our measurements of inertial effects for finite size particles can therefore be consistently interpreted as a dominant role of *sampling* rather than *filtering*, contrary to the point particle case [6, 9]. The dominant role of *sampling* is also consistent with the fact that velocity statistics of our particles (not shown here) are found identical to that of the carrier flow (obtained from classical hotwire anemometry), a feature also shown numerically in the context of *sweep-stick* mechanism [36] but which is at odds from usual predictions based for instance on the Tchen & Hinze theory or its extensions [23].

Chapter 6

Two Time Statistics

In the Lagrangian study of particle transport in turbulent flow, we are not only concerned with the particle's statistical properties but are also keen to investigate and explore the multiple-time scale nature of these statistical properties. Here the specific area of focus is to determine how these statistics change with the change in time scale. In this chapter we will study different properties of particle dynamics, determined at different time scales and present the discussions on their multiple-time scale behavior.

6.1 Lagrangian Velocity Increments

The velocity increments are used to characterize the temporal evolution of particle dynamics i.e. the particle's velocity statistics from integral to dissipative scales and it is defined as:

$$\delta_t v(t) = v(t+\tau) - v(t) \tag{6.1}$$

where, τ characterizes the time lag at which statistics are calculated.

In order to characterize in detail the Lagrangian statistics of particle velocities we have determined the PDFs of velocity increments for all studied data sets. These velocity increments PDFs for three neutrally buoyant experiment data sets are shown in FIG. 6.1 (a), (b) and (c) for particles sizes 12.5, 21 and 25.1 respectively and for heavy

particles data sets $\varphi = 13.5, \Gamma = 6.34$; $\varphi = 12.4, \Gamma = 47$ and $\varphi = 21.05, \Gamma = 41.1$ are shown in figures FIG. 6.1 (d), (e) and (f) respectively. The logarithm of PDFs is plotted against velocity increments normalized with its variance. The PDFs are shifted vertically in order to increase the readability of the viewer. It can be observed that regardless of particle size and relative density, the Lagrangian statistics are intermittent i.e. the shape of velocity PDFs depends upon the time scale on which they are determined.

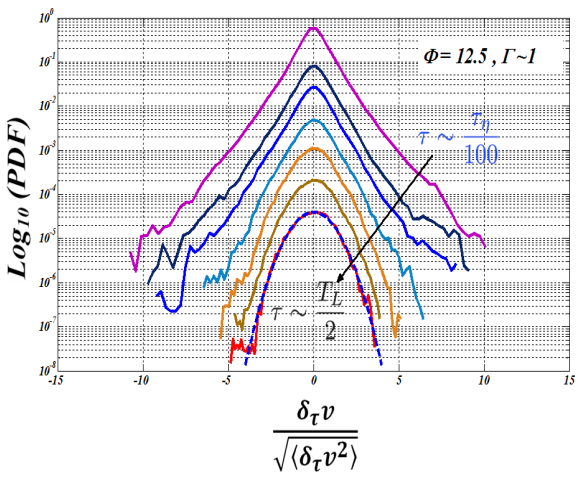

(a)

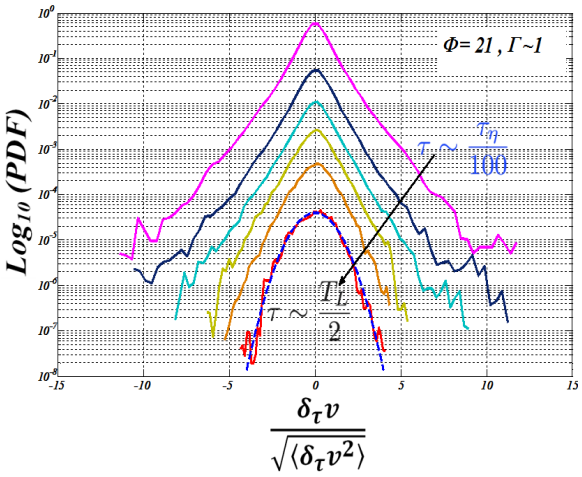

(b)

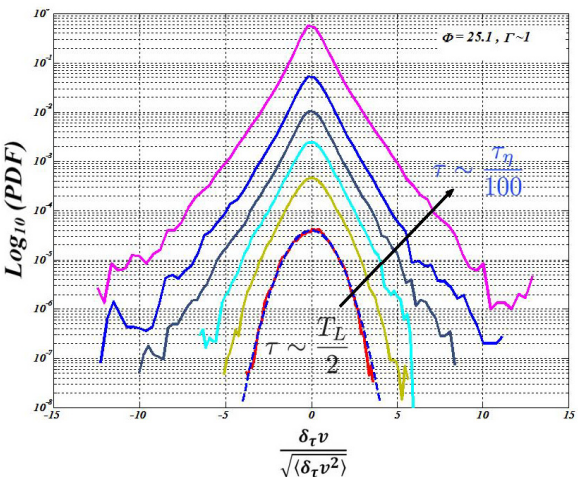

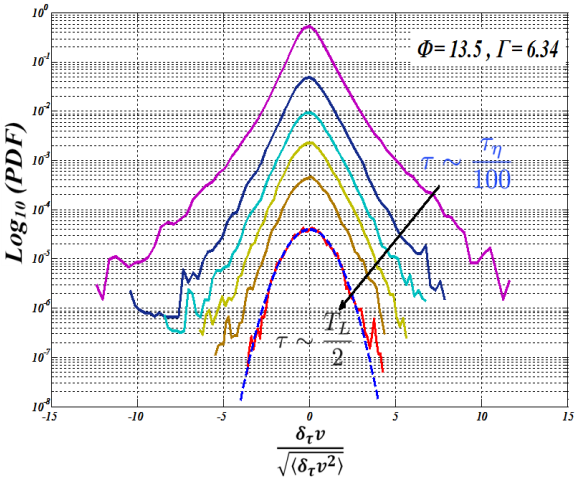

(c) (d)

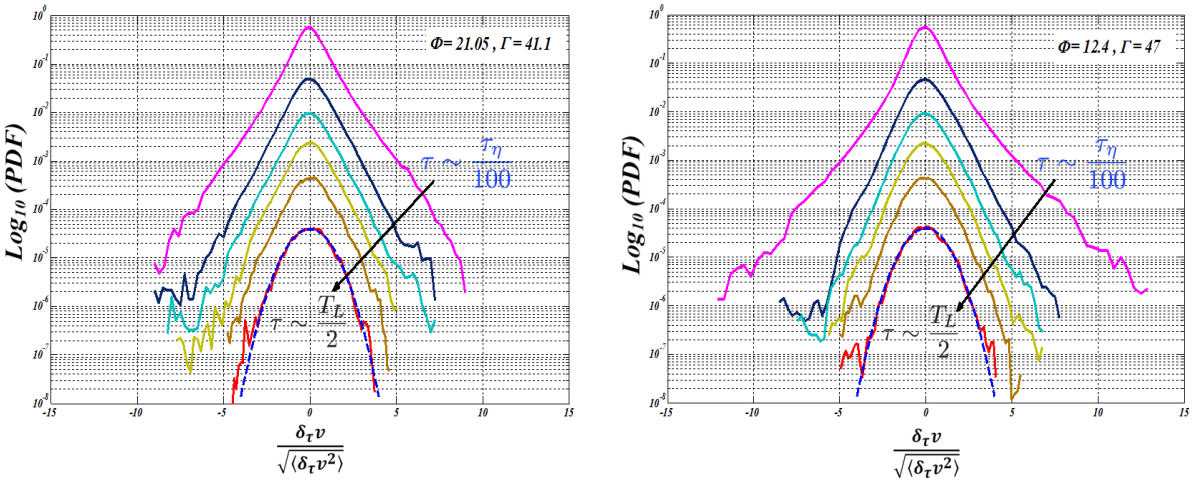

(e) (f)

FIG. 6.1 - Normalized probability density functions of velocity increments (a) $\varphi = 12.54, \Gamma \sim 1$ (b) $\varphi = 21, \Gamma \sim 1$ (c) $\varphi = 25.1, \Gamma \sim 1$ (d) $\varphi = 13.5, \Gamma = 6.34$ (e) $\varphi = 21.05, \Gamma = 41.1$ (f) $\varphi = 12.4$ and $\Gamma = 47$.

For all presented velocity increment PDFs we can clearly notice that, for the largest time increment, the PDFs are Gaussian (as the two signals tend to become independent). As we decrease the time increment the PDFs start to deviate from Gaussian and tend to have spread tails for the small increments indicating the intermittent statistics of Lagrangian velocities. For the smallest time scale, when the time lag tends to zero, increments represent the acceleration of the particles, the corresponding PDFs show the events of very high acceleration which occur with a probability much greater than in a Gaussian distribution. However it is essential to investigate the manner in which PDF tails spread with time lag from that of Gaussian to wide tails.

6.2 Flatness

The spreading of PDF tails is represented by flatness and its evolution with time lag τ. In FIG. 6.2, the flatness of all neutrally buoyant data set has been plotted as a function of time increments normalized with dissipative time scale. We can see that for small time increments, all sets have flatness in between 7.2 and 9, corresponding to acceleration flatness. As the time increment is increased the flatness decreases gradually and for large time increments it tends to achieve an asymptotic value of 3 which is the flatness of a Gaussian distribution. We also noted that some kind of "hump" can be observed at time lags close to τ_η. However, we couldn't find any systematic trend of the evolution of the flatness with neutrally buoyant particle size. The spreading of the curves shown in FIG. 6.2 is most likely due to statistical uncertainties in the estimation of the flatness of the PDFs.

We have, however, identified a clear effect of particles density on the evolution of the increments flatness with τ. An example of this behavior is shown in FIG. 6.3, in which the evolution of flatness with time for same size particles $\varphi \sim 16.6$ with different relative densities is shown.

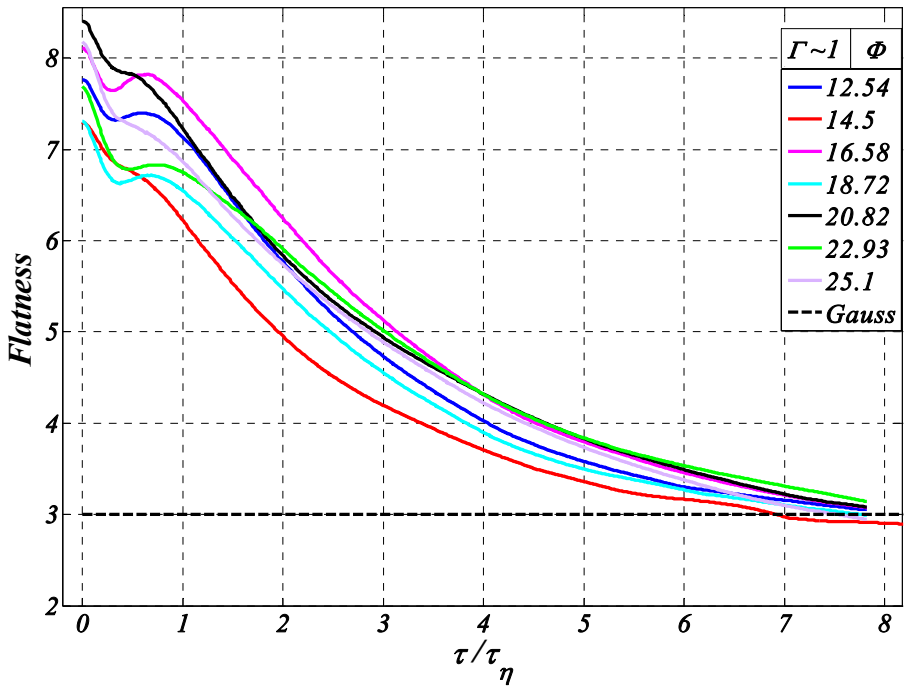

FIG. 6.2 - Flatness variation as a function of time increments normalized with dissipative time scale, the flatness of Gaussian in dashed line.

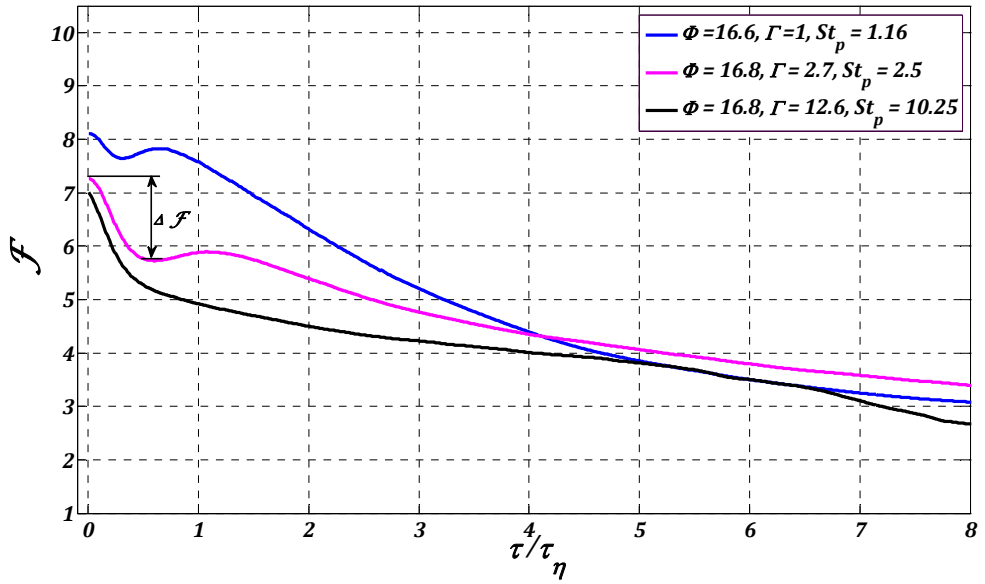

FIG. 6.3 - Variation of flatness as a function of time increments for three different relative densities ($\Gamma \sim 1, 2.5$ and 12.5) of a particular particle size $\varphi \sim 16.6$.

From FIG. 6.3, it can be observed that the flatness variation pattern for neutrally buoyant and heavy particles is not the same. For neutrally buoyant particles, there is a kind of "hump" where the flatness first decreases unless a trough is reached which is followed by an inflexion near τ_η. From this point on, the flatness gradually decreases until it reached a plateau around 3 which is the flatness of Gaussian distribution. In the case of heavy particles with relative density $\Gamma \sim 2.5$, the initial decrease or fall in flatness is greater than neutrally buoyant particles. Like neutrally buoyant this fall is followed by a hump again near τ_η and later on the flatness decreases gradually and tends to attain flatness of Gaussian distribution for large time increments. For particles with relative density $\Gamma \sim 12.5$, we did not observe the hump effect; first the flatness decreases quickly with time and then starts decreasing slowly like in other cases, similar behavior has been observed for high relative density particles. If we consider the flatness of these increments for smallest time increments then no specific trend is observed in the entire size and relative density range that has been studied. However, we did observe some systematic trends in the initial decrease in flatness $\Delta\mathcal{F}$ as we increase particle relative density. We have studied this initial fall of flatness; the change in flatness $\Delta\mathcal{F}$ is plotted for all data sets in FIG. 6.4, and for data sets having size $\varphi \sim 16.6$ with different relative densities in FIG. 6.5.

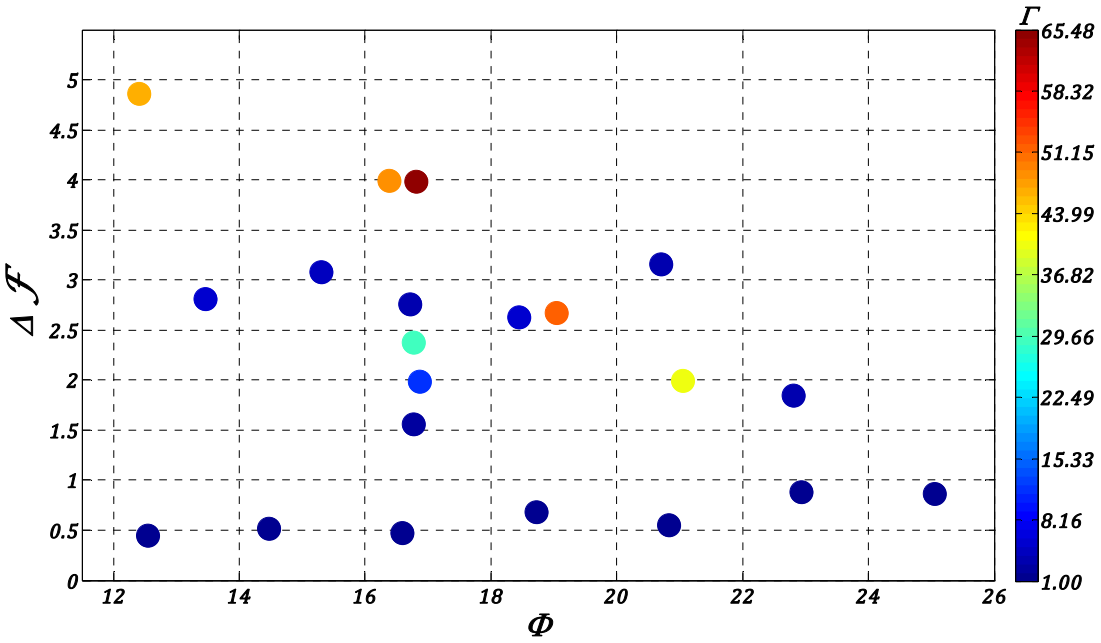

FIG. 6.4 - Initial fall in flatness as function of particle size φ and relative density Γ.

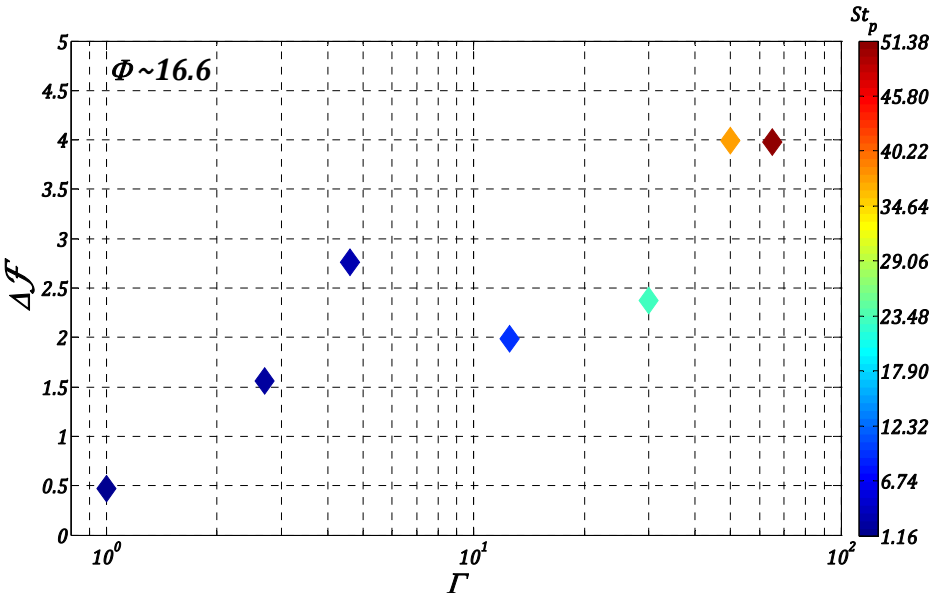

FIG. 6.5– Initial fall in flatness for different relative densities of particle size φ~ 16.6.

From FIG. 6.4, we can clearly notice that the fall in flatness is much greater for heavier particles as compared with neutrally buoyant particles. This means that heavy

particle velocity increment PDFs remain near Gaussian for most of the time lags and then suddenly deforms to have spread tails for small time increments and is contrary to the case with neutrally buoyant particles where this initial flatness fall was not adverse and velocity PDFs turned Gaussian gradually. This trend somehow reminds the prediction from point particle models, where acceleration tends to become Gaussian as inertia increases. Our results show that such a trend is effectively not observed for acceleration (or very small scale increments), but is present for increments at a larger scale, around τ_η. This suggests that one of the limitations of point particles models is their inability to reproduce the intense small scale dynamics of the particles, which in spite of an apparently large Stokes number remains present.

6.3 Lagrangian Velocity Autocorrelations

The Lagrangian velocity autocorrelations for all the data sets were calculated in the following manner:

$$R_{vv}(\tau) = \frac{\langle v(t)v(t+\tau)\rangle}{\langle (v(t))^2\rangle} \tag{6.2}$$

Note that for each individual track, velocity is centered using the ensemble average velocity and correlation is normalized using the ensemble velocity variance. After having repeated the same procedure for all velocity signals of the particular data set, the ensemble average was calculated for these autocorrelations. In FIG. 6.6, some typical velocity autocorrelations are shown for different particle sizes and densities. We can notice the correlations do not converge for long time scales, which is due to the fact

that the particles are not tracked for long times because of the limited measurement volume and the high mean flow velocity.

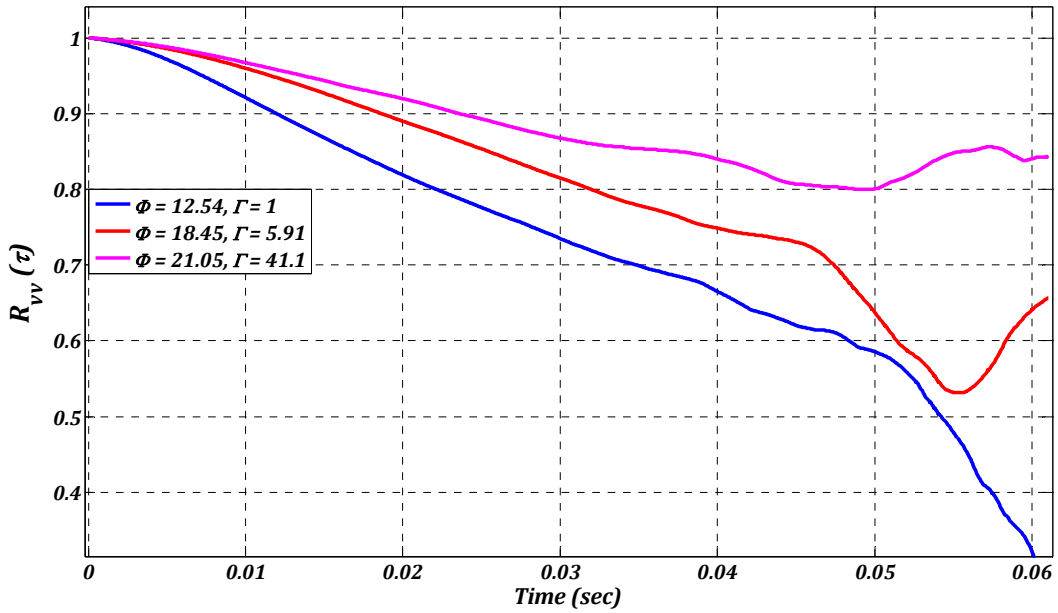

FIG. 6.6 – Lagrangian velocity autocorrelations for data sets $\varphi = 12.54$ $\Gamma = 1$, $\varphi = 18.45$, $\Gamma = 5.91$, and $\varphi = 21.05$, $\Gamma = 41.1$. We can observe the loss of convergence for long time scales.

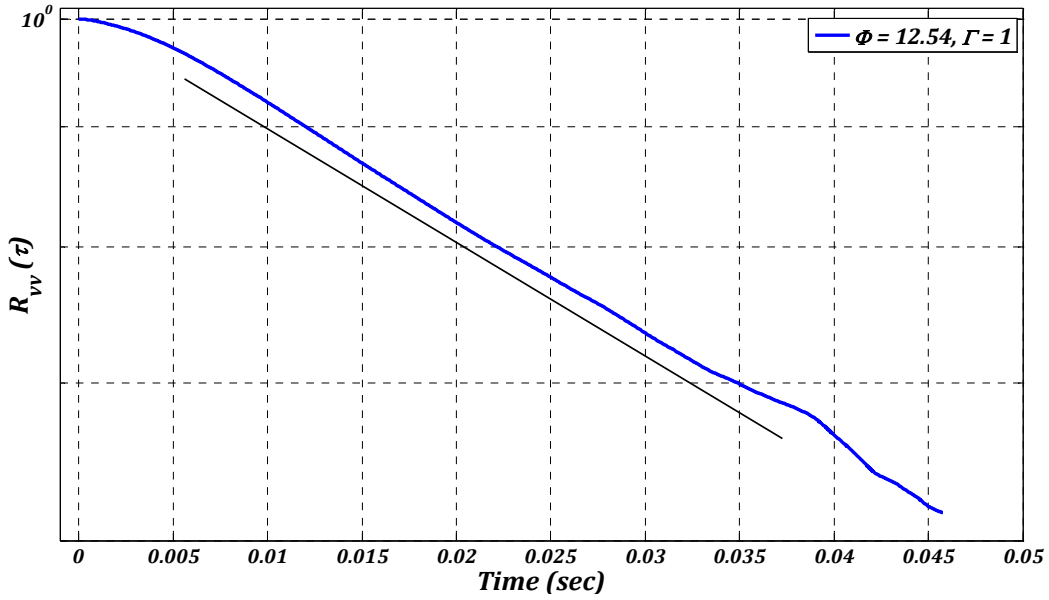

FIG. 6.7 – Logarithmic plot of a specimen of Lagrangian velocity autocorrelation w.r.to time, we can observe an exponential decay. Straight line shows the region where the correlation decays exponentially.

In FIG. 6.7, where logarithm of autocorrelation is plotted w.r.to time, we can see the initial curve at short time scale and then a straight line which indicates an exponential decay. This is characteristic of a two time scale dynamics, one short time scale T_2 and the other corresponding to the particles Lagrangian de-correlation time scale T_L.

For real tracers, the small time scale is usually ascribed to dissipation and finite Reynolds number effects [84]. In the present case of inertial particles, the small time scale curvature is believed to be due to the finite sizes and inertia of the particle and it corresponds to turbulent kinetic energy filtering by its diameter. This in case of fluid tracers i.e. for particles smaller than kolmogorov length scale and having the same density as that of carrier fluid, is equivalent to dissipative or kolmogorov time scale τ_η. The long time scale on the other hand gives an idea of integral time scale of the carrier fluid as experienced by the particles. Both of these characteristic time scales were believed to change with particle size and density. FIG. 6.8 and FIG. 6.9 show a variation in small and large time scales w.r.to size and density. Therefore, there was a need for a systematic study in order to have a clear picture how these time scales vary and which scaling do they follow, if there is any. For this purpose, all the autocorrelations were matched by fitting Sawford's two-time-stochastic model [84] which is based upon the second order Lagrangian stochastic equation. The velocity autocorrelation function form corresponding to Sawford's model is given as under:

$$R_{vv}(\tau) = \frac{T_L e^{-|\tau|/T_L} - T_2 e^{-|\tau|/T_2}}{T_L - T_2} \tag{6.3}$$

where, in spite of τ_η, T_2 was used which represents the turbulent fluctuation filtering of the energy spectrum at scales corresponding to particles diameter in order to take into account finite size effects.

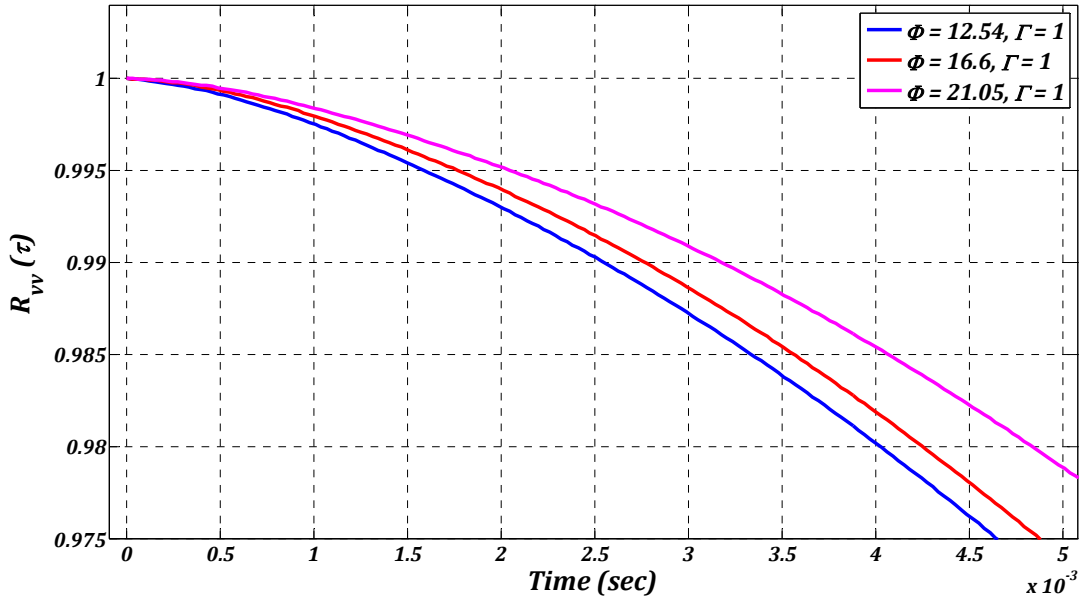

FIG. 6.8 – Lagrangian velocity autocorrelation for three different sizes of neutrally buoyant data sets, showing the variation in small time scale with respect to size.

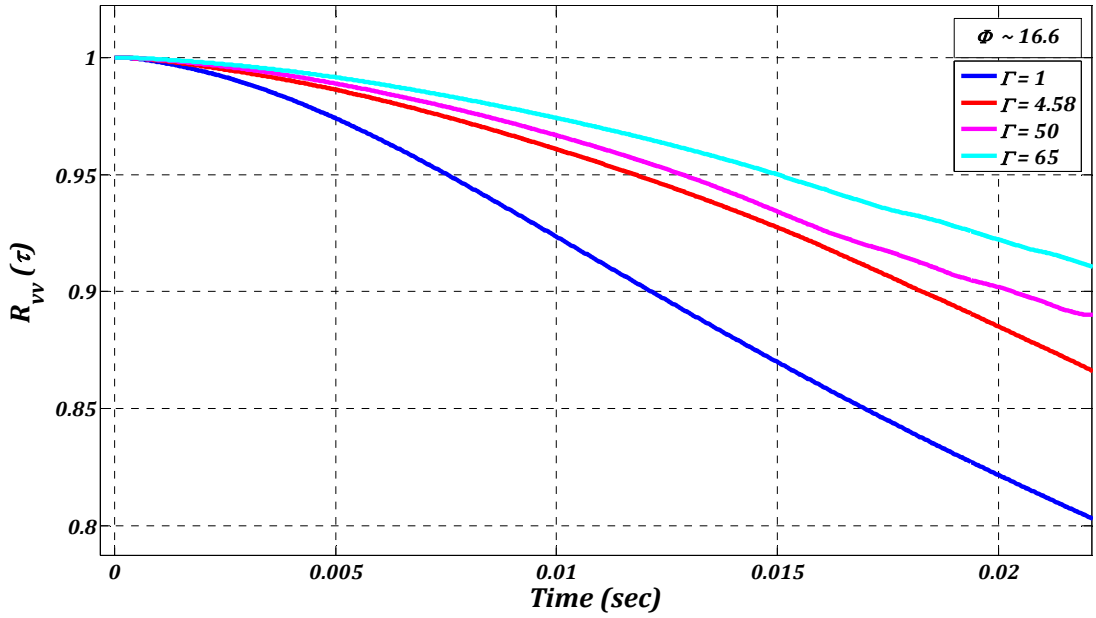

FIG. 6.9 –Particle density effects on Lagrangian velocity autocorrelation for particle size $\varphi = 16.6$.

An example of fitting this autocorrelation function with our data is shown in FIG. 6.10, it can be seen that a good extent of curve fitting has been achieved which ensures good estimation of correlation times. The data fitting was done for different time periods, the corresponding time scales were noted and then their mean values and errors were determined. These results for neutrally buoyant, $\Gamma \sim 5$, and $\Gamma \sim 50$ are shown in FIG. 6.11 to FIG. 6.19. The results that we have obtained by fitting the autocorrelations do not devise a theory or any methodology; even then it is worth mentioning.

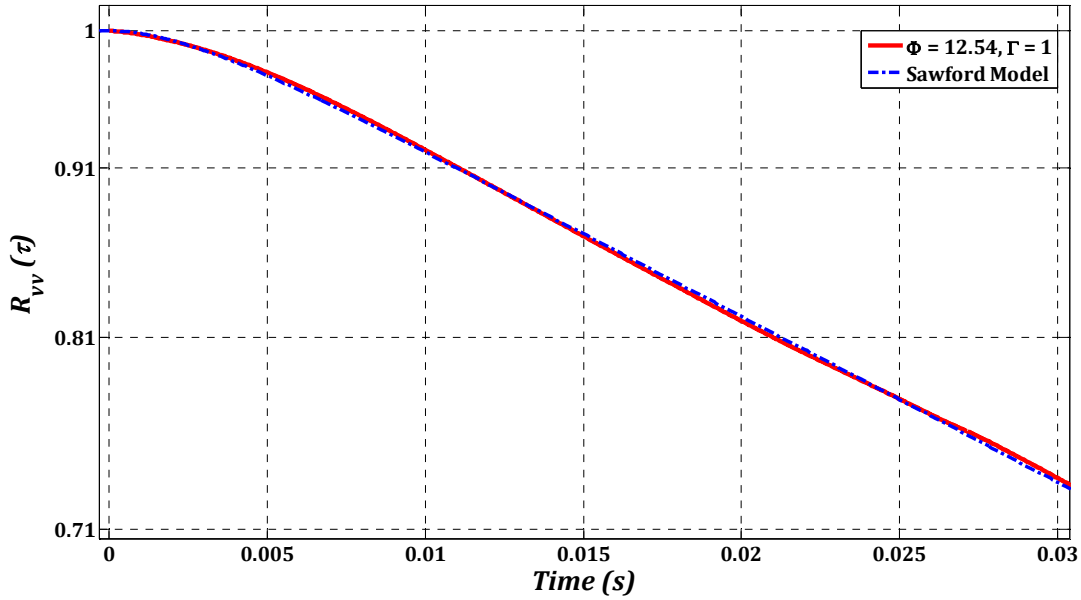

FIG. 6.10 – Fitting the Lagrangian velocity autocorrelation with Sawford's two-times stochastic model.

In FIG. 6.11, we observe a gradual increase in small time scale T_2 and then saturation near $\varphi \sim 18.7$ around a value of $3.8\,ms$, and then we observe a sudden increase in it. On the other hand the integral time scale (see FIG. 6.12) remains nearly

constant up to $\varphi \sim 18.7$ and, then we see a sudden drop in Lagrangian integral time scale which rises again and attains the constant time value. The Lagrangian Taylor micro-scale $\tau_\lambda = \sqrt{2T_L T_2}$ (which corresponds to the curvature of the autocorrelation at zero time lag), is plotted in FIG. 6.13. We observe a linear increase in τ_λ with particle diameter, with a possible inflection around $\varphi \sim 18.7$. The trend of the correlation time T_L is particularly appealing. It presents a minimum for $\varphi \sim 20$. In our flow this corresponds precisely to the Taylor microscale λ of the carrier flow. Though further systematic studies at different Reynolds number would be required to be conclusive, our measurements therefore suggest that neutrally buoyant particles with size λ decorrelate significantly faster, as a result of stronger turbulent fluctuations occurring at this scale [42].

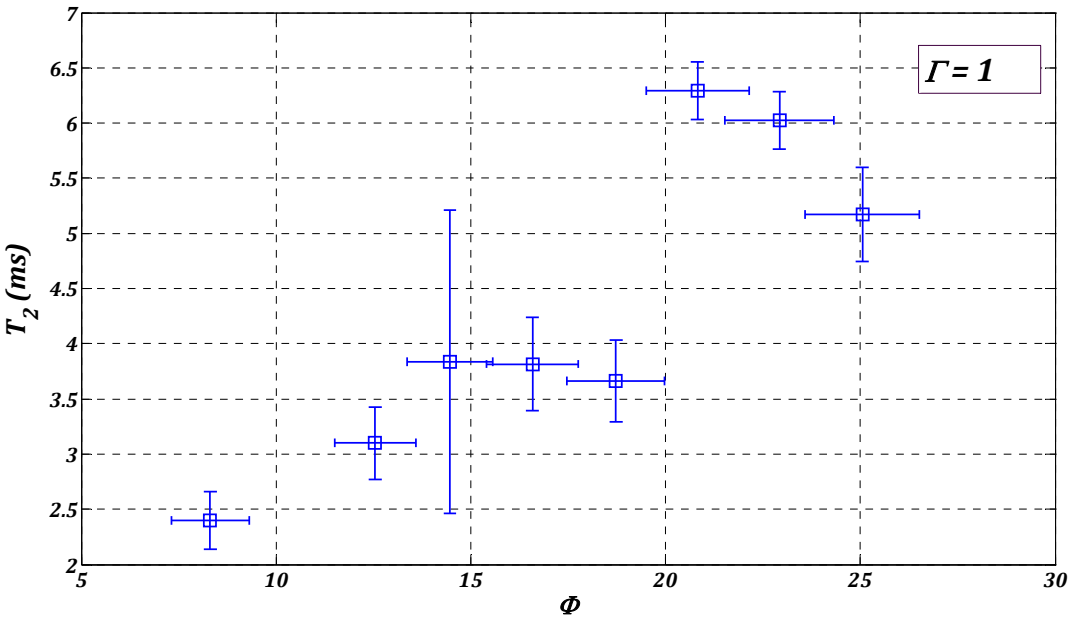

FIG. 6.11 - The small time scale obtained through fitting the autocorrelations with Sawford's model for all neutrally buoyant data sets as function of particle diameter.

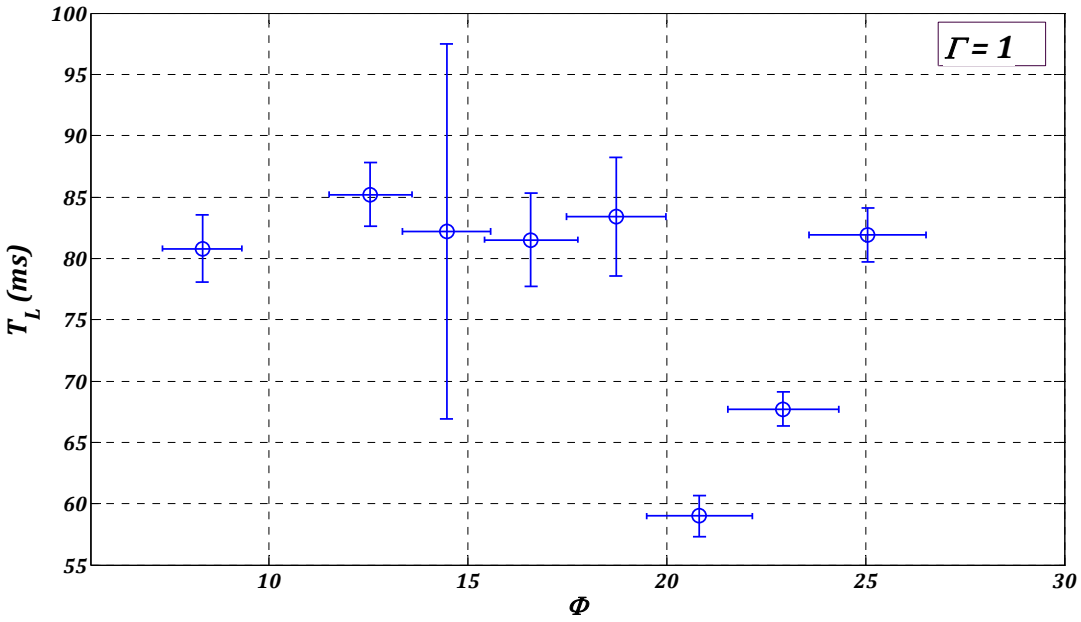

FIG. 6.12 – The integral time scale obtained through fitting the autocorrelations with Sawford's model for all neutrally buoyant data sets as function of particle diameter.

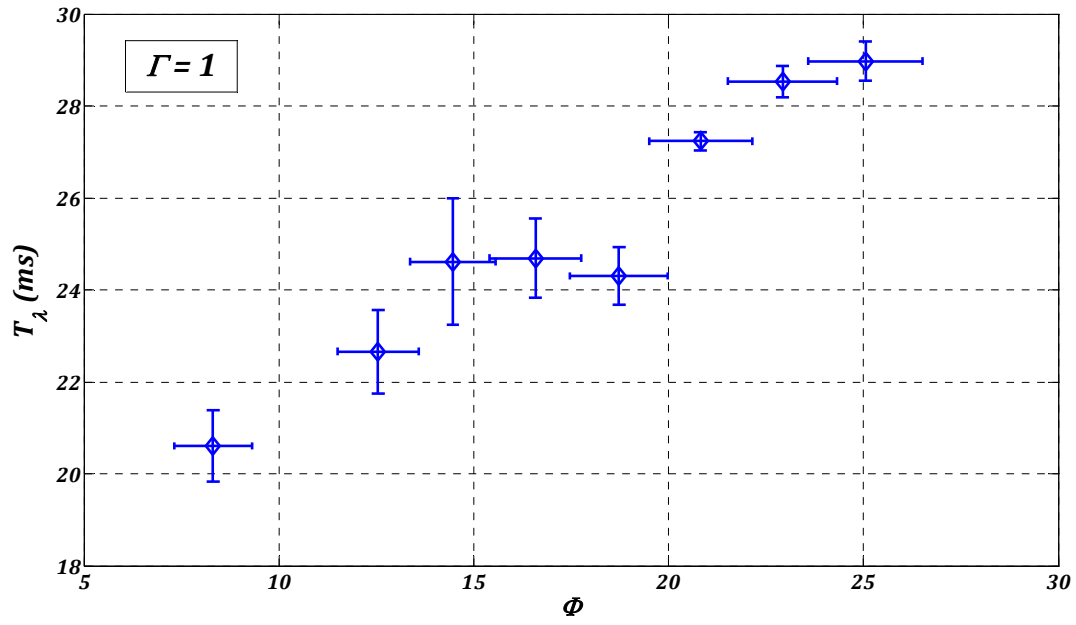

FIG. 6.13 – Taylor micro-scale calculated from small and large time scales which were obtained fitting the autocorrelations with Sawford's model for all neutrally buoyant data sets as function of particle diameter.

If we consider the evolution of these time scales with relative density for a fixed particle size, some interesting phenomena are observed; which are to some extent compatible with the particle's acceleration which we have discussed in the previous chapter. Both for T_2 and τ_λ, we observe initially a gradual and approximately linear increase with particle relative density until $\Gamma \sim 12.5$ (FIG. 6.14 (a) and (b)), which is near to the transition relative density $\Gamma^*(\varphi)$ around which lies two different regimes of particle acceleration (refer to FIG. 5.24), which for the considered particle size is considered to be near 10. Above this relative density these time scales decrease and tend to saturate an asymptotic value for high relative densities.

As for the de-correlation time T_L (FIG. 6.14 (c)), we observe that it first increases rapidly with density, then drops around $\Gamma^*(\varphi)$ and increases again. This particular trend is in good agreement with FIG. 6 of the DNS by Jung et al. [43] on the behavior of suspended heavy particles and fluid particles as seen by the fluid in which they have plotted the Lagrangian integral time of the fluid seen by the particle for a range or particle stokes number.

(a)

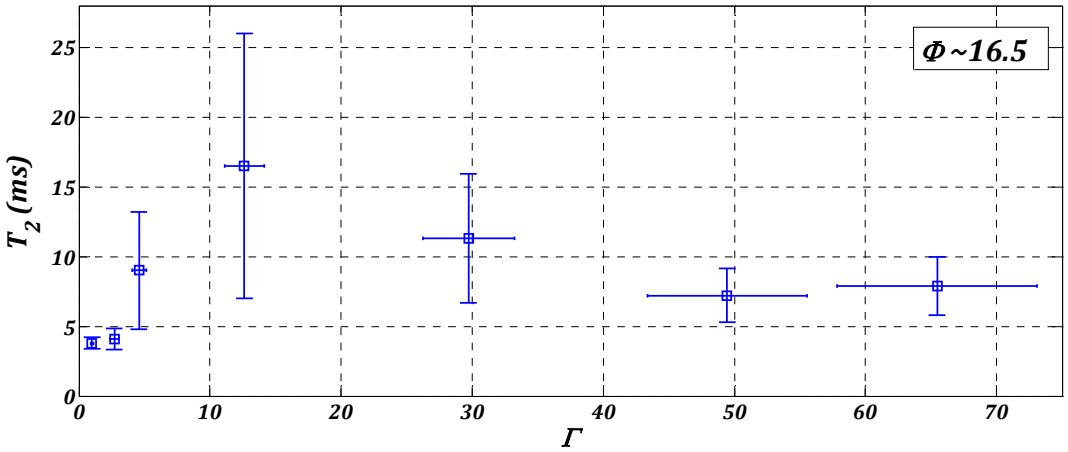

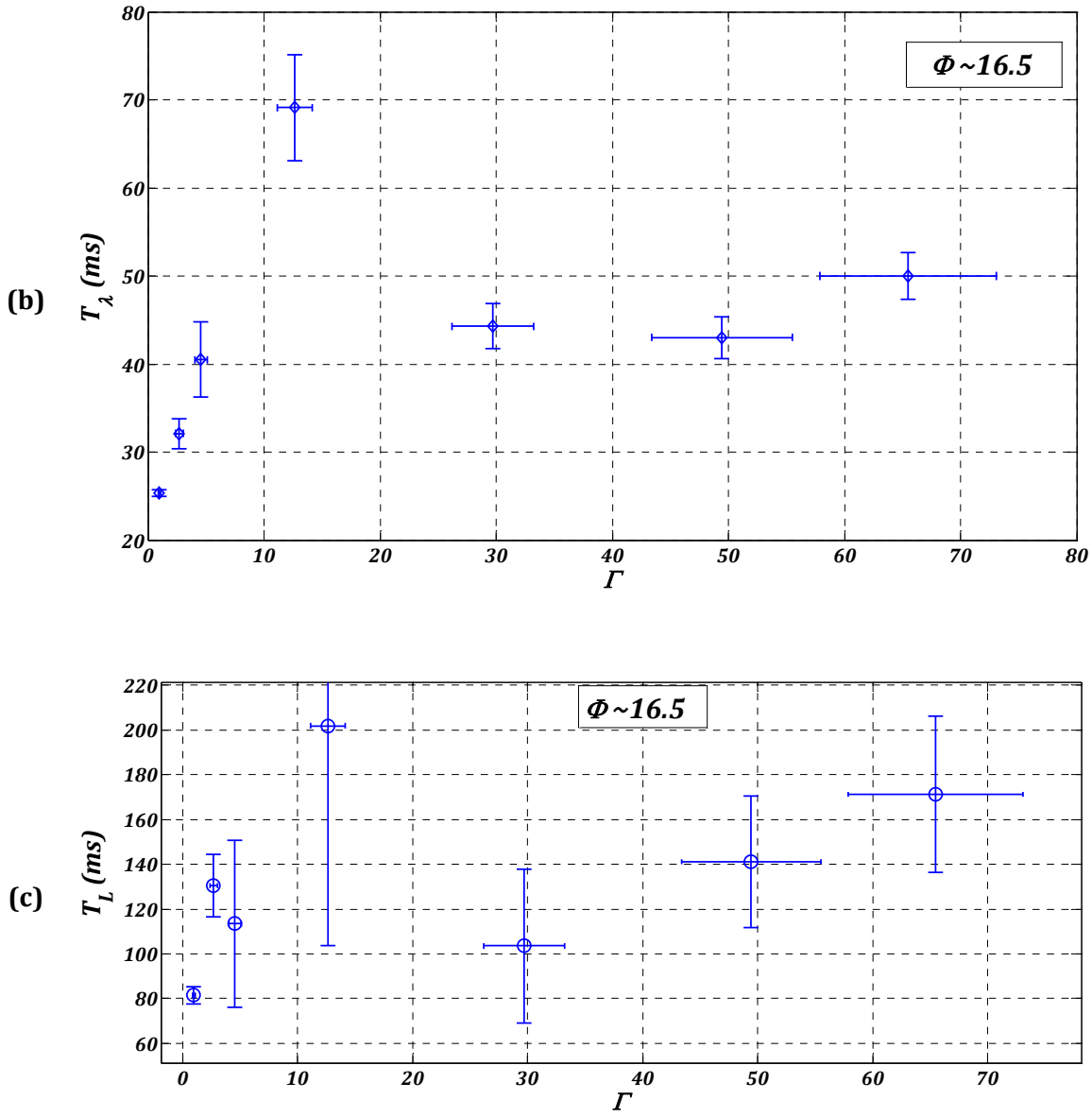

FIG. 6.14 – Evolution of time scales for fixed particle size as a function of particle density (a) T_2 (b) τ_λ (c) T_L.

6.4 Acceleration Autocorrelation

In FIG. 6.12, an example of the acceleration autocorrelation of z component is shown and defined by following relation:

$$R_a(\tau) = \frac{\langle a(t)a(t+\tau)\rangle}{\langle a(t)^2\rangle} \tag{6.4}$$

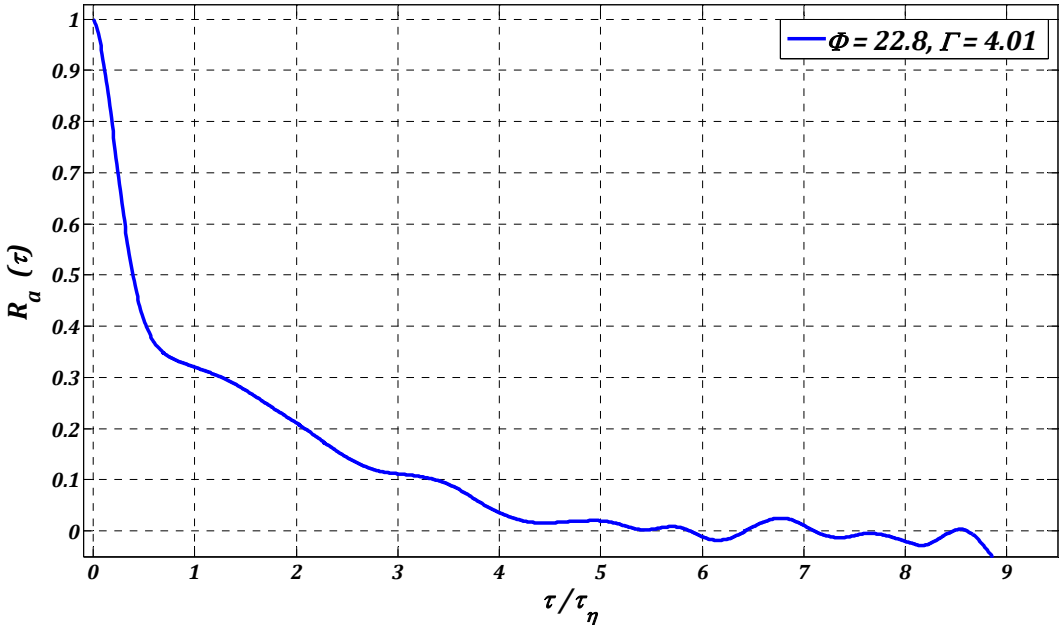

FIG. 6.15 – The autocorrelation of acceleration component a_z for data set φ 22.8, $\Gamma = 4.01$.

It has been observed that the acceleration autocorrelation decays to zero for neutrally buoyant experiments in between $3\tau_\eta \rightarrow 4\,\tau_\eta$ and $4\tau_\eta \rightarrow 7\,\tau_\eta$ for heavier particles. We notice that the decay to zero is not continuous; at first the acceleration de-correlates with large slope and then decays further to zero with relative lesser slope. In order to quantify the acceleration decorrelation we have determined a time named as integral acceleration time τ_{int} which is defined as next:

$$\tau_{int} = \int_0^{\tau_0} R_a(\tau)d\tau \tag{6.5}$$

where, τ_0 is the time when the acceleration autocorrelation decays to zero. The time τ_{int} which is equivalent to the area under the acceleration autocorrelation curve gives us a direct idea of the particles response to turbulent forcing. In FIG. 6.16, we have plotted time τ_{int} normalized with dissipative time scale τ_η for neutrally buoyant particles data set. We observe for first three data sets ($\varphi = 2.54$, $\varphi = 14.45$ and $\varphi = 16.6$ the normalized time remains constant and then it increases in general with particle size.

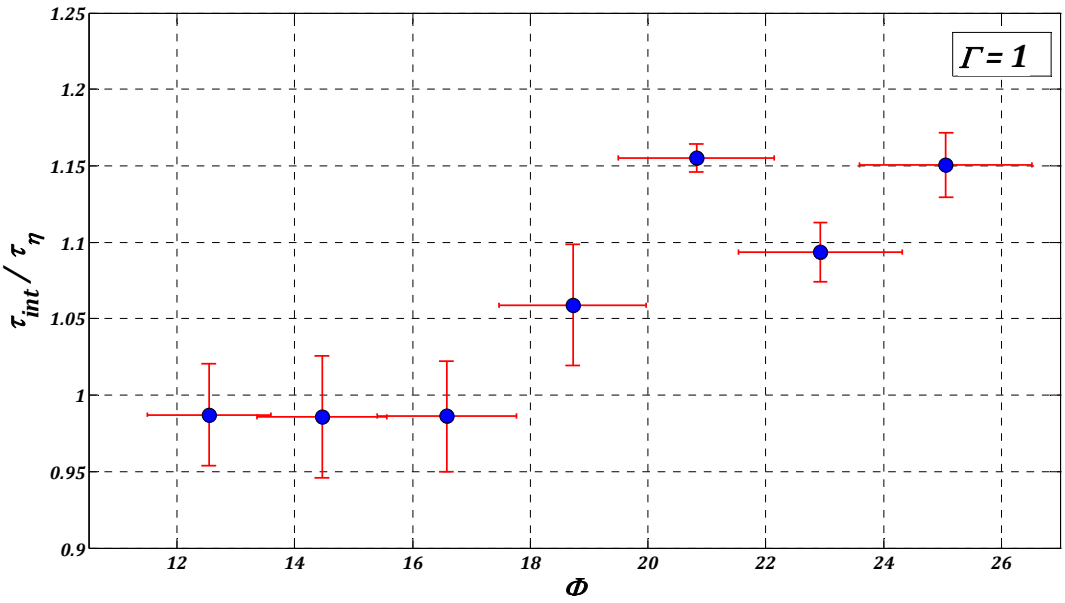

FIG. 6.16 - Normalized integral acceleration time for different particle sizes of neutrally buoyant data sets.

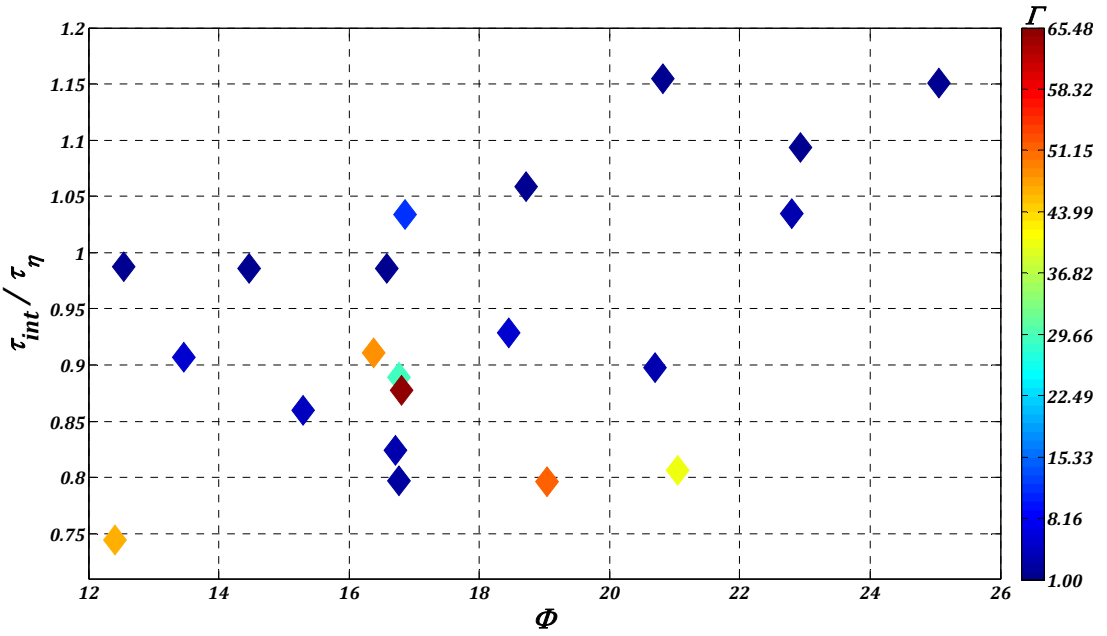

FIG. 6.17 – Normalized integral acceleration time for all data sets as a function of particle size and relative density.

6.5 Discussion

An important and interesting remark that can be made here is on the variation of integral acceleration time τ_{int}, which when normalized with τ_η varies up to only 7% with a mean value of around 1.06 or in absolute terms it remains always of the same order of magnitude with a minimum, mean and maximum of 2.5, 3.6 and 4.5 milliseconds respectively. As we have pointed out earlier that τ_{int} reflects the real response time of the particles to the turbulent forcing that includes all the hydrodynamic forces being acting upon them. We have learned from our results that even if we vary the particle size from nearly $12\eta \rightarrow 26\eta$; and the particle relative density from neutrally buoyant to nearly 70 the particle response time to the turbulent forcing doesn't vary much. On the contrary, the modified particle response time τ_p,

which was determined after taking into account the finite particle Reynolds number approximation in order to have a better estimation of drag force, vary itself two orders of magnitudes for our data sets. This large variation in particles response time leads us to a Stokes number varying from $0.9 \rightarrow 52$ which correspond from tracer to inertial particles (see FIG. 6.18 for comparison). If we consider our case in the framework of point particle models one should expect a great differences in particle dynamics for this range of stokes numbers, but this is not the case.

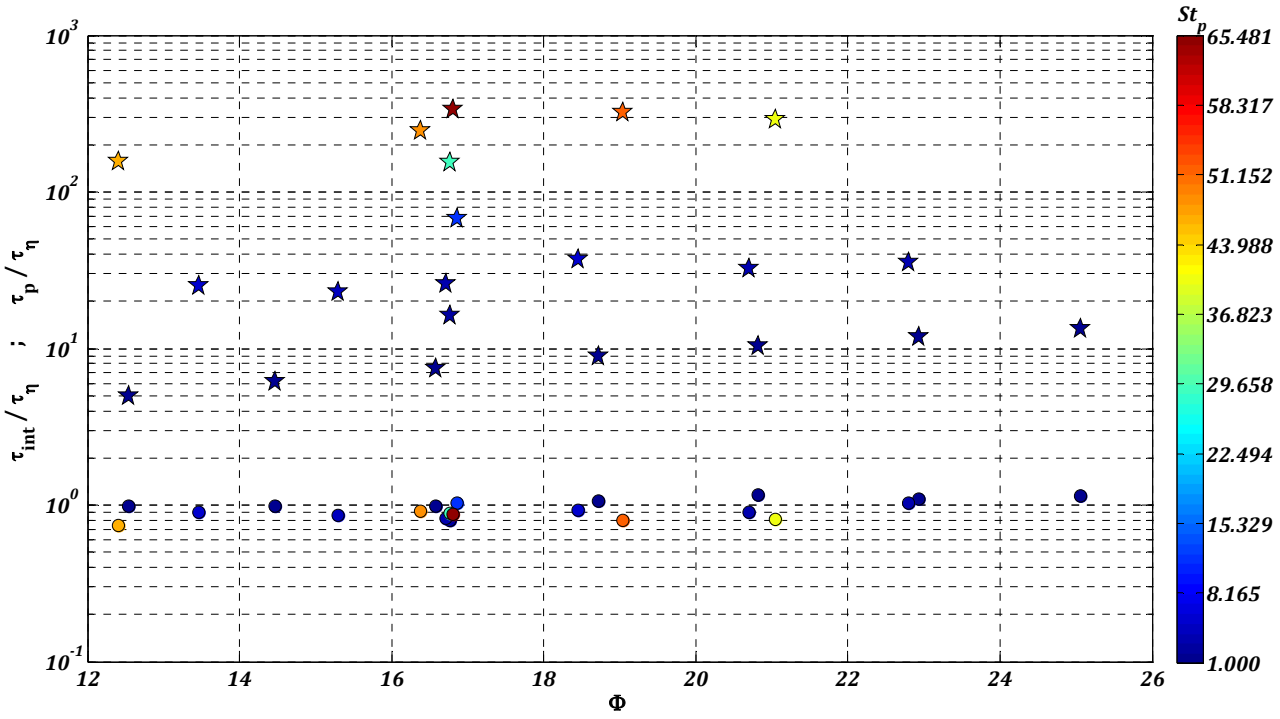

FIG. 6.18 – Comparison of particles Stokes number St with the experimentally observed effective Stokes number.

In fact the finite size effects cannot be taken into account only by one parameter i.e. Stokes number defined using classical or modified particles response time. Thus, we define an effective or experimental stokes number St_{eff} which is based upon the actual

response time of the particles τ_{int}. For our data sets this effective stokes number varies from $0.1 \rightarrow 0.2$, which seem quite reasonable if we want to interpret particle dynamics from point particle models point of view in a sense that particle dynamics do not change much because effective stokes number is almost constant. This can be further understood if we again compare Tchen & Hinze theory with actual particle response time τ_{int}. This is shown in FIG. 6.19, from where we observe that using particles real response time our data falls in the region where particle and fluid fluctuations doesn't vary with stokes and seem to be in good accordance with theoretical predictions.

On the other hand the point particle models lack in capturing the physics of finite size particle dynamics. For example in case of finite size particles, the added mass force, Faxén corrections, lift and history forces are believed to play an important role and a proper model taking into account these forces need to be develop.

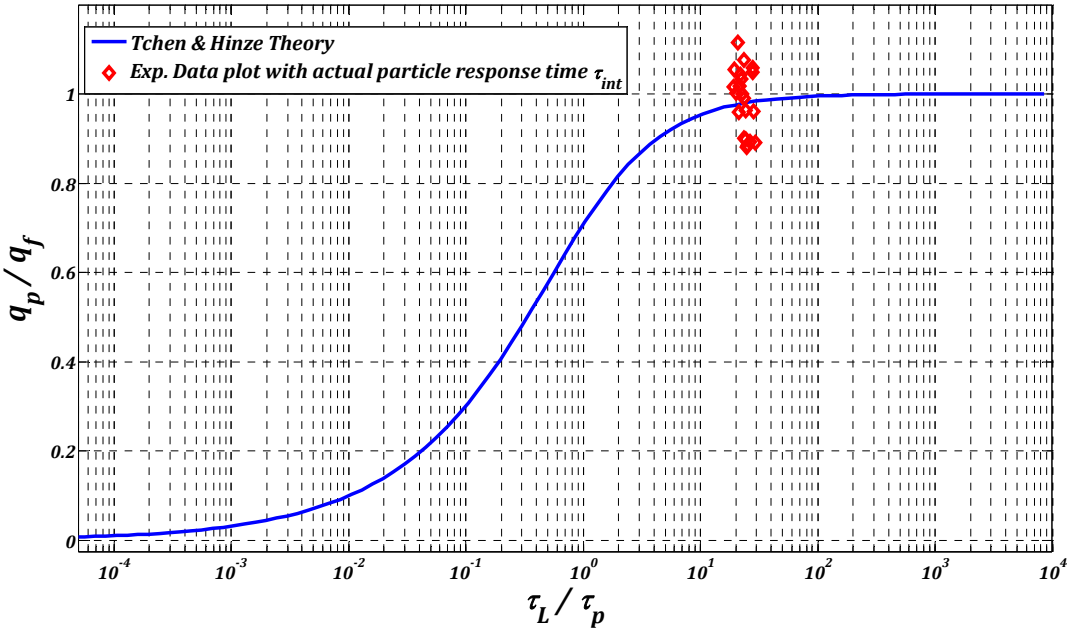

FIG. 6.19 – Comparison of our experimental data with Tchen & Hinze Theory for the turbulent energy transfer from fluid to particle as a function of Lagrangian integral time and particle response time ratio. In this figure the particle response time τ_{int} was deduced from their acceleration component autocorrelation.

Conclusion

The novel Ultrasonic Doppler Velocimetry along with versatile particle generation machine has allowed us to explore the material particle's finite size and density effects on their Lagrangian dynamics in turbulent flow. In the context of present research work, we have covered the so far unexplored range of particles sizes $10 \leq \varphi \leq 30$ (which lie in the inertial range scales of turbulence) and the particle relative densities of $1 \leq \Gamma \leq 70$. First, we have studied in detail the statistics of Lagrangian velocity and its autocorrelations. Second, the acceleration statistics were explored, as acceleration reflects a direct measure of turbulent forcing experienced by the particles. In addition to that we also studied the Lagrangian intermittency.

Concerning the Lagrangian velocity statistics, we have observed that the PDFs remain Gaussian for all the studied data sets. The root mean square velocity was found neither depending upon particle size nor on particle density in contrast with usual predictions based for instance on Tchen & Hinze theory and its extensions [88, 42, 23]. Furthermore, the Lagrangian velocity statistics of the particles were observed to be identical to the Eulerian velocity statistics of the carrier flow. The Lagrangian integral time scale for same particle size was observed to depend upon the particles density, with heavier particles having longer correlation times. In the case of neutrally buoyant particles a minimum of correlation time was observed for particle size around $D \sim \lambda$. This should be further verified by doing experiments at different Reynolds numbers.

The normalized Lagrangian acceleration PDFs were found to be strongly non-Gaussian. These PDFs for the entire range of investigated particle sizes and relative

densities were observed to be the same, which shows the robustness of normalized acceleration statistics. Our normalized acceleration PDFs were found to match that of sub-kolmogorov size ($\phi \sim 0.01$) inertial particles obtained by [4] in a similar wind tunnel experiment. This indicates that (i) if there is any change in particles normalized acceleration PDFs as predicted by point particle models, it might only be expected to occur for even smaller particles (as also suggested by [6]); (ii) an asymptotic acceleration PDF is rapidly reached as particles become finite sized. Another interesting observation is that the normalized acceleration PDFs for finite size particles measured in wind tunnel experiments does not match the PDFs measured in von Kármán flows. These findings raise the question of the (non)universality of the small scale particles dynamics: how do large scale properties of the carrier flow (for instance anisotropy and confinement) affect the dynamics of the particles? This question should be addressed in the forthcoming studies.

Contrary to normalized acceleration PDFs which were found independent of particles size and density, clear effects of these two parameters were observed on particle's acceleration variance. It was found that, for heavy particles, finite size effects can be trivially extrapolated neither from the heavy point particle limit nor from the finite size neutrally buoyant case as both of these limits predict a monotonic decrease of acceleration variance with increasing inertia, contradictory with the trends measured for finite size heavy particles. Observed finite size and density effects cannot be accounted by simple *filtering* arguments based only upon Stokes number effects as in the point particle case. A *sampling* scenario, in the spirit of *sweep-stick* mechanisms seems more adequate to possibly describe the simultaneous influence of density and

size. From the acceleration autocorrelations it was remarked that for the entire particle sizes and densities data sets, their response time to the turbulent forcing was always of the order of Kolmogorov's time scale. This infers that the actual particles forcing time differs from the conventional Stokes time which, within our data sets, would be expected to change over more than three orders of magnitude.

The Lagrangian acceleration statistics were found to be intermittent for the entire data sets studied. The signature of intermittency was noticed to depend upon particles density. This has been analyzed in terms of the time evolution of the flatness of the Lagrangian velocity increments. For all particle densities, the flatness was found identical at the smallest scales (i.e. acceleration doesn't change). However density dependence is observed for increasing time increments: the heavier the particles the more rapidly the flatness drops when the time scale increases from dissipative to inertial range. This suggests that : (i) at small scales, the Lagrangian dynamics results from the same forcing mechanism (very likely dominated by the pressure gradients of the carrier flow) regardless of particle density ; (ii) inertial effects associated with particle density mostly affect the Lagrangian dynamics at time scales corresponding to inertial range scales of the carrier flow.

The present study has given birth to important questions regarding finite size particles dynamics in turbulent flows. In order to further endorse our results it would be interesting to repeat similar measurements at different Reynolds numbers, to examine, for example, the diminution of Lagrangian velocity correlation time around $D \sim \lambda$ and to explore the Reynolds number dependence of the normalized acceleration

PDFs form. Moreover, a much deeper investigation of the influence of large scale properties of the carrier flow (for e.g. anisotropy and confinement) on particles acceleration PDFs is required. It would also be interesting to study the dynamics of particles lighter than fluid ($\Gamma < 1$). Measurements by Volk et al. [90], with air bubbles in a water von Kármán flow, suggest that this could help exploring the relevance of the sampling scenario mentioned above as lighter particles should accumulate in high vorticity regions and sample complementary regions of the flow compared with heavy particles. Finally, it is our hope that this exhaustive study will help the integration of particles finite size and density effects in existing dynamical models.

References

[1] Mohamed Abbad, Mustapha & Souhar. Effects of the history force on an oscillating rigid sphere at low reynolds number. *Experiments in Fluids*, 36:775–782(8), May 2004.

[2] A. Aliseda, A. Cartellier, F. Hainaux, and J. C. Lasheras. Effect of preferential concentration on the settling velocity of heavy particles in homogeneous isotropic turbulence. *Journal of Fluid Mechanics*, 468(-1):77–105, 2002.

[3] T. R. Auton, J. C. R. Hunt, and M. Prud'Homme. The force exerted on a body in inviscid unsteady non-uniform rotational flow. *Journal of Fluid Mechanics Digital Archive*, 197:241–257, 1988.

[4] S. Ayyalasomayajula, A. Gylfason, L. R. Collins, E. Bodenschatz, and Z. Warhaft. Lagrangian Measurements of Inertial Particle Accelerations in Grid Generated Wind Tunnel Turbulence. *Physical Review Letters*, 97(14):144507, October 2006.

[5] S. Ayyalasomayajula, A. Gylfason, and Z. Warhaft. Lagrangian measurements of fluid and inertial particles in decaying grid generated turbulence. In Yukio Kaneda, editor, *IUTAM Symposium on Computational Physics and New Perspectives in Turbulence*, volume 4, pages 171–175, Nagoya, Japan, September, 11-14 2006. Nagoya University, Springer.

[6] S. Ayyalasomayajula, Z. Warhaft, and L. R. Collins. Modeling inertial particle acceleration statistics in isotropic turbulence. *Physics of Fluids*, 20(9):095104, 2008.

[7] L. Wakaba S. Balachandar. On the added mass force at finite reynolds and acceleration numbers. *Theoretical and Computational Fluid Dynamics*, 21:147–153, 2007.

[8] A.M. Basset. Treatise on hydrodynamics. *Treatise on Hydrodynamics*, 2:285–297, 1888.

[9] J. Bec, L. Biferale, G. Boffetta, A. Celani, M. Cencini, A. Lanotte, S. Musacchio, and F. Toschi. Acceleration statistics of heavy particles in turbulence. *Journal of Fluid Mechanics*, 550:349, 2006.

[10] L. Biferale, G. Boffetta, A. Celani, A. Lanotte, and F. Toschi. Lagrangian statistics in fully developed turbulence. *Journal of Turbulence*, 7:N6, 2006.

[11] M. S. Borgas. The multifractal lagrangian nature of turbulence. *Philosophical Transactions Of The Royal Society Of London Series A-Mathematical Physical And Engineering Sciences*, 342(1665):379–411, 1993.

[12] M. S. Borgas. Self-similarity and multifractals in turbulence. *Physics Of Fluids A-Fluid Dynamics*, 5(12):3181–3185, 1993.

[13] V. J. Boussinesq. Sur la résistance qu'oppose un liquide indéfini en repos. *C.R. Acad. Sci.*, 100:935–937, 1885.

[14] Phillip P. Brown and Desmond F. Lawler. Sphere drag and settling velocity revisited. *Journal of Environmental Engineering*, 129(3):222–231, 2003.

[15] Eugene J. Chang and Martin R. Maxey. Unsteady flow about a sphere at low to moderate reynolds number. Part 1. Oscillatory motion. *Journal of Fluid Mechanics Digital Archive*, 277(1):347–379, 1994.

[16] Eugene J. Chang and Martin R. Maxey. Unsteady flow about a sphere at low to moderate reynolds number. Part 2. Accelerated motion. *Journal of Fluid Mechanics Digital Archive*, 303(1):133–153, 1995.

[17] L. Chen, S. Goto, and J. C. Vassilicos. Turbulent clustering of stagnation points and inertial particles. *Journal of Fluid Mechanics*, 553(1):143–154, 2006.

[18] Laurent Chevillard. Description multifractale unifiée du phénomène d'intermittence en turbulence Eulérienne et Lagrangienne. PhD thesis, L'UNIVERSITÉ BORDEAUX I, 2004.

[19] Grace J. R. Clift, R. and M.E. Weber. Bubbles, drops and particles. *Academic*, 1978.

[20] C. T. Crowe, T. R. Troutt, and J. N. Chung. Numerical models for two-phase turbulent flows. *Annual Review Of Fluid Mechanics*, 28:11–43, 1996.

[21] David S. Dandy and Harry A. Dwyer. A sphere in shear flow at finite Reynolds number: effect of shear on particle lift, drag, and heat transfer. *Journal of Fluid Mechanics Digital Archive*, 216(1):381–410, 1990.

[22] E. Deutsch. Dipersion de particules dans une turbulence homogène isotrope stationnaire calculée par simulation numérique directe des grandes échelles. PhD thesis, EDF-DRD, 1992.

[23] E. Deutsch and O. Simonin. Large eddy simulation applied to the motion of particles in stationary homogeneous fluid turbulence. *In Turbulence Modification in Mutliphase Flows*, 110:35–42, 1991.

[24] Van Dyke. *An Album of Fluid Motion*. The Parabolic Press, 1982.

[25] H. Faxén. Der widerstand gegen die bewegung einer starren kugel in einer zum den flussigkeit, die zwischen zwei parallelen ebenenwinden eingeschlossen ist. *Ann. Phys.*, 68:89–119, 1922.

[26] Pascal Fede. Modélisation et simulation de l'influence de la turbulence sur les collisions dans les écoulements mono- et bi-solides. PhD thesis, INP Toulouse, 2004.

[27] J. R. Fessler, J. D. Kulick, and J. K. Eaton. Preferential concentration of heavy-particles in a turbulent channel flow. *Physics Of Fluids*, 6(11):3742–3749, 1994.

[28] JohnR. Fessler and John K. Eaton. Turbulence modification by particles in a backward-facing step flow. *Journal of Fluid Mechanics*, 394(1):97–117, 1999.

[29] Pierre Fevrier. Etude numérique des effets de concentration préférentielle et de corrélation spatiale entre vitesses de particules solides en turbulence homogène isotrope stationnaire. PhD thesis, INP Toulouse, 2000.

[30] Patrick Flandrin. *Temps-fréquence*. Hermès, 1993.

[31] P. D. Friedman and J. Katz. Mean rise rate of droplets in isotropic turbulence. *Physics of Fluids*, 14(9):3059–3073, 2002.

[32] Uriel Frisch. *Turbulence: The Legacy of A. N. Kolmogorov*. Cambridge University Press, 1995.

[33] Yves Gagne. *Contribution à l'étude expérimentale de l'intermittence de la turbulence à petite échelle*. PhD thesis, Université de Grenoble, 1980.

[34] R. Gatignol. The faxen formulae for a rigid particle in an unsteady non-uniform stokes flow. *Journal de Mécanique Théorique et Appliquée*, 2:143–160, 1983.

[35] Phillipe Gervais. *Mesure acoustique de vitesse lagrangienne dans un jet d'air turbulent*. PhD thesis, Université Joseph Fourier I, 2005.

[36] S. Goto and J. C. Vassilicos. Sweep-Stick Mechanism of Heavy Particle Clustering in Fluid Turbulence. *Physical Review Letters*, 100(5):054503, February 2008.

[37] Toshiyuki Gotoh and Daigen Fukayama. Pressure spectrum in homogeneous turbulence. *Phys. Rev. Lett.*, 86(17):3775–3778, Apr 2001.

[38] Dario Vincenzi Haitao Xu., Nicholas T. Ouellette and Eberhard Bodenschatz. Acceleration correlations and pressure structure functions in high-reynolds number turbulence. *Physical Review Letters*, 99:204501, 2007.

[39] Odar & Hamilton. Forces on a sphere accelerating in a viscous fluid. *Journal of Fluid Mechanics*, 18:302–314, 1964.

[40] Reginald J. Hill and James M. Wilczak. Pressure structure functions and spectra for locally isotropic turbulence. *Journal of Fluid Mechanics Digital Archive*, 296(1):247–269, 2006.

[41] T. Ishihara, Y. Kaneda, M. Yokokawa, K. Itakura, and A. Uno. Small-scale statistics in high-resolution direct numerical simulation of turbulence: Reynolds number dependence of one-point velocity gradient statistics. *Journal Of Fluid Mechanics*, 592:335–366, 2007.

[42] J.O.Hinze. *Turbulence*. McGraw-Hill, 1959.

[43] Jaedal Jung, Kyongmin Yeo, and Changhoon Lee. Behavior of heavy particles in isotropic turbulence. *PHYSICAL REVIEW E*, 77(1, Part 2), JAN 2008.

[44] Wouter; Schneider Kai Kadoch, Benjamin; Bos. Extreme Lagrangian acceleration in confined turbulent flow. *Physical Review Letters*, 100:4, 2008.

[45] Inchul Kim, Said Elghobashi, and William A. Sirignano. On the equation for spherical-particle motion: effect of Reynolds and acceleration numbers. *Journal of Fluid Mechanics*, 367(1):221–253, 1998.

[46] A.N. Kolmogorov. The local structure of turbulence in incompressible viscous fluid for very large Reynolds numbers. *Dokl. Akad. Nauk SSSR*, 30:9–13, 1941a.

[47] A.N. Kolmogorov. Dissipation of energy in the locally isotropic turbulence. *Dokl. Akad. Nauk SSSR*, 32:16–18, 1941b.

[48] Austin R. Frey Alan B. Coppens James V. Sanders L. E. Kinsler, Lawrence E. Kinsler. *Fundamentals of Acoustics*. John Wiley & Sons Inc, 1999.

[49] A. La Porta, Greg A. Voth, Alice M. Crawford, Jim Alexander, and Eberhard Bodenschatz. Fluid particle accelerations in fully developed turbulence. *Nature*, 409(6823):1017–1019, February 2001.

[50] B. J. Lazaro and J. C. Lasheras. Particle dispersion in the developing free shear-layer .1. unforced flow. *Journal Of Fluid Mechanics*, 235:143–178, 1992.

[51] B. J. Lazaro and J. C. Lasheras. Particle dispersion in the developing free shear-layer .2. forced flow. *Journal Of Fluid Mechanics*, 235:179–221, 1992.

[52] M. Lesieur. *Turbulence in Fluids*. Kluwer Academic Press, 1990.

[53] J. L. Lumley. Two-phase and non-newtonian flows. *Topics in Physics*, 12:290–324, 1978.

[54] Paul Manneville. *Instabilities, chaos and turbulence*. Imperial College Press, London, 2004. Includes bibliography and index.

[55] Martin R. Maxey and James J. Riley. Equation of motion for a small rigid sphere in a nonuniform flow. *Physics of Fluids*, 26(4):883–889, 1983.

[56] M.R. Maxey. The equation of motion for a small rigid sphere in a nonuniform or unsteady flow. ASME FED-Vol. 166, 57-62, Intl. Symp. on Gas-Solid Flows, June 1993.

[57] Nicolas Mazellier. *Dynamique spatio-temporelle du champ de vorticité en turbulence : mesures par corrélation acoustique dynamique.* PhD thesis, Université Joseph-Fourier - Grenoble I, 2005.

[58] Irene M Mazzitelli and Detlef Lohse. Lagrangian statistics for fluid particles and bubbles in turbulence. *New Journal of Physics*, 6:203, 2004.

[59] R. Mei. An approximate expression for the shear lift force on a spherical particle at finite reynolds number. *International Journal of Multiphase Flow*, 18(1):145 – 147, 1992.

[60] R. Mei. Velocity fidelity of flow tracer particles. *Experiments in Fluids*, 22:1–13, 1996.

[61] R. Mei and J. F. Klausner. Unsteady force on a spherical bubble at finite reynolds-number with small fluctuations in the free-stream velocity. *PHYSICS OF FLUIDS A-FLUID DYNAMICS*, 4(1):63–70, JAN 1992.

[62] Renwei Mei. Flow due to an oscillating sphere and an expression for unsteady drag on the sphere at finite reynolds number. *Journal of Fluid Mechanics Digital Archive*, 270(-1):133–174, 1994.

[63] R. Mei and R. J. Adrian. Flow past a sphere with an oscillation in the free-stream velocity and unsteady drag at finite Reynolds-number. *JOURNAL OF FLUID MECHANICS*, 237:323–341, APR 1992.

[64] R. Mei, C.J. Lawrence, and R.J. Adrian. Unsteady drag on a sphere at finite Reynolds-number with small fluctuations in the free-stream velocity. *JOURNAL OF FLUID MECHANICS*, 233:613–631, DEC 1991.

[65] A.S. Monin and A.M. Yaglom. *Statistical Fluid Mechanics*. MIT Press, 1975.

[66] N. Mordant, A. M. Crawford, and E. Bodenschatz. Experimental lagrangian acceleration probability density function measurement. *Physica D: Nonlinear Phenomena*, 193(1-4):245–251, June 2004.

[67] N. Mordant, J. Delour, E. Léveque, O. Michel, A. Arnéodo, and J.-F. Pinton. Lagrangian velocity fluctuations in fully developed turbulence: scaling, intermittency and dynamics. *Journal of Statistical Physics*, 113:701–717, 2003.

[68] N. Mordant, P. Metz, O. Michel, and J. F. Pinton. Measurement of lagrangian velocity in fully developed turbulence. *Physical Review Letters*, 87(21):214501, November 2001.

[69] Nicolas Mordant, Alice M. Crawford, and Eberhard Bodenschatz. Three-dimensional structure of the lagrangian acceleration in turbulent flows. *Phys. Rev. Lett.*, 93(21):214501, Nov 2004.

[70] Nicolas Mordant, Emmanuel Lévêque, and Jean-François Pinton. Experimental and numerical study of the lagrangian dynamics of high reynolds turbulence. *New Journal of Physics*, 6:116, 2004.

[71] N. Mordant and J.-F. Pinton. Velocity measurement of a settling sphere. *The European Physical Journal B*, 18(2):343–352, 2000.

[72] A.M. Obukhov. *Dokl. Akad. Nauk SSSR*, 66:17, 1949.

[73] A.M. Obukhov. Some specific features of atmospheric turbulence. *Journal of Fluid Mechanics*, 13:77–81, 1962.

[74] C.W. Oseen. Hydrodynamik. *Akademische, Leipzig*, 1927.

[75] Nicholas T. Ouellette. *Probing The Statistical Structure Of Turbulence With Measurements Of Tracer Particle Tracks*. PhD thesis, Cornell University, 2006.

[76] Nicholas T Ouellette, Haitao Xu, Mickaël Bourgoin, and Eberhard Bodenschatz. Small-scale anisotropy in lagrangian turbulence. *New Journal of Physics*, 8(6):102, 2006.

[77] Stephen B. Pope. *Turbulent flows*. Cambridge University Press, 2000.

[78] Nauman M. Qureshi, Mickael Bourgoin, Christophe Baudet, Alain Cartellier, and Yves Gagne. Turbulent transport of material particles: An experimental study of finite size effects. *Physical Review Letters*, 99(18):184502, 2007.

[79] Qureshi, N. M., Arrieta, U. , Baudet, C. , Cartellier, A. , Gagne, Y. , and Bourgoin, M. . Acceleration statistics of inertial particles in turbulent flow. *The European Physical Journal B*, 66(4):531–536, dec 2008.

[80] L.F. Richardson. *Weather Prediction by Numerical Process*. Cambridge University Press, 1922.

[81] J Fabre J RIVERO, M Magnaudet. New results on the forces exerted on a spherical body by an accelerated flow. *COMPTES RENDUS DE L ACADEMIE DES SCIENCES SERIE II*, 312:1499–1506, 1991.

[82] P. G. Saffman. The lift on a small sphere in a slow shear flow. *Journal of Fluid Mechanics Digital Archive*, 22(02):385–400, 1965.

[83] Juan P. L. C. Salazar, Jeremy de Jong, Lujie Cao, Scott H. Woodward, Hui Meng, and Lance R. Collins. Experimental and numerical investigation of inertial particle clustering in isotropic turbulence. *Journal of Fluid Mechanics*, 600(1):245–256, 2008.

[84] B. L. Sawford. Reynolds number effects in lagrangian stochastic models of turbulent dispersion. *Physics of Fluids A: Fluid Dynamics*, 3(6):1577–1586, 1991.

[85] S. Schreck and S. J. Kleis. Modification of grid-generated turbulence by solid particles. *Journal Of Fluid Mechanics*, 249:665–688, 1993.

[86] W. H. Snyder and J. L. Lumley. Some measurements of particle velocity autocorrelation functions in a turbulent flow. *Journal of Fluid Mechanics Digital Archive*, 48(01):41–71, 1971.

[87] K. D. Squires and J. K. Eaton. Preferential concentration of particles by turbulence. *Physics Of Fluids A-Fluid Dynamics*, 3(5):1169–1179, 1991.

[88] C.M. Tchen. *Mean value and correlation problems connected with the motion of small particles suspended in a turbulent fluid*. PhD thesis, Delft, 1940.

[89] Prakash Vedula and P. K. Yeung. Similarity scaling of acceleration and pressure statistics in numerical simulations of isotropic turbulence. *Physics of Fluids*, 11(5):1208–1220, 1999.

[90] R. Volk, E. Calzavarini, G. Verhille, D. Lohse, N. Mordant, J.-F. Pinton, and F. Toschi. Acceleration of heavy and light particles in turbulence: Comparison between experiments and direct numerical simulations. *Physica D*, 237(14-17):2084, 2008.

[91] Romain Volk, Nicolas Mordant, Gautier Verhille, and Jean-Francois Pinton. Measurement of particle and bubble accelerations in turbulence. *EPL*, 2007.

[92] Greg A. Voth, A. La Porta, Alice M. Crawford, Jim Alexander, and Eberhard Bodenschatz. Measurement of particle accelerations in fully developed turbulence. *Journal of Fluid Mechanics*, 469(1):121–160, 2002.

[93] L. P. Wang and M. R. Maxey. Settling velocity and concentration distribution of heavy-particles in homogeneous isotropic turbulence. *Journal Of Fluid Mechanics*, 256:27–68, 1993.

[94] Haitao Xu and Eberhard Bodenschatz. Motion of inertial particles with size larger than kolmogorov scale in turbulent flows. *Physica D: Nonlinear Phenomena*, 237(14-17):2095 – 2100, 2008. Euler Equations: 250 Years On - Proceedings of an international conference.

[95] Haitao Xu, Mickaël Bourgoin, Nicholas T. Ouellette, and Eberhard Bodenschatz. High order lagrangian velocity statistics in turbulence. *Physical Review Letters*, 96:024503, January 2006.

[96] C. Y. Yang and U. Lei. The role of the turbulent scales in the settling velocity of heavy particles in homogeneous isotropic turbulence. *Journal Of Fluid Mechanics*, 371:179–205, 1998.

[97] T. S. Yang and S. S. Shy. The settling velocity of heavy particles in an aqueous near-isotropic turbulence. *Physics of Fluids*, 15(4):868–880, 2003.

[98] P. K. Yeung. Lagrangian investigations of turbulence. 34:115–142, 2002.